



## On the link between nonlinear extensional rheology and morphology of polymeric fibers

Wingstrand, Sara Lindeblad

*Publication date:*  
2017

*Document Version*  
Publisher's PDF, also known as Version of record

[Link back to DTU Orbit](#)

*Citation (APA):*  
Wingstrand, S. L. (2017). *On the link between nonlinear extensional rheology and morphology of polymeric fibers*. Technical University of Denmark.

---

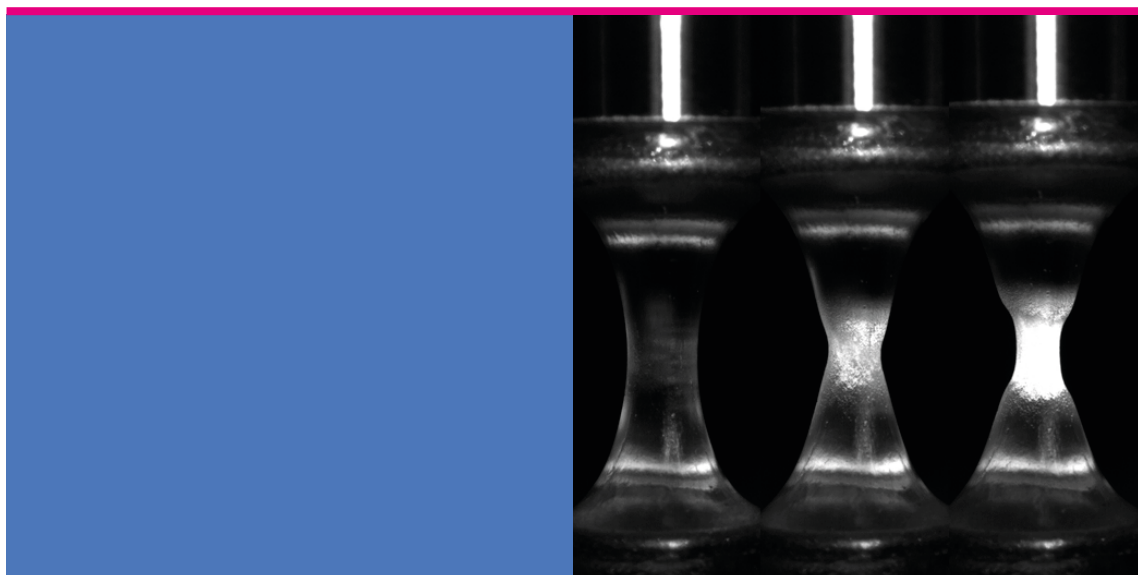
### General rights

Copyright and moral rights for the publications made accessible in the public portal are retained by the authors and/or other copyright owners and it is a condition of accessing publications that users recognise and abide by the legal requirements associated with these rights.

- Users may download and print one copy of any publication from the public portal for the purpose of private study or research.
- You may not further distribute the material or use it for any profit-making activity or commercial gain
- You may freely distribute the URL identifying the publication in the public portal

If you believe that this document breaches copyright please contact us providing details, and we will remove access to the work immediately and investigate your claim.

# ON THE LINK BETWEEN NONLINEAR EXTENSIONAL RHEOLOGY AND MORPHOLOGY OF POLYMERIC FIBERS



**Sara Lindeblad Wingstrand**

PhD Thesis  
2017

# On the link between nonlinear extensional rheology and morphology of polymeric fibers

Sara Lindeblad Wingstrand



Kongens Lyngby 2017

Technical University of Denmark  
Department of Chemical and Biochemical Engineering  
Søltofts Plads, building 229,  
2800 Kongens Lyngby, Denmark  
Phone +45 4525 2825  
[kt@kt.dtu.dk](mailto:kt@kt.dtu.dk)  
[www.kt.dtu.dk](http://www.kt.dtu.dk)

# Summary (English)

---

The mechanical properties of semi-crystalline polymeric products are highly dependent on morphology obtained during processing. For example, an ultra-high modulus polyethylene fiber owes its strength to the formation of extended chain crystals rather than folded chain crystals during fiber spinning. The imposed rate of deformation along with the molecular architecture of the polymer determines the extent of molecular deformation in the flow and which, in turn, dictates the morphology of the final product. Rheology, commonly known as "the study of flow", can link molecular architecture to the final morphology. While numerous experimental investigations on the effect of shear flow on crystallization and the final morphology of semicrystalline materials exists, analogous studies performed in extension are much more limited. This is due to experimental difficulties that only recently have been resolved with development of the filament stretching rheometer.

This thesis studies the link between the structure of a polymer liquid on the molecular level and the morphology obtained by application of extensional flow. A filament stretch rheometer enabling a controlled uniaxial extension of a viscous liquid while simultaneously monitoring the response is used. This is combined with other means of characterization, primarily ex-situ X-ray. Complexity of the investigated systems increases throughout the thesis. First, amorphous model fluids of polystyrene and poly(methyl methacrylate) are investigated to gain insight into the fundamental dynamics of linear polymer melts and solutions. We find experimental evidence that the recently proposed phenomenon of friction reduction can explain the difference in extensional behavior for diluted and undiluted polymeric liquids. Second, semicrystalline systems (high density and low density polyethylene) in extensional flow are investigated as well as the morphology obtained after cessation of the flow and quenching of the melt. Chain conformation in the melt just before quench and the final crystalline orientation are variables directly correlated with the measured stress at quench. Last, the stabilizing effect of flow-induced crystallization on uniaxially extended filaments above the equilibrium melting temperature is investigated. Polyethylene in dilution and in melts is used. Experiments on the polyethylene solutions reveal that although the samples phase separate, flow induced crystallization

prevents the filament from complete disintegration and failure. In the undiluted polyethylene, we find that the flow induced crystallization prevents brittle fracture during stretching. The more recently proposed description of the nucleating melt as a crosslinking network is found to be in good agreement with the measured extensional response. Overall, the filament stretch rheometer enables true metrics for the deforming material (e.g., true stress, true strain), different from engineering properties to be measured, thus excluding any instrumental effects. For this reason, extensional rheology which uses the filament stretching technique is found to be a powerful tool for the study of molecular dynamics in strong flows and its link to the obtained morphology.

# Summary (Danish)

---

Mekaniske egenskaber for semikrystallinske polymerprodukter afhænger af den morfologi som opnås under fremstilling. Et eksempel er ultra stærke polyethylenfibre hvor den høje styrke skyldes at de dannede krystaller under fiber spindingen indeholder udstrakte frem for foldede polymerkæder. Kombinationen af hastigheden hvormed materialet deformeres og polymerens molekulære arkitektur afgør graden af molekyledeformation under flow som endvidere bestemmer morfologien af det endelige produkt. Reologi (studie af flow) kan agere bindeled mellem molekulær arkitektur og den endelige morfologi. Der eksisterer mange eksperimentelle studier som omhandler effekten af forskydningsflow på krystallisation og opnået morfologi i semikrystallinske materialer. Antallet af lignende studier i forlængelsesflow er langt mindre. Dette skyldes eksperimentelle udfordringer som kun nyligt er blevet løst med udviklingen af filament træk reometeret.

Denne afhandling undersøger sammenhængen mellem strukturen af polymervæsker på molekylært niveau og morfologien som opnås i forlængelsesflow. Filament træk reometeret, som muliggør kontrolleret forlængelse af en viskøs væske samt måling af dens respons i flowet, er anvendt. Dette er kombineret med andre typer målinger, primært ex-situ røntgen spredning. Komplexiteten af de undersøgte systemer stiger i løbet af afhandlingen. Først er studier på amorfe systemer af polystyren og polymetylmetakrylat undersøgt for at opnå viden om lineære opløsningers og lineære smelters fundamentale dynamik. Vi finder eksperimentel evidens for at den nyligt fremsatte teori om friktions reduktion kan forklare forskellen i forlængelses respons mellem fortyndede og ufertyndede polymer væsker. Derefter studeres semikrystallinske systemer (både lav densitet og høj densitet polyethylen) i forlængelsesflow samt morfologien, som opnås efter ophør af flow og bratkøling af smelten. Kædekonformation i smelten lige inden bratkøling og den endelige krystallinske orientering er direkte forbundet gennem den målte spænding i væsken lige inden bratkøling. Sidst undersøges effekten af flowinduceret krystallisation på stabiliteten af filementer i forlængelsesflow over smeltepunktet. Både fortyndet og ufertyndet polyethylen er undersøgt. Undersøgelserne på fortyndet polyethylen viser at flowinduceret krystallisation forhindrer at filamenterne knækker grundet faseseparation. For de ufertyndede polyethylen observeres det at flowinduceret krystallisation forhindrer brud af smelten under for-

længelse. Resultaterne viser yderligere at den krystalliserende smelte kan beskrives som et krydsbundet netværk. Overordnet set, muliggør filament stræk reometeret måling af virkelige egenskaber (lokal spænding, og lokal deformation), forskelligt fra "engineering" egenskaber, hvilke ekskluderer indflydelse fra instrumentering. Derfor er forlængelses reologi, ved hjælp af forlængelses reometert, et stærkt analyseværktøj til studier vedrørende sammenhængen mellem molekylær dynamik i kraftigt deformerende flow og den efterfølgende opnåede morfologi.

# Preface

---

This thesis presents the result of my PhD carried out at the Technical University of Denmark under the Danish Polymer Center. The work has been performed over a time period of three years from September 15th, 2014, to September 15th, 2017 under the supervision of Prof. Ole Hassager and co-supervision by Assoc. Prof. Peter Szabo. Funding for the project was provided by Johanne and Aage Louis-Hansen Fonden.

The PhD study has resulted in the following publications:

- S.L. Wingstrand, N.J. Alvarez, Q. Huang, and O. Hassager, “Linear and non-linear universality in the rheology of polymer melts and solutions.” *Phys. Rev. Lett.* 115 (7), 78302 (2015). - **Chapter 2**
- S.L. Wingstrand, N.J. Alvarez, O. Hassager, and J.M. Dealy, “Oscillatory squeeze flow for the study of linear viscoelastic behavior.” *J. Rheol.* 60 (3), 407–418 (2016). - **Appendix F**
- S.L. Wingstrand, M. van Drongelen, K. Mortensen, R.S. Graham, Q. Huang, and O. Hassager, “Influence of extensional stress overshoot on crystallization of LDPE.” *Macromolecules.* 50 (3), 1134–1140 (2017). - **Chapter 3**
- S.L. Wingstrand, L. Imperiali, R. Stepanyan, and O. Hassager, “Extension induced Phase separation and crystallization in semidilute solutions of ultra high molecular weight polyethylene.” (submitted) - **Chapter 5**
- S.L. Wingstrand, B. Shen, J.A. Kornfield, K. Mortensen, D. Parisi, D. Vlasopoulos and O. Hassager, “Rheological Link between polymer melts with a high molecular weight tail and enhanced formation of shish-kebabs.” (submitted) - **Chapter 4**

Furhtermore, the following manuscript is in preparation:

- S.L. Wingstrand, B. Shen, J.A. Kornfield, A. Borger, K. Mortensen and O. Hassager, "Shish formation above the melting temperature stabilizes filaments of HDPE in extensional flow" (to be submitted) - **Chapter 6**

I would like to thank my Supervisor Prof. Ole Hassager for all the guidance and especially for giving me so much freedom on this project. I would like to thank the Hassager group for good discussions and for an open scientific environment. In particular, I would like to express my gratitude to Qian Huang and Martin van Drongelen for teaching me about extensional rheology and crystallinity in polymers, respectively, and for all the feedback and advice along the way. I would like to thank my colleagues at DPC and the workshop for being fun, smart, and always willing to help. Some people claim that obtaining a PhD is a lonely journey—I never felt that way because of you. I would like to thank my external academic and industrial collaborators Prof. Kell Mortensen, Prof. Julie A. Kornfield, Bo Shen, Anine Borger, Luna Imperiali, Roman Stepanyan, Assistant Prof. Nicolas J. Alvarez, and Prof. John Dealy for their dedication, enthusiasm and their hard work.

Finally I would like to thank Tammes, Mum, Dad, Vibe, Gulvet and last but not least my dog, Leffe, for all your support ♡

Lyngby, September 15, 2017

A handwritten signature in black ink that reads "Sara Wingstrand". The script is cursive and fluid, with the first letters of "Sara" and "Wingstrand" being capitalized and prominent.

Sara Lindeblad Wingstrand

---

## List of abbreviations

<b>CLF</b>	Contour length fluctuations
<b>DE</b>	Doi-Edwards
<b>DSC</b>	Differential scanning calorimetry
<b>DTD</b>	Dynamic tube dilation
<b>FIC</b>	Flow-induced crystallization
<b>FSR</b>	Filament stretching rheometer
<b>HDPE</b>	High density polyethylene
<b>HMMSF</b>	Hierarchical multimode stress function
<b>HT-GPC</b>	High temperature - gel permeation chromatography
<b>LDPE</b>	Low density polyethylene
<b>LVE</b>	Linear viscoelastic envelope
<b>PE</b>	Polyethylene
<b>PMMA</b>	Poly(methyl methacrylate)
<b>PO</b>	Paraffin oil
<b>PS</b>	Polystyrene
<b>SANS</b>	Small-angle neutron scattering
<b>SAOS</b>	Small-amplitude oscillatory shear
<b>SAXS</b>	Small-angle X-ray scattering
<b>SER</b>	Sentmanat fixture
<b>TGA</b>	Thermogravimetric analysis
<b>TTS</b>	Time temperature superposition
<b>WAXD</b>	Wide-angle X-ray diffraction
<b>UHMw</b>	Ultra high molecular weight
<b>UHMWPE</b>	Ultra high molecular weight polyethylene



# Contents

---

Summary (English)	i
Summary (Danish)	iii
Preface	v
List of Abbreviations	vii
<b>1 Introduction</b>	<b>1</b>
1.1 The dynamics of polymer chains in melts and solutions . . . . .	1
1.1.1 Characteristic relaxation times . . . . .	2
1.2 Molecular deformation in fast flows . . . . .	3
1.2.1 Uniaxial extension - inherently a strong flow . . . . .	4
1.2.2 Filament stretch rheometry (FSR) . . . . .	6
1.2.3 The nonlinear behavior of polymers in extensional flow . . . . .	7
1.3 The influence of fast flows on the crystallization of polymers . . . . .	8
1.4 Thesis motivation . . . . .	9
1.4.1 Thesis outline . . . . .	10
<b>2 Linear and nonlinear universality in the rheology of polymer melts and solutions</b>	<b>13</b>
2.1 Adjustment of tube dimensions and friction reduction . . . . .	14
2.2 Materials . . . . .	16
2.3 Linear and nonlinear rheology . . . . .	16
2.4 Discussion . . . . .	19
<b>3 Influence of extensional stress overshoot on crystallization of LDPE</b>	<b>23</b>
3.1 Experimental details . . . . .	26
3.1.1 Materials and method . . . . .	26
3.1.2 Ex-situ X-ray measurements . . . . .	26
3.2 Results and discussion . . . . .	27
3.3 Conclusion . . . . .	33

<b>4</b>	<b>Rheological link between polymer melts with a high molecular weight tail and enhanced formation of shish-kebabs</b>	<b>35</b>
4.1	Materials and methods . . . . .	37
4.2	Results and discussion . . . . .	39
4.2.1	HMMSF modelling and analysis of chain stretch . . . . .	40
4.2.2	Herman's orientation factor and stress at quench . . . . .	43
4.3	Conclusion . . . . .	45
<b>5</b>	<b>Extension induced phase separation and crystallization in semidilute solutions of ultra-high molecular weight polyethylene</b>	<b>47</b>
5.1	Introduction . . . . .	48
5.2	Materials and methods . . . . .	49
5.2.1	Combined filament stretch rheometry and high speed imaging of non-sticky samples . . . . .	50
5.3	Results and discussion . . . . .	52
5.3.1	Linear rheology . . . . .	52
5.3.2	Uniaxial extensional behavior . . . . .	54
5.4	Conclusion . . . . .	62
<b>6</b>	<b>Shish formation above the melting temperature stabilizes filaments of HDPE in extensional flow</b>	<b>65</b>
6.1	Materials and methods . . . . .	67
6.2	Results and discussion . . . . .	69
6.2.1	Shish nucleation and growth during extension . . . . .	69
6.2.2	Stabilization of flow and critical strain for shish formation . . . . .	71
6.2.3	Strain hardening due to crystallization . . . . .	71
6.2.4	Modelling the influence of shish on extensional rheology . . . . .	73
6.2.5	Herman's Orientation and stress at quench . . . . .	74
6.3	Conclusion . . . . .	76
<b>7</b>	<b>Conclusions, perspectives and outlook</b>	<b>77</b>
7.1	Outlook . . . . .	79
<b>A</b>	<b>Supplemental material for: Chapter 2</b>	<b>81</b>
A.1	Article in its published format . . . . .	81
A.2	Supplemental Material . . . . .	87
<b>B</b>	<b>Supplemental material for: Chapter 3</b>	<b>95</b>
B.1	Article in its published format . . . . .	95
B.2	Supplemental Material . . . . .	103
<b>C</b>	<b>Supplemental material for: Chapter 4</b>	<b>109</b>
<b>D</b>	<b>Supplemental material for Chapter 5</b>	<b>119</b>

<b>E Supplemental material for: Chapter 6</b>	<b>121</b>
<b>F Additional publication: "Oscillatory squeeze flow for the study of linear viscoelastic behavior"</b>	<b>123</b>
<b>Bibliography</b>	<b>137</b>



# Introduction

---

## 1.1 The dynamics of polymer chains in melts and solutions

An unperturbed polymer chain in a melt or solution constantly reshapes itself due to thermal fluctuations [1]. The rate of reshaping determines the linear rheology (i.e., flow dynamics at small deformations). In dilute solutions the dynamics of a linear polymer chain is well captured by the Rouse model [2]. The model neglects any chemical and hydrodynamic interaction and describes the polymer chain as a random walk of  $N$  number of Kuhn steps (a Gaussian chain) [3, 4].

For entangled polymeric liquids, one model in particular has been proven successful in predicting the linear viscoelastic rheology. This model is called the "tube model", and it is based on ideas introduced by de Gennes, Doi and Edwards [5, 6]. The basic concept behind the tube model is depicted in Figure 1.1. Here, a polymer in an entangled melt is reduced to a primitive chain with limited ability to move in its transverse direction due to entanglements with neighboring chains (Figure 1.1a). Effectively, the entanglements can be regarded as constituents of a tube surrounding the test chain (Figure 1.1b). In order for the polymer to relax, it has to reptate—a snakelike motion—out of the confining tube. The primitive chain between two entanglements is described by the Rouse model as a random walk of  $N_e$  Kuhn steps (Figure 1.1c). The tube model combined with the Rouse model, with additions such as contour length fluctuation (CLF), dynamic tube dilation (DTD), arm retraction and sticky Rouse, enables the rheology of a vast range of polymeric systems to be described [7, 8, 9, 10]. Examples of polymeric systems that have been successfully modelled include anything from simple linear melts, solutions, binary blends, and polydisperse melts to complicated branched chain architectures such as stars, combs,

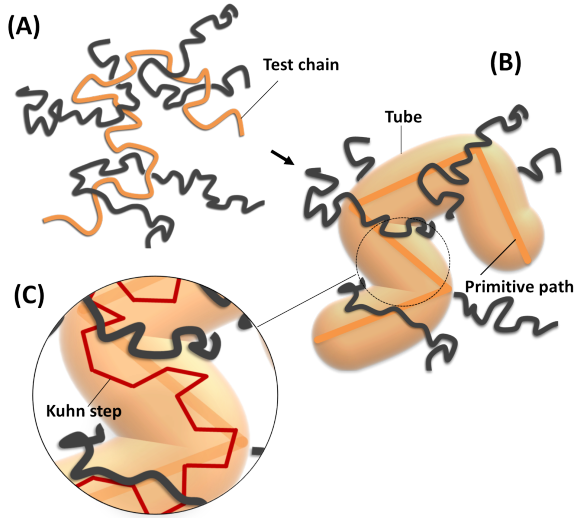


**Figure 1.1:** A sketch of the tube analogy for entangled polymeric liquids. (a) A primitive entangled polymer chain in a melt. The polymer test chain is well entangled with neighboring polymer chains. (b) A simplified picture of the polymer melt applied in the original tube model. Here, the entanglements constitute a tube with a primitive path. (c) An enlargement of one entanglement segment showing how the test chain is reduced to a random distribution of connected Kuhn steps.

PomPom, and more recently, supramolecular systems [11, 12].

The tube model contains only three material parameters: the relaxation time of one entanglement  $\tau_e$ , the number of entanglements  $Z = N/N_e$  and as the plateau modulus  $G_N^0$  (i.e., the modulus obtained for the corresponding cross-linked material with no free ends):  $\tau_e$  and  $G_N^0$  are material characteristics [13], while  $Z$  is a function of the molecular weight.

### 1.1.1 Characteristic relaxation times

The Rouse model and the tube model enable characteristic relaxation times of a polymeric liquid to be defined. For a linear unentangled polymer (i.e., in a dilute solution), the characteristic relaxation time is the Rouse relaxation time [2]. It is related to the number of Kuhn steps  $N$  and the relaxation time of one Kuhn step  $\tau_0$  as follows:

$$\tau_R = \tau_0 N^2 = \tau_e Z^2 \quad (1.1)$$

As seen,  $\tau_R$  can be expressed in terms of tube model parameters ( $\tau_e$  and  $Z$ ) even though it is derived for an unentangled polymer chain. Evidently, linear entangled polymer chains also have a Rouse relaxation time. It is invisible in the linear regime as the relaxation process is dominated by reptation. The reptation time ( $\tau_d$ ) is given by [6]:

$$\tau_d = 3\tau_e Z^3 \quad (1.2)$$

The above relation holds for large values of  $Z$  (i.e.,  $Z > 100$ ). For polymers having  $10 < Z < 100$ , the exponent in Eq. (1.2) is closer to 3.4 due to CLF [14]. Unlike  $\tau_R$ , which is independent of concentration,  $\tau_d$  scales with the polymer weight fraction  $\phi$ . In a molecular solvent, it scales linearly with  $\phi$ . This scaling is also valid for binary blends satisfying the Struglinski-Graessley criterion, which is  $Gr = \frac{Z_L}{Z_S} > 1$ , where  $Z_L$  and  $Z_S$  are the number of entanglements for the long and short component, respectively. The criterion is derived from the argument that the constrain release by Rouse (i.e., the combined reptation of the short chains and Rouse relaxation of the long chains) must be faster than the reptation time of the long chains [15]. Larson and Park later reconsidered the problem and showed that  $Gr > 0.064$ , which is the more widely used version of the Struglinski-Graessley criterion [16].

Polydisperse systems are more complicated. Rather than having a single Rouse and reptation time, the distribution in molecular weight causes the liquid to have a corresponding distribution of relaxation times—one Rouse/reptation time for each molecular weight fraction  $i$ . The Rouse relaxation time  $\tau_{R,i}$  for a given molecular weight fraction is still given by Eq. (1.1). Reptation in a polydisperse sample is complicated. One has to consider reptation as a hierarchical relaxation where the short chains relax first, thus diluting the long chains [17].

## 1.2 Molecular deformation in fast flows

Polymer chains can be deformed by flow if the deformation rates are sufficiently high. The degree of chain deformation is evaluated on the basis of the Weissenberg number  $Wi$ , which weighs the rate of deformation to the relaxation rate of the polymer [18].

$$\text{SHEAR} \quad Wi = \dot{\gamma}\tau \quad (1.3)$$

$$\text{EXTENSION} \quad Wi = \dot{\epsilon}\tau \quad (1.4)$$

Here,  $\tau$  can be any characteristic relaxation time, and  $\dot{\gamma}$  and  $\dot{\epsilon}$  the deformation rates imposed on the liquid in shear and extension, respectively [19]. The range of accessible deformation rates is limited by the instrument, while the characteristic relaxation time is determined by the polymer. For the characteristic Rouse and reptation time, corresponding Weissenberg numbers  $Wi_R \propto Z^2$  and  $Wi_d \propto Z^3$ , respectively, are defined. It follows that for any given deformation rate,  $Wi_R < Wi_d$ .

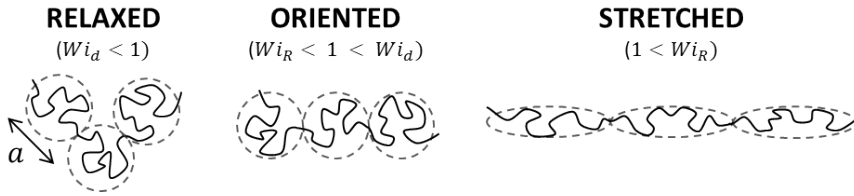


**Figure 1.2:** A sketch illustrating the three regimes of chain deformation—relaxed (left), oriented (middle), and stretched (right).

Classical polymer physics operates with three regimes of chain deformation for entangled systems—relaxed, oriented, and stretched. Figure 1.2 shows the fundamental difference between the three regimes. The circles indicate one entanglement segment, also known as a Gaussian "blob" [20, 21]. In the relaxed state ( $Wi_d < 1$ ), the chain can be described by a random walk of  $Z$  Gaussian blobs of diameter  $a$ . The equilibrium primitive path  $L_{eq}$  is thus given by  $L_{eq} = Za$ . The average end-to-end distance  $\langle R \rangle^2$  can be expressed as:

$$\langle R \rangle^2 = Za^2 = Nb^2, \quad (1.5)$$

where  $b$  is the length of a Kuhn step. In the oriented regime ( $Wi_R < 1 < Wi_d$ ), the blobs start to align and the expression for  $\langle R \rangle^2$  (Eq. (1.5)) no longer applies. The blob diameter does not change, and the primitive path  $L$  is unchanged as well ( $L = L_{eq}$ ). In the case of a fully oriented chain,  $\langle R \rangle^2 = L_{eq}^2$ . For the stretched state ( $Wi_R > 1$ ), the blobs are deformed. For a mild stretch, the chain conformation remains Gaussian within the elongated blob. For a large stretch, the conformation becomes non-Gaussian. In the extreme case of a fully stretched chain, the primitive path is given by  $L = Nb$ . From this, one can define the maximum stretch ratio  $\lambda_{max} = \frac{Nb}{Za} = \sqrt{N_e}$ , where  $N_e = \frac{N}{Z}$  is the number of Kuhn steps per entanglement segment. The exact onset of chain stretch is an ongoing discussion. Some claim that chain stretch already occurs at  $Wi_R > 0.5$  [22, 23], while others propose a concentration dependency such that chain stretch occurs at  $Wi_R > \phi$  [24].

### 1.2.1 Uniaxial extension - inherently a strong flow

Extensional flow, also referred to as a shear free flow [19], exists in various forms: uniaxial, planar, and biaxial extension. Uniaxial extension in Cartesian coordinates comprise an elongation along one axis  $z$  and, due to mass conservation, a contraction along the two remaining axes,  $y$  and  $x$  (see Figure 1.3). In planar extension, the contraction only occurs along one axis  $y$  while  $x$  remains unchanged. A biaxial extension, the inverse of a uniaxial extension, comprises an extension along two axes  $y$  and  $x$  while the contraction occurs along the last axis  $z$ . This work concerns only

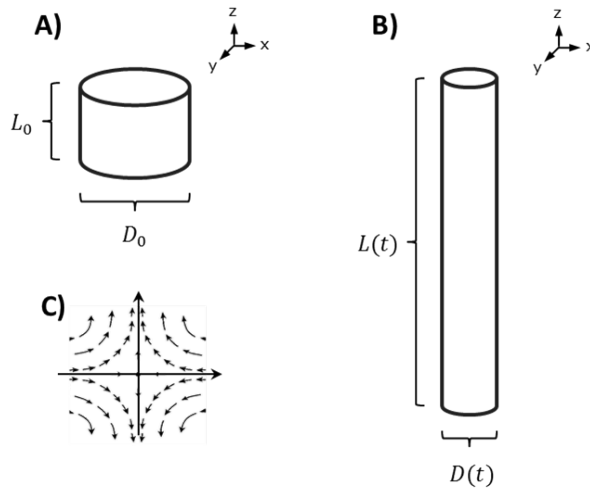


**Figure 1.3:** A sketch of uniaxial flow in cylindrical coordinates. (A) Initial cylinder of diameter  $D_0$  and length  $L_0$ . (B) Uniaxially deformed cylinder with diameter  $D(t)$  and length  $L(t)$ . (C) Stream lines around the midplane of the cylinder during deformation.

uniaxial extension; hence, planar and biaxial extension are not discussed further.

The strain measure in a homogeneous uniaxial extension is known as the Hencky strain  $\varepsilon$ :

$$\varepsilon = \ln \frac{L(t)}{L_0} \quad (1.6)$$

$L_0$  and  $L(t)$  are the initial length and the length at time  $t$ , respectively. For an incompressible fluid,  $\varepsilon$  can be obtained from the change in diameter as well:

$$\varepsilon = -2 \ln \frac{D(t)}{D_0} \quad (1.7)$$

with  $D_0$  and  $D(t)$  being the diameter analogues to  $L_0$  and  $L(t)$ , respectively.

Uniaxial extension is vastly different from shear in terms of polymer rheology. Inherently, uniaxial flow is considered a strong flow relative to shear as it contains a deformation gradient in the same direction as the deformation. Additionally, unlike shear, extension contains no potential for molecular tumbling [25]. Extensional flows are found in many polymer processing unit operations, such as fiber spinning and blow moulding. However, the literature on controlled uniaxial extension of polymeric liquids is limited relative to the number of studies conducted in shear. That is due to

experimental difficulties that only recently have been resolved with the development of the Sentmanat fixture (SER) and the filament stretch rheometer (FSR) [26, 27].

### 1.2.2 Filament stretch rheometry (FSR)

The filament stretch rheometer developed at the Technical University of Denmark enables a viscous liquid to be extended uniaxially. The advantage over other extensional rheometers is the active feedback control loop that prevents filament failure caused by necking instability [28, 29, 30] and that enables the performance of various types of experiments, such as constant rate (all the way to steady state), creep, and stress relaxation [31, 32]. The commercially available tabletop version (VADER 1000 from Rheofilament) is illustrated in Figure 1.4. The device consists of a top and a bottom plate, between which the sample is sandwiched; a laser micrometer is situated in the midplane of the sample, a load cell is mounted on the bottom plate and a convection oven with quartz windows encloses the sample. The sample is deformed by movement of the top plate. The no-slip boundary condition at the plates results in an inhomogeneous uniaxial deformation. As a consequence, the strain measure based on the change in length (Eq. (1.6)) is no longer a true measure of strain but rather a nominal strain measure,  $\varepsilon_N$ . The true Hencky strain is measured locally in the midfilament plane using the change in diameter  $\varepsilon$  (Eq. 1.7). The sample is assumed to possess rotational symmetry in the pulling direction and axis symmetry across the midfilament plane. Neglecting inertia and surface tension, the corresponding mean extensional stress difference in the midfilament plane  $\langle \sigma_{zz} - \sigma_{rr} \rangle$  is given as follows [33]:

$$\langle \sigma_{zz} - \sigma_{rr} \rangle = \frac{F(t) - \frac{1}{2}m_f g}{\frac{\pi}{4}D(t)^2} \quad (1.8)$$

Here,  $F(t)$  is the force exerted by the fluid on the force cell,  $m_f$  is the mass of the sample, and  $g$  is the gravitational acceleration.

At low sample aspect ratios, a significant shearing contribution due to the no-slip boundary condition on the plates is present. This contribution is accounted for by using following approximation [34]:

$$\langle \sigma_{zz} - \sigma_{rr} \rangle = \frac{F(t) - \frac{1}{2}m_f g}{\frac{\pi}{4}D(t)^2} \cdot \frac{1}{1 + \left(\frac{D(t)}{D_0}\right)^{10/3} \exp(-\Lambda_i^3)/(3\Lambda_i^2)} \quad (1.9)$$

Here,  $\Lambda_i = L_i/D_i$  is the initial aspect ratio of the sample, with  $L_i$  and  $D_i$  being the initial length and diameter of the sample before prestretching. The last factor corrects for the shearing contribution at low  $\varepsilon(t)$ .

An additional feature of the VADER 1000 is filament quenching. The oven can be pushed upwards within 1 s, leaving the sample exposed to ambient conditions. The

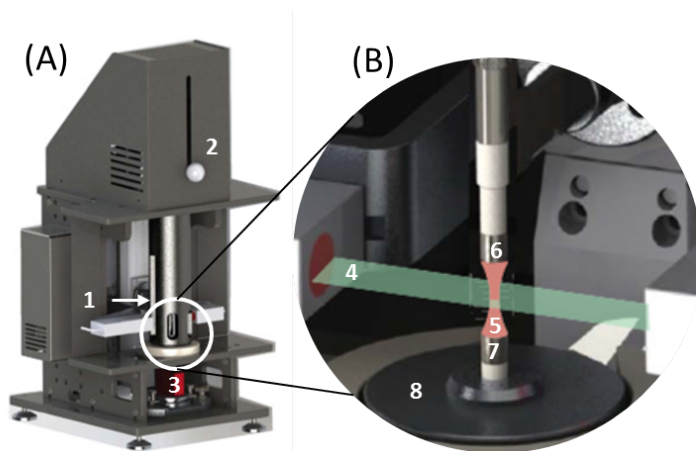


**Figure 1.4:** A sketch of the tabletop filament stretch rheometer (VADER 1000). (A) shows the entire instrument with the oven (1), oven knob (2), and force cell (3). (B) A magnification of the circled area in (A) with the oven pushed back. Here, the laser sheet (4), sample (5), top and bottom plate (6,7), and oven floor with nitrogen inlet (8) are shown. The sketch is modified from [35]

resulting quench rate have been estimated to ( $\sim 10\text{K/s}$ ) in the presence of a mild  $N_2$  flow. Movement of the top plate is automatically disabled once the oven is opened to prevent further stretching of the quenched filament.

**Constant Hencky strain rate experiments** This study mostly reports the results of constant rate experiments. Here, the Hencky strain rate ( $\dot{\epsilon}$ ) is kept constant throughout the stretch according to the following:

$$\epsilon(t) = -2 \ln \left( \frac{D(t)}{D_0} \right) = \dot{\epsilon} t \quad (1.10)$$

### 1.2.3 The nonlinear behavior of polymers in extensional flow

Strain hardening is believed to be a result of chain stretch and is identified as an upwards departure from the linear viscoelastic envelope (LVE) in a plot of the stress growth coefficient  $\eta_E^+ = \langle \sigma_{zz} - \sigma_{rr} \rangle / \dot{\epsilon}$  versus time. The degree of strain hardening in polymeric liquids depends on the chain architecture of the polymer (e.g., linear, branched, comb, etc.) along with the molar mass and the extent of dilution. Factors like these influence the relaxation times and mechanisms causing the nonlinear

behaviour to differ.

### 1.3 The influence of fast flows on the crystallization of polymers

Deformation of polymer chains, particularly the high molar mass fraction, in strong flow fields influences the morphology obtained upon cooling and the cessation of the flow [36, 37]. The deformation of polymer chains by flow favors crystallization, kinetically and thermodynamically. Kinetically, crystallization occurs because the stretched chains resemble the crystalline ordering, lowering the kinetic barrier needed for the polymer to crystallize. Thermodynamically, it occurs due to the entropy loss upon molecular ordering that chain stretch induces [38]. In semicrystalline polymers, chain deformation not only increases the rate of crystallization, but in some cases, it also increases the structure of the formed crystallites [38, 39]. Figure 1.5 illustrates the various crystalline morphologies obtainable for polyethylene (PE) depending on the extent of molecular deformation prior to crystallization. Under quiescent conditions, PE forms pointlike nuclei and crystallize into randomly oriented spherulites [40]. When crystallization occurs from a state at which the polymer chains are sufficiently aligned by the flow, needlelike nuclei are likely to form, resulting in shish-kebab structures [41, 42]. This type of morphology is initiated by the formation of crystalline fibrils (shish) oriented along the flow direction, followed by the subsequent growth of lamellae stacks perpendicular to the flow direction (kebabs). Depending on the extent of molecular deformation, twisted or straight kebabs are obtained (Type I and Type II, respectively). Type I forms at milder conditions compared to Type II.

Nuclei are created from so-called precursors—a rather fuzzy concept of locally aligned chain segments with an increased potential for nucleus formation [44]. Precursors are either pointlike or threadlike, giving rise to pointlike or needlelike nuclei, respectively. The type and density of precursors can be divided in three regimes directly related to the three states of chain deformation (relaxed, oriented, and stretched) defined by the Weissenberg number  $Wi$  (see Section 1.2). 1) In the relaxed state ( $Wi_d < 1$ ), no enhancement of precursor formation relative quiescent conditions is obtained. As a result, the morphology is indifferent from structures obtained under quiescent conditions. That is a few but large spherulites. 2) In the oriented state ( $Wi_R < 1 < Wi_d$ ), an increase of pointlike precursor density is obtained [45]. The resulting increased number of nuclei results in a faster crystallization rate. The morphology of the fully crystallized sample contains an increased number of spherulites with a smaller radius relative to the spherulites obtained under quiescent conditions. 3) The stretched state ( $Wi_R > 1$ ) promotes formation of threadlike precursors initiating formation of shish through needlelike nucleation [46].

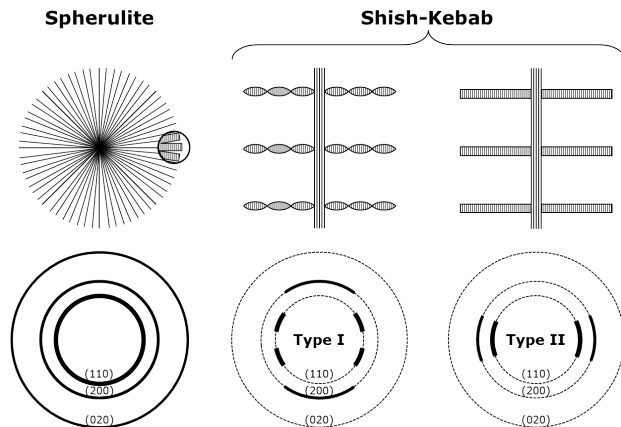


**Figure 1.5:** (Top) A schematic showing crystal structures of PE. Spherulitic morphology (left) is obtained under quiescent conditions, shish-kebab of Type I with twisted lamellae (middle) is obtained under conditions at which an intermediate backbone stretch occurs, and shish-kebab of Type II with straight lamellae (right) is obtained for a large backbone stretch. (Bottom) Corresponding 2D wide-angle x-ray diffraction (WAXD) patterns along with diffraction planes given in brackets. (Adapted from van Dronghen et. al [43])

The vast majority of studies investigating the influence of flow on crystallization in polymers, employs the Janeschitz-Kriegl protocol [47, 36, 48, 49]. Here a sample is heated well above its equilibrium melting temperature  $T_m$  to erase all thermo-mechanical history. The temperature is subsequently lowered to a temperature below, but close, to  $T_m$  where the quiescent crystallization rate is slow. The application of a fast flow in this regime causes a significant increase in the rate of crystallization referred to as flow-induced crystallization (FIC) [46]. One advantage of this protocol is that it enables FIC kinetics, such as crystalline nucleation and growth rates, to be studied in isothermal conditions [50].

## 1.4 Thesis motivation

Solid properties of semicrystalline polymeric materials depend on crystallinity, which in turn depends on flow and rheology [51]. Connecting the three (rheology, crystallinity, and solid properties) on a fundamental level is still an open problem [46]. Much experimental modelling work has been done on flow-induced crystallization (FIC) in shear, especially studies concerning kinetics [46, 52]. Due to experimen-

tal difficulties, studies connecting crystallization and rheology in extension are quite limited [53, 54, 55, 56, 27], especially studies concerning large deformations ( $\varepsilon > 4$ ).

The aim of this study is to connect extensional rheology and crystalline morphology in polyethylene, experimentally. All studies evolve around the FSR, and the experiments are designed to investigate areas that cannot be explored by currently available alternatives (e.g., SER). Such areas comprise experiments performed at high Hencky strains,  $\varepsilon > 3.5$ , or experiments requiring an active control scheme (e.g., steady flow, stress overshoot or stress undershoot). Most morphological studies are performed using ex-situ X-ray scattering; that is, small-angle X-ray scattering (SAXS) and/or wide-angle X-ray scattering (WAXD). All the systems investigated contain a high molar mass component to facilitate chain deformation during stretching. The data are interpreted from the established framework for polymer physics, combining knowledge of chain architecture, molecular composition, and rheology. With this work, I hope to provide insight into the extensional dynamics of polymeric liquids as well as its influence on subsequent crystallization.

### 1.4.1 Thesis outline

The thesis is arranged such that the complexity of the studied system increases as one advances through the chapters. The studied systems can be grouped into three categories of increasing complexity during extension: 1) amorphous polymeric liquids in uniaxial extension, 2) uniaxial extension and subsequent non-isothermal crystallization, and 3) isothermal crystallization during uniaxial extension. To a large extent, Chapters 2–6 are identical to the published/submitted/to-be-submitted articles. Some parts, however, are left out, moved to the introduction, or placed in the appendices to avoid unnecessary repetition. Each chapter contains an introduction specific to the story in question, a description of the materials and method, and a presentation, discussion, and conclusion of the findings.

Chapter 2 belong in category 1) and concerns the fundamental question of universality in the dynamics of polymer melts and solutions. Experimentally, we show that by incorporating recent ideas about friction reduction [57] in the design of a polymer solution, the rheological behavior of a polymer melt can be mimicked, both in the linear and the nonlinear regime.

Chapters 3 and 4 belong in category 2). The materials are semicrystalline systems of various chain architectures. Using the FSR in combination with ex-situ SAXS and WAXD, we study the response of the melts in extensional flow as well as the obtained morphology after the cessation of flow and quench to room temperature. The experiments are inspired by analogous experiments performed on deuterated amorphous systems in which the structure was investigated ex-situ using small-

angle neutron scattering (SANS) [58]. The experiments are conducted at well above  $T_m$  to prevent that FIC occurs during the extensional experiment. The advantage of this protocol is that a qualified estimate of the molecular configuration, due to significant advancements in nonlinear rheological theories, is obtained. Thus, the molecular configuration just before quench can be compared with the morphology of the fully crystallized sample. The disadvantage, however, is that the crystallization is nonisothermal; hence, crystallization kinetics of such systems is complicated to elucidate.

Chapters 5 and 6 belong in category 3). Here, FIC above  $T_m$  is investigated in extensional flow. We use ex-situ SAXS and high-speed imaging to visualize the effect of the flow on crystallization. In addition, the time-temperature superposition (TTS) principle is used to gain insight into the dynamics during stretching. TTS enables the design of extensional stretch experiments performed at different temperatures to have the same stress-strain-response, assuming no crystallization is induced. The failure of TTS is a sign that additional dynamics, apart from chain dynamics, has taken place (e.g., FIC). We use the success/failure of TTS to interpret the onset and progression of FIC in PE both in melt and in solution.

Chapter 7 summarizes the contributions of this PhD study to the field of extensional rheology and the crystallization of polymers. It highlights key findings as well as missing pieces in the puzzle that can be explored in future studies.

Appendices A-E contain supplemental material for the corresponding Chapters 2–6, respectively. If the the article on which a chapter is based, is published, the appendix contains the article in its published format, as well. The supplemental material contains information unnecessary for the main message of the the story but relevant for parties interested in reproducibility, validity, or just details in general. Examples of information found in these appendices are detailed experimental procedures, uncertainty assessments, descriptions of implementations of models in MatLab, un-normalized plots of data, and technical drawings.

Appendix F contains a review article on oscillatory squeeze flow in its full length and original layout. This article reports work performed as a part of this PhD study; however, the scope of the article is too far from the scope of the thesis to make a chapter.



## CHAPTER 2

# Linear and nonlinear universality in the rheology of polymer melts and solutions

---

Understanding the dynamics of polymeric liquids has great importance in the design and processing of soft materials. While slow flow dynamics is now resolved, fast flow dynamics is still unsolved, especially due to the lack of experimental evidence. We here manipulate a poly(methyl methacrylate) solution into exhibiting the same flow behavior as a polystyrene melt. Strikingly similar responses of the fluids are seen both in slow and very fast flow. With this discovery we show that dynamics in polymeric liquids can be generalized and captured in one single polymer physics model.

Universality of molecular dynamics is a fundamental assumption in polymer physics [59, 60]. It is the underlying framework of the most successful theoretical model, known as the tube model [5, 6]. The significance of this assumption is that model systems at room temperature, i.e., polymer solutions, could be used to represent polymer melts at elevated temperatures. While the existence of a room temperature model material would be highly desirable, unfortunately a polymer solution with the same fast flow dynamics (nonlinear behavior) as a polymer melt has not yet been observed. It was recently shown that two linear polymeric systems with the same number of entanglements exhibit identical slow flow dynamics (linear behavior), but strikingly different nonlinear behavior [61]. The lack of evidence of universality in strongly nonlinear conditions leaves one wondering whether such an assumption is valid. For two polymeric systems to have identical flow dynamics, researchers have hypothesized that they must have the same following characteristics: (i) the same number of entanglements, (ii) the same degree of flexibility (number of Kuhn segments per entanglement), and, very recently, (iii) the same potential for monomeric friction reduction [57]. Whereas systems with identical characteristics (i) and (ii) have been studied [62, 63], systems with the same characteristics (i)–(iii) have not, the reason being that usually characteristic (ii) can never be adjusted without compromising characteristic (iii).

This study observes universal behavior between a polymer solution and a polymer melt with the same three characteristics, confirming the assumption of universality in polymer physics for both linear and nonlinear dynamics. The following is a brief description of how to manipulate all three characteristics independently.

## 2.1 Adjustment of tube dimensions and friction reduction

The number of entanglements per chain ( $Z$ ), characteristic (i), is solely responsible for the linear response of a polymeric liquid [61]. It is given by the ratio of Kuhn steps in the entire chain ( $N$ ) over Kuhn steps per entanglement segment ( $N_e$ ), or analogously on a molar mass basis

$$Z = \frac{N}{N_e} = \frac{M_w}{M_e}. \quad (2.1)$$

Here,  $M_w$  and  $M_e$  are the molar masses of the entire chain and one entanglement segment, respectively. As  $M_e$  is independent of polymer molar mass, the number of entanglements can be adjusted from the molar mass of the polymer as it scales linearly with  $M_w$ . The addition of a solvent to a polymer melt increases  $M_e$ . However,

a proportional change in  $M_w$  may be used to keep the number of entanglements unchanged.

The number of Kuhn steps per entanglement  $N_e$ , characteristic (ii), becomes important in the nonlinear regime [64].  $N_e$  describes the rigidity of an entanglement segment and is used in several nonlinear models [65, 66, 67, 12, 68, 69]. For an undiluted polymer,  $N_e$  is determined by its chemistry alone. Adding a solvent to an entangled polymeric liquid will increase the spacing between entanglements, thus increasing the number of Kuhn steps per entanglement segment. In a solution with a given polymer concentration ( $\phi$ ) the number of Kuhn steps between entanglements ( $N_e(\phi)$ ) scales as

$$N_e(\phi) = N_e(1)\phi^{-\alpha}. \quad (2.2)$$

Here,  $N_e(\phi)$  is the number of Kuhn steps per entanglement segment for the undiluted system and  $\alpha$  is the dilution exponent with a value between 1 and 1.3, depending on concentration [70]. It is realized that dilution increases  $N_e$ ; hence, the only way to match  $N_e$  between a polymer melt and a solution is to have two different chemistries. Thus, by allowing a change in chemistry and molecular weight, both  $N_e$  and  $Z$  can be adjusted independently.

As previously mentioned, no two polymer liquids having identical characteristics (i) and (ii) (i.e., the same  $N_e$  and  $Z$ ) have shown the same nonlinear behavior. In fact, evidence of the contrary is available [61]. Hence, experimental evidence suggests that  $Z$  and  $N_e$  alone cannot account for the nonlinear behavior of polymeric liquids. This is why the third concept, monomeric friction reduction, proposed by Ianniruberto and co-workers is important [57]. Friction reduction, characteristic (iii), encountered in nonlinear flows, arises from the anisotropic environment locally around the polymer chain [57, 71]. In the case of diluted polymers, traditional (small) solvent molecules remain isotropic even at large deformations, inhibiting any flow-induced monomeric friction reduction. The very nature of friction reduction seemingly disrupts any possibility of ever obtaining a solution that behaves as a melt, unless the solvent molecule possesses the same potential for friction reduction as the polymer itself, i.e., such as in the case of oligomers. Using oligomers (polymers with less than 100 repeating units) as the solvent is a potential method of matching the friction reduction between the polymer and the solvent. Molecular dynamics simulations of polystyrene oligomers have shown that the degree of friction reduction in fast shear flows indeed increases with increasing molar mass of the oligomers [61]. Hence, we hypothesize that the friction reduction of a polymer solution increases as the number of oligomer Kuhn steps  $N_s$  increases. Yet, in order not to create a binary blend of polymers where  $N_e$  is fixed,  $N_s$  must be smaller than  $N_e$  to avoid forming any additional entanglements, i.e.,  $N_s/N_e < 1$ . On the contrary  $N_s/N_e$  should be as large as possible in order to

**Table 2.1:** Material characteristics of PS melts and PMMA solutions.

Sample	$\phi$	$\alpha$	$Z$	$N_e$	$N_s/N_e$
PS-285k	1.00	...	21	22	...
PMMA-270k/o-4k	0.45	1.17	20	23	0.67
PS-100k	1.00	...	7.7	22	...
PMMA-86k/o-4k	0.51	1.08	7.0	20	0.59

have a similar potential for anisotropy and hence friction reduction as a melt.

## 2.2 Materials

Solutions investigated in this study are prepared from poly(methyl methacrylate) (PMMA) with  $M_w = 86$  kg/mol (PMMA-86k) and  $M_w = 270$  kg/mol (PMMA-270k). From the linear rheology,  $Z$  is estimated to be 14 for PMMA-86k and 52 for PMMA-270k, see Appendix A.2 for details.  $N_e$  is estimated to be 10 and 9, respectively [72] [73]. Oligo(methyl methacrylates) of various lengths are investigated as the solvent for the samples. Among the various options (see Appendix A.2), an oligomer of  $M_w = 3.5$  kg/mol (referred to as o-4k) is found to be the most optimal solvent for this study, i.e., the longest solvent molecule that does not form entanglements. The reference materials that we aim to mimic using PMMA are two polystyrene (PS) melts. They have previously been characterized by Nielsen et al. and Huang et al. [61, 74], one with  $M_w$  equal to 103 kg/mol the other with 285 kg/mol, referred to as PS-100k and PS-285k, respectively. Undiluted PS is known to have  $M_e = 13.3$  kg/mol and analogously  $N_e = 22$  [61, 13]. Characteristics of these samples related to the tube model are given in Table 2.1. Diluting PMMA-86k and PMMA-270k in o-4k yields the solutions PMMA-86k/o-4k and PMMA-270k/o-4k, respectively, with the characteristics given in Table 2.1. Values of  $Z$  and  $N_e$  for the PMMA solutions and the reference PS melts are in good agreement (within  $\pm 10\%$ ). Furthermore, we observe that  $N_s/N_e$  for the PMMA solutions are close to 1 without exceeding it, as required.

## 2.3 Linear and nonlinear rheology

The linear and nonlinear response of the PMMA solutions and PS melts are shown in Figures 2.1a and b, respectively. The linear response is obtained from a small amplitude oscillatory shear (SAOS) flow whereas nonlinear characterization is obtained from uniaxial extension (see Appendix A.2 for experimental details).

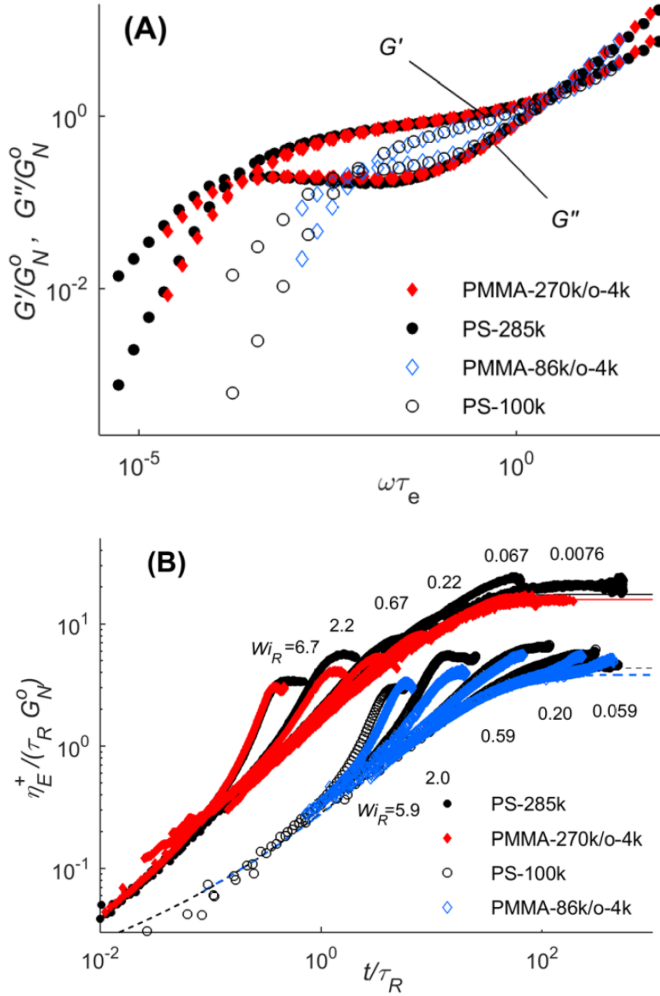


**Figure 2.1:** Nondimensional mechanical response of the PS melts and the PMMA solutions. Samples have a similar number of Kuhn steps between entanglements  $N_e$ , degree of friction reduction, and pairwise matching number of entanglements  $Z$ . Closed symbols indicate samples with  $Z \approx 20$ , open symbols samples with  $Z \approx 7$ . Black indicates reference data for pure polystyrene melts [61, 74]. (A) The linear response from small amplitude oscillatory shear, expressed in terms of normalized dynamic moduli versus normalized frequency. (B) The response of melts and solutions in extensional flow at various nondimensional rates of deformation ( $W_{iR}$ ). The results are expressed in terms of the normalized stress growth coefficient. Samples with  $Z \approx 7$  have been shifted horizontally one order of magnitude higher for clarity. Solid and dashed lines are linear predictions obtained from fits of the SAOS data.

The linear response (Figure 2.1a) is expressed in terms of the dynamic moduli  $G'$  and  $G''$  versus frequency ( $\omega$ ), representing the elastic and viscous response of the fluid, respectively. The solvent is expected to contribute an amount to  $G'' = (1 - \phi)\eta_s\omega$ , where  $\eta_s = 410 \text{ Pa s}$  is the solvent viscosity. Hence, the solvent only contributes a negligible amount to the moduli and the solvent does not affect the universality argument. The dynamic moduli have been normalized by the characteristic plateau modulus ( $G_N^0$ ), a hypothetical value of the plateau in  $G'$  for  $\omega \rightarrow \infty$ . Frequency is normalized by the characteristic time  $\tau_e$  related to the second crossover of the dynamic moduli. The parameters  $G_N^0$ ,  $\tau_e$ , and  $Z$  may be extracted from models such as the Baumgaertel-Schausberger-Winter spectrum or the Likhtman-Mcleish model (see the Appendix A.2) [75, 10].

From the linear characterization in Figure 2.1a, it is seen how samples with the same  $Z$  overlap, as expected. Tube stretch and friction reduction are inactive under these conditions and, consequently,  $N_e$  as well as the type of solvent are irrelevant for the observed similarity.

The most severe nonlinear behavior of polymers is encountered in extension, including uniaxial extension. This study employs the filament stretching rheometer (see Section 1.2.2) to measure the fast flow dynamics of melts and solutions [26, 32, 28]. The instrument measures the stress in the polymer sample by monitoring the axial force and the midfilament diameter. This study performs extensional measurements at a controlled rate, the Hencky strain rate  $\dot{\epsilon}$ . The resulting response of the polymeric liquids is shown in Figure 2.1(b). It displays the transient behavior in terms of the extensional stress growth coefficient, given by

$$\eta_E^+(t) = \frac{\sigma_{zz} - \sigma_{rr}}{\dot{\epsilon}} \quad (2.3)$$

Here,  $\sigma_{zz}$  and  $\sigma_{rr}$  represent the axial and radial component of the stress tensor, respectively. Normalization of  $\eta_E^+(t)$  is based on a characteristic viscosity given by the plateau modulus  $G_N^0$  and the characteristic Rouse relaxation time scale for the whole polymer chain  $\tau_R = \tau_e Z^2$  (see Appendix A.2 for more details). In addition, the linear prediction obtained from fitting the Baumgaertel-Schausberger-Winter spectrum to the SAOS data is shown as solid and dashed lines in Figure 2.1(b).

Each upturn represents a single filament stretch experiment, performed at a given constant  $\dot{\epsilon}$ . To enable comparison, strain rates are given in terms of nondimensional Weissenberg numbers ( $Wi_R = \dot{\epsilon}\tau_R$  indicated at each experiment) instead of the absolute value  $\dot{\epsilon}$ .  $Wi_R$ , as described in Section 1.2, compares the Rouse relaxation time of the chain contour length  $\tau_R$  to the imposed rate of deformation  $\dot{\epsilon}$  [18]. As long as  $Wi_R < 1$  the number of Kuhn lengths between entanglements  $N_e$  is unimportant. However, for  $Wi_R > 1$  motions on the scale of a Kuhn length occur, and therefore

$N_e$  becomes an important parameter. In a similar way friction reduction is only activated in a highly anisotropic environment experienced at  $Wi_R > 1$ , where chains are aligned and stretched [23].

In Figure 2.1(b) good agreement with the linear prediction is observed for  $Wi_R \ll 1$ , as expected. At larger  $Wi_R$  a clear deviation from linear behavior is observed. This upward deviation of  $\eta_E^+(t)$  from the linear prediction is known as strain hardening. The most important characteristic is that the transient behavior of PS melts and PMMA solutions stretched at the same  $Wi_R$  is the same for all time, for all experiments. This similarity between melt and solution behavior has, to our knowledge, never been observed before.

A plateau region is observed for  $\eta_E^+(t)$ , towards the end of each stretch experiment in Figure 2.1(b). Here, the polymeric liquids reach a steady state extensional viscosity  $\eta_E$ . These values are plotted against  $Wi_R$  in Figure 2.2. In the linear regime, extensional viscosity  $\eta_E$  is often expressed in terms of the zero shear rate viscosity  $\eta_0$ , where  $\eta_E = 3\eta_0$ . Theoretically,  $\eta_E/3\eta_0 \rightarrow 1$  as  $Wi_R \rightarrow 0$  for linear polymeric liquids, as is indeed the case here.

The PMMA solutions prepared in this work exhibit an initial increase in  $\eta_E$ , followed by a steady decrease. The increase is more pronounced for a low number of entanglements both for the solutions and the melts. Furthermore, for liquids with a sufficiently high number of entanglements,  $\eta_E$  follows the power law  $\eta_E \propto Wi_R^{-0.5}$ , previously only observed for polymer melts [31]. Overall, the PMMA solutions and PS melts with the same three characteristics behave identically.

## 2.4 Discussion

The ability of the oligomer to induce friction reduction can be explained from the concept of average orientation introduced by Yaoita et al. [71]. Assuming an isotropic solvent, they model friction reduction by introducing an average orientation tensor  $\bar{\mathbf{S}} = \phi \mathbf{S}_p$  with  $\mathbf{S}_p$  being the polymer orientation tensor. The greater the average orientation, the greater the friction reduction. It is seen that the average orientation clearly is reduced as the concentration of polymer  $\phi$  is reduced, and consequently the degree of friction is reduced.

In this work, the o-4k solvent is orientable, i.e., nonisotropic. Intuitively, there must be an additional contribution to the average orientation from the solvent such that  $\bar{\mathbf{S}} = \phi \mathbf{S}_p + (1 - \phi) \mathbf{S}_s$  where  $\mathbf{S}_s$  is the orientation tensor of the solvent. Therefore, the average orientation of the solution is higher than if a molecular (isotropic) solvent were used, promoting friction reduction as expected in a melt. Note that in the

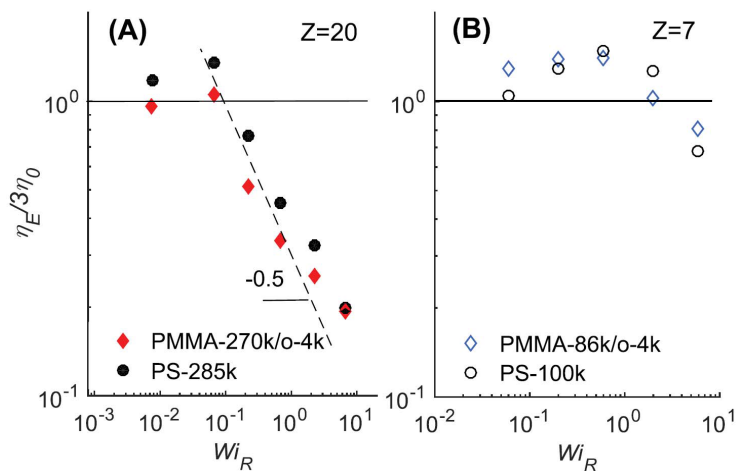


**Figure 2.2:** Normalized steady state viscosity as a function of the Weissenberg number. (A) Compares samples with  $Z \approx 20$ . (B) Compares samples with  $Z \approx 7$ . Black indicates reference data [61, 74].

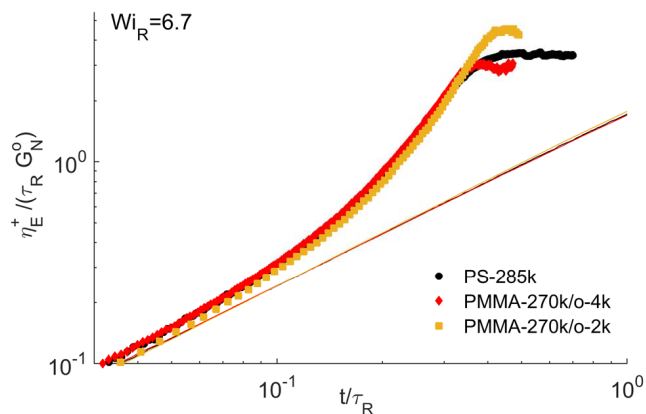


**Figure 2.3:** Normalized stress growth coefficient (symbols) for three different polymers extended at a Weissenberg number  $Wi_R = 6.7$ . Solid lines indicate the predicted linear response. Black indicates reference data [61].

limiting case where  $\mathbf{S}_s \approx \mathbf{S}_p$  there should be little difference between a melt and a solution.

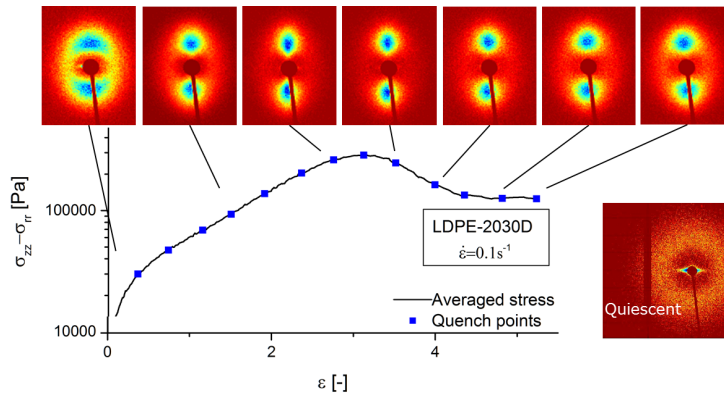
To demonstrate this concept further, the effect of using a solvent molecule with  $M_w = 2.1$  kg/mol (o-2k), i.e., half the size of the utilized o-4k, is seen in Figure 4. It is seen that the steady state viscosity of the PMMA solution containing the o-2k solvent (PMMA-270k/o-2k) exceeds that of the two others, PMMA-270k/o-4k and PS-285k. This supports the hypothesis that the o-2k solvent contributes less to the average orientation than the o-4k, resulting in less friction reduction.

To conclude, we have shown experimentally that universality of polymer dynamics can be extended from the linear regime far into the nonlinear regime. The concept of monomeric friction reduction seems valid and perfectly explains the previously unsolved discrepancy between the response of polymer melts and solutions in fast flows where both  $Z$  and  $N_e$  are the same. As a result the number of characteristics needed to fully describe flows of polymeric liquids across all deformation regimes can be narrowed down to the three presented here.

These results have both positive and negative implications, the positive being that we now have a method of systematically designing model materials for linear entangled polymers and most likely other macromolecules and polymers with other types of architectures due to the proof of universality [76]. Unfortunately, the influence of friction reduction means that diluting polymers with conventional molecular solvents can never result in a proper model material for a polymeric melt since a disparity in friction reduction between the polymer and solvent increases the strain hardening behavior. Hence, the use of polymeric solutions as model materials for polymeric melts seems very limited. The important take home message is that this data set offers a complete experimental framework for which to test all future models, which evidently must include physics relating to the number of entanglements, the flexibility of the chain, and the monomeric friction reduction of both the polymer and solvent when applicable. In closing we remark that universality has been demonstrated on the macroscopically observable stress. It is interesting to consider whether this reflects universality on the molecular level, which in the future could be observed by techniques such as dielectric spectroscopy or neutron scattering [77, 78].



# Influence of extensional stress overshoot on crystallization of LDPE



Low density polyethylene (LDPE) shows a stress overshoot in start-up of strong uni-axial extensional flows of constant rate. It is believed that the overshoot is caused by a contraction of the polymer backbone due to alignment of the long chain branches. The consequence being, that the molecular strain of the backbone does not increase monotonically with the global strain of the melt. In this study we investigate the semicrystalline morphology of LDPE quenched before, after and at the overshoot. We do this by combining filament stretching rheometry with ex-situ X-ray scattering. It is found that the overshoot indeed is reflected in the orientation of the crystalline domains of the quenched filaments. In a broader

perspective, we show that the final crystalline morphology is determined by the stress at quench - not the strain at quench. With these findings we confirm that the much debated overshoot has a physical origin. More importantly, we conclude that even for complex architectures like branched systems, the crystalline orientation is determined by the backbone stretch rather than the global stretch of the material.

The molecular architecture of polymers influences melt rheology, crystallization kinetics, and solid state mechanical properties [79, 80, 81, 82]. A classical example is the effect of introducing long-chain branching in polyethylene yielding low density polyethylene (LDPE) as opposed to the linear analog of high density (HDPE) [83]. In the case of melt rheology, introduction of branches results in longer relaxation times, often several orders of magnitude, depending on the degree of branching and length of the branches [84]. This, however, is not the only rheological consequence of introducing branches. For the past decade, it has been known that branched polymer melts in start-up of nonlinear uniaxial extension show a fundamentally different behavior from linear polymers in such flows [85]. Linear polymers deformed at a constant extension rate (Hencky strain rate  $\dot{\epsilon}$ ) initially show a gradual increase in stress. At higher strains ( $\epsilon$ ), the stress saturates and remains at steady value [86]. Branched polymers, on the other hand, exhibit a stress overshoot before reaching steady state [85]. The overshoot has been explained using the argument that branches enhance the friction between a single molecule and its surroundings causing the backbone to be stretched further than its linear analog would be. However, as the arms along with the rest of the molecule, are aligned by the flow, the friction decreases and the backbone contracts to a less stretched configuration at which the steady stress is reached [85, 87]. This process is often referred to as branch point withdrawal [20]. A sketch of LDPE's nonlinear extensional behavior along with the molecular interpretation is shown in Figure 3.1.

The extensional stress overshoot and the subsequent steady regime have not been extensively studied. It was originally reported by Rasmussen et al. observing the overshoot in constant rate experiments using a filament stretch rheometer (FSR) [85]. The results gave rise to discussions on whether the overshoot was a material property or an experimental artifact. [88, 89, 90]. In the wake of this debate followed a limited number of publications that further investigated the phenomenon. The experiments consisted of stress relaxation, creep and cross-slot flow combined with birefringence. They all confirmed the existence of an overshoot [91, 92, 93, 94]. To our knowledge no one has yet looked at the overshoot effect on the final crystalline morphology of LDPE. This, however, is a problem of interest as the crystal morphology of polyethylene (PE) is known to change depending on processing conditions [51] (see Section 1.3).

It is a long-standing tenet that chain stretch is the key determining factor for flow-induced crystallization [48]. Indeed, this postulation is a key assumption of molecular

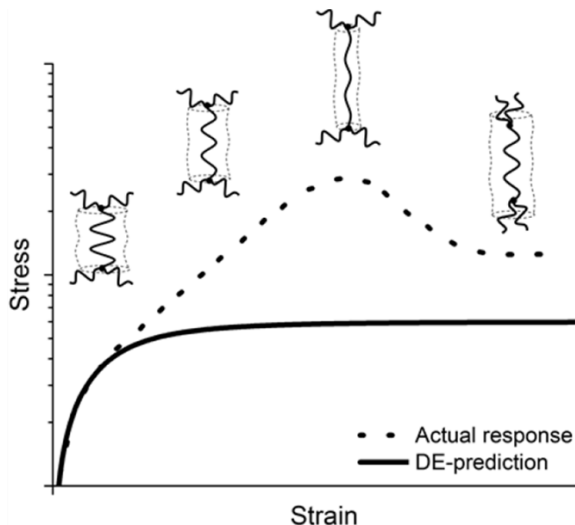


**Figure 3.1:** Schematic of the overshoot observed in nonlinear uniaxial extension of LDPE (- -). The classical Doi-Edwards (DE) prediction is shown as a reference (-). The proposed transient molecular conformation (flow direction is vertical) is shown as well for selected points along the stress curve.

models [52, 95]. However, it has not been possible to directly verify this central idea from shear experiments. Because of vorticity, shear flow is not strong enough to make large extension of polymer chains compared to extensional flow. This is where the overshoot in extension becomes interesting for the crystallization properties. If the proposed molecular picture is correct and hence that the backbone is stretched further at the stress maximum compared to the steady state stress, samples quenched and crystallized at the stress maximum (intermediate Hencky strains) would show a greater orientation compared to samples quenched in the steady flow regime (high Hencky strains). This is somewhat counterintuitive as one would expect to find the most oriented structures at the highest strains - not at intermediate strains as proposed above.

In this work we use a commercial LDPE to investigate the influence of the stress overshoot in the melt on the final morphology of the solid LDPE filaments. In order to do so, we study filaments stretched above the melting temperature at several constant deformation rates [96] and quenched before, during and after the overshoot in nonlinear uniaxial extension. The nonisothermally crystallized filaments are characterized ex-situ using small-angle X-ray scattering (SAXS) and wide-angle X-ray diffraction (WAXD) to determine the morphology and the degree of orientation. Finally we attempt to link the stress at quench to the final morphology by estimating the stretch

of the backbone during extension.

## 3.1 Experimental details

### 3.1.1 Materials and method

A commercial long-chain branched polyethylene "Lupolen 3020D" from BASF was used in this study. The sample has a weight-average molar mass  $M_w$  of  $300\,000\text{ g mol}^{-1}$ , a polydispersity index (PDI) of 8, and a melting point ( $T_m$ ) of  $114\text{ }^\circ\text{C}$  [91]. The rheology of the system is well known and exhibits a clear overshoot in nonlinear extension [85, 91, 92].

The samples were stretched at a constant Hencky strain rate using the FSR (VADER 1000) described in Chapter 1.2.2 and subsequently quenched at various Hencky strains. The experimental procedure was carried out as follows. LDPE discs of varying height ( $0.5 - 3\text{ mm}$ ) and diameter ( $5.4 - 9\text{ mm}$ ) were placed in the FSR, heated to  $150\text{ }^\circ\text{C}$ , prestretched to a desired  $D_0$ , and then left to relax for more than 15 min to erase any residual orientation left in the sample. The temperature was lowered to the experimental temperature, and uniaxial stretching was performed. The samples were quenched to room temperature at the desired Hencky strain  $\epsilon_q$  by opening the oven. (See Appendix B.2 for sketch of the thermal protocol employed during filament stretch and quench). A light flow of nitrogen gas ( $25\text{ }^\circ\text{C}$ ) was applied to accelerate the quenching. From numerical simulations the quench rate was estimated to  $10\text{ K s}^{-1}$ . Since the stress relaxation times have been estimated around 100 s, the quenching process is expected to be almost instantaneous in most situations [91]. In order for all the samples to experience the same quench history, all experiments were designed in such a way that the diameter at the point of quenching ( $D_q$ ) was  $\sim 0.55\text{ mm}$ . In order to achieve this for samples with different  $\epsilon_q$  all samples were prestretched accordingly using Eq. (1.10), with  $D(t) = D_q$  such that  $D_0$  is the adjustable parameter.

### 3.1.2 Ex-situ X-ray measurements

WAXD and SAXS were performed on the quenched filaments utilizing a SAXSLAB instrument (Ganesha from SAXSLAB, Denmark) with a 300k Pilatus detector of pixel sizes  $172 \times 172\text{ }\mu\text{m}$ . The filaments were mounted vertically such that the X-ray beam passed through the midplane of the filament where the deformation history is known. The X-ray wavelength was  $1.54\text{ \AA}$  for both WAXD and SAXS while the distance to the detector was  $\sim 118\text{ mm}$  for the WAXD measurements and either

$\sim 1020$  or  $\sim 2240$  nm for the SAXS measurements. 2D intensity patterns of good resolution were obtained using an exposure time of 5 min.

The orientation of the crystalline domains, expressed in terms of Herman's orientation factor  $F_H$ , was determined on the basis of the large scale structural characteristics from kebabs which is seen as the lobes in SAXS (see Figure 3.3) [43]. Herman's orientation factor  $F_H$  is given by Eqs. (3.1) and (3.2), assuming axial symmetry along the stretch direction [97]:

$$F_H = \frac{3 \langle \cos^2 \phi \rangle - 1}{2} \quad (3.1)$$

Here  $\langle \cos^2 \phi \rangle$  is the average cosine squared of the angle between the normal of the lamellae kebab stacks and the flow direction, estimated from integrals of the azimuthal SAXS intensity profiles (see Appendix B.2 for an example of an azimuthal intensity profile):

$$\langle \cos^2 \phi \rangle = \frac{\int_0^{\pi/2} I(\beta) \cos^2 \beta \sin \beta \, d\beta}{\int_0^{\pi/2} I(\beta) \sin \beta \, d\beta} \quad (3.2)$$

Here  $I$  the scattering intensity and  $\beta$  is the azimuthal angle.  $F_H$  gives an overall indication of the crystalline orientation based on scattering from kebabs in the crystalline domains. From the definition in Eqs. (3.1) and (3.2), isotropic orientation of crystallites gives  $F_H = 0$ . Complete orientation with respect to the flow direction, i.e. shish oriented 100 % along the flow direction and kebabs only growing perpendicular to it, gives  $F_H = 1$ . The opposite scenario where shish grows perpendicular to the flow, would yield  $F_H = -1/2$ .

## 3.2 Results and discussion

The nonlinear rheological response of the Lupolen 3020D in uniaxial extension is shown in Figure 3.2a and b. Symbols along the stress curve indicate points at which samples were quenched and nonisothermally crystallized. In Figure 3.2b it is seen that filaments were quenched at Hencky strains before the overshoot, at the overshoot, after the overshoot and well into the steady regime. At the highest strain rates  $\dot{\epsilon} = 0.3 \text{ s}^{-1}$  and  $0.6 \text{ s}^{-1}$  it was not possible to obtain points past the overshoot due to fracture of the filament [98]. In Figure 3.2b samples stretched at  $\dot{\epsilon} = 0.1 \text{ s}^{-1}$  and varying temperatures are seen. No significant change in the stress response for LDPE above  $T_m$  is observed - only an expected small, vertical shift which is explained by the time-temperature superposition principle[99]. Below  $T_m$  there seems to be a small

indication of crystallization taking place toward the very end of the experiments. This effect is best seen for the stretch performed at  $T = 110^\circ\text{C}$  where a small upturn appears around a Hencky strain  $\varepsilon = 3$ . An experiment performed at an even lower temperature  $T = 108^\circ\text{C}$  was also conducted. Here the rate of crystallization was so severe that the stress response diverged completely and fracture occurred before the end of the experiment, disqualifying the sample for further testing.

Figures 3.2c and d show orientation of the crystalline domains for the quenched samples, whose nonlinear response is shown in Figures 3.2a and b, respectively. The orientation is expressed in terms of Herman's orientation factor ( $F_H$ ) extracted from SAXS images [97] (e.g. top row of Figure 3.3). Overall the orientation in Figure 3.2c and d mirrors the stress response in melt state (a) and (b), respectively. For the samples stretched at  $\dot{\varepsilon} = 0.03\text{s}^{-1}$  and  $0.1\text{s}^{-1}$  in Figure 3.2c where a number of samples have been quenched at different strain values, an overshoot in the orientation at intermediate strains is observed; i.e., the overshoot in the melt state is reflected in the final orientation of the filaments which further proves that the overshoot is real. We note that one data point at  $(\varepsilon, \dot{\varepsilon}) = (3.1, 0.1\text{s}^{-1})$  seems lower than expected, although the measurement has been repeated several times (error bars are less than the size of the symbol). This is the point at which the arms, according to theory, should collapse leaving the backbone to retract. Stress relaxation data obtained by Huang et al. shows that the rate of relaxation increases at this point and this was further justified from simulations performed by Hawke et al. [91, 87]. The consequence of an increased rate of relaxation is that the rate of quenching has to be faster in order for the backbone not to contract before crystallization takes place. With that in mind, it is very likely that the point would lie higher if the rate of quenching had been faster. This is further supported by the fact that reducing the difference between the experimental temperature and  $T_m$  (i.e. increasing the rate of quench) by just a few degrees produce a significantly higher orientation despite the fact that the stress at quench is very similar (see Figure 3.2d).

Figure 3.3 shows a representative range of SAXS patterns (top row) and WAXD patterns (bottom row) from samples in Figure 3.2. The patterns from left to right have been quenched at increasing stresses which seems to correlate with the anisotropy of the patterns.

The SAXS patterns are characterized by a two-point-pattern with intensity peaks along the meridian. This indicates the presence of aligned lamellae planes perpendicular to the flow direction (kebabs) [100]. The "tear drop" shape of the two last samples (c) and (d) indicates a mixed spacing between lamellae planes which is a known result of interlocking of the side branches [101]. The long spacing is more constant for the two first samples (a) and (b) as the stress at quench is lower and hence less interlocking occurs.

The WAXD patterns in Figure 3.3 show a gradual change in orientation of crystal

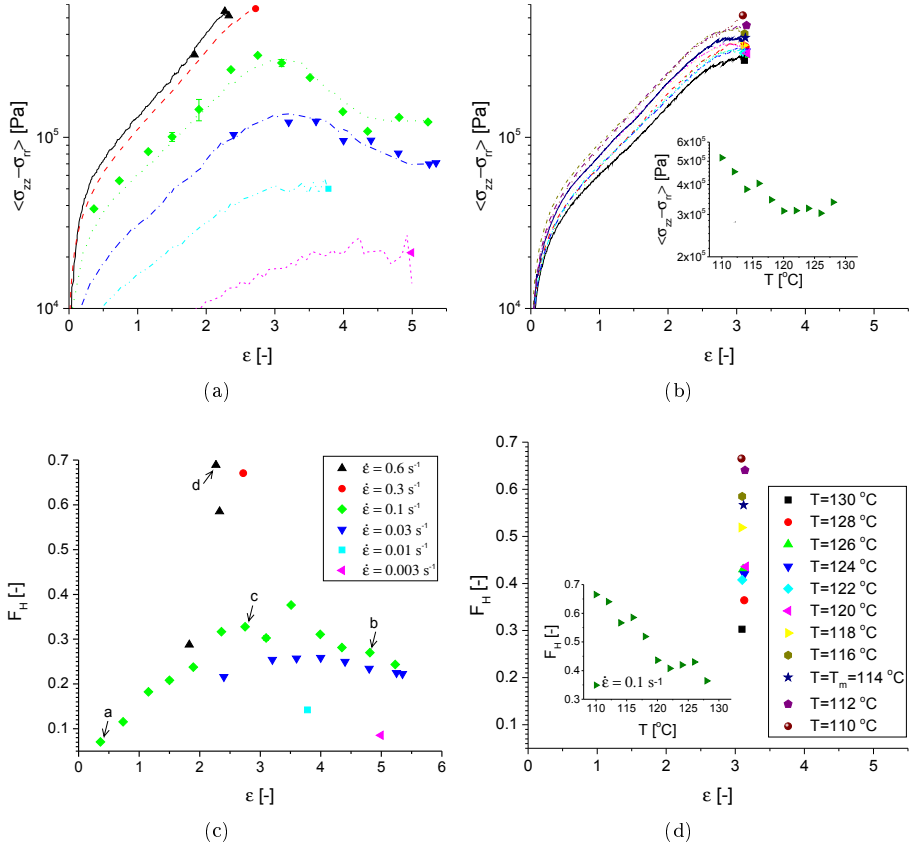


**Figure 3.2:** Top row: nonlinear response of Lupolen 3020D in extension expressed in terms of stress versus Hencky strain for samples stretched at (a) 130 °C for varying  $\dot{\epsilon}$  (b) varying stretch temperatures but constant  $\dot{\epsilon} = 0.1 \text{ s}^{-1}$  quenched at  $\epsilon = 3.1$ . (lines indicate the averaged stress curves of stretch experiments performed at a given  $\dot{\epsilon}$  and  $T$ , symbols indicate points at which filaments were quenched.). Bottom row: orientation of crystalline domains in the quenched filaments expressed in terms of Herman's orientation factor versus Hencky strain at quench for (c) the samples whose nonlinear response is given in (a), and (d) for samples whose nonlinear response is given in (b). X-ray patterns for data points marked a, b, c and d in (c) are shown in Figure 3.3. Legends in (c) and (d) also apply to (a) and (b), respectively. The insets in (b) and (d) show the same stress and orientation data as the main plot, but as a function of temperature instead of strain.

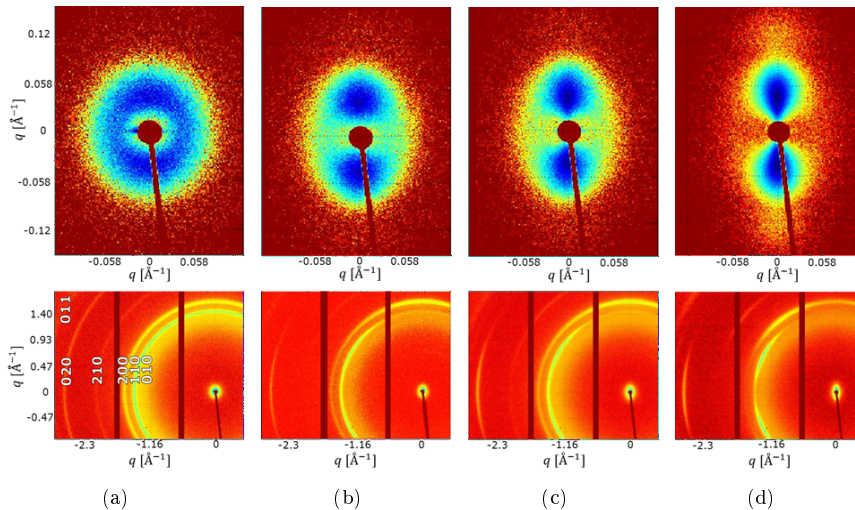


**Figure 3.3:** SAXS (top) and WAXD (bottom) patterns of LDPE filaments quenched at various stress (a) 30 , (b) 126, (c) 262 and (d) 518 kPa. All filaments have been elongated at  $T = 130^\circ\text{C}$ , and flow direction is vertical.

planes from almost isotropic of to highly unidirectional. For sample (a) the random orientation suggests a morphology dominated by spherulites. The WAXD patterns of samples (b) and (c) are rather similar, with intensity peaks along the meridian, off-axis and equatorial for crystal planes (110), (200), and (020), respectively. This is a clear indication of shish-kebab structures with twisted lamellae [43]. The only difference between sample (b) and (c) is that the intensity peaks of (c) are narrower, indicating a greater alignment of domain structures relative to (b). That is despite the fact that (b) has been quenched at higher  $\varepsilon$  (quench at steady state for  $\dot{\varepsilon} = 0.1\text{ s}^{-1}$ ) than (c) (quench at stress max for  $\dot{\varepsilon} = 0.1\text{ s}^{-1}$ ). The last sample quenched at a very high stress shows an interesting feature. The intensity peak of the (200) plane has shifted to the off axis. This indicates a kebab structure of mixed twisted and straight lamellae [102]. This type of morphology is rare for LDPE and to our knowledge it has never been reported. However it has been observed for HDPE [102].

Both the raw SAXS and WAXD patterns (Figure 3.3) and the similarity in the stress in melt state and orientation in solid state (Figure 3.2) suggest that stress at quench and final morphology of the solid samples are closely related. This is confirmed in Figure 3.4 where Herman's orientation factor for all samples in this study is plotted against the stress at quench.

The stress during deformation reflects the molecular configuration. More specifically

the deviation from linear behavior in the response of a polymeric liquid in flow is a result of the polymer being deformed beyond its equilibrium configuration (random coil) [19]. Generally, there are two types of chain deformation in entangled polymer systems - the mildly deformed state (oriented) and the highly deformed state (stretched) [103], see Section 1.2 for further explanation.

The oriented state is successfully modeled using the classical Doi-Edwards (DE) model [6]. Unfortunately this model is incapable of capturing many of the nonlinear phenomena seen in extension e.g. strain hardening and stress overshoot. The DE-model has served as a basis upon which a number of more complex models have been built in order to capture the nonlinear phenomena mentioned above. A common feature of these models is that they ascribe deviations from the DE-model to some form of backbone stretch  $\lambda$  [103]. The difference between the models lies in the physics included in order to predict the evolution of the backbone stretch. A wide range of phenomena can be included depending on the composition of the fluid and the architecture of the molecules, e.g., interchain tube pressure, [104], finite extensibility [12], friction reduction [57], and branch point withdrawal [20].

One model, the pom-pom model, originally introduced by McLeish & Larson in 1998, has proven quite effective in capturing the nonlinear behavior of LDPE [20]. In particular, Huang et. al showed that the multimode version [105, 106] captures the transient nonlinear response of LDPE up until the stress maximum. Hawke et. al extended the model by incorporating entanglement loss and obtained a model that can predict nonlinear behavior of LDPE including stress overshoot, steady stress and the increased relaxation rate at the overshoot.

Regardless of  $\dot{\varepsilon}$ ,  $\varepsilon$  and  $T$ , all samples seem to fall onto the same mastercurve, however, with some scattering. It seems that stress at quench is the governing parameter for the final morphology which is in line with ideas formulated in 1994 by P. Tas [107]. It is also in agreement with very recent nonequilibrium in-situ crystallization data on linear and cross-linked polyethylenes [108]. One reason behind this collapse of data onto one master curve can be found by looking at nonlinear constitutive models for polymeric liquids.

In this work we focus on the chain stretch and its relation to the final morphology. We use a simplified version of the multimode pom-pom to extract a chain stretch ( $\lambda$ ) from experimental data.  $\tau_{b,i}$  are time constants and  $g_i$  are corresponding moduli obtained by fitting a multimode Maxwell model to the linear data (see Appendix B.2 for values of the constants and the linear rheological response). At the conditions employed in this study, it is primarily the two longest modes that stretch during deformation [91]. As  $g_1 \ll g_2$ , the contribution of the longest mode (mode 1) to the stress and, probably, to the crystallization is small compared to mode 2. We thus define  $\lambda$  as the average stretch of the two longest modes and express the stress  $\sigma$  as

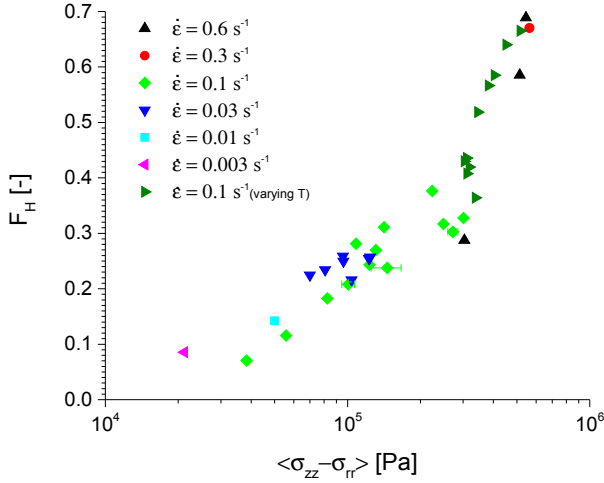


**Figure 3.4:** Herman's orientation factor vs stress at quench. All samples have been stretched at  $T = 130 \text{ }^\circ\text{C}$  except (green  $\blacktriangleright$ ) which have been stretched at varying  $T$  from 110 to  $130 \text{ }^\circ\text{C}$

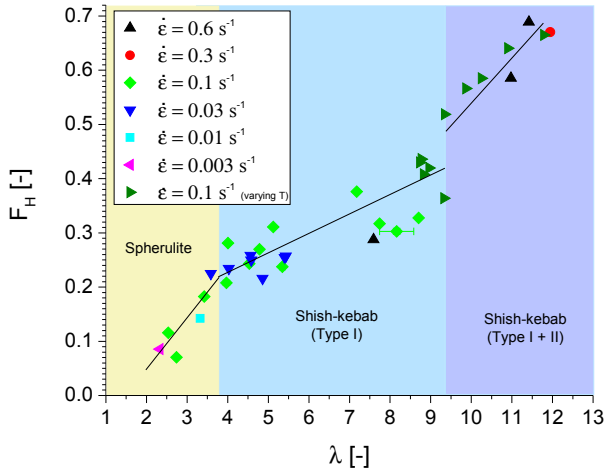


**Figure 3.5:** Herman's orientation factor vs average stretch of the backbone for the two highest Maxwell models. Vertical lines indicate regions of different morphologies.

follows:

$$\sigma = 3 \left( \lambda^2(t) \sum_{i=1}^2 g_i \mathbf{S}_i(t) + \sum_{i=3}^p g_i \mathbf{S}_i(t) \right) \quad (3.3)$$

$\mathbf{S}_i = \mathbf{A}_i / \text{Tr } \mathbf{A}_i$  is the normalized orientation tensor expressed by the conformation tensor ( $\mathbf{A}_i$ ) whose evolution is given by

$$\frac{D}{Dt} \mathbf{A}_i = \boldsymbol{\kappa} \cdot \mathbf{A}_i + \mathbf{A}_i \cdot \boldsymbol{\kappa}^T - \frac{1}{\tau_{b,i}} (\mathbf{A}_i - \mathbf{I}) \quad (3.4)$$

with initial condition  $\mathbf{A}_i = \mathbf{I}$  where  $\mathbf{I}$  is the unit tensor.  $\boldsymbol{\kappa}$  is the transpose of the velocity gradient tensor ( $\nabla \mathbf{v}^\dagger$ ). As seen, the only free parameter in this model is the average chain stretch  $\lambda$  which is obtained by fitting the model to the experimental data. In so doing, an estimate of the chain stretch at quench for each of the samples was obtained.

Figure 3.5 shows the Herman's orientation factor,  $F_H$  as a function of the extracted chain stretch  $\lambda$ . It is seen that there is a good correlation between the chain stretch in the melt state and the final crystalline orientation. Furthermore it is seen that the slope changes going from a spherulitic morphology to an oriented morphology and again going from shish-kebabs of Type I to the intermediate morphology of mixed Type I and II shish-kebabs.

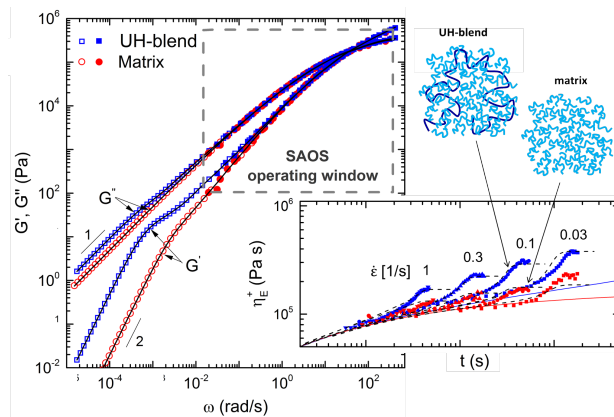
We note that the maximum values of  $\lambda$  in Figure 3.5 are much in excess of the maximum value computed from the number of Kuhn steps between entanglements which is less than 3 for PE [13]. This could indicate that entanglements have been lost in the stretching process or it may be an artefact of the simplified Pom-Pom analysis. Regardless, we believe that the segments have been stretched close to their maximum length (outside the Gaussian regime) since some polymer filaments fractured.

### 3.3 Conclusion

In summary, we have shown that the stress overshoot observed in uni-axial extension of LDPE is reflected in the final morphology of the quenched samples. To our knowledge this is the first time that a decrease in degree of crystalline orientation with increasing strain has been reported. This, first of all, confirms that the stress overshoot has a real physical origin. It also confirms that the stretch of the backbone does govern the final morphology of the crystallized sample even for a complex architecture like long chain branched PE. Finally, we conclude that the backbone stretch

is reflected in the extensional stress which is directly measurable. Hence stress in the melt state is the key parameter needed in order to connect chain extension and crystal morphology.

# Rheological link between polymer melts with a high molecular weight tail and enhanced formation of shish-kebabs



Presence of an ultra high molecular weight (UHMw) fraction in flowing polymer melts, is known to facilitate formation of oriented crystalline structures significantly. The UHMw fraction manifests itself as a minor

tail in the molar mass distribution and is hardly detectable in the canonical characterization methods. In this study, alternatively, we demonstrate how the nonlinear extensional rheology reveals to be a very sensitive characterization tool for investigating the effect of the UHMw-tail on the structural ordering mechanism. Samples containing an UHMw-tail relative to samples without, exhibit a clear increase in extensional stress that is directly correlated with the crystalline orientation of the quenched samples. Extensional rheology, particularly, in combination with linear creep measurements, thus enables the conformational evolution of the UHMw-tail to be studied and linked to the enhanced formation of oriented structures.

The morphology of semicrystalline polymeric products varies greatly depending on the imposed flow conditions during melt processing and on the molecular chain architecture [97, 43]. The combination of flow and chain architecture determines the degree of chain stretch and hence the structure into which, the polymer crystallizes [52, 48]. The morphology is important for the mechanical properties of the final product. Especially, the creation of oriented crystal structures (shish) rather than isotropic structures (spherulites) is key to enhancement of directional mechanical strength [109, 110, 51, 38].

One way to obtain shishes from a molten, relaxed polymer melt is by application of flow. A sufficiently strong flow will result in stretching of the chains [103, 68]. Under the right thermal conditions, the stretched chains form needlelike nuclei from which shish-structures are grown [36, 111]. Formation of shish is enhanced by the presence of a small fraction of chains having a molar mass considerably higher than the rest of the melt - " an ultra high molecular weight tail (UHMw-tail)" [42, 41, 112, 113, 114, 44, 115, 116]. Even when the concentration of UHMw chains is so low that they hardly affect most other properties of the melt, such as the viscosity measured in the conventionally used frequency range, thermal properties and quiescent crystallization kinetics, they significantly enhance the formation of shish [42].

One property that has not been investigated for semicrystalline polymers containing an nearly invisible high molecular weight tail, is their response in controlled uniaxial extensional flow. Inherently, extensional flows are considered strong flows whereby their ability to stretch the polymer molecules is much greater than shear flow [19, 117]. Furthermore the extensional response of the liquid is extremely sensitive to stretching of the chains. Due to experimental difficulties, the number of studies connecting crystallization and rheology in extension is quite limited [118, 56, 108, 27, 53]. Studies on semicrystalline systems of known molecular composition are still to be studied in controlled uniaxial extension.

In this work we investigate the role of the high molecular weight tail in controlled uniaxial extension as well as the morphology obtained after quenching of the melt. We

**Table 4.1:** Material characteristics for the UH-blend and the matrix. solutions.

Sample	$\phi$ (w frac)	$M_n$ (kg/mol)	$M_w$ (kg/mol)	$M_z$ (kg/mol)	$T_m$ (°C)
Matrix	-	40	156	495	138.4 $\pm$ 0.5
UH-blend	0.01	40	156	550	138.9 $\pm$ 0.5

compare a blend of 1% UHMw polyethylene (UHMwPE) in a matrix of commercial high density polyethylene (HDPE) with the pure matrix, referred to as the "UH-blend" and the "matrix", respectively. The standard characteristic properties, like weight average molar mass  $M_w$  and melting temperature  $T_m$ , are nearly identical for the two samples. We study the rheological behavior in the linear regime using small-amplitude oscillatory shear (SAOS) in combination with creep, and in the nonlinear regime using uniaxial extension combined with ex-situ small-angle X-ray scattering (SAXS).

## 4.1 Materials and methods

Blending of UHMwPE ( $M_w = 4000$  kg/mol) and commercial HDPE (632-D1 from Dow,  $M_w = 156$  kg/mol) was carried out in solution using hot xylene with subsequent precipitation in cold methanol according to procedures described elsewhere [119, 120]. The density of the commercial HDPE was  $0.958$  g/cm<sup>3</sup> which is high, hence the degree of branching was assumed to be very small. The molecular weight distribution (MWD) for the UH-blend and the matrix, obtained from high temperature gel permeation chromatography (HT-GPC) is shown in Figure 4.1. The number, weight and z-average molar masses ( $M_n$ ,  $M_w$  and  $M_z$  respectively) as well as  $T_m$  are shown in Table 4.1.

For the rheological characterization we used samples in the form of thin discs (8 mm diameter and 0.8-2 mm in height). The discs were prepared utilizing vacuum moulding at  $175$  °C for 25 min to ensure proper erasing of any thermo-mechanical history.

SAOS was carried out in a strain controlled ARES G2 rheometer (TA instruments) and creep in a stress controlled rheometer MCR702 (Anton Paar, Austria). In both cases an 8 mm plate-plate geometry was used and the measurements were carried out in inert atmosphere ( $N_2$ ). For SAOS, we performed frequency sweeps at temperatures between  $140 - 190$  °C. For creep, measurements were carried out at  $150$  °C at different stresses. The creep compliance data was converted into dynamic compliance and then to dynamic moduli  $G'$  and  $G''$  by Fourier transformations using a multimode Maxwell fit and the software NLReg based on a generalized Tikhonov regularization

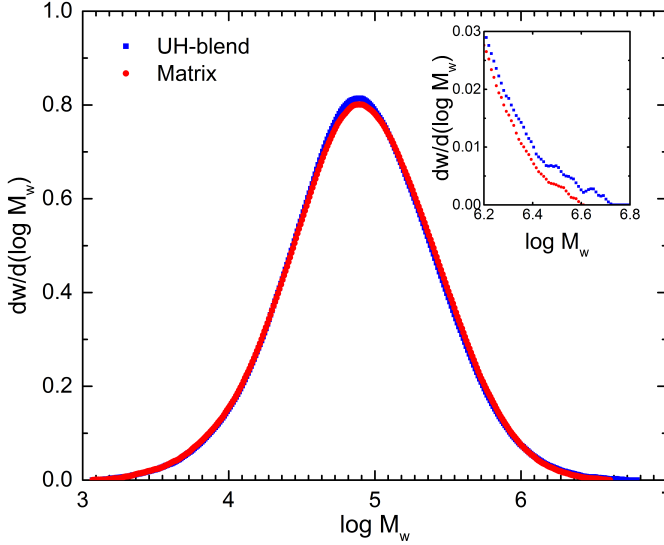


**Figure 4.1:** Molecular weight distribution of the UH-blend (blue) and the matrix (red). The inset shows a magnification of the high molecular weight region.

[121] (see Appendix C for further experimental details and compliance curves). For each sample, SAOS and inverted creep data were shifted via time-temperature superposition principle and combined into one master curve at the reference temperature  $T = 140^\circ\text{C}$ .

We performed nonlinear extensional rheology using the Filament Stretch Rheometer (VADER 1000 from Rheofilament). Uniaxial extensional experiments at a constant Hencky strain rates were performed at  $140^\circ\text{C}$  and the filaments were quenched to room temperature at  $\varepsilon = 5.5$  at a rate  $> 10\text{K/s}$ . The diameter at quench for all samples were  $0.47 - 0.5$ . (see Appendix C for further details on extension)

Ex-situ SAXS patterns from the midfilament plane of quenched samples were collected using a SAXSLAB instrument (Ganesha from SAXSLAB, Denmark) with a 300k Pilatus detector (pixel sizes  $172 \times 172\ \mu\text{m}$ ). The wavelength of the X-ray beam was  $1.54\ \text{\AA}$  and the sample-to-detector distance was  $1491\text{mm}$ . Exposure times were  $10 - 170\text{min}$ .

We use Herman's orientation factor  $F_H$  extracted from SAXS patterns as a measure for the average degree of crystalline orientation in the quenched samples [97]. This method is described in Chapter 3.1.2. The shish contribution was subtracted according to the procedure described in Appendix C.

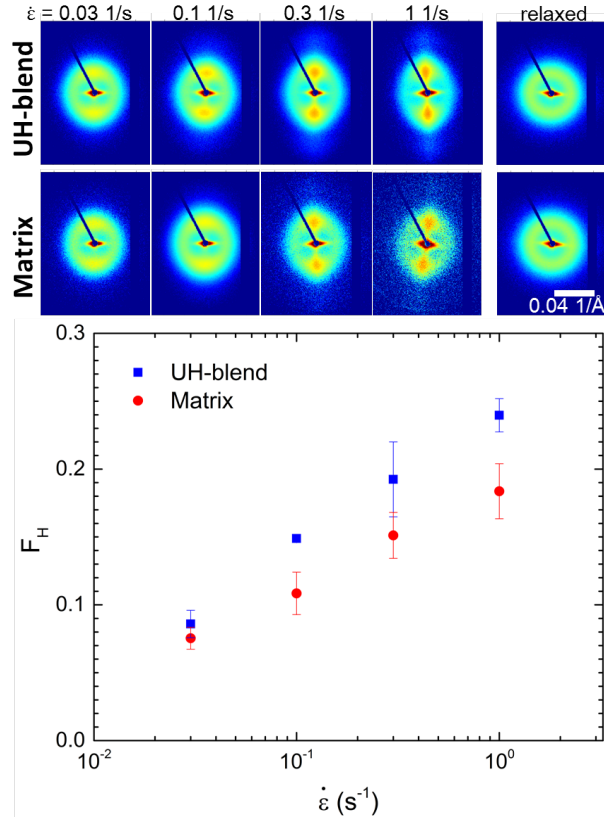


**Figure 4.2:** Herman's orientation factor of the quenched samples versus Hencky strain rate imposed during stretching for the UH-blend (blue symbols) and the matrix (red symbols). SAXS patterns are shown above with the stretching direction vertical.

## 4.2 Results and discussion

Figure 4.2 shows the SAXS patterns along with Herman's orientation factor versus the Hencky strain rate during stretching. While both samples show a systematic increase with extension rate, the orientation factor for the UH-blend is clearly higher relative to the matrix especially at high rates. The enhanced formation of oriented structures upon addition of just small amounts of UHMw-component is thus confirmed for extensional flows, which is in agreement with previous studies showing same effect for shear flows [42].

The linear rheology and nonlinear extensional rheology of the two samples are shown in Figures 4.3a and b, respectively. The linear responses (Figure 4.3a) are modelled using a multi mode Maxwell spectrum, a discrete spectrum of relaxation times  $\tau_i$  with corresponding moduli  $g_i$  (see Appendix C). Both data and corresponding fits for the two samples are identical in the high frequency region that corresponds to relaxation on length scales shorter than the entire length of the UHMw-tail. A significant difference in behavior is detected only in the region just before the terminal regime, i.e., the regime where  $G'$  and  $G''$  reach slopes of 2 and 1, respectively. The addition of 1 w% UHMwPE is responsible for the formation of a shoulder in  $G'$ , indicative of an additional mode which slows-down the terminal relaxation substantially (see also the difference in zero-shear-rate viscosity in Appendix C Figure 5S). Indeed, for the 10th Maxwell mode ( $\tau_{10} = 10^3$  s see inset in Figure 4.3a) the difference in  $g_{10}$  between the two samples is a factor of  $\sim 10^3$ . It turns out that the 10th mode of the matrix can be left out without compromising the Maxwell fit, while it is essential for the fit of the UH-blend. For the linear data, it is important to note that the spectrum obtainable from SAOS (i.e. data contained in the grey square) suggests that the two samples are identical, just like the MWD and  $T_m$  suggested. Only with the additional creep data, can any significant difference be detected as pointed out by Münstedt and co-workers [122, 123].

The nonlinear extensional response (Figure 4.3b), reported in terms of the extensional stress growth coefficient  $\eta_E^+ = (\sigma_{zz} - \sigma_{rr})/\dot{\epsilon}$  shows a clear difference between the two samples. Although both samples strain harden, the extent of strain hardening is much larger for UH-blend relative to the matrix. Initially all samples follow the LVE prediction and overlap at small  $t$  and all samples reach steady elongational flow prior to the quench at  $\epsilon = 5.5$  (Figure 4.3b inset).

### 4.2.1 HMMSF modelling and analysis of chain stretch

The extensional response is modelled using the hierarchical multimode molecular stress function (HMMSF) as it is able to properly capture the transient and steady state response of a polydisperse polymer melt using only one nonlinear fit parameter  $G_D$  [124]. The model considers the polydisperse samples as a collection of chain segments of various relaxation times obtained from the multimode Maxwell model[125]. Once a segment is relaxed it acts as a solvent for the remaining unrelaxed chains. The nonlinear parameter  $G_D$  is a point along the relaxation modulus  $G(t)$  that separates permanently diluted segments from dynamically diluted segments.  $G_D$  is associated with a time constant  $\tau_D$  defined by  $G_D = G(\tau_D)$  for the onset of dynamic dilution. The extra stress tensor, calculated as a sum of stress contributions from each Maxwell

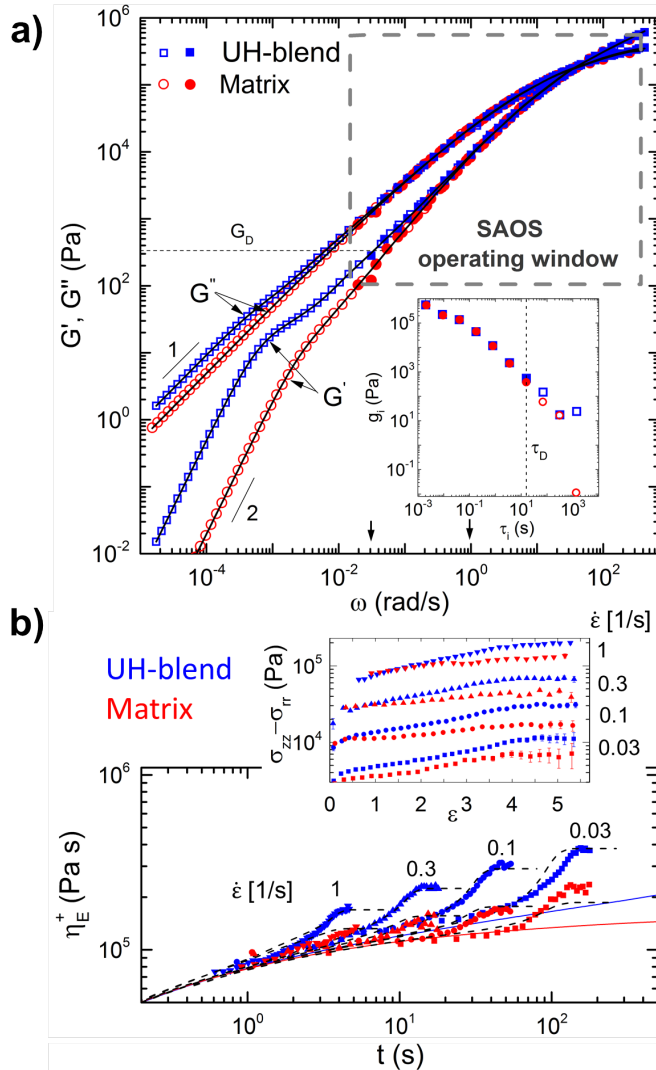


**Figure 4.3:** Rheology of the UH-blend (blue symbols) and the matrix (red symbols) at 140 °C. (a) Linear oscillatory response terms of storage ( $G'$ ) and loss modulus ( $G''$ ). closed symbols (incl. insert) shows data obtained via SAOS, open symbols indicate data obtained via creep. Solid black lines show the prediction by the multimode Maxwell model (10 modes). Arrows on the x-axis indicate the range of  $\dot{\epsilon}$  in extension. The inset shows the moduli  $g_i$  of the multimode Maxwell spectra versus the time constants  $\tau_i$ . (b) Nonlinear extensional response in terms of extensional stress growth coefficient. Blue and red lines indicate the linear viscoelastic envelope (LVE) obtained from the multimode Maxwell model. Black dashed lines show the prediction by the HMMSF model using the nonlinear fitting parameter  $G_D = 350$  Pa (see text). The inset shows the extensional stress as a function of Hencky strain.

mode, is given by:

$$\boldsymbol{\sigma} = \sum_i \int_{-\infty}^t \frac{\partial G_i(t-t')}{\partial t'} \mathbf{S}_{\text{DE}}^{\text{IA}}(t, t') f_i(t, t')^2 dt' \quad (4.1)$$

Here  $G_i$  is the relaxation modulus and  $f_i$  is the stretch of chain segments of mode  $i$ .  $\mathbf{S}_{\text{DE}}^{\text{IA}}$  is the Doi-Edwards orientation tensor with the independent alignment assumption [6]. Both  $\mathbf{S}_{\text{DE}}^{\text{IA}}$  and  $f_i$  are functions of the observation time  $t$  and the time  $t'$  at which new tube segments are created by reptation. Consequently, the middle segments of the chains will be more stretched and oriented compared to outer segments that relax much faster. The relaxation modulus is only a function of the difference between the observation time and the segment creation time:

$$G_i(t-t') = g_i \exp\left(-\frac{t-t'}{\tau_i}\right) \quad (4.2)$$

The evolution of  $\mathbf{S}_{\text{DE}}^{\text{IA}}$  can conveniently be described by the a product of the Finger strain tensor  $\mathbf{B}$  and a damping function  $h(\varepsilon)$ :

$$\mathbf{S}_{\text{DE}}^{\text{IA}}(t, t') = h(t, t') \mathbf{B}(t, t') \quad (4.3)$$

We use the analytic expression of  $h(t, t')$  as found in Urakawa et al. [126] but good approximations exist as well [127, 128]. We use the definition of  $\mathbf{B}$  given by Bird et al. [19] and the stretch of chain segments  $f_i$  is defined as the inverse relative tube diameter  $f_i(t, t') = a_0/a_i(t, t')$ . The evolution of  $f_i$  is given by a convective term and two relaxation terms:

$$\frac{\partial f_i}{\partial t} = f_i (\boldsymbol{\kappa} : \mathbf{S}) - 3 \frac{f_i - 1}{\tau_i} \left(1 - \frac{2}{3} w_i^2\right) - \frac{2}{3} \frac{f_i^2 (f_i^3 - 1)}{\tau_i} w_i^2 \quad (4.4)$$

Here  $\boldsymbol{\kappa}$  is the velocity gradient tensor. The parameter  $w_i$  is the fraction of dynamically diluted chain segments of mode  $i$ , which is only less than 1 for modes that have  $\tau_i > \tau_D$ . The chain segments that have  $\tau_i < \tau_D$  are considered as permanently diluted.

$$w_i^2 = \frac{1}{G_D} \sum_j g_j \exp\left(-\frac{\tau_i}{\tau_j}\right) \quad \text{for } \tau_i > \tau_D \quad (4.5)$$

$$w_i^2 = 1 \quad \text{for } \tau_i < \tau_D \quad (4.6)$$

The HMMSF predictions, shown in Figure 4.3b, have been obtained with the non-linear parameter  $G_D = 350$  Pa adjusted to describe the steady extensional stress

values. In addition, the success of the fit is crucially dependent upon the application of the complete low frequency response in the linear regime. The combination of creep and controlled extension thereby enables the evolution of the stretch for each mode to be studied in detail. The HMMSF modelling reveals that the difference does indeed arise from the very large stretch of the highest modes that furthermore have a squared contribution to stress. As a result the stress contribution at  $\dot{\epsilon} = 0.1\text{s}^{-1}$  from the longest mode is 53 Pa for the matrix while it is 17610 Pa for the UH-blend (see Figure 4.4a).

In trying to explain *why* the presence of a UHMw-tail increases the potential for oriented structures we utilize relations connecting chain stretch and nucleation rates in combination with the HMMSF model. Peters and co-workers have found that the rate of shish nucleation  $\dot{N}_s$  in a polymer melt containing a small UHMw-fraction has a power law dependency on the stretch  $\lambda$  of the UHMw-component [129, 37, 95]. Specifically they find that  $\dot{N}_s \propto \lambda^4 - 1$  at the onset of crystallization. In the present study where the molar masses of the matrix and the blend are not completely separated, it is not solely the UHMw-component that is stretching, but the highest molar mass fraction of the matrix as well. To account for that, we calculate an average crystallization rate proportionality ( $\langle \lambda^4 - 1 \rangle$ ) from the stretch  $f_i$  of each mode in the HMMSF model weighted by  $g_i$ :

$$\langle \lambda^4 - 1 \rangle = \frac{1}{G_N^0} \sum_i g_i (\langle f_i^4 \rangle - 1) \quad (4.7)$$

where  $G_N^0 = 2.5\text{ GPa}$  is the plateau modulus [13] and

$$\langle f_i^4 \rangle = \frac{\int_{-\infty}^t (\partial G_i(t-t')/\partial t') f_i(t, t')^4 dt'}{\int_{-\infty}^t (\partial G_i(t-t')/\partial t') dt'} \quad (4.8)$$

Figure 4.4 shows the obtained values of  $\langle \lambda^4 - 1 \rangle$  for both samples. At the highest Hencky strain rate investigated ( $\dot{\epsilon} = 1\text{ s}^{-1}$ ), the value of  $\langle \lambda^4 - 1 \rangle$  for the UH-blend is a factor of 4 higher than that of the matrix. Hence, according to the model, the addition of 1 w% UHMwPE to the matrix, would result in an increase by a factor of 4 in  $\dot{N}_s$ .

### 4.2.2 Herman's orientation factor and stress at quench

To elucidate the connection between crystalline orientation and flow we plot in Figure 4.5 the final crystalline orientation  $F_H$  versus steady stress. Although the data

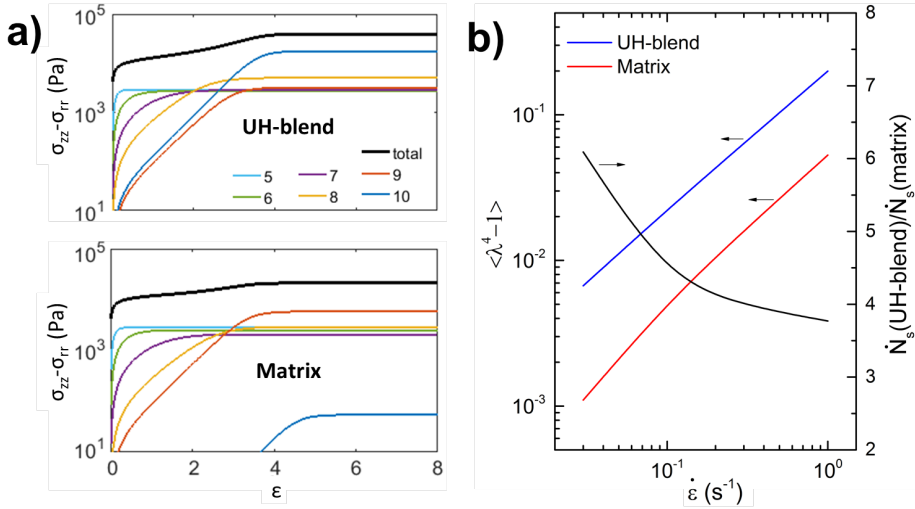


**Figure 4.4:** Analysis of the UHMw-tail effect using the HMMSF model (a) Extensional stress. Coloured lines indicate the contribution from the different modes to the total stress (black line). Note the difference between the two samples for the longest mode (10th mode). (b) crystallization rate at the point of quench. Red and blue lines indicate average crystallization rate proportionality of the matrix and the UH-blend, respectively. The black line indicates the ratio of shish nucleation rate between UH-blend and matrix.

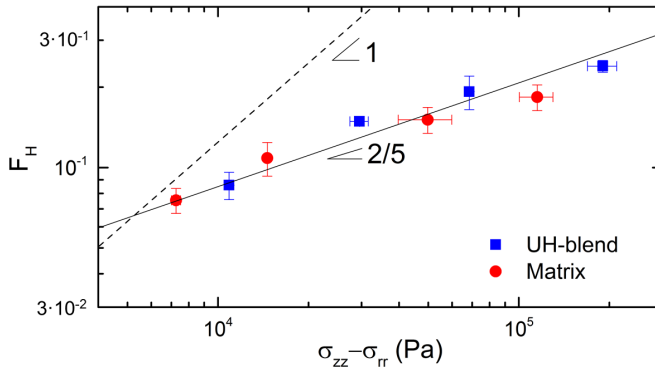


**Figure 4.5:** Herman's orientation factor versus steady state stress. Blue symbols for the UH-blend, red symbols for the matrix. Black solid and dashed line shows the apparent slope of 2/5 and the expected trend for amorphous systems, respectively.

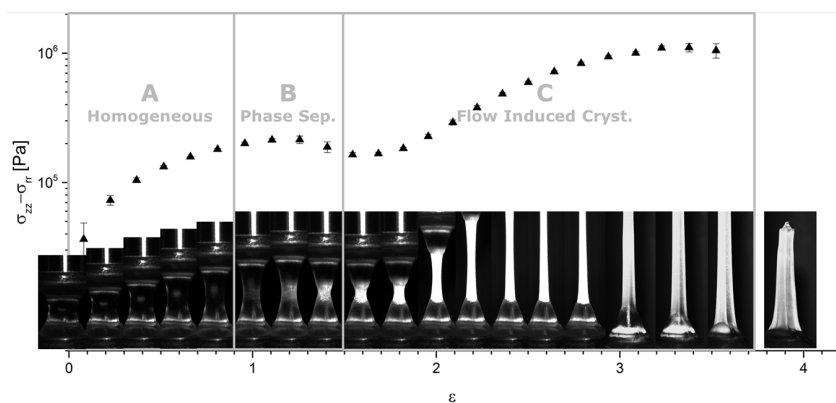
contain some uncertainty,  $F_H$  for the two samples appear to collapse onto a single master curve. The experimental relationship between orientation and stress shows a power law dependency with a slope of  $2/5$  rather than the linear relation reported for non-crystallizing systems [22]. The apparent collapse of data onto one master curve is in accordance with previous findings for long chain branched polyethylene in Chapter 3.

### 4.3 Conclusion

We have shown that a very small fraction of UHMw-component in a semicrystalline polymer melt changes the extensional rheology as well as the final morphology significantly. The link between extensional rheology and enhanced formation of oriented structures lies in their mutual inherent sensitivity to chain stretch. The extensional response enables the evolution of the high molecular weight tail stretch to be studied in detail, up to steady flow. Thus we conclude that nonlinear extensional rheology particularly in connection with linear creep, provides a powerful tool for the study of threadlike precursors and shish formation in polymers of high polydispersity and/or with a UHMw-tail.



# Extension induced phase separation and crystallization in semidilute solutions of ultra-high molecular weight polyethylene



We investigate the influence of controlled uniaxial extension on various flow-induced phenomena in semidilute solutions of ultra-high molecular weight polyethylene. Concentrations range from 9w% to 29w% and the choice of solvent is paraffin oil (PO). The start-up extensional behavior

is measured at various Hencky strain rates and at two different temperatures (150 °C and 170 °C) well above the melting point. At  $\varepsilon > 0.9$  the qualitative behavior of the samples differs significantly depending on the imposed conditions and the concentration of the samples. Overall, we propose two flow scenarios: Scenario 1 - flow-induced phase separation resulting in an unstable bulky filament and Scenario 2 - flow-induced phase separation and crystallization resulting in a stable deformation and a smooth, strongly strain hardening filament. Scenario 2 is observed only at 150 °C at high Hencky strains and high concentrations. Scenario 1, observed at both temperatures, is most pronounced at low rates and/or high concentrations.

## 5.1 Introduction

Ultra-high modulus polyethylene fibers are spun from solutions of ultra-high molecular weight polyethylene (UHMwPE) [38]. To a large extent, fiber spinning processes comprise uniaxial extension upon extrusion and drawing of the polymeric liquid. The processability of UHMwPE solutions is thus determined by the rheological characteristics primarily in extension, yet controlled rheological studies of PE solutions have been reported only for shear flows [41].

In shear, UHMwPE solutions exhibit significant nonlinear characteristics [130]. The long chains are easily deformed by flow, causing the solutions to be highly shear thinning. Several studies on UHMwPE solutions utilize paraffin oil (PO) as a solvent. It is a convenient solvent due to its low volatility and the fact that the chemical composition is the same as that of UHMwPE. Extensive work on UHMwPE/PO solutions in shear have been performed by Murase and co-workers [131, 132, 133, 134]. Apart from significant shear thinning they discovered other highly nonlinear phenomena in these systems. They found that multiple states of heterogeneities can be initiated by flow under the right conditions. At high shear rates the UHMwPE/PO solutions experience concentration fluctuations that eventually develop into actual phase separation [131]. In addition, at temperatures above, but close to, the equilibrium melting point  $T_m$ , the UHMwPE rich phase crystallizes into highly oriented structures [132, 133]. These flow-induced phenomena have been found to play a huge role in the structural development of UHMwPE fibers during processing [134] as well as the final fiber strength [109, 110]. Unfortunately, the deformation in a spin-line is ill defined and lacks control of the deformation. As a result, the imposed deformation is quantified in terms of take-up speed or other measures related to the instrument rather than local deformation of the material.

Due to experimental challenges regarding both control of the deformation and the

non-stick nature of the samples, studies on polyethylene solutions in controlled extensional flows have, to our knowledge, never been performed. In this study we characterize solutions of UHMwPE in controlled uniaxial extension. The solvent is PO and the samples are measured at constant deformation rates at temperatures well above  $T_m$ . Extension of these non-sticky samples are performed using the filament stretch rheometer (FSR) with a modified sample plate design to prevent slip off. Conditions under which flow-induced phase separation and flow-induced crystallization (FIC) occur, are identified using simultaneous high speed imaging. We map the regimes of the different flow-induced phenomena with respect to imposed deformation rate, polymer concentration, and temperature.

## 5.2 Materials and methods

UHMwPE of  $M_w = 3\,500\,000$  g/mol, supplied by DSM and paraffin oil (containing 0.2 w% antioxidant: 2,6-di-tert-butyl-p-cresol) were mixed in an extruder. In total, three solutions were prepared containing 5 w%, 10 w% and 20 w% UHMwPE. The solutions were extruded directly into a mould and moulded into discs of diameter  $D_0 = 8$  mm and height  $h_0 = 6$  mm.

**Thermogravimetric analysis (TGA) and differential scanning calorimetry (DSC)** Upon cooling to room temperature, some solvent was expelled from the samples due to crystallization of the UHMwPE. Hence, before initiating rheological characterizations, the concentration of polymer in the samples was determined using TGA (Discovery TGA from TA Instruments). Concentrations were determined from the integrals under the clearly separated PO and UHMwPE peaks (see Appendix D). The melting point was determined by DSC with an auto sampler from TA instruments (Discovery DSC from TA Instruments). In Table 5.1, specifications are given regarding polymer concentration obtained from TGA and melting temperature  $T_m$  obtained from DSC. Table 5.1 also gives the average number of entanglements  $Z$  and the Flory-Huggins predicted  $T_m$ . The number of entanglements is given by  $Z = (M_w/M_e)\phi$  where the molar mass between entanglements  $M_e = 1120$  g/mol [84]. The Flory-Huggins predicted  $T_m$  is given by [135]

$$\frac{1}{T_m} - \frac{1}{T_m^0} \cong \frac{R}{\Delta H_f} [(1 - \phi) - \chi(1 - \phi^2)] \quad (5.1)$$

The equilibrium melting point of the bulk polymer  $T_m^0$  is set to 145 °C and  $\Delta H_f = 3900$  kJ/mol is the heat of fusion [132]. The interaction parameter  $\chi$  is set to 0 as the chemical composition of PE and PO is the same.

Melting temperatures measured by DSC are higher than predicted by Eq. (5.1).

**Table 5.1:** Material characteristics for solutions of UHMwPE in PO.

Sample	$\phi$ [w%]	$T_m^a$ [ $^{\circ}C$ ]	$T_m^b$ [ $^{\circ}C$ ]	$Z$
PE/PO-29%	28.7	123.5	119.2	960
PE/PO-17%	16.8	121.6	115.8	560
PE/PO-9%	8.8	118.9	113.6	293

<sup>a)</sup> from DSC

<sup>b)</sup> from Eq. (5.1)

This difference is expected as melting of the PE crystals during the DSC heating ramp does not take place instantaneously. Kinetic delay pushes the melting to higher temperatures in the DSC and thus it tends to overestimate the  $T_m$ .

**Small-amplitude oscillatory shear** The linear rheology of the solutions was measured in SAOS. An ARES G2 rheometer from TA Instruments was used with a 25 mm plate-plate geometry. To prevent degradation of the sample, measurements were carried out in the presence of nitrogen. The samples were heated to 170  $^{\circ}C$  and to erase all thermo-mechanical history. Frequency spectra were collected for  $T = 150$   $^{\circ}C$  and 170  $^{\circ}C$ . At temperatures above 170  $^{\circ}C$  the loss of solvent was significant enough that reproducibility was compromised. Frequency sweeps obtained at different temperatures were shifted and combined into one master curve for each sample.

### 5.2.1 Combined filament stretch rheometry and high speed imaging of non-sticky samples

Extensional rheometry was carried out on the VADER 1000 filament stretch rheometer (FSR) (see Section 1.2.2 for details) with a modified sample plate design.

**Plate design for measuring non-sticky samples** The FSR-technique relies on the sample sticking to the end plates during the stretch experiment. Slip-off is an issue even for the most studied polymer in the FSR, polystyrene (PS). With PS, it is possible to circumvent this problem by increasing the prestretch, i.e., increasing the initial area that sticks to the plate relative to the area of the midfilament plane. Increasing the prestretch was not sufficient in the case of the PE/PO solutions as the presence of PO resulted in greasy samples that slipped off very easily. To overcome slip-off, several new plate geometries were designed. The best design is shown in Figure 5.1a and is in the following referred to as the "mushroom plate". The mushroom plate differs from the standard plate (Figure 5.1b) in the way that it has an

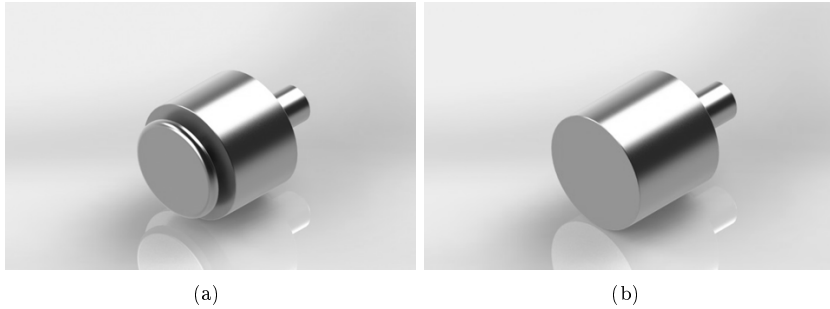


**Figure 5.1:** Sketch of plate designs. (a) The mushroom plate design developed for extensional stretching experiments of non-sticky samples. (b) The original plate design for sticky samples.

extra plate on top of the standard plate separated by a small rod. The additional plate and rod is referred to as the "mushroom". The mushroom plate required a special moulding procedure inside the FSR in order to anchor the "mushroom" into the fluid. The moulding procedure is illustrated in Figure 5.2. First, the sample disc was sandwiched between the two plates and thick tin foil was wrapped around the plates. Second, the sample was heated to  $165^{\circ}\text{C}$  and the top plate was lowered so that the polymer filled the entire space. As a result, the sample encapsulated the mushroom so that it acted as an anchor upon stretching.

**Filament stretching at a constant strain rate with simultaneous high-speed imaging** We conducted experiments at a constant Hencky strain rate  $\dot{\epsilon}$  such that throughout the entire experiment the strain increased linearly with time:  $\epsilon = \dot{\epsilon}t$ . The procedure for each stretch experiment was as follows. After moulding in the FSR as described in the previous section, the sample was heated to  $165^{\circ}\text{C}$  before it was pre-stretched and relaxed for 15 – 60 min depending on the relaxation times of the sample. The temperature was then changed to the experimental temperature at which the sample was stretched at a constant rate. High-speed imaging of the sample during the stretching experiment was performed with a high speed camera (FASTCAM Mini UX100 from Photron) and a LED light source. Both were placed on the same side of the sample where windows in the oven enabled the stretch to be captured. The frame rate was relatively low (50-1000 fps) and determined by the stretch rate of the given experiment - higher strain rates required higher frame rates.

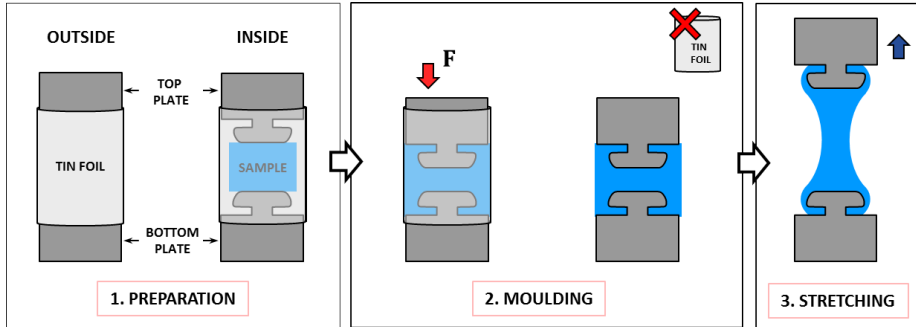


**Figure 5.2:** Sketch of moulding procedure in the FSR using mushroom plates. 1. Preparation: Initial placement of the polymer disc between the bottom and top plates with a piece of tin foil wrapped around it. 2: Moulding: (left) Moulding procedure where the sample is heated above  $T_m$  and the top plate is lowered by applying a force  $F$ . (right) after moulding where the tin foil has been removed. 3. Stretching: The anchoring effect of the mushroom during stretching preventing slip-off.

## 5.3 Results and discussion

### 5.3.1 Linear rheology

The linear rheology of the three samples along with respective multimode Maxwell model fittings are seen in Figure 5.3a. The response is given in terms of storage and loss moduli  $G'$  and  $G''$ , respectively. The first crossover is captured for PE/PO-9 while for PE/PO-17 and PE/PO-29 the first crossover can be estimated by extrapolating  $G'$ ,  $G''$  to lower frequencies. The inverse value of the estimated first crossover frequency gives an indication of the average relaxation time by reptation. Due to instrument limitations, it was not possible to reach the terminal regime of the samples (the region where  $G'$  and  $G''$  reach a slope of 2 and 1, respectively) or the second crossover found at higher frequencies. For the three samples the average reptation time is in the order of  $10^2 - 10^3$ s.

The vertical shift between the samples arises from differences in concentration. This is in accordance with the tube model stating that the plateau modulus  $G_N^0$  scales with  $\phi$  as follows  $G_N^0(\phi) \propto \phi^{1+\alpha}$  with the dilution exponent  $\alpha = 1$  or  $1.3$  [61, 70]. The plateau modulus is the value observed in  $G'$  in the plateau region for a monodisperse well entangled polymeric liquid. For undiluted polymers, this value is a material constant and for PE at  $150^\circ\text{C}$  the value is  $G_N^0 = 2.6$  GPa [13]. The plateau region is not clearly identified in these samples due to both polydispersity and the limited range of experimentally accessible frequencies  $\omega$ . As an approximation for  $G_N^0$  we use  $G'_{max}$

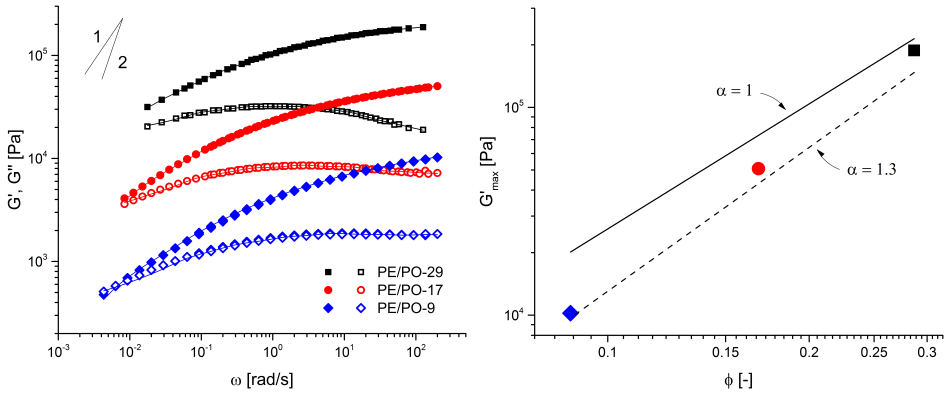


**Figure 5.3:** Linear response of PE/PO solutions at 150°C. (a) Dynamic frequency sweep expressed in terms of storage modulus  $G'$  (closed symbols) and loss modulus  $G''$  (open symbols). Lines represent best fit of the multimode Maxwell model. (b) Evolution of  $G'_{max}$  with concentration. Solid and dashed lines represent the tube model predicted evolution of  $G'_N$  with  $\phi$  using  $\alpha = 1$  and  $\alpha = 1.3$ , respectively.

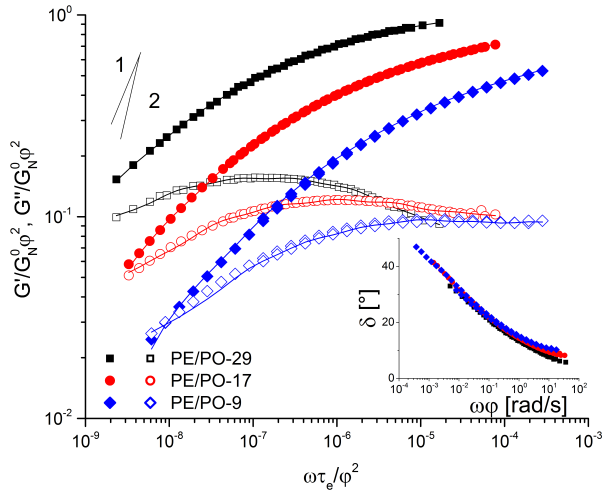


**Figure 5.4:** Nondimensional linear response of PE/PO solutions. Closed symbols represent normalized storage modulus and open symbols represent normalized loss modulus. Lines represent best fit of the multi mode Maxwell model. The insert shows the phase angle versus frequency shifted by concentration.

which is the value of  $G'$  at the highest measured frequency where the smallest slope of  $G'$  for all samples is measured. Figure 5.3b compares the value of  $G_N^0$  predicted by the tube model with the approximated values using  $G'_{max}$ . The approximated values are relatively close to the prediction. For the given concentration range, the value of  $\alpha$  is expected to be 1. In this case, the approximated values increasingly diverge from the prediction as the concentration decreases. This divergence is expected since  $G'$  at lower concentrations shows a less pronounced plateau compared to the higher concentrations.

Figure 5.4 shows the normalized linear response of the three solutions. Normalization is performed in accordance with the tube model. Vertically, the data is normalized by  $G_N^0 \phi^{1+\alpha}$  assuming  $\alpha = 1$ . Horizontally, the data is normalized by the relaxation time of one entanglement  $\tau_e$  which can be estimated experimentally from the second crossover. As already mentioned, the limited range of accessible frequencies using SAOS does not allow for the second crossover to be determined experimentally. Instead, we approximate  $\tau_e$  using scaling laws derived from the tube model combined with the value  $\tau_e = 1.1 \cdot 10^{-8}$  s for undiluted PE. According to the tube model, dilution pushes entanglements along the chain further apart, thus increasing  $\tau_e$ . If the solvent and the polymer are isofrictional, the entanglement relaxation time of a diluted polymer chain scales with  $\phi^{-2}$  [17]. As the chemical composition of PE and PO are the same, we assume PO to be an isofrictional solvent to PE.

The data in Figure 5.4 have been normalized so that the hypothetical second crossover for the three samples overlap at  $\omega\tau_e/\phi^2 = 1$ . Fixing the second crossover of all samples at the same position reveals that the plateau region (the frequency range between the first crossover and the second estimated crossover at  $\omega\tau_e/\phi^2 = 1$ ) most likely stretches over eight to ten decades. The large span of the plateau confirms that the samples are highly entangled. The sample of highest concentration (PE/PO-29) shows the widest span of the plateau region, indicating the highest number of entanglements. The sample of lowest concentration (PE/PO-9) shows the narrowest plateau region, indicating the lowest number of entanglements. This trend is in accordance with values given in Table 5.1. Another way to normalize  $\omega$  is by the reptation time  $\tau_d \propto \phi$  [14, 61]. The insert in Figure 5.4 shows the phase angle  $\delta$  versus  $\omega\phi$ . Curves for all three samples overlap at low frequencies, suggesting that the solutions are well mixed and homogeneous in the linear regime.

### 5.3.2 Uniaxial extensional behavior

The extensional stress growth coefficient  $\eta_E^+$  for samples stretched at 150 °C and 170 °C is shown in Figures 5.5a and b, respectively. The extensional response at the two temperatures differs significantly. While most samples at 150 °C show an undershoot followed by strain hardening, most samples at 170 °C simply strain soften.

The observed behavior in Figures 5.5a and b is unusual for several reasons. First, the qualitative behavior at the two temperatures is not the same throughout the entire stretch. It means that time temperature superposition principle (TTS) does not apply, which it normally does for homogeneous polymeric liquids [99, 136]. Second, while strain softening and stress undershoot is a standard behavior for polymers in shear, it is unusual in extension [117]. Third, none of the stretch experiments reach a steady state extensional viscosity [86, 62]. The three identified abnormalities (TTS failure, strain softening, and absent steady state) suggest that dynamics other than standard chain dynamics are present. As already mentioned, PE/PO systems are known to phase separate upon deformation in shear. Under certain conditions, this phase separation also induces crystallization. High-speed imaging of the filaments during stretching suggests that in extension, both phase separation and crystallization occur and, indeed, causing the observed unusual behavior. We define two fundamentally different scenarios encountered during stretching. Scenario 1: Phase separation and Scenario 2: Flow-induced crystallization. Depending on the imposed conditions, all samples undergo either Scenario 1 or 2 during stretching. Following is a detailed description of the two scenarios.

**Scenario 1 - Phase separation** Samples stretched at 170°C appear to phase separate at  $\varepsilon > 0.9$  causing the observed strain softening of the samples in Figure 5.5b. Cromer et al. have investigated conditions for amplification of concentration fluctuations in polymer solutions undergoing planar extensional flow [137]. Using a two-fluid model with a Rolie-Poly model for the polymer, they predict growth of concentration fluctuations in steady extensional flow with amplification peaks near  $\dot{\varepsilon} \sim \tau_d$  and  $\dot{\varepsilon} \sim \tau_R$  where  $\tau_d$  and  $\tau_R$  are the reptation time and the Rouse time for the Rolie-Poly model, respectively. In our experiments, we have a broad spectrum of relaxation times with stretch rates within the corresponding range. It is therefore plausible that the same mechanism is responsible for growth of concentration fluctuations in our experiments once a significant orientation of the polymer chains has been established, which is to be expected around a Hencky strain of unity in agreement with our observations for onset of turbidity. We propose that concentration fluctuation ultimately results in phase separation and eventual filament disintegration.

The progression of the phase separation differs depending on the imposed rate and concentration of the sample. For samples stretched at 170°C, the largest difference in behavior is observed between samples of high concentration stretched at low rates (Figure 5.6) and samples of low concentration stretched at high rates (Figure 5.7).

For samples of high concentration stretched at low rates, phase separation induces multiple large cracks in the midfilament region (see Figure 5.6), a behavior remi-

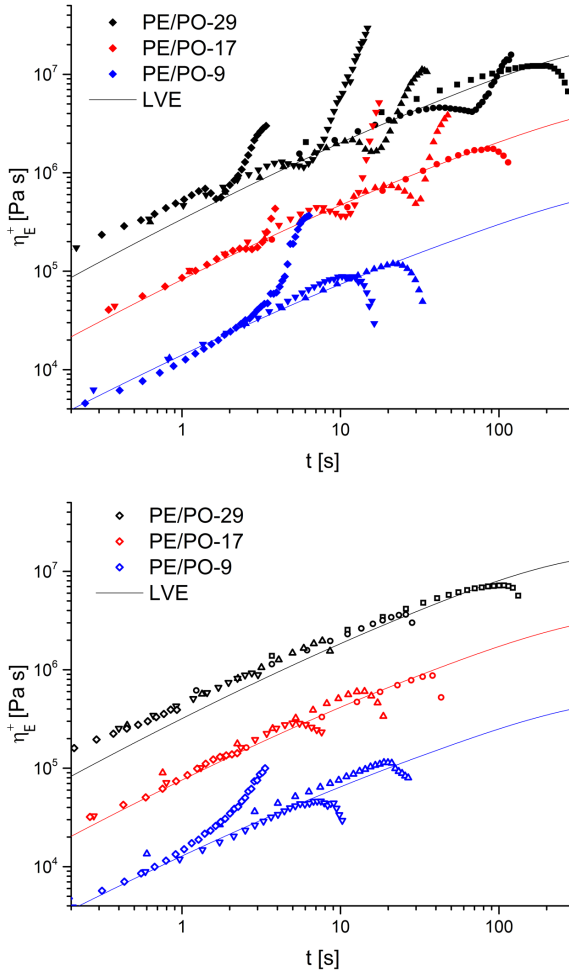


**Figure 5.5:** Nonlinear extensional response of PE/PO-solutions at constant Hencky strain rates. (a) Response at 150 °C. Hencky strain rates (from left to right). PE/PO-29 (Black symbols):  $\dot{\epsilon} = 1, 0.3, 0.1, 0.03, 0.01 \text{ s}^{-1}$ , PE/PO-17 (Red symbols):  $\dot{\epsilon} = 1, 0.3, 0.1, 0.03 \text{ s}^{-1}$ , PE/PO-9 (Blue symbols):  $\dot{\epsilon} = 1, 0.3, 0.1 \text{ s}^{-1}$ . (b) Response at 170 °C. Hencky strain rates (from left to right). PE/PO-29 (Black symbols):  $\dot{\epsilon} = 1.4, 0.41, 0.14, 0.041, 0.014 \text{ s}^{-1}$ , PE/PO-17 (Red symbols):  $\dot{\epsilon} = 1.5, 0.44, 0.15, 0.044 \text{ s}^{-1}$ , PE/PO-9 (Blue symbols):  $\dot{\epsilon} = 1.5, 0.44, 0.15 \text{ s}^{-1}$ . Lines represent the linear viscoelastic envelope obtained from the multimode Maxwell model.

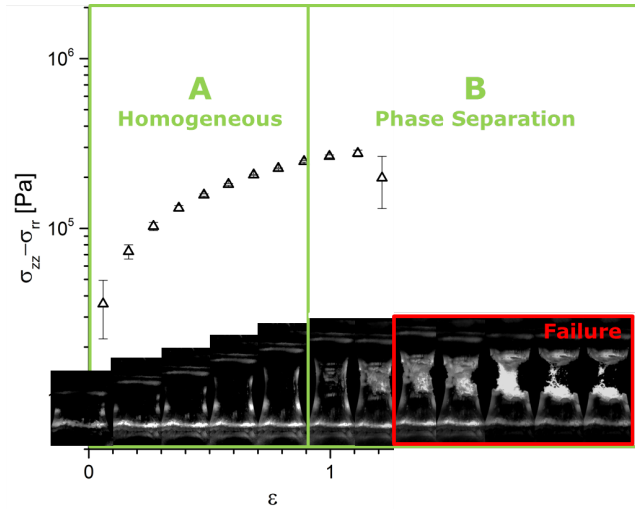


**Figure 5.6:** Example of phase separation and filament failure for samples of high concentration stretched at low rates. The sample is PE/PO-29 stretched at  $170^\circ\text{C}$  and  $\dot{\epsilon} = 0.014\text{s}^{-1}$ . The red inset shows the filament failure. Here the strain scale does not apply as the failure occurs on a time scale  $< 2\text{s}$ . Images are collected through crossed polarizers with light source and camera on the same side.

niscient of crazing. Filament failure follows immediately after, which makes Hencky strains  $\epsilon > 1.5$  inaccessible. As such, the rapid filament failure cannot be considered a brittle fracture [98]. The reason is that the failure is not caused by a single crack propagation, but by multiple cracks propagating simultaneously.

Samples of low concentration stretched at high rates also phase separate (see Figure 5.7). As opposed to the above mentioned case, the range of accessible strains as well as the type of filament failure differs. Phase separation in Figure 5.7 is identified as a slight onset of turbidity in the midfilament region at  $\epsilon \approx 0.9$ . The phase separation propagates at increasing  $\epsilon$  and is seen as an increase in turbidity. At  $\epsilon > 3$  the phase separation is so pronounced that the surface of the filament becomes uneven and lumpy. Failure of the filament occurs through thinning of the filament, during which phase separation is even more evident.

The stretch experiments presented in Figures 5.6 and 5.7 show the extremes of Scenario 1. All samples stretched at  $170^\circ\text{C}$  show a behavior somewhere between the two presented extremes. Figure 5.8 shows the gradual transition from one extreme to the other for PE/PO-17 and the following two trends should be noted. First, with increasing  $\dot{\epsilon}$ , the degree of strain softening decreases. Second, with increasing  $\dot{\epsilon}$ , the

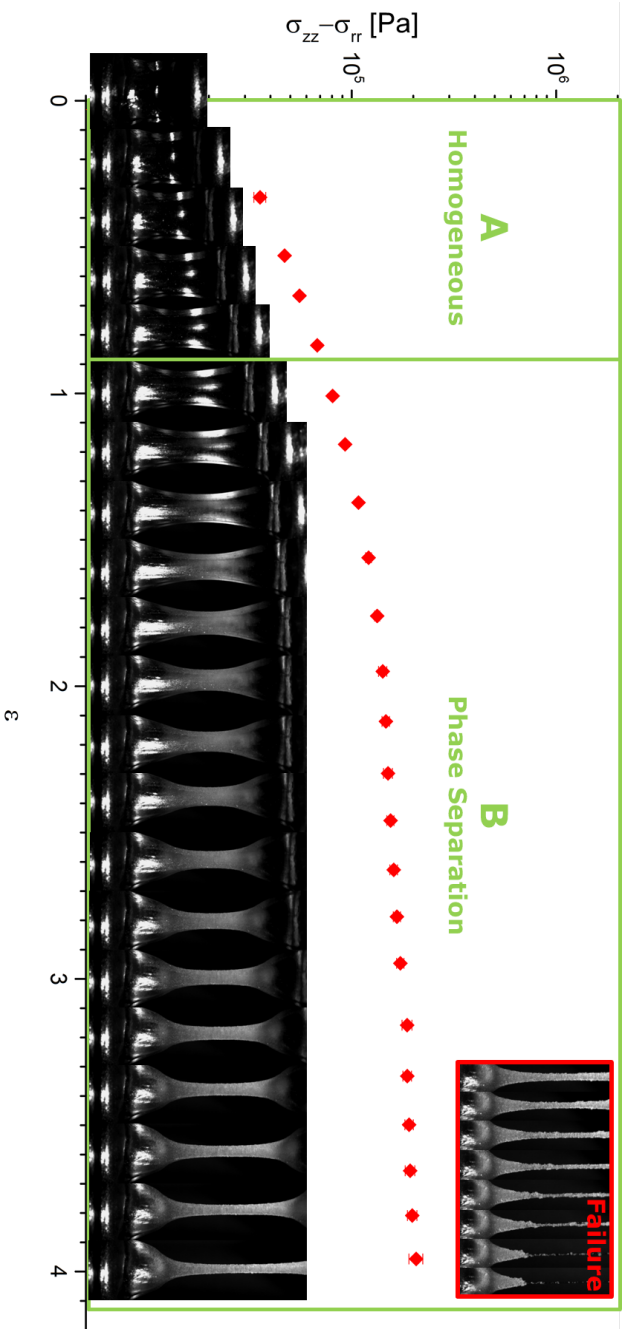


**Figure 5.7:** Example of phase separation and filament failure for samples of low concentration stretched at high rates. The sample is PE/PO-17 stretched at 170 °C and  $\dot{\epsilon} = 1.5s^{-1}$ . The red inset shows the filament failure. Here the strain scale does not apply as the failure occurs on a time scale  $\approx 2s$

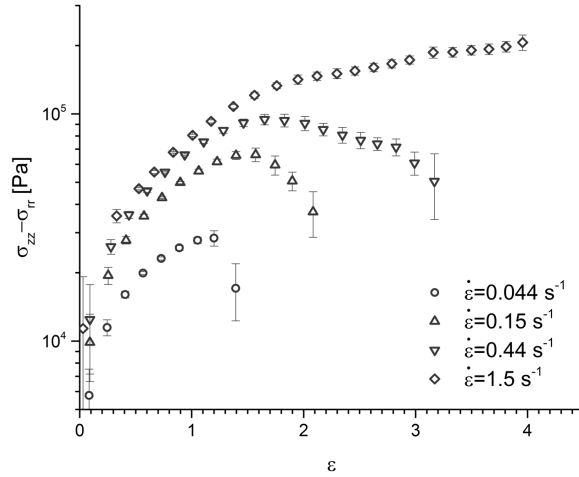


**Figure 5.8:** Extensional stress versus Hencky strain for stretches of PE/PO-17 at 170 °C.

maximum  $\varepsilon$  increases. We hypothesize that both trends are a result of an increased chain stretch for increasing  $\dot{\varepsilon}$ .

Samples stretched using 150 °C at low rates (i.e. experiments that do not show strain hardening) seem to follow Scenario 1, as well.

**Scenario 2 - Flow-induced crystallization** The strain hardening behavior of all samples stretched at 150 °C originates from FIC. None of the samples stretched at 170 °C show signs of FIC.

An example of a stretch in which FIC occurs is shown in Figure 5.9. Analogous to Scenario 1, the sample is still believed to undergo phase separation at  $\varepsilon \approx 0.9$ , due to the observed strain softening behavior combined with the onset of turbidity. At  $\varepsilon \approx 1.5$  the midfilament region of the sample transforms from turbid to opaque. Simultaneously, the midfilament region decreases spontaneously, suggesting an increase, in density while the stress starts to rise again. All three observations (turbid-opaque transition, density increase and strain hardening) are clear signs of flow-induced crystallization. At  $\varepsilon > 1.5$  a crystallized neck region develops from the midfilament region causing the significant strain hardening behavior. The transition from molten sample near the plates to the neck area is characterized by an abrupt decrease in diameter along with a sharp transition from transparent to opaque. While the midfilament is deformed, the neck area is extended axially by pulling from the molten sample reserve at the end plates and into the crystallizing neck. Hence the

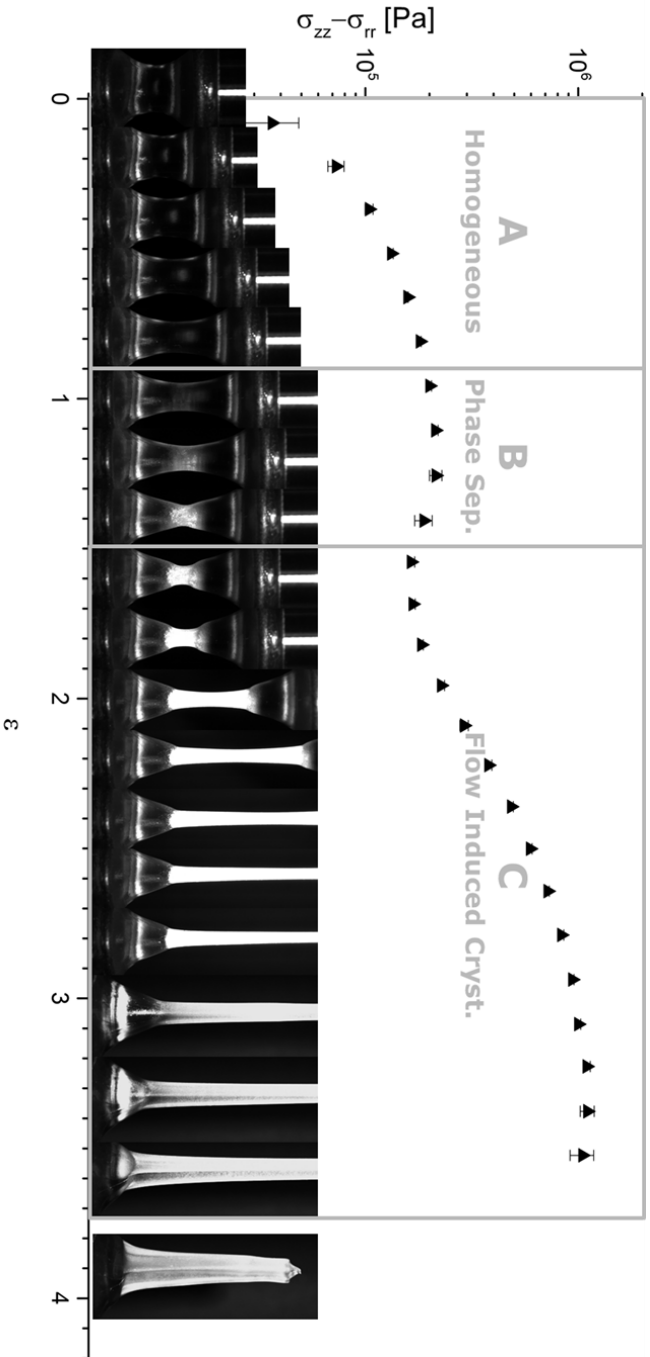


**Figure 5.9:** Example of FITC for stretch experiments performed at 150 °C. The sample is PE/PO-29 stretched at  $\dot{\epsilon} = 0.1 \text{ s}^{-1}$ . Images are collected through crossed polarizers with light source and camera on the same side. The four images to the far left are taken from a replica of the stretch.

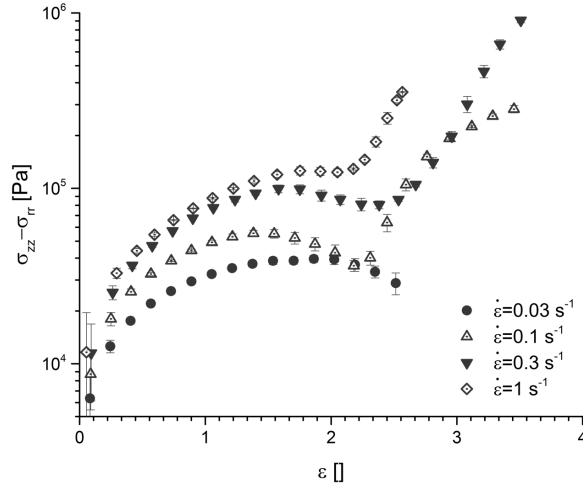


**Figure 5.10:** Extensional stress versus Hencky strain for stretches of PE/PO-17 at 150 °C.

reserve of molten sample gradually decreases. At  $\epsilon > 3$  most of the sample is incorporated into a long crystallized neck. At this point the control scheme starts to fail, not because of an uneven filament, but because the top plate reaches its maximum speed. Furthermore, end plate instability is observed due to the high deformation rates close to the plates [26]. At sufficiently high stresses the filament fractures in a brittle manner. DSC measurements of the the midfilament region after stretching a sample under the same conditions as in Figure 5.7 showed a rise in  $T_m$  of 2.8 °C. The increase in  $T_m$  is further proof that FIC has taken place [138].

Figure 5.10 shows the stress response of PE/PO-17 at various  $\dot{\epsilon}$  at 150 °C. The stress undershoot is less pronounced for increasing  $\dot{\epsilon}$  suggesting a higher degree of chain stretch, similar to Scenario 1.

### 5.3.2.1 Significance of time temperature superposition principle

High-speed imaging reveals that at small deformations  $\epsilon < 0.9$  all samples appear transparent both in Scenario 1 and Scenario 2. The transparency suggests that the samples are homogeneous (i.e. no phase separation or FIC) at strains  $\epsilon < 0.9$ . To confirm homogeneity, we compare the normalized extensional response measured at 150 °C and 170 °C (see Figures 5.11a, b and c). Here we assume that TTS works also for the nonlinear response. The characteristic time constant used in normalization is the average Rouse relaxation time  $\tau_R = \tau_e Z^2$ . As  $\tau_e \propto \phi^{-2}$  and  $Z^2 \propto \phi^2$  it is evident

that  $\tau_R$  is independent of dilution and thus all samples have the same value of  $\tau_R$ . We use previously defined values of the undiluted UHMwPE to estimate  $\tau_R$  for the solutions. At 150 °C we obtain  $\tau_R = 0.11\text{s}$  and with a shift factor  $a_T = 1.47$ , we obtain  $\tau_R = 0.075\text{s}$  at 170 °C. The normalized stretch rates are given in terms of the Rouse Weissenberg number  $Wi_R = \dot{\epsilon}\tau_R$ . It weighs the rate of deformation relative to the rate of relaxation of the weight-average polymer chain of the sample. Keeping in mind that the sample is highly polydisperse and that  $\tau_R$  is based on the weight average molar mass, the fractions of higher molar mass in the samples will have much higher  $\tau_R$ . It is thus possible to observe nonlinear behavior even at  $Wi < 1$ .

At small strains, the normalized extensional behavior of all samples in Figures 5.11a, b and c follow the LVE and obey TTS. The fact that the normalized extensional response follows the LVE and obey TTS confirms that at small deformations the samples are homogeneous and that the rheology is governed solely by chain dynamics. We observe that in many cases TTS holds in the strain softening region. This suggests that although the samples are phase separated, the response is still governed by chain dynamics only. However, at larger strains the breakdown of TTS confirms that an additional phenomenon (in this case FIC) occur with a temperature dependency different from that of chain dynamics. The onset of FIC moves towards earlier times for increasing  $Wi_R$ . This is in accordance with general theories stating that the onset of FIC is governed by chain stretch [37].

## 5.4 Conclusion

We have investigated the influence of controlled extensional flow on solutions of UHMwPE in PO at temperatures well above  $T_m$ . We find that at  $\epsilon > 0.9$  the extensional behavior differs fundamentally with concentration, temperature, and imposed deformation rate. Overall, the observed behaviors can be divided into two Scenarios: 1 - Phase separation and 2 - FIC. Flow-induced crystallization (Scenario 2) was observed for high  $Wi_R$  and high  $\phi$  at 150 °C. As concentration increases, FIC levels can be detected at lower  $Wi_R$ . E.g., for PE/PO-29, FIC is observed at  $Wi_R$  as low as 0.0033, while for PE/PO-9, the lowest  $Wi_R$  at which FIC is observed is 0.11. The time at which onset of FIC is observed decreases with increasing  $Wi_R$ . The earlier onset of FIC upon increasing  $Wi_R$  is in accordance with the general belief that FIC is governed by chain stretch that also increases with  $Wi_R$ . At lower  $Wi_R$  and  $\phi$  the filament only appeared to phase separate (Scenario 1). At 170 °C, all samples followed Scenario 1. The observed flow-induced phenomena (phase separation and crystallization) are in general agreement with previous studies performed in controlled shear and along a fiber spin-line in which the deformation cannot be controlled. To reach a better understanding, controlled extensional rheology in combination with in-situ light scattering or even X-ray scattering will be needed.

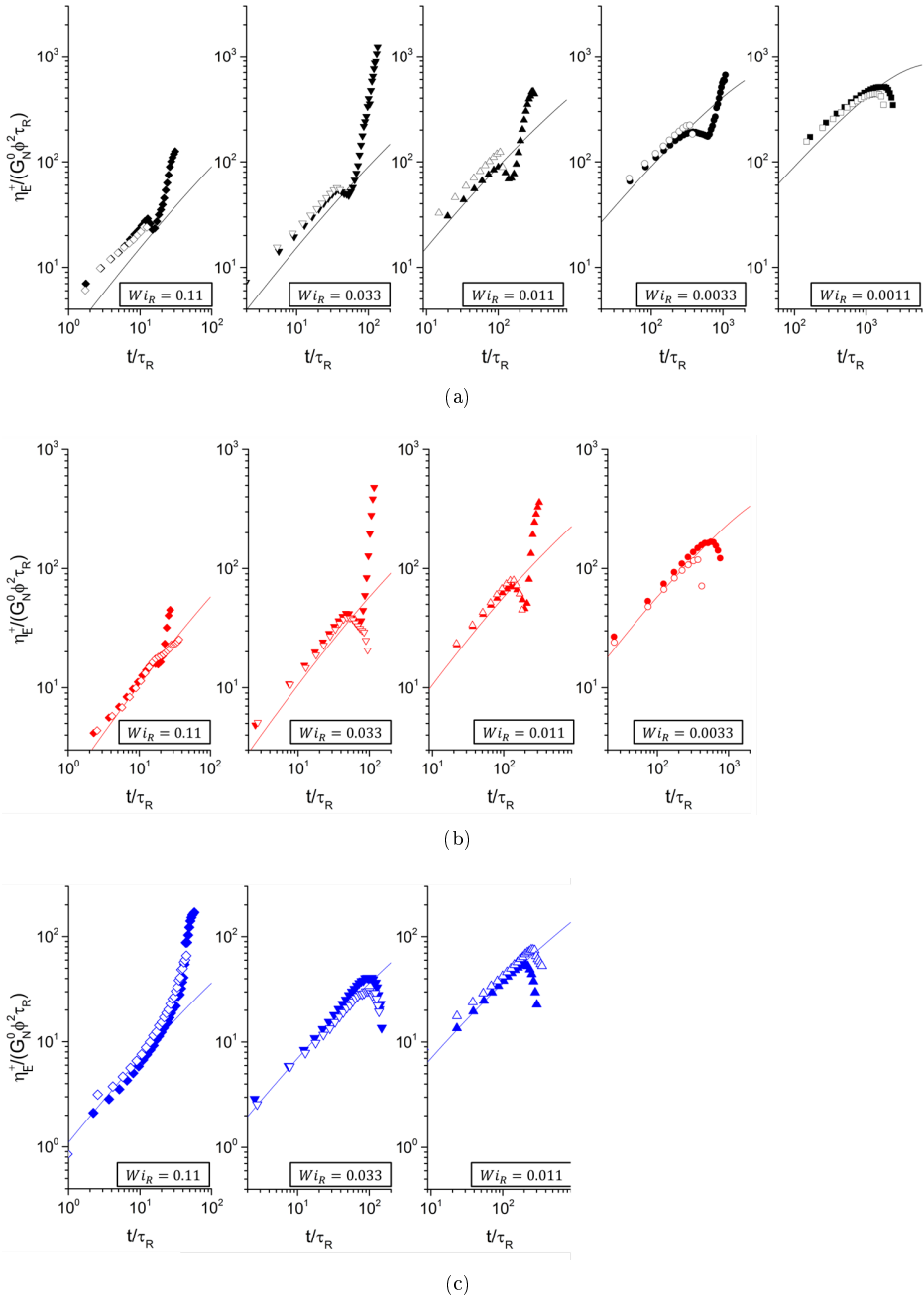
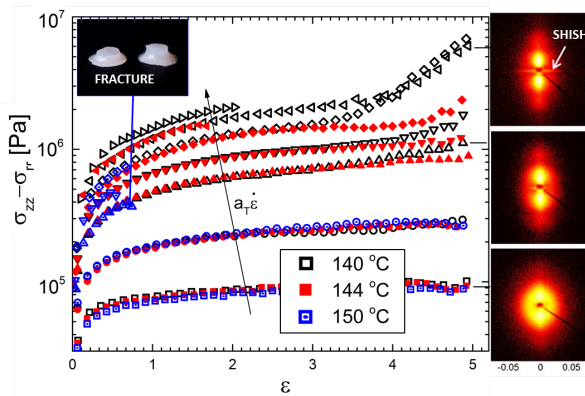


**Figure 5.11:** Normalized nonlinear extensional response at various Weissenberg numbers for (a) PE/PO-29, (b) PE/PO-17 and (c) PE/PO-9. (Closed symbols) indicate stretching experiments performed at 150 °C, (Open symbols) indicate stretching experiments performed at 170 °C. Weissenberg numbers apply to both open and closed symbols.



# Shish formation above the melting temperature stabilizes filaments of HDPE in extensional flow



This work concerns extension induced crystallization of a commercial high density polyethylene at different temperatures above the equilibrium melting temperature. We compare the nonlinear response during stretching to the morphology obtained in the quenched fibers after cessation of the flow. At high temperatures, the samples undergo brittle fracture whereas samples stretched at lower temperatures (still above  $T_m$ ) do not. Instead, they exhibit a strain hardening behavior that does not follow time tem-

perature superposition. We propose that stabilization of the filament at lower temperatures, as well as the failure of time temperature superposition, is caused by flow-induced nucleation and growth of shish structures oriented along the flow direction. Further justification is given by showing that small-angle X-ray scattering performed on quenched filament deformed at high Hencky strain rates in the melt, demonstrate a clear increase in the amount of shish relative to the filaments stretched at low Hencky strain rates. We find the critical strain for the onset of shish formation to be 0.8, which is significantly lower than the values reported in the existing literature. We model the influence of shish nucleation on the rheological response in extension using the hierarchical multimode stress function, which is modified to include the stretched network assumption. Finally we show that a mastercurve of crystalline orientation for all temperatures is obtained when Herman's orientation factor is plotted against stress at quench.

The mechanism of flow-induced formation of shish-kebab structures is an old problem, but it has yet to be fully understood because of its complexity [36]. Some aspects of the problem, however, have been resolved. Combined rheology and in-situ scattering methods have revealed that stretching of the high-molecular-weight fraction upon the application of flow causes the formation of needlelike nuclei [45, 38]. These nuclei grow into shish and only at a much later stage does the overgrowth of kebabs occur [120]. These needlelike nuclei are believed to be caused by threadlike precursors [46, 139]. However, the nature of these precursors and the mechanism of their formation in the flow remain to be resolved. For threadlike precursors to arise, some degree of deformation is necessary. The extent of deformation needed, is still open to question [140]. Furthermore, how to interpret a melt containing precursors is still not completely clear. Recent studies suggest that considering the precursoring melt as a stretched network [55, 118, 141, 129, 37] yields a better description than the traditional coil-stretch transition proposed by Keller and Kolnar [38].

Resolving these questions is important, as flow-induced shish-kebab structures tremendously enhance the mechanical properties of the final material. What is not so often emphasized, however, is the fact that these structures influence the mechanical melt properties, too. Recently, Li and co-workers found that after an extensional step strain of an iPP melt is imposed, flow-induced shish prevents the sample from necking. Necking is the result of a flow instability that arises in uncontrolled extension [28]. While the failure caused by necking is an interesting and relevant problem, it does not reveal insights into the true strength of the material and the reinforcement upon shish formation. A true fracture experiment can reveal the strength of a melt in extension, as well as the mechanism of failure, as performed by Huang et al. on amorphous systems [98]. The fracture mechanics of semicrystalline systems undergoing FIC have yet to be studied in controlled extension.

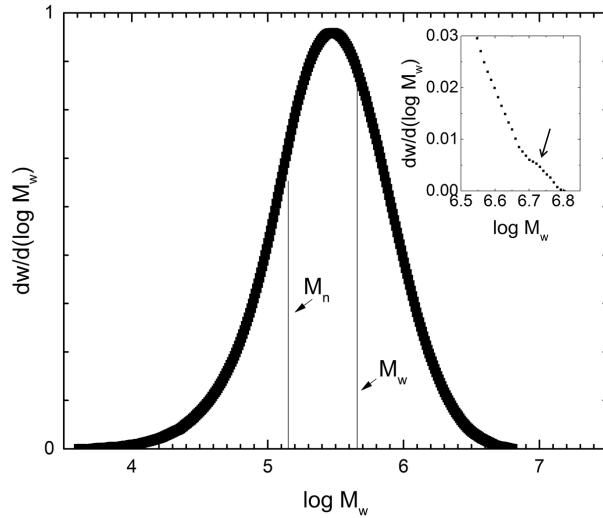


**Figure 6.1:** Molecular weight distribution of PE-460k. The horizontal black lines indicate the number average molar mass  $M_n$  and weight average molar mass  $M_w$ . The inset shows a magnification of the highest molecular weight fraction with an arrow pointing to an apparent shoulder in the molar mass distribution.

In this work, we study the reinforcement by shish nucleation and growth of filaments in controlled uniaxial extensional flow. The material is a commercial HDPE, and all experiments are performed above the melting temperature at constant deformation rates. Using the FSR, we study the extensional response of the melt during shish nucleation by monitoring the true stress of the melt up to Hencky strains of 5. Ex-situ SAXS reveals the effect of FIC on the morphology of the filaments after the cessation of the flow.

## 6.1 Materials and methods

We used a commercial HDPE (CP00416-021 from Chevron Philips), referred to as "PE-460k", which has 0.2 short-chain branches/1000 backbone carbons. The molecular weight distribution obtained from HT-GPC is shown in Figure 6.1, from which  $M_w = 460\text{kg/mol}$  and  $\text{PDI} = 2.7$ , were determined. (Note: the values of  $M_w$  and PDI given by the supplier were slightly higher at  $530\text{kg/mol}$  and 3.0, respectively). The melting temperature determined via DSC was  $138.0\text{ }^\circ\text{C}$ .

The linear rheology of the sample was characterized in SAOS and linear creep, as

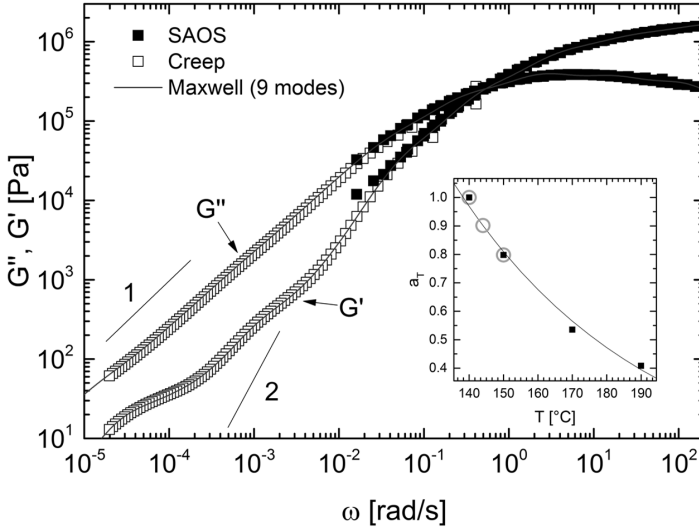


**Figure 6.2:** Linear rheology of PE-460k at  $T_0 = 140\text{ }^\circ\text{C}$  given in terms of storage modulus  $G'$  and loss modulus  $G''$ . Closed symbols indicate data obtained via SAOS, and open symbols indicate data obtained via creep. Lines show the fit of the multimode Maxwell model (nine modes). The inset shows the horizontal shift factors obtained from SAOS (black squares), along with the Arrhenius prediction (black line) with the use of the activation energy  $E_a = 12.45\text{ kJ/mol/K}$  and the reference temperature  $T_0 = 140\text{ }^\circ\text{C}$ . Gray circles indicate the temperatures at which extensional measurements were performed, as well as the corresponding shift factors used for adjusting the Hencky strain rates.

described in Chapter 4. Inverted creep data obtained at  $150\text{ }^\circ\text{C}$  and the frequency sweeps from SAOS obtained at  $140\text{--}190\text{ }^\circ\text{C}$  were combined using the time temperature superposition principle (TTS) to obtain mastercurves of dynamic moduli over a wide range of frequencies (see inset in Figure 6.2). Because of the very high molecular weight tail (see Figure 6.1), the terminal regime at which  $G'$  and  $G''$  reach a slope of 2 and 1, respectively, was inaccessible experimentally, even in creep. The horizontal shift factors  $a_T$  used in the creation of the mastercurves are shown in Figure 6.2 inset along with the Arrhenius fit for which we obtained an activation energy  $E_a = 12.45\text{ kJ/mol/K}$  [99]. The linear response was fitted by the multimode Maxwell model using nine modes (see Figure 6.2 for the fitting and Appendix E for the values of Maxwell moduli and corresponding time constants)

We conducted uniaxial extensional experiments at constant Hencky strain rates  $\dot{\epsilon}$ . VADER 1000 (see Section 1.2.2) was used, and the experimental procedure of filament stretching was analogous to that described in Chapter 4. The experiments were

performed at three different temperatures (140 °C, 144 °C and 150 °C) and terminated by quenching to room temperature at a Hencky strain  $\varepsilon = 5$ . We used shift factors determined from SAOS (see Figure 6.2) to adjust the Hencky strain rates such that all samples were stretched at the same relative rates  $a_T \dot{\varepsilon}$  irrespective of temperature.

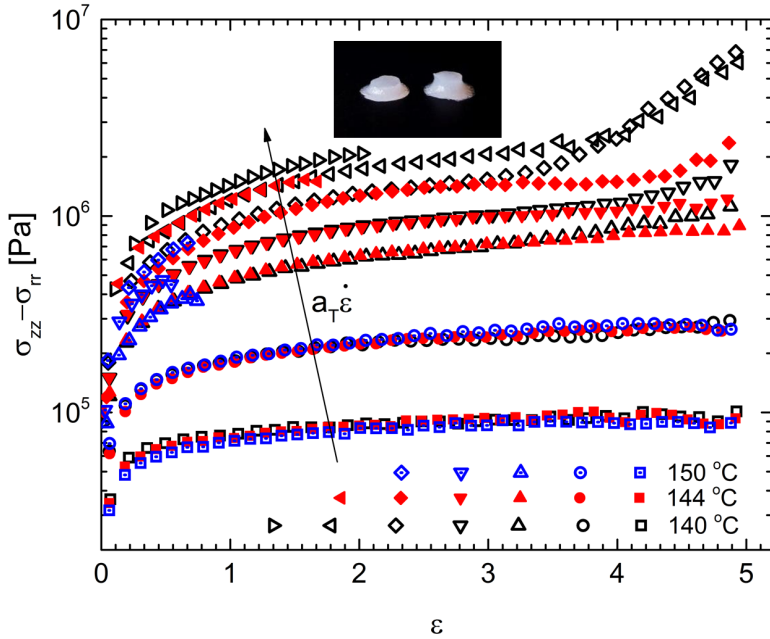
Small angle X-ray scattering (SAXS) of the quenched filaments was performed using a Rigaku S-MAX 3000 system with a Gabriel design Multiwire, gas-filled proportional type detector (resolution: 200 microns). The sample-to-detector distance was 1525 mm and the exposure time for each pattern was 15–30 min. Patterns were collected from the mid-filament plane of the samples. For the shortest filaments in which the exact position of the midfilament plane was challenging to determine, axial scans were performed by collecting patterns for every 0.5 mm in the midfilament region. (see Appendix E for details on axial scans). Calibration of the scattering vector  $q$  was performed using silver behenate. Herman's orientation factor was extracted from SAXS using the method described in Chapter 4 and Appendix C, with the only difference being the use of a Gaussian distribution instead of a Lorentzian one to fit the azimuthal intensity peaks.

## 6.2 Results and discussion

### 6.2.1 Shish nucleation and growth during extension

The extensional response of PE-460k is shown in terms of extensional stress versus strain in Figure 6.3. At low rates  $a_T \dot{\varepsilon} = 0.01$  and  $0.03 \text{ s}^{-1}$ , the response is independent of temperature, thus, TTS applies in this region. At rates  $a_T \dot{\varepsilon} \geq 0.1 \text{ s}^{-1}$ , TTS breaks down and the response becomes highly temperature dependent. At 150 °C, the sample undergoes brittle fracture and cannot be stretched beyond  $\varepsilon = 0.8$ . At 140 °C and 144 °C the sample can be stretched without fracture, but the strain hardening is significantly more pronounced at 140 °C than at 144 °C. We believe that the breakdown of TTS is a result of flow-induced crystallization (FIC) although all experiments are performed above  $T_m$ . Previous studies have shown that the FIC of polyethylene in strong flows, is, indeed possible above  $T_m$  [142, 44, 56]. This phenomenon is only possible because of the transition from the folded chain crystals that make up spherulites and kebabs to the considerably more stable extended chain crystals found in shish. Hence, we expect the strain hardening to result from shish nucleation and growth alone.

The SAXS patterns obtained for the quenched filaments after the cessation of flow is shown in Figure 6.4 and reveal an increasing anisotropy with the Hencky strain rate. The lobes stemming from the scattering between kebabs intensifies along the



(a)

**Figure 6.3:** Response of PE-460k in uniaxial extension of constant  $\dot{\epsilon}$  at  $T = 140^\circ\text{C}$  (black symbols),  $T = 144^\circ\text{C}$  (red symbols) and  $T = 150^\circ\text{C}$  (blue symbols). Most extensional flow experiments were terminated at  $\epsilon = 5$  by quenching. Some experiments terminated earlier because of filament fracture. The photo shows a sample at room temperature that has undergone brittle fracture during uniaxial flow. The relative Hencky strain rates following the black arrow (bottom to top) are  $a_T \dot{\epsilon} = 0.01, 0.03, 0.1, 0.175, 0.3, 0.54$  and  $1.0 \text{ s}^{-1}$ .

meridian, and even more importantly, an equatorial shish streak of increasing intensity develops. The intensification of the kebab lobes suggests an overall increase in crystalline orientation. The intensified shish streak indicates an increased amount of shish [51], a result that excellently agrees with the rheological response in Figure 6.3 showing an increase in strain hardening with the Hencky strain rate. For the range of low Hencky strain rates where TTS applies, no clear sign of shish formation is detected.

### 6.2.2 Stabilization of flow and critical strain for shish formation

As already mentioned, samples stretched at 150 °C undergoes brittle fracture [98] to prevent the sample from being stretched above  $\varepsilon = 0.8$  for  $a_T \dot{\varepsilon} \geq 0.1$ . Lowering the temperature to 144 °C enables stretching without fracture at rates up to  $a_T \dot{\varepsilon} = 0.3 \text{ s}^{-1}$ . At 140 °C, rates up to  $a_T \dot{\varepsilon} = 0.54 \text{ s}^{-1}$  can be reached. We hypothesize that the nucleation and growth of shish at 140 and 144 °C reinforce the filament. Consequently at 140 and 144 °C stretch experiments without brittle fracture can be carried out at higher rates relative to 150 °C (where no shish is believed to be formed). Perhaps the most interesting result that the fracture/no fracture observations provide is the insight into *when* the onset of crystallization occurs or, more specifically, the value of the critical strain for shish formation  $\varepsilon_c$ . Previously reported values of  $\varepsilon_c$  are all  $> 1.5$  [140, 118, 56]. Here, both for 140 and 144 °C, we find that  $\varepsilon_c$  has to be 0.8 or even less for shish to prevent fracture that otherwise occurs at this strain. From the TTS success/failure transition in Figure 6.3, defining a critical stress  $\sigma_c$  between 100 and 500 kPa for the onset of shish, is possible as well.

### 6.2.3 Strain hardening due to crystallization

Figure 6.3 also shows that for  $a_T \dot{\varepsilon} = 0.1$  and  $0.3 \text{ s}^{-1}$ , the responses at 140 and 144 °C overlap for  $\varepsilon < 3$ . Above  $\varepsilon = 3$ , however, the behavior at the two temperatures differs. At 140 °C the stress shows a clear increase in slope with increasing  $\varepsilon$ . At 144 °C the degree of strain hardening is smaller. As demonstrated by Hadinata et al., the upturn at both temperatures can be explained by FIC when the extensional response is compared with the prediction of the hierarchical multimode stress function (HMMSF) [124, 125], as shown in Figures 6.5a and b, (see Section 4.2.1 for the description of the HMMSF model). For the two temperatures, the deviation at  $\varepsilon > 3$  from the model prediction clearly suggests a structural change of the melt. At  $\varepsilon < 3$  the measured response is relatively well captured by the HMMSF model that only considers chain dynamics. However, the melt fractures at 150 °C, so some structural change must take place for the lower temperatures at  $\varepsilon < 3$ , as well. Based on the ideas introduced

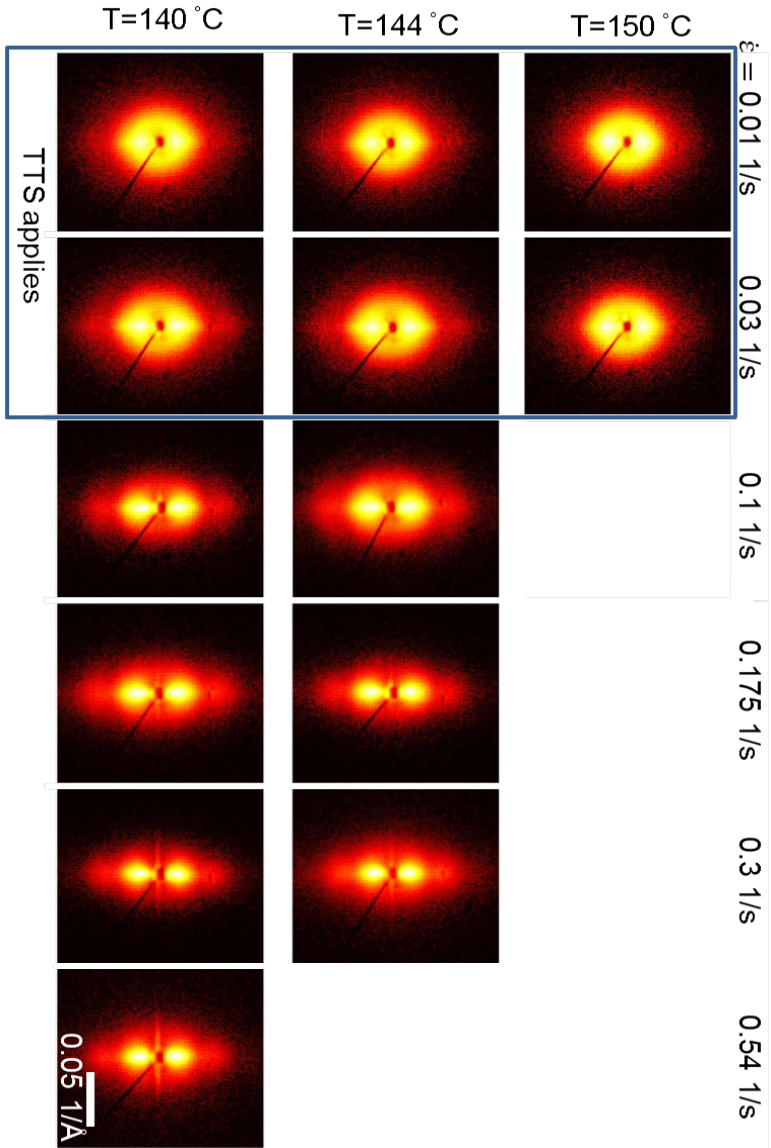


**Figure 6-4:** SAXS patterns of PE-460k filaments at room temperature after uniaxial stretch above  $T_m$  and quench at  $\epsilon = 5$ . The stretching direction is vertical. The blue square indicates samples at conditions under which TTS applies in the melt

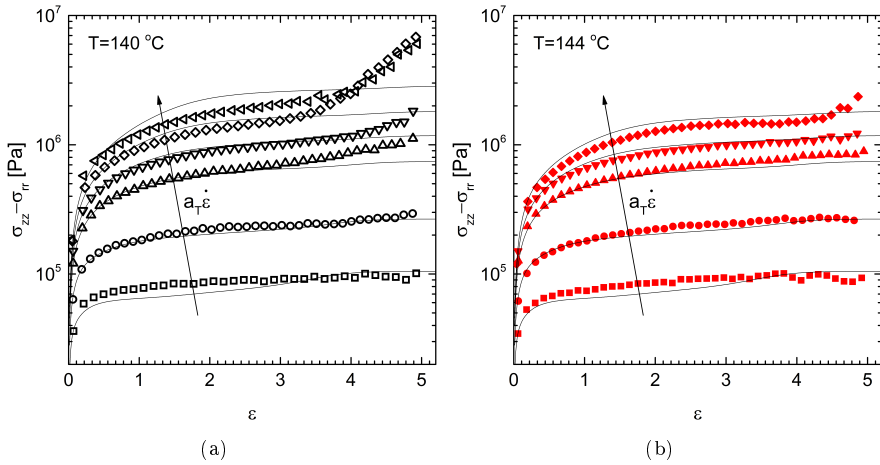


**Figure 6.5:** Comparison of the measured extensional stress (symbols) and HMMSF-predicted extensional stress (lines) of PE-460k. The value of nonlinear fit parameter  $G_D = 600$  Pa, and nine Maxwell modes are used in the modelling of the stretch experiments (a) at  $T = 140^\circ\text{C}$  and (b) at  $T = 144^\circ\text{C}$ . The relative Hencky strain rates in both figures following the black arrow (bottom to top) are  $a_T \dot{\epsilon} = 0.01, 0.03, 0.1, 0.175, 0.3 \text{ s}^{-1}$  and, only in (a),  $0.54 \text{ s}^{-1}$ .

by Eder and Janeschitz-Kriegl threadlike precursors can be thought to create a loosely cross-linked network governed by chain dynamics [48]. If the density of cross-links is small, the polymer chain on short time scales will only have time to relax locally and, therefore, does not feel a cross-link further down the chain. As a result, the cross-link will have no influence on the extensional rheology at short times in this case at  $\epsilon < 3$ . At longer times, the cross-link hinders the complete relaxation of a chain. Therefore, the chains are stretched further than predicted by chain dynamics, causing the upward deviation from the HMMSF model. For the sample stretched at  $140^\circ\text{C}$  we observe a rate-independent stress versus strain for  $a_T \dot{\epsilon} = 0.3$  and  $0.54 \text{ s}^{-1}$  above  $\epsilon = 4$ . Essentially, this is the defining characteristic of a solid.

#### 6.2.4 Modelling the influence of shish on extensional rheology

Flow-induced crystallization can be modelled in several ways. In this study, we use a very simple approach in which we consider the threadlike precursors to act as cross-links as explained above. This approach is inspired by the works of Zuidema et al. and Roozmond et al. [129, 37].

We incorporate crystallization into the HMMSF model by, using this picture of a stretched network. If just a few nuclei exist, the melt is very weakly cross-linked, and therefore, only the longest modes of relaxation are hindered. If the nucleation density is high, the relaxation of the faster modes are hindered as well. The modes prevented from relaxation by cross-links are set to have a relaxation time  $\tau_i = \infty$ . These modes are referred to as locked modes. The modes are hierarchically locked meaning that a fast mode  $i$  cannot lock unless all modes slower than  $i$  are locked, as well. In this first attempt, we assume that the cross-linking density is constant throughout the stretch, which most likely is untrue. Hence, the number of locked modes during a given stretch is constant. The number of locked modes also serves as a fitting parameter. Furthermore, we neglect changes in density caused by crystallization as well as any influence from the spatial growth of nuclei. Both assumptions are expected to be valid only during the initial stage of crystallization, when the sizes of crystalline domains are small and hence, the degree of crystallinity limited.

Figures 6.6a and b show the results of the modelling for 140 and 144 °C, respectively. This approach, indeed, enables the influence of shish formation on the extensional rheology to be captured qualitatively. Even the solid-like behavior observed at 140 °C is accounted for. From the model we learn that because the cross-links prevent the locked long modes from relaxing at high strains, the locked modes become highly stretched and thus alone govern the extensional response. The large portion of unlocked chain segments that can relax is insignificant to the overall behavior.

### 6.2.5 Herman's Orientation and stress at quench

The modelling has shown that the response of the crystallizing melt can be modelled by considering the melt as a cross-linked network of increasing cross-link density. This result suggests that although the melt is crystallizing, the response is governed primarily by the dynamics of uncrystallized chains locked between nuclei. Consequently, the previously suggested relationship between stress at quench and Herman's orientation factor (Chapters 3 and 4) should apply for this sample as well, despite the fact that it crystallizes during the stretch. Figure 6.7 shows the Herman's orientation factor against the stress at quench for samples stretched at all three temperatures.

The orientation for all filaments, irrespective of the temperature during stretching, fall onto the same master curve. The mastercurve seems to have two regions. 1) A region in which the  $F_H$  follows a power law with an exponent of  $2/5$ , similar trends observed in Chapters 3 and 4 and 2) a plateau where the orientation saturates and stays constant around  $F_H \sim 0.7$ . The maximum theoretical value of Herman's orientation factor  $F_{H,max} = 1$  (perfect unidirectional orientation). Thus,  $F_H$  cannot keep increasing and a plateau region in which  $F_{H,max} = 1$  is expected for the ideal

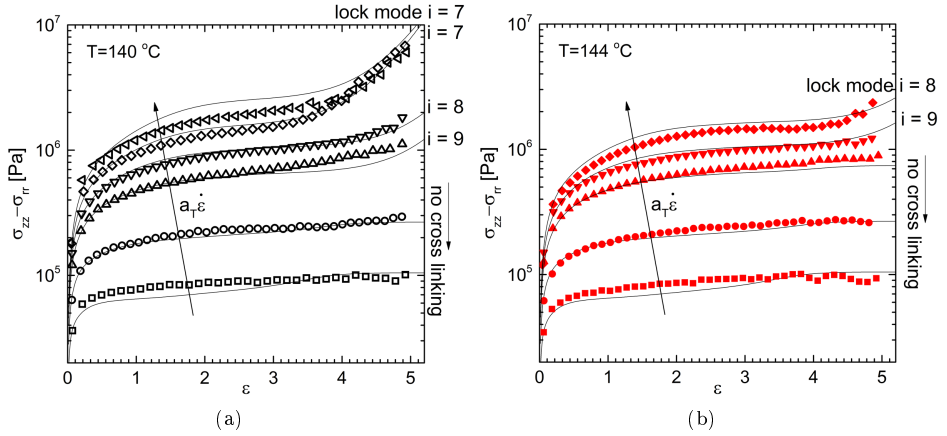


**Figure 6.6:** Comparison of the measured extensional stress (symbols) and HMMSF predicted extensional stress using locked modes (lines) of PE-460k (a) at  $T = 140^\circ\text{C}$  and (b)  $T = 144^\circ\text{C}$ . The value of nonlinear fit parameter  $G_D = 600$ , Pa and nine Maxwell modes are used in the modelling. The 1st Maxwell mode is the fastest, whereas the 9th mode is the slowest. The relative Hencky strain rates in both figures following the black arrow (bottom to top) are  $a_T \dot{\epsilon} = 0.01, 0.03, 0.1, 0.175, 0.3 \text{ s}^{-1}$  and (only in a)  $0.54 \text{ s}^{-1}$ . The fastest mode that is locked because of cross-linking for each stretch is also shown. A locked mode  $i = 7$  means that the 7th, 8th and 9th mode have  $\tau_i = \infty$ .

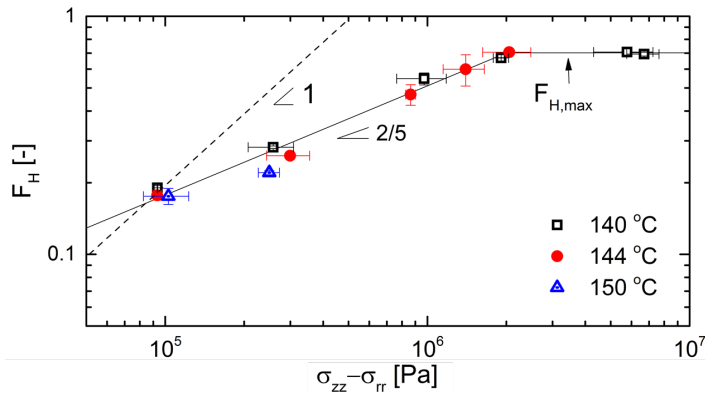


**Figure 6.7:** Herman's orientation in quenched filaments versus the stress at quench. Symbols indicate filaments stretched at  $140^\circ\text{C}$  (black),  $144^\circ\text{C}$  (red), and  $150^\circ\text{C}$  (blue). The solid line is a guide to the eye showing two regions: one with a slope of 2/5 followed by a plateau region. The dashed line shows the linear relation observed in amorphous systems.

case. Polymers are far from ideal. In fact, creating perfectly oriented shish-kebabs is impossible. The maximum shish-kebab orientation of a given polymer most likely depends on the chain architecture and is expected to be lower than the theoretical maximum value of 1. For PE-460k,  $F_{H,max}$  is 0.7. Once this value is reached, the length and number of shish can still increase, but the orientation stays unchanged.

## 6.3 Conclusion

We have shown that flow-induced shish nucleation and growth in uniaxial extension above  $T_m$  can stabilize the filaments and prevent true fracture. We find the critical strain for the onset of shish formation to be less than 0.8, which is much lower than previously reported values. We have shown that under the conditions tested here, the qualitative influence of crystallization on the extensional rheology can be captured by incorporating cross-linking into the HMMSF model. The success of the modelling suggests that the response of the liquid is governed by the dynamics of chains locked between nuclei. Thus, we find that Herman's orientation factor in the quenched filament is a universal function of the stress at quench.

Contributors to this work was Bo Shen and Prof. Julie Kornfield who provided the material. Daniele Parisi and Prof. Dimitris Vlassopoulos performed linear creep experiments and Anine Borger and Prof. Kell Mortensen performed the SAXS measurements. The SAXS measurements were carried out at Core Facilities in the College of Engineering at Drexel University, who is gratefully acknowledged.

# Conclusions, perspectives and outlook

---

With this work we aimed to connect uniaxial extensional rheology and crystallization in polymers. The study was heavily focused on the rheological aspect of this problem in terms of both experiments and analysis because this is where we could bring something new to the table. During the past decade, the general knowledge of dynamics in extensional flow has increased tremendously. This knowledge is of utmost importance in terms of understanding flow induced crystallization, in particular formation of extended chain crystals (shish). This study served to bring rheology and FIC closer by applying the most recently acquired knowledge of polymers in extension and studying its influence on crystallization. The Chapters of the thesis can be divided into three categories: 1) Amorphous polymers in uniaxial extension, 2) uniaxial extension and subsequent non-isothermal crystallization, and 3) isothermal crystallization during uniaxial extension. Key findings in these categories are summarized in the following.

**Amorphous polymers in uniaxial extension (Chapter 2)** While the field of extensional rheology has advanced significantly, there are still unresolved questions. One question still unresolved is the discrepancy between the extensional response in diluted and undiluted linear polymer systems. One very recent explanation for this discrepancy is the idea of friction reduction [57]. From this idea and through careful consideration regarding solvent molecular weight, as well as the molar mass and the concentration of PMMA, we show that it is possible to design a PMMA solution with the same linear and nonlinear response as a PS melts. The investigations confirm that the idea of friction reduction is a plausible cause of the apparent qualitative difference in behavior between polymer melts and solutions.

**Crystallization from a stretched state (Chapters 3 + 4)** These studies concern extensional experiments on LDPE and HDPE, and the morphology obtained upon cessation of the flow investigated by ex-situ SAXS and WAXD. The experimental temperature is high enough that no crystallization occurs during deformation and therefore complexity of the system is kept down relative to systems in which crystallization occurs during flow. Quenching rate relative to the relaxation times of the molecules is fast. Consequently, the polymers do not have time to relax before crystallization, which enables the molecular conformation extracted from the extensional response to be compared with the final morphology. Not surprisingly, molecular deformation before quench, and the morphology of the quenched filament is directly correlated. The investigations of LDPE show that the extensional overshoot can indeed be attributed to branch point withdrawal as the orientation of samples quenched at the stress maximum shows a greater orientation than samples quenched after the overshoot. For HDPE, we find that stress increase upon addition of a very small fraction of UHMwPE scales with increased orientation observed after quench. Therefore a very important point of these experiments is the importance of measuring the rheological response of the high molecular weight component. This is broadly overlooked in experimental studies while most model theories specifically focus on the high molecular weight component. We propose to measure the low frequency regime using linear creep experiments in combination with nonlinear extension. Creep gives insight into the isolated response of the high molecular weight component while extension yields its behavior in strong flows.

**Extension induced crystallization above  $T_m$  (Chapters 5 + 6)** These studies concern crystallization above  $T_m$  induced by application of strong flow. We use polyethylene both in the form of a commercial HDPE and as UHMwPE in solutions of paraffin oil. For both types of systems we observe a stabilizing effect of FIC in the filaments. In solution, FIC prevents the flow induced phase separation from proceeding to the point of filament failure, while in the melt FIC prevents brittle fracture. We find evidence that the initiation of FIC occurs at Henky strains less than 0.8 which is lower than previously reported values determined by scattering methods. This suggests that precursors form at an even lower strain than previously anticipated. Furthermore the cohesive effect of precursoring is so strong that it prevents brittle fracture of the fluid. Modification of the HMMSF model to include various degrees of cross-linking reveals that FIC in HDPE can be described as a stretching network, which is in agreement with recent studies.

Considering the thesis as a whole, a general trend is worth mentioning. Chapter 3, 4 and 6 independently find a correlation between the stress at quench and Herman's orientation factor determined from SAXS. The systems investigated in these chapters are vastly different in terms of chain architecture and whether FIC occurs or not. Despite these differences, we find that the extracted orientation factors fall onto the

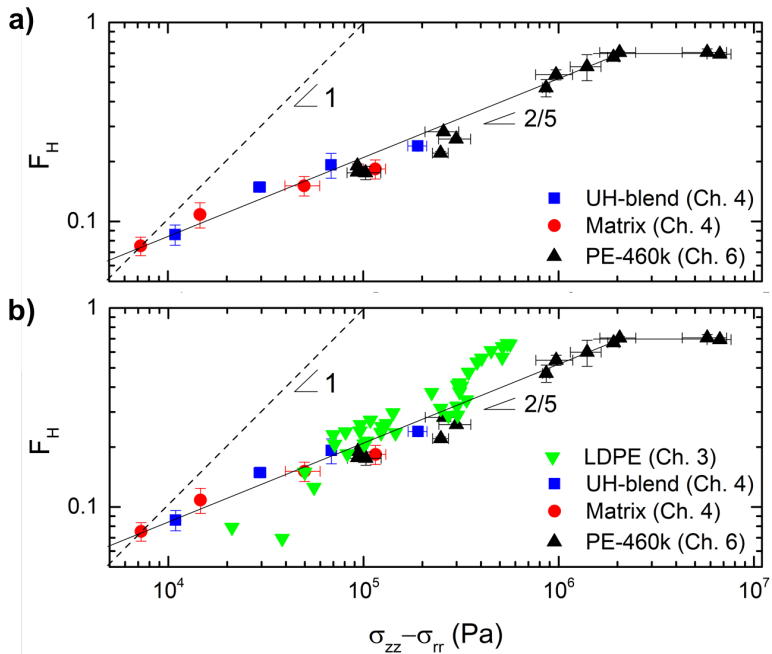


**Figure 7.1:** Herman's orientation in quenched filaments versus the stress at quench. (a) Shows data for HDPE obtained in Chapter 4 (blue and red symbols) and 6 (black symbols). (b) shows the same data as in (a) but with additional data from Chapter 3 on LDPE.

same mastercurve when plotted against the stress at quench (see Figures 7.1a and b). Correlations like these can only be revealed if one measures true properties - not take-up speed along a spinline, not engineering stress, not draw ratio - and overall this study proves the importance of extensional rheology in understanding FIC.

## 7.1 Outlook

In closing I would like to present my reflections and proposals for future studies in the three above mentioned categories:

**Amorphous polymers in uniaxial extension (Chapter 2)** The attention on friction reduction as a way to explain the difference between polymer melts and

solutions in extension is quite recent. More experimental studies and modelling are needed in order for it to be generally accepted. Several ongoing projects are centered around proving or disproving this theory [86, 143]. In order for the idea of friction reduction to be valid, the solvent molecules (oligomeric PMMA) for the PMMA solutions in Chapter 2 should orient in the flow. A very interesting project would be to replace oligomeric PMMA with deuterated analogs and perform SANS experiments either in-situ or on quenched filaments. This could reveal whether the solvent molecules of these systems orient or not and thus if friction reduction exists.

**Crystallization from a stretched state (Chapters 3 + 4)** A great advantage of these studies relative to studies in which FIC occurs is the reduced complexity of the extensional flow as it stays homogeneous. Consequently, the molecular conformation at quench is more easily related to the morphology after quench. It would be interesting to extend this connection one step further and measure the strength (e.g. Young's modulus) of the filaments created on the FSR. This way the molecular conformation at quench can be related to the final mechanical properties at room temperature.

**Extension induced crystallization above  $T_m$  (Chapters 5 + 6)** During this PhD study, several very interesting findings have been published [144, 145]. Currently, the group of Prof. Liangbin Li has the ability to perform in-situ X-ray measurements on extensional flows using the SER fixture [108, 146, 141, 118]. Together with recent developments in modelling, the solution to the problem of how to treat a precursoring/nucleating melt in flow is becoming more clear [37]. From these works, it seems, an accurate description of a melt, in which precursors are forming, is by a network of increasing cross-linking density. The precursors initiating the network formation, however, is still not understood. Recently, new insight into the persistence of precursors at elevated temperatures has been published [147]. It is shown here that precursors persist at higher temperatures and longer times than generally expected. Hence it seems that although the effect of precursoring on FIC is unravelling, the true nature of precursors is still to be discovered. Future studies combining the FSR with in-situ scattering methods would be of great advantage.

APPENDIX A

# Supplemental material for: Chapter 2

---

Linear and nonlinear universality in the rheology of  
polymer melts and solutions"

A.1 Article in its published format

## Linear and Nonlinear Universality in the Rheology of Polymer Melts and Solutions

Sara L. Wingstrand,<sup>1</sup> Nicolas J. Alvarez,<sup>2</sup> Qian Huang,<sup>1</sup> and Ole Hassager<sup>1,\*</sup>

<sup>1</sup>Danish Polymer Center, Department of Chemical and Biochemical Engineering, Technical University of Denmark, Building 227, 2800 Kgs. Lyngby, Denmark

<sup>2</sup>Department of Chemical and Biological engineering, Drexel University, Philadelphia, Pennsylvania 19104, USA

(Received 5 May 2015; published 13 August 2015)

Understanding the dynamics of polymeric liquids has great importance in the design and processing of soft materials. While slow flow dynamics is now resolved, fast flow dynamics is still unsolved, especially due to the lack of experimental evidence. We here manipulate a poly(methyl methacrylate) solution into exhibiting the same flow behavior as a polystyrene melt. Strikingly similar responses of the fluids are seen both in slow and very fast flow. With this discovery we show that dynamics in polymeric liquids can be generalized and captured in one single polymer physics model.

DOI: 10.1103/PhysRevLett.115.078302

PACS numbers: 47.57.Ng, 83.10.Kn, 83.60.Bc, 83.60.Df

Universality of molecular dynamics is a fundamental assumption in polymer physics [1,2]. It is the underlying framework of the most successful theoretical model, known as the tube model [3,4]. The significance of this assumption is that model systems at room temperature, i.e., polymer solutions, could be used to represent polymer melts at elevated temperatures. While the existence of a room temperature model material would be highly desirable, unfortunately a polymer solution with the same fast flow dynamics (nonlinear behavior) as a polymer melt has not yet been observed. It was recently shown that two linear polymeric systems with the same number of entanglements exhibit identical slow flow dynamics (linear behavior), but strikingly different nonlinear behavior [5]. The lack of evidence of universality in strongly nonlinear conditions leaves one wondering whether such an assumption is valid.

For two polymeric systems to have identical flow dynamics, researchers have hypothesized that they must have the same following characteristics: (i) the same number of entanglements, (ii) the same degree of flexibility (number of Kuhn segments per entanglement), and, very recently, (iii) the same potential for monomeric friction reduction [6]. Whereas systems with identical characteristics (i) and (ii) have been studied [7,8], systems with the same characteristics (i)–(iii) have not, the reason being that usually characteristic (ii) can never be adjusted without compromising characteristic (iii).

This study observes universal behavior between a polymer solution and a polymer melt with the same three characteristics, confirming the assumption of universality in polymer physics for both linear and nonlinear dynamics. The following is a brief description of how to manipulate all three characteristics independently.

Adjustment of the three characteristics (i)–(iii) is based on the tube model depicted in Fig. 1. Here, a polymer in an entangled melt is reduced to a primitive chain with limited ability to move in its transverse direction due to

entanglements with neighboring chains [Fig. 1(a)]. Effectively, the entanglements can be regarded as constituents of a tube surrounding the test chain [Fig. 1(b)]. The primitive chain itself can be described by a random walk of Kuhn steps [Fig. 1(c)].

The number of entanglements per chain  $Z$ , characteristic (i), is solely responsible for the linear response of a polymeric liquid [5]. It is given by the ratio of Kuhn steps in the entire chain  $N$  over Kuhn steps per entanglement segment  $N_e$ , or analogously on a molar mass basis

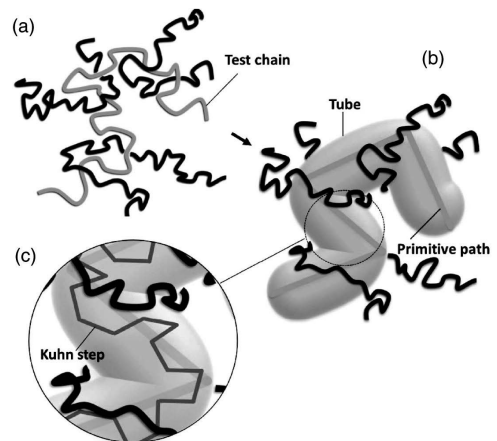


FIG. 1 (color online). Sketch of the tube analogy for entangled polymeric liquids. (a) A primitive entangled polymer chain in a melt. The polymer test chain is well entangled with neighboring polymer chains. (b) The simplified picture of the polymer melt applied in the original tube model. Here, the entanglements constitute a tube with a primitive path. (c) Enlargement of one entanglement segment showing how the test chain is reduced to a random distribution of connected Kuhn steps.

$$Z = \frac{N}{N_e} = \frac{M_w}{M_e}. \quad (1)$$

Here,  $M_w$  and  $M_e$  are the molar masses of the entire chain and one entanglement segment, respectively. As  $M_e$  is independent of polymer molar mass, the number of entanglements can be adjusted from the molar mass of the polymer as it scales linearly with  $M_w$ . The addition of a solvent to a polymer melt increases  $M_e$ . However, a proportional change in  $M_w$  may be used to keep the number of entanglements unchanged.

The number of Kuhn steps per entanglement  $N_e$ , characteristic (ii), becomes important in the nonlinear regime [9].  $N_e$  describes the rigidity of an entanglement segment and is used in several nonlinear models [10–15]. For an undiluted polymer,  $N_e$  is determined by its chemistry alone. Adding a solvent to an entangled polymeric liquid will increase the spacing between entanglements, thus increasing the number of Kuhn steps per entanglement segment. In a solution with a given polymer concentration  $\phi$  the number of Kuhn steps between entanglements  $N_e(\phi)$  scales as

$$N_e(\phi) = N_e(1)\phi^{-\alpha}. \quad (2)$$

Here,  $N_e(1)$  is the number of Kuhn steps per entanglement segment for the undiluted system and  $\alpha$  is the dilution exponent with a value between 1 and 1.3, depending on concentration [16]. It is realized that dilution increases  $N_e$ ; hence, the only way to match  $N_e$  between a polymer melt and a solution is to have two different chemistries. Thus, by allowing a change in chemistry and molecular weight, both  $N_e$  and  $Z$  can be adjusted independently.

As previously mentioned, no two polymer liquids having identical characteristics (i) and (ii) (i.e., the same  $N_e$  and  $Z$ ) have shown the same nonlinear behavior. In fact, evidence of the contrary is available [7]. Hence, experimental evidence suggests that  $Z$  and  $N_e$  alone cannot account for the nonlinear behavior of polymeric liquids. This is why the third concept, monomeric friction reduction, proposed by Ianniruberto and co-workers is important [6].

Friction reduction, characteristic (iii), encountered in nonlinear flows, arises from the anisotropic environment locally around the polymer chain [6,17]. In the case of diluted polymers, traditional (small) solvent molecules remain isotropic even at large deformations, inhibiting any flow-induced monomeric friction reduction. The very nature of friction reduction seemingly disrupts any possibility of ever obtaining a solution that behaves as a melt, unless the solvent molecule possesses the same potential for friction reduction as the polymer itself, i.e., such as in the case of oligomers.

Using oligomers (polymers with less than 100 repeating units) as the solvent is a potential method of matching the friction reduction between the polymer and the solvent. Molecular dynamics simulations of polystyrene oligomers

have shown that the degree of friction reduction in fast shear flows indeed increases with increasing molar mass of the oligomers [6]. Hence, we hypothesize that the friction reduction of a polymer solution increases as the number of oligomer Kuhn steps  $N_s$  increases. Yet, in order not to create a binary blend of polymers where  $N_e$  is fixed,  $N_s$  must be smaller than  $N_e$  to avoid forming any additional entanglements, i.e.,  $N_s/N_e < 1$ . On the contrary  $N_s/N_e$  should be as large as possible in order to have a similar potential for anisotropy and hence friction reduction as a melt.

The solutions investigated in this study are prepared from poly(methyl methacrylate) (PMMA) with  $M_w = 86$  kg/mol (PMMA-86k) and  $M_w = 270$  kg/mol (PMMA-270k). From linear characterization,  $Z$  is estimated to be 14 for PMMA-86k and 52 for PMMA-270k, see the Supplemental Material [18] for details.  $N_e$  is estimated to be 10 and 9, respectively [19]. Oligo(methyl methacrylates) of various lengths are investigated as the solvent for the samples. Among the various options (see the Supplemental Material [18]), an oligomer of  $M_w = 3.5$  kg/mol (referred to as o-4k) is found to be the most optimal solvent for this study, i.e., the longest solvent molecule that does not form entanglements.

The reference materials that we aim to mimic using PMMA are two polystyrene (PS) melts. They have previously been characterized by Nielsen *et al.* and Huang *et al.* [5,21], one with  $M_w$  equal to 103 kg/mol the other with 285 kg/mol, referred to as PS-100k and PS-285k, respectively. PS is known to have  $M_e = 13.3$  kg/mol and analogously  $N_e = 22$  [5,22]. Characteristics of these samples related to the tube model are given in Table I.

Diluting PMMA-86k and PMMA-270k in o-4k yields the solutions PMMA-86k/o-4k and PMMA-270k/o-4k, respectively, with the characteristics given in Table I. Values of  $Z$  and  $N_e$  for the PMMA solutions and the reference PS melts are in good agreement (within  $\pm 10\%$ ). Furthermore, we observe that  $N_s/N_e$  for the PMMA solutions are close to 1 without exceeding it, as required.

The linear and nonlinear response of the PMMA solutions and PS melts are shown in Figs. 2(a) and 2(b), respectively. The linear response is obtained from a small amplitude oscillatory shear (SAOS) flow whereas nonlinear characterization is obtained from uniaxial extension.

TABLE I. Material characteristics of PS melts and PMMA solutions.

Sample	$\phi$	$\alpha$	$Z$	$N_e$	$N_s/N_e$
PS-285k	1.00	...	21	22	...
PMMA-270k/o-4k	0.45	1.17	20	23	0.67
PS-100k	1.00	...	7.7	22	...
PMMA-86k/o-4k	0.51	1.08	7.0	20	0.59

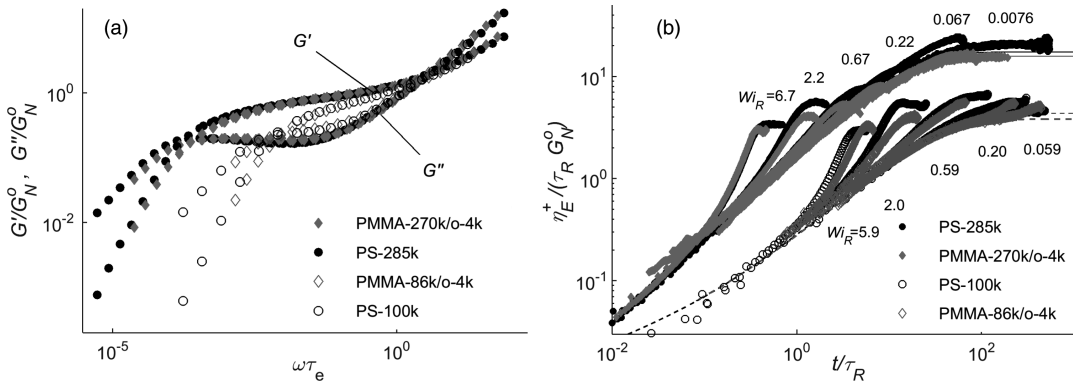


FIG. 2 (color online). Nondimensional mechanical response of PS melts and PMMA solutions. Samples have a similar number of Kuhn steps between entanglements  $N_e$ , degree of friction reduction, and pairwise matching number of entanglements  $Z$ . Closed symbols indicate samples with  $Z \approx 20$ , open symbols samples with  $Z \approx 7$ . Black indicates reference data for pure polystyrene melts [5,21]. (a) Linear response from small amplitude oscillatory shear, expressed in terms of normalized dynamic moduli versus normalized frequency. (b) Response of melts and solutions in extensional flow at various nondimensional rates of deformation ( $Wi_R$ ). Results are expressed in terms of the normalized stress growth coefficient. Samples with  $Z \approx 7$  have been shifted horizontally one order of magnitude higher for clarity. Solid and dashed lines are linear predictions obtained from fits of the SAOS data.

The linear response [Fig. 2(a)] is expressed in terms of the dynamic moduli  $G'$  and  $G''$  versus frequency  $\omega$ , representing the elastic and viscous response of the fluid, respectively. The solvent is expected to contribute an amount to  $G'' = (1 - \phi)\eta_s\omega$ , where  $\eta_s = 410$  Pa s is the solvent viscosity. Hence, the solvent only contributes a negligible amount to the moduli and the solvent does not affect the universality argument. The dynamic moduli have been normalized by the characteristic plateau modulus  $G_N^0$ , a hypothetical value of the plateau in  $G'$  for  $\omega \rightarrow \infty$ . Frequency is normalized by the characteristic time  $\tau_e$  related to the second crossover of the dynamic moduli. The parameters  $G_N^0$ ,  $\tau_e$ , and  $Z$  may be extracted from models such as the Baumgaertel-Schausberger-Winter spectrum or the Likhtman-McLeish model (see the Supplemental Material [18]) [23,24].

From the linear characterization in Fig. 2(a), it is seen how samples with the same  $Z$  overlap, as expected. Tube stretch and friction reduction are inactive under these conditions and, consequently,  $N_e$  as well as the type of solvent are irrelevant for the observed similarity.

The most severe nonlinear behavior of polymers is encountered in extension, including uniaxial extension. This study employs a filament stretching rheometer to measure the fast flow dynamics of melts and solutions [25]. It is equipped with an active control scheme [26] to avoid filament instability as described by Fielding [27]. The instrument measures the stress in the polymer sample by monitoring the axial force and the midfilament diameter. This study performs extensional measurements at a controlled rate, the Hencky strain rate  $\dot{\epsilon}_0$ . The resulting

response of the polymeric liquids is shown in Fig. 2(b). It displays the transient behavior in terms of the extensional stress growth coefficient, given by

$$\eta_E^+(t) = \frac{\sigma_{zz} - \sigma_{rr}}{\dot{\epsilon}_0}. \quad (3)$$

Here,  $\sigma_{zz}$  and  $\sigma_{rr}$  represent the axial and radial component of the stress tensor, respectively. Normalization of  $\eta_E^+$  is based on a characteristic viscosity given by the plateau modulus  $G_N^0$  and a characteristic relaxation time scale for the whole polymer chain  $\tau_R = \tau_e Z^2$  (see the Supplemental Material [18] for more details). In addition, the linear prediction obtained from fitting the Baumgaertel-Schausberger-Winter spectrum to the SAOS data is shown as solid and dashed lines in Fig. 2(b).

Each upturn represents a single filament stretch experiment, performed at a given constant  $\dot{\epsilon}_0$ . To enable comparison, strain rates are given in terms of nondimensional Weissenberg numbers ( $Wi_R = \dot{\epsilon}_0 \tau_R$  indicated at each experiment) instead of the absolute value  $\dot{\epsilon}_0$ .  $Wi_R$  compares the Rouse relaxation time of the chain contour length  $\tau_R$  to the imposed rate of deformation  $\dot{\epsilon}_0$  [28]. As long as  $Wi_R < 1$  the number of Kuhn lengths between entanglements  $N_e$  is unimportant. However, for  $Wi_R > 1$  motions on the scale of a Kuhn length occur, and therefore  $N_e$  becomes an important parameter. In a similar way friction reduction is only activated in a highly anisotropic environment experienced at  $Wi_R > 1$ , where chains are aligned and stretched [29].

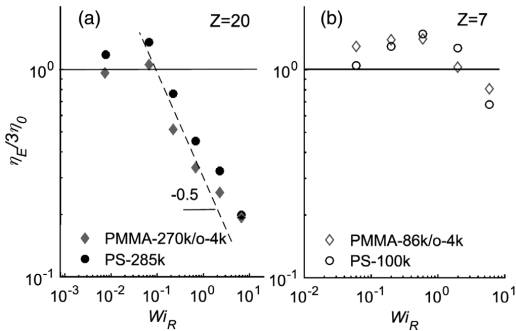


FIG. 3 (color online). Normalized steady state viscosity as a function of the Weissenberg number. Panel (a) compares samples with  $Z \approx 20$ . Panel (b) compares samples with  $Z \approx 7$ . Black indicates reference data [5,21].

In Fig. 2(b) good agreement with the linear prediction is observed for  $Wi_R \ll 1$ , as expected. At larger  $Wi_R$  a clear deviation from linear behavior is observed. This upward deviation of  $\eta_E^+$  from the linear prediction is known as strain hardening. The most important characteristic is that the transient behavior of PS melts and PMMA solutions stretched at the same  $Wi_R$  is the same for all time, for all experiments. This similarity between melt and solution behavior has, to our knowledge, never been observed before.

A plateau region is observed for  $\eta_E^+$ , towards the end of each stretch experiment in Fig. 2(b). Here, the polymeric liquids reach a steady state extensional viscosity  $\eta_E$ . These values are plotted against  $Wi_R$  in Fig. 3. In the linear regime, extensional viscosity  $\eta_E$  is often expressed in terms of the zero shear rate viscosity  $\eta_0$ , where  $\eta_E = 3\eta_0$ . Theoretically,  $\eta_E/3\eta_0 \rightarrow 1$  as  $Wi_R \rightarrow 0$  for linear polymeric liquids, as is indeed the case here.

The PMMA solutions prepared in this work exhibit an initial increase in  $\eta_E$ , followed by a steady decrease. The increase is more pronounced for a low number of entanglements both for the solutions and the melts. Furthermore, for liquids with a sufficiently high number of entanglements,  $\eta_E$  follows the power law  $\eta_E \propto (Wi_R)^{-0.5}$ , previously only observed for polymer melts [30]. Overall, the PMMA solutions and PS melts with the same three characteristics behave identically.

The ability of the oligomer to induce friction reduction can be explained from the concept of average orientation introduced by Yaoita *et al.* [17]. Assuming an isotropic solvent, they model friction reduction by introducing an average orientation tensor  $\bar{S} = \phi S_p$  with  $S_p$  being the polymer orientation tensor. The greater the average orientation, the greater the friction reduction. It is seen that the average orientation clearly is reduced as the concentration of polymer  $\phi$  is reduced, and consequently the degree of friction is reduced.

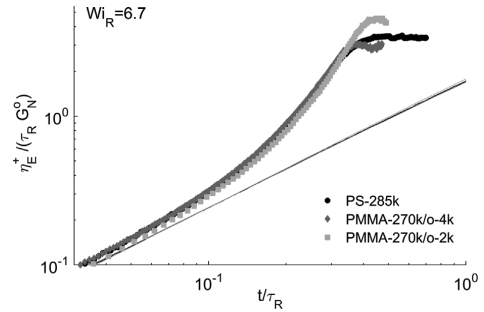


FIG. 4 (color online). Normalized stress growth coefficient (symbols) for three different polymers extended at a Weissenberg number  $Wi_R = 6.7$ . Solid lines indicate the predicted linear response. Black indicates reference data [5].

In this work, the o-4k solvent is orientable, i.e., non-isotropic. Intuitively, there must be an additional contribution to the average orientation from the solvent such that  $\bar{S} = \phi S_p + (1 - \phi)S_s$  where  $S_s$  is the orientation tensor of the solvent. Therefore, the average orientation of the solution is higher than if a molecular (isotropic) solvent were used, promoting friction reduction as expected in a melt. Note that in the limiting case where  $S_s \approx S_p$  there should be little difference between a melt and a solution.

To demonstrate this concept further, the effect of using a solvent molecule with  $M_w = 2.1$  kg/mol (o-2k), i.e., half the size of the utilized o-4k, is seen in Fig. 4. It is seen that the steady state viscosity of the PMMA solution containing the o-2k solvent (PMMA-270k/o-2k) exceeds that of the two others, PMMA-270k/o-4k and PS-285k. This supports the hypothesis that the o-2k solvent contributes less to the average orientation than the o-4k, resulting in less friction reduction.

To conclude, we have shown experimentally that universality of polymer dynamics can be extended from the linear regime deep into the nonlinear regime. The concept of monomeric friction reduction seems valid and perfectly explains the previously unsolved discrepancy between the response of polymer melts and solutions in fast flows where both  $Z$  and  $N_e$  are the same. As a result the number of characteristics needed to fully describe flows of polymeric liquids across all deformation regimes can be narrowed down to the three presented here.

These results have both positive and negative implications, the positive being that we now have a method of systematically designing model materials for linear entangled polymers and most likely other macromolecules and polymers with other types of architectures due to the proof of universality [31]. Unfortunately, the influence of friction reduction means that diluting polymers with conventional molecular solvents can never result in a proper model material for a polymeric melt since a disparity in

friction reduction between the polymer and solvent increases the strain hardening behavior. Hence, the use of polymeric solutions as model materials for polymeric melts seems very limited. The important take home message is that this data set offers a complete experimental framework for which to test all future models, which evidently must include physics relating to the number of entanglements, the flexibility of the chain, and the monomeric friction reduction of both the polymer and solvent when applicable.

In closing we remark that universality has been demonstrated on the macroscopically observable stress. It is interesting to consider whether this reflects universality on the molecular level, which in the future could be observed by techniques such as dielectric spectroscopy or neutron scattering [32,33].

Please contact Ole Hassager to gain access to the raw data.

We thank Evelyne van Ruymbeke at Université Catholique de Louvain for motivating the field of study. Financial support from the Aage og Johanne Louis-Hansen Foundation and the European Union (SUPOLEN, Initial Training Networks) is gratefully acknowledged.

\*oh@kt.dtu.dk

- [1] D. J. Read, D. Auhl, C. Das, J. den Doelder, M. Kapnistos, I. Vittorias, and T. C. B. McLeish, *Science* **333**, 1871 (2011).
- [2] M. W. Collis, A. K. Lele, M. R. Mackley, R. S. Graham, D. J. Groves, A. E. Likhtman, T. M. Nicholson, T. C. B. McLeish, L. R. Hutchings, C. M. Fernyhough, and R. N. Young, *J. Rheol.* **49**, 501 (2005).
- [3] P. G. de Gennes, *J. Chem. Phys.* **55**, 572 (1971).
- [4] M. Doi and S. F. Edwards, *The Theory of Polymer Dynamics* (Clarendon, Oxford, 1986), p. 391.
- [5] Q. Huang, O. Mednova, H. K. Rasmussen, N. J. Alvarez, A. L. Skov, and O. Hassager, *Macromolecules* **46**, 5026 (2013).
- [6] G. Ianniruberto, A. Brasiello, and G. Marrucci, *Macromolecules* **45**, 8058 (2012).
- [7] Q. Huang, N. J. Alvarez, Y. Matsumiya, H. K. Rasmussen, H. Watanabe, and O. Hassager, *ACS Macro Lett.* **2**, 741 (2013).
- [8] T. Sridhar, M. Acharya, D. a. Nguyen, and P. K. Bhattacharjee, *Macromolecules* **47**, 379 (2014).
- [9] C. Luap, C. Müller, T. Schweizer, and D. C. Venerus, *Rheol. Acta* **45**, 83 (2005).
- [10] J. Fang, M. Kröger, and H. C. Öttinger, *J. Rheol.* **44**, 1293 (2000).
- [11] H. K. Rasmussen and Q. Huang, *J. Non-Newtonian Fluid Mech.* **204**, 1 (2014).
- [12] T. Yaoita, T. Isaki, Y. Masubuchi, H. Watanabe, G. Ianniruberto, and G. Marrucci, *Macromolecules* **44**, 9675 (2011).
- [13] E. van Ruymbeke, J. Nielsen, and O. Hassager, *J. Rheol.* **54**, 1155 (2010).
- [14] R. S. Graham, A. E. Likhtman, T. C. B. McLeish, and S. T. Milner, *J. Rheol.* **47**, 1171 (2003).
- [15] D. J. Read, K. Jagannathan, S. K. Sukumaran, and D. Auhl, *J. Rheol.* **56**, 823 (2012).
- [16] E. van Ruymbeke, Y. Masubuchi, and H. Watanabe, *Macromolecules* **45**, 2085 (2012).
- [17] T. Yaoita, T. Isaki, Y. Masubuchi, H. Watanabe, G. Ianniruberto, and G. Marrucci, *Macromolecules* **45**, 2773 (2012).
- [18] See Supplemental Material at <http://link.aps.org/supplemental/10.1103/PhysRevLett.115.078302> for further information regarding materials and method, data fitting and extracted material parameters along with raw data.
- [19] Values differ between the two PMMAs due to a difference in tacticity [20].
- [20] K. Fuchs, C. Friedrich, and J. Weese, *Macromolecules* **29**, 5893 (1996).
- [21] J. K. Nielsen, H. K. Rasmussen, O. Hassager, and G. H. McKinley, *J. Rheol.* **50**, 453 (2006).
- [22] L. J. Fetters, D. J. Lohse, and R. H. Colby, in *Physical Properties of Polymers Handbook*, edited by J. E. Mark, 2nd ed. (Springer, New York, 2007), p. 1073.
- [23] M. Baumgaertel, A. Schausberger, and H. H. Winter, *Rheol. Acta* **29**, 400 (1990).
- [24] A. E. Likhtman and T. C. B. McLeish, *Macromolecules* **35**, 6332 (2002).
- [25] A. Bach, H. Koblitz, P. Longin, and O. Hassager, *J. Non-Newtonian Fluid Mech.* **108**, 163 (2002).
- [26] J. M. Román Marín, J. K. Huusom, N. J. Alvarez, Q. Huang, H. K. Rasmussen, A. Bach, A. L. Skov, and O. Hassager, *J. Non-Newtonian Fluid Mech.* **194**, 14 (2013).
- [27] S. M. Fielding, *Phys. Rev. Lett.* **107**, 258301 (2011).
- [28] J. M. Dealy, *Rheol. Bull.* **79**, 14 (2010).
- [29] O. Hassager, K. Mortensen, A. Bach, K. Almdal, H. K. Rasmussen, and W. Pyckhout-Hintzen, *Rheol. Acta* **51**, 385 (2012).
- [30] A. Bach, K. Almdal, H. K. Rasmussen, and O. Hassager, *Macromolecules* **36**, 5174 (2003).
- [31] R. G. Larson, *Science* **318**, 57 (2007).
- [32] K. Horio, T. Uneyama, Y. Matsumiya, Y. Masubuchi, and H. Watanabe, *Macromolecules* **47**, 246 (2014).
- [33] A. Blanchard, R. S. Graham, M. Heinrich, W. Pyckhout-Hintzen, D. Richter, A. E. Likhtman, T. C. B. McLeish, D. J. Read, E. Straube, and J. Kohlbrecher, *Phys. Rev. Lett.* **95**, 166001 (2005).

## A.2 Supplemental Material

Supplemental material contains following:

- Materials and methods
- Supplementary text
- Tables S-I, S-II, S-III, S-IV, S-V
- Figures S-1, S-2

**Supporting Online Material for:**  
**Linear and Nonlinear Universality in the Rheology of Polymer Melts and Solutions**

Sara L. Wingstrand<sup>1</sup>, Nicolas J. Alvarez<sup>2</sup>, Qian Huang<sup>1</sup>, Ole Hassager<sup>1\*</sup>

## **Materials and Method**

### **Synthesis and chromatography**

Polymers of varying molar masses were provided by Polymer standard service (PSS) except one which was provided by Sigma-Aldrich. Specifications on starting materials are given in table S-I.

**Preparation of solutions** was performed according to the following procedure. Before utilizing the polymers, they were dried under vacuum for min. 48 h (Binder vacuum oven, 70 °C, 0.1 bar). Subsequently, the solutions were prepared by mixing polymer and oligomer in amounts corresponding to the desired final concentration and dissolving in dichloromethane (DCM). The amount of DCM was adjusted such that the concentration of polymer in the mixture was  $< 0.1 c^*$ . Here  $c^*$  is the concentration separating dilute solutions from a semi-dilute solutions [1]. The mixture was sealed and gently stirred overnight ( $> 12$  h).

The mixture of polymer, oligomer and DCM was poured into a form made from thick aluminum foil and covered with regular perforated aluminum foil. The form was left in the fume hood until all DCM appeared to be evaporated ( $> 12$  h) and a solid film had formed. The size of the aluminium form was adjusted such that the thickness of the remaining polymer film was 50 – 150  $\mu\text{m}$ . Gently, flakes of film was peeled off the aluminum foil, and dried in the vacuum oven at 70 °C for  $> 48$  h. Specifications on the solutions are given in table S-II.

**Size exclusion chromatography (SEC)** was used as a means to characterize the prepared solutions and starting materials, with respect to 1) composition, 2) polydispersity indexes (PDI's), 3) check for thermal degradation after mechanical characterization.

Sample was weighed (5 – 10 mg) and dissolved in 1 – 2 mL eluent which in this case was stabilized THF. SEC was performed using a Viscotek VE 2001 GPC Solvent/Sample module together with a Viscotek TriSEC 302 Triple Array Detector. The columns were a PL Guard and two PL gel mixed D columns and calibration was made on the basis of PMMA standards. At least two SEC measurements were performed per solution to confirm that they were homogeneous.

**Differential scanning calorimetry (DSC)** was used to determine  $T_g$  of raw materials and the final solutions. 3 – 5 mg sample was placed in a hermeneutic pan and DSC was carried out using a TA Q1000 with autosampler. Standard Heat-Cool-Heat procedure was performed with a heating rate of 10 °C/min.

#### **Mechanical spectroscopy**

Mechanical characterization of both diluted and undiluted polymers was performed using two different rheometers, an Ares G2 rheometer from TA Instruments and an in-house developed filament stretching rheometer (FSR). For both instruments samples were shaped into small discs of varying height and diameter using a vacuum mould. Moulding was carried out at approximately 80 °C above  $T_g$  of the samples.

**Small amplitude oscillatory shear (SAOS)** was carried out in the TA Instruments Ares G2 rheometer under  $N_2$  atmosphere. The geometry was an 8 mm plate-plate geometry with a gap of ~0.8 mm. Frequency sweeps were conducted at minimum three different temperatures for each sample in the range of 30 – 100 °C above  $T_g$ . Resulting spectra were subsequently shifted to obtain a single master curve for each sample at 150 °C. The horizontal shift factors ( $a_T$ ) are given in table S-III. To ensure reproducibility at least two samples per material was tested and all frequency sweeps were repeated.

**Uniaxial extension** was performed using the in-house developed filament stretching rheometer (FSR) [2]. Samples were in most cases moulded into discs of 5.4 mm and a height of 1.5 – 2.5 mm. In a few cases discs with a diameter of 8 mm were used to enable higher strain rates to be achieved. For each stretch experiment a sample was placed

on the bottom plate, heated 50 – 70 °C above  $T_g$ . Once the sample had melted, it was squeezed for 5 min by lowering the upper plate. Subsequently the sample was pre-stretched to a diameter of 2.5 – 5.2 mm depending on the subsequent strain rate, the temperature was then lowered to 30 – 50 °C above  $T_g$  where the sample was left to relax until the normal force was 0 g. The sample was then stretched at a constant Hencky strain rate ( $\dot{\epsilon}_0$ ). If the measurement was not conducted at 150 °C it was subsequently shifted to 150 °C using the shift factors given in table S-III. Repetition of stretch experiments was performed for at least 3 different strain rates per material to ensure reproducibility.

### Supplementary text

**Data fitting** of SAOS data was carried out using the BSW-spectrum. The procedure is described in Huang et al. [3]. The resulting BSW parameters are given in table S-IV. The fitting parameters of the BSW-spectrum ( $G_N^0$ ,  $\tau_c$  and  $\tau_m$ ) were used for the estimation of the three original tube model parameters ( $G_N^0$ ,  $\tau_e$  and  $Z$ ) as follows:

$$\begin{aligned} G_N^0(\text{Tube}) &= G_N^0(\text{BSW}) \\ \tau_e(\text{Tube}) &= \tau_c(\text{BSW}) \\ Z(\text{Tube}) &\propto \left( \frac{\tau_m(\text{BSW})}{\tau_c(\text{BSW})} \right)^{\frac{1}{3.4}} \end{aligned}$$

Procedure on how  $N_e$  and  $N_s/N_e(1)$  are determined is described in the primary text. All tube model parameters are given in table S-V. For comparison, the parameters estimated using the Likhtman-Mcleish (LM) model (from the RepTate software) has been added as well [22].

**Selection of samples** for nonlinear testing was based on getting the highest ratio of  $N_s/N_e(1)$  without creating additional entanglements. The longest solvent o-15k, clearly creates additional entanglements evident from  $G'$ ,  $G''$  of PMMA-270k/o-15k in fig. S-1(A). The poor fit of the BSW and the narrow gap between  $G'$  and  $G''$  in the upper plateau region suggests that PMMA-270k/o-15k resemble a binary blend rather than a solution.

Consequently o-15k does not qualify as a solvent. Neither of the two shorter solvents o-2k and o-4k, creates additional entanglements.

**table S-I: Specifications on starting materials.**

Full name	Abbreviation	$M_w^a$	$PDI^a$	$PDI^b$	$T_g^b$	Supplier
Poly(methyl methacrylate)-270k	PMMA-270k	270	1.09	1.09	141.8	PSS
Poly(methyl methacrylate)-86k	PMMA-86k	86	1.02	1.08	122.8	PSS
Oligo(methyl methacrylate)-15k	o-15k	15	-	1.85	98.6	Aldrich
Oligo(methyl methacrylate)-4k	o-4k	3.5	1.04	1.10	98.9	PSS
Oligo(methyl methacrylate)-2k	o-2k	2.1	1.10	1.22	72.5	PSS

<sup>a</sup> Values provided by supplier

<sup>b</sup> Values measured in-house

**table S-II: Specifications on prepared PMMA solutions obtained from SEC and DSC analysis.**

Sample name	Polymer	Solvent	$\phi$ [vol%]	$T_g$ [°C]
PMMA-270k/o-2k	PMMA-270k	o-2k	43 ( $\pm 1$ )	108.6
PMMA-270k/o-4k	PMMA-270k	o-4k	44 ( $\pm 1$ )	120.7
PMMA-270k/o-15k	PMMA-270k	o-15k	41 ( $\pm 1$ )	123.6
PMMA-86k/o-4k	PMMA-86k	o-4k	51 ( $\pm 1$ )	106.9

**table S-III: Horizontal shift factors ( $a_T$ ) used for creating master curves at  $T_{ref} = 150$  °C.**

Sample	$a_T$ (130 °C $\rightarrow T_{ref}$ )	$a_T$ (140 °C $\rightarrow T_{ref}$ )	$a_T$ (170 °C $\rightarrow T_{ref}$ )	$a_T$ (190 °C $\rightarrow T_{ref}$ )	$a_T$ (210 °C $\rightarrow T_{ref}$ )	$a_T$ (220 °C $\rightarrow T_{ref}$ )
PMMA-270k	-	-	0.0230	-	-	0.0000700
PMMA-270k/o-2k	19.9	-	0.0577	0.00767	-	-
PMMA-270k/o-4k	-	-	0.0718	0.00906	-	0.000586
PMMA-270k/o-15k	-	-	0.0706	0.00843	-	0.000557
PMMA-86k	-	10.8	0.0416	0.00345	-	-
PMMA-86k/o-4k	-	-	0.0668	0.00726	0.00119	-

table S-IV: Material properties of PMMA melts and solutions along with the reference PS melts [3,5] at 150 °C. Values are obtained from BSW fitting with  $n_e$  and  $n_g$  held constant at 0.7 and 0.23, respectively.

Sample	$G_N^0$ [kPa]	$\tau_m$ [s]	$\tau_c$ [s]	$n_e$ [-]	$n_g$ [-]	$\eta^0$ [MPa s]
PMMA-270k	408	229000	0.802	0.23	0.7	17500
PMMA-270k/o-2k	125	933	0.0397	0.23	0.7	21.9
PMMA-270k/o-4k	121	2610	0.235	0.23	0.7	59.3
PMMA-270k/o-15k	125	3230	0.748	0.23	0.7	76.3
PS-285k	248	117	0.00823	0.23	0.7	5.43
PMMA-86k	1070	537	0.147	0.23	0.7	109
PMMA-86k/o-4k	181	29.4	0.0917	0.23	0.7	1.07
PS-100k	283	2.47	0.00572	0.23	0.7	0.138

table S-V: Tube model parameters for PMMA melts and solutions along with the reference PS melts [3,5]. Values in bold font are obtained from fitting the BSW spectrum, non-bold font are values obtained using the LM-model.

Sample	$G_N^0$ [kPa]	$\tau_e$ [s]	Z	$N_e$	$N_s/N_e(1)$
PMMA-270k	<b>408</b>	<b>0.80</b>	<b>52</b>	<b>9</b>	-
	395	1.16	48	9	-
PMMA-270k/o-2k	<b>125</b>	<b>0.0397</b>	<b>25</b>	<b>18</b>	<b>0.40</b>
	130	0.0442	25	18	0.38
PMMA-270k/o-4k	<b>121</b>	<b>0.235</b>	<b>20</b>	<b>23</b>	<b>0.67</b>
	126	0.285	19	23	0.63
PMMA-270k/o-15k	<b>125</b>	<b>0.748</b>	<b>15</b>	<b>30</b>	<b>2.9</b>
	175	0.608	14	33	2.7
PS-285k	<b>248</b>	<b>0.00823</b>	<b>21</b>	<b>22</b>	-
	256	0.00981	21	23	-
PMMA-86k	<b>1070</b>	<b>0.147</b>	<b>14</b>	<b>10</b>	-
	1149	0.156	15	10	-
PMMA-86k/o-4k	<b>181</b>	<b>0.0917</b>	<b>7.0</b>	<b>20</b>	<b>0.59</b>
	200	0.0899	7.7	19	0.60
PS-100k	<b>283</b>	<b>0.00572</b>	<b>7.7</b>	<b>22</b>	-
	331	0.00457	8.5	20	-

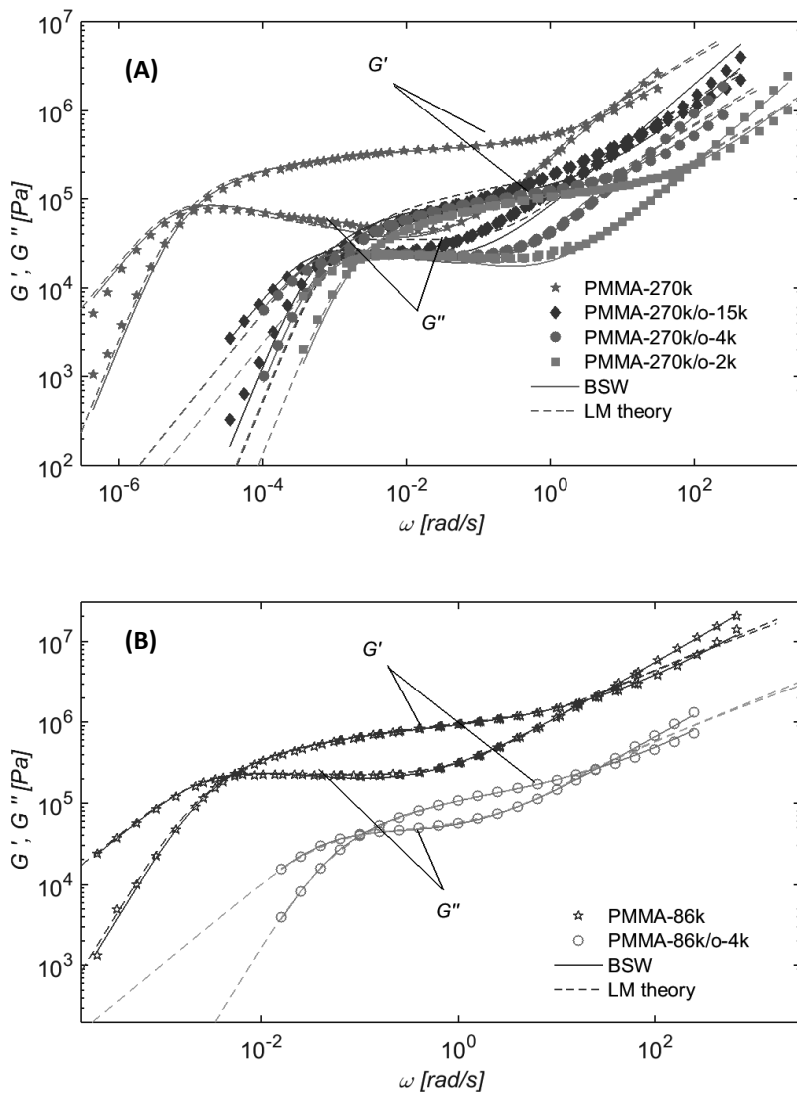
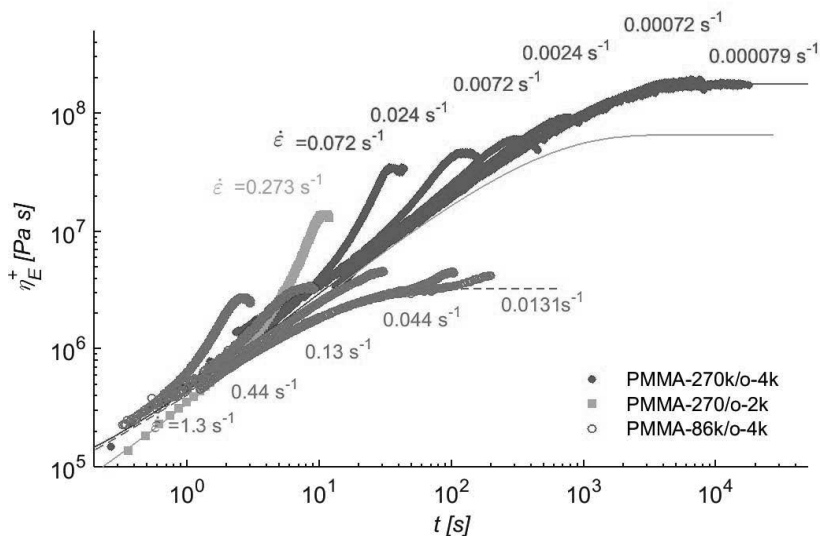


fig. S-1: Measured dynamic moduli  $G'/G''$  (open or closed symbols) at 150 °C along the BSW fitting (solid lines) and fit of LM-theory (dashed lines) of (A) undiluted PMMA-270k and solutions hereof, (B) undiluted PMMA-86k and solutions hereof.



**fig. S-2: Extensional stress growth coefficient at 150 °C for PMMA solutions containing o-4k and o-2k solvent. Solid and dashed lines indicate the linear prediction using the BSW-spectrum.**

## References in Supplemental Material

- [1] K. Mortensen, in *Advanced functional molecules and polymers. Vol. 2. processing and spectroscopy*, edited by H. S. Nelwa (Overseas Publishers Association, Amsterdam, 2001), pp. 223–269.
- [2] J. M. Román Marín, J. K. Huusom, N. J. Alvarez, Q. Huang, H. K. Rasmussen, A. Bach, A. L. Skov, and O. Hassager, *J. Nonnewton. Fluid Mech.* **194**, 14 (2013).
- [3] Q. Huang, O. Mednova, H. K. Rasmussen, N. J. Alvarez, A. L. Skov, and O. Hassager, *Macromolecules* **46**, 5026 (2013).
- [4] A. E. Likhtman and T. C. B. McLeish, *Macromolecules* **35**, 6332 (2002).
- [5] J. K. Nielsen, H. K. Rasmussen, O. Hassager, and G. H. McKinley, *J. Rheol.* **50**, 453 (2006).

APPENDIX B

# Supplemental material for: Chapter 3

---

Influence of extensional stress overshoot on crystallization of LDPE

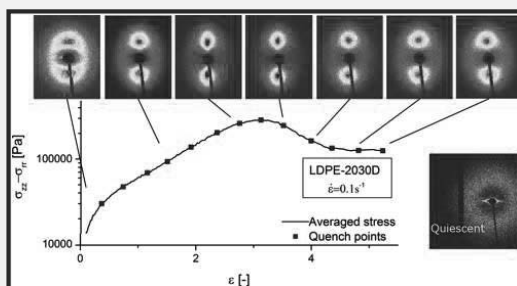
B.1 Article in its published format

## Influence of Extensional Stress Overshoot on Crystallization of LDPE

Sara Lindeblad Wingstrand,<sup>†</sup> Martin van Drongelen,<sup>†</sup> Kell Mortensen,<sup>‡</sup> Richard S. Graham,<sup>§</sup> Qian Huang,<sup>†</sup> and Ole Hassager<sup>\*,†</sup><sup>†</sup>Department of Chemical and Biochemical Engineering, Danish Polymer Center, Technical University of Denmark, DK-2800 Kgs. Lyngby, Denmark<sup>‡</sup>Niels Bohr Institute, X-ray and Neutron Science, University of Copenhagen, DK-2100 København Ø, Denmark<sup>§</sup>School of Mathematical Sciences, University of Nottingham, Nottingham NG7 2RD, U.K.

## Supporting Information

**ABSTRACT:** Low-density polyethylene (LDPE) shows a stress overshoot in start-up of strong uniaxial extensional flows of constant rate. It is believed that the overshoot is caused by a contraction of the polymer backbone due to alignment of the long chain branches—the consequence being that the molecular strain of the backbone does not increase monotonically with the global strain of the melt. In this study we investigate the semicrystalline morphology of LDPE quenched before, after, and at the overshoot. We do this by combining filament stretching rheometry with ex-situ X-ray scattering. It is found that the overshoot indeed is reflected in the orientation of the crystalline domains of the quenched filaments. In a broader perspective, we show that the final crystalline morphology is determined by the stress at quench—not the strain at quench. With these findings we confirm that the much debated overshoot has a physical origin. More importantly, we conclude that even for complex architectures like branched systems, the crystalline orientation is determined by the backbone stretch rather than the global stretch of the material.



The molecular architecture of polymers influences melt rheology, crystallization kinetics, and solid state mechanical properties.<sup>1–4</sup> A classical example is the effect of introducing long-chain branching in polyethylene yielding low-density polyethylene (LDPE) as opposed to the linear analogue of high density (HDPE).<sup>5</sup> In the case of melt rheology, introduction of branches results in longer relaxation times, often several orders of magnitude, depending on the degree of branching and length of the branches.<sup>6</sup> This, however, is not the only rheological consequence of introducing branches. For the past decade, it has been known that branched polymer melts in start-up of nonlinear uniaxial extension show a fundamentally different behavior from linear polymers in such flows.<sup>7</sup> Linear polymers deformed at a constant extension rate (Hencky strain rate  $\dot{\epsilon}$ ) initially show a gradual increase in stress. At higher strains ( $\epsilon$ ) the stress saturates and remains at a plateau called the steady state stress.<sup>8</sup> Branched polymers, on the other hand, exhibit a stress overshoot before reaching steady state.<sup>7</sup> The overshoot has been explained using the argument that branches enhance the friction between a single molecule and its surroundings, causing the backbone to be stretched further than its linear analogue would be. However, as the arms along with the rest of the molecule are aligned by the flow, the friction decreases and the backbone contracts to a less stretched configuration at which the steady state stress is reached.<sup>7,9</sup> This process is often referred to as branch point

withdrawal.<sup>10</sup> A sketch of LDPE's nonlinear extensional behavior along with the molecular interpretation is shown in Figure 1.

The extensional stress overshoot and the subsequent steady state have not been extensively studied. It was originally reported

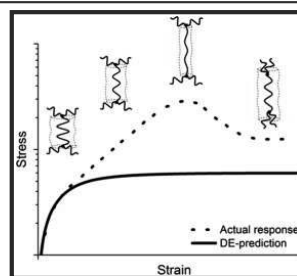


**Figure 1.** Sketch of the overshoot observed in nonlinear uniaxial extension of LDPE (---). The classical Doi and Edwards (DE) prediction is shown as a reference (—). The proposed transient molecular conformation (flow direction is vertical) is shown as well for selected points along the stress curve.

Received: November 28, 2016

Revised: January 4, 2017

by Rasmussen et al.<sup>7</sup> observing the overshoot in constant rate experiments using a filament stretch rheometer (FSR). The results gave rise to discussions on whether the overshoot was a material property or an experimental artifact.<sup>11–13</sup> In the wake of this debate followed a limited number of publications that further investigated the phenomenon. The experiments consisted of stress relaxation, creep, and cross-slot flow combined with birefringence. They all confirmed the existence of an overshoot.<sup>14–17</sup> To our knowledge no one has yet looked at the overshoot effect on the final crystalline morphology of LDPE. This, however, is a problem of interest as the crystal morphology of polyethylene (PE) is known to change depending on processing conditions.<sup>18</sup> Under quiescent conditions, the melt will form pointlike nuclei and crystallize into randomly oriented spherulites.<sup>19</sup> When crystallization occurs from a state at which the polymer chains are sufficiently aligned by the flow, threadlike precursors are likely to form resulting in shish-kebab structures.<sup>20,21</sup> This type of morphology consists of crystalline fibrils (shish) oriented along the flow direction with lamellae stacks growing perpendicular to the flow direction (kebabs). Depending on the extent of molecular deformation prior to crystallization, twisted or straight kebabs are obtained (Type I and Type II, respectively). Type I forms at milder conditions compared to Type II.

It is a long-standing tenet that polymer stretch is the key determining factor for flow-induced crystallization.<sup>22</sup> Indeed, this postulation is a key assumption of molecular models.<sup>23,24</sup> However, it has not been possible to directly verify this central idea from shear experiments. Because of vorticity, shear flow is not strong enough to make large extension of polymer chains compared to extensional flow. This is where the overshoot in extension becomes interesting for the crystallization properties. If the proposed molecular picture is correct and hence the backbone is stretched further at the stress maximum compared to the steady state stress, samples quenched and crystallized at the stress maximum (intermediate Hencky strains) would show a greater orientation compared to samples quenched at the steady state (high Hencky strains). This is somewhat counterintuitive as one would expect to find the most oriented structures at the highest strains—not at intermediate strains as proposed above.

In this work we use a commercial LDPE to investigate the influence of the stress overshoot in the melt state on the final morphology of the solid LDPE filaments. In order to do so, we study filaments stretched above the melting temperature at several constant deformation rates<sup>25</sup> and quenched before, during, and after the overshoot in nonlinear uniaxial extension. The nonisothermally crystallized filaments are characterized *ex-situ* using small-angle X-ray scattering (SAXS) and wide-angle X-ray diffraction (WAXD) to determine the morphology and the degree of orientation. Finally, we attempt to link the stress at quench to the final morphology by estimating the stretch of the backbone during extension.

## EXPERIMENTAL DETAILS

**Materials.** A commercial long-chain branched polyethylene “Lupolen 3020D” from BASF was used in this study. The sample has a weight-average molecular weight  $M_w$  of 300 000 g mol<sup>-1</sup>, a polydispersity index (PDI) of 8, and a melting point ( $T_m$ ) of 114 °C.<sup>14</sup> The rheology of the system is well-known and exhibits a clear overshoot in nonlinear extension.<sup>7,14,15</sup>

**Filament Stretching and Quenching.** Nonlinear extension of the LDPE was carried out using a filament stretch rheometer (VADER 1000 from Rheofilament, first generation). The device consists of a top and a bottom plate between which the sample is sandwiched, a laser

micrometer situated in the midplane of the sample, a load cell mounted on the bottom plate, and a convection oven. The advantage of this device is twofold. First of all, this device enables a viscous liquid to be extended uniaxially in a controlled manner via a feed back control loop enabling the performance of various types of experiments such as constant rate, creep, stress relaxation, etc.<sup>26,27</sup> Second, the oven can be removed manually within 1 s, enabling fast quenching of the filament to room temperature. Movement of the top plate is automatically disabled once the oven is opened to prevent further stretching of the crystallizing filament.

In this study the samples are stretched at a constant Hencky strain rate ( $\dot{\epsilon}$ ) according to the following:

$$\epsilon(t) = -2 \ln \left( \frac{D(t)}{D_0} \right) = \dot{\epsilon} t \quad (1)$$

Here  $\epsilon(t)$  is the Hencky strain while  $D_0$  and  $D(t)$  are the diameter at  $t = 0$  and diameter during a stretch experiment, respectively. The corresponding mean extensional stress difference in the midfilament plane ( $\sigma_{zz} - \sigma_{rr}$ ) is given by<sup>28</sup>

$$\langle \sigma_{zz} - \sigma_{rr} \rangle = \frac{F(t) - m_t g / 2}{\frac{\pi}{4} D(t)^2} \frac{1}{1 + \left( \frac{D(t)}{D_0} \right)^{10/3} \exp(-\Lambda_1^3) / (3\Lambda_1^2)} \quad (2)$$

Here  $F(t)$  is the force exerted by the fluid on the force cell,  $m_t$  is the mass of the sample,  $g$  is the gravitational acceleration, and  $\Lambda_1 = L_z/D_z$  is the initial aspect ratio of the sample with  $L_z$  and  $D_z$  being the initial length and diameter of the sample before prestretching. The last factor corrects for the shear contribution at low  $\epsilon(t)$ .

The experimental procedure was carried out as follows. LDPE discs of varying height (0.5–3 mm) and diameter (5.4–9 mm) were placed in the FSR, heated to 150 °C, prestretched to a desired  $D_0$ , and then left to relax for more than 15 min to erase any residual orientation left in the sample. The temperature was lowered to the experimental temperature, and uniaxial stretching was performed. The samples were quenched to room temperature at the desired Hencky strain  $\epsilon_q$  by opening the oven. (See the Supporting Information for sketch of the thermal protocol employed during filament stretch and quench.) A light flow of nitrogen gas (25 °C) was applied to accelerate the quenching. From numerical simulations the quench rate was estimated to 10 K s<sup>-1</sup>. Since the stress relaxation times have been estimated around 100 s, the quenching process is expected to be almost instantaneous in most situations.<sup>14</sup>

In order for all the samples to experience the same quench history, all experiments were designed in such a way that the diameter at the point of quenching ( $D_q$ ) was  $\sim 0.55$  mm. In order to achieve this for samples with different  $\epsilon_q$  all samples were prestretched accordingly using eq 1, with  $D(t) = D_q$  and  $D_0$  as the adjustable parameters.

**Ex-Situ X-ray Measurements.** WAXD and SAXS were performed on the quenched filaments utilizing a SAXSLAB instrument (Ganesha from SAXSLAB, Denmark) with a 300k Pilatus detector with pixel sizes 172 × 172  $\mu\text{m}$ . The filaments were mounted vertically such that the X-ray beam passed through the midplane of the filament where the deformation history is known. The X-ray wavelength was 1.54 Å for both WAXD and SAXS while the distance to the detector was  $\sim 118$  mm for the WAXD measurements and either  $\sim 1020$  or  $\sim 2240$  mm for the SAXS measurements. 2D intensity patterns of good resolution were obtained using an exposure time of 5 min.

The orientation of the crystalline domains was determined on the basis of the large scale structural characteristics from kebabs which is seen as the lobes in SAXS (see Figure 3).<sup>29</sup> Herman's orientation factor  $F_H$  is calculated from eqs 3 and 4, assuming axial symmetry along the stretch direction:<sup>30</sup>

$$F_H = \frac{3 \langle \cos^2 \phi \rangle - 1}{2} \quad (3)$$

Here  $\langle \cos^2 \phi \rangle$  is the average cosine squared of the angle between the normal of the lamellae kebab stacks and the flow direction, estimated

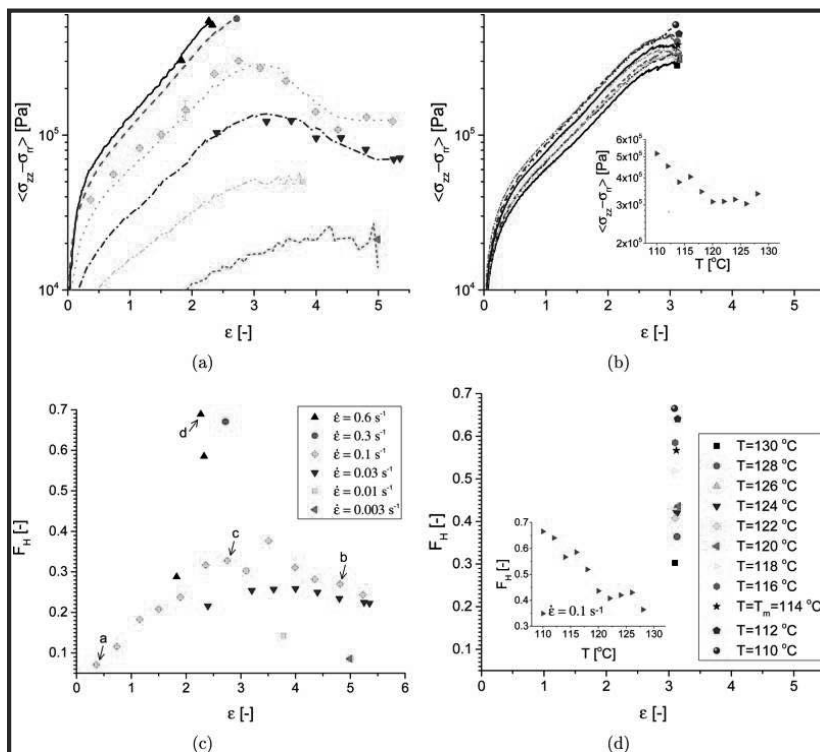


**Figure 2.** Top row: nonlinear response of Lupolen 3020D in extension expressed in terms of stress versus Hencky strain for samples stretched at (a) 130 °C for varying  $\dot{\epsilon}$  (b) varying stretch temperatures but constant  $\dot{\epsilon} = 0.1$  s<sup>-1</sup> quenched at  $\epsilon = 3.1$ . (Lines indicate the averaged stress curves of stretch experiments performed at a given  $\dot{\epsilon}$  and  $T$ ; symbols indicate points at which filaments were quenched.). Bottom row: orientation of crystalline domains in the quenched filaments expressed in terms of Herman's orientation factor versus Hencky strain at quench for (c) the samples whose nonlinear response is given in (a) and (d) for samples whose nonlinear response is given in (b). X-ray patterns for data points marked a, b, c, and d in (c) are shown in Figure 3. Legends in (c) and (d) also apply to (a) and (b), respectively. The insets in (b) and (d) show the same stress and orientation data as the big plot, but as a function of temperature instead of strain.

from integrals of the azimuthal SAXS intensity profiles (see Supporting Information for an example of an azimuthal intensity profile):

$$\langle \cos^2 \phi \rangle = \frac{\int_0^{\pi/2} I(\beta) \cos^2 \beta \sin \beta \, d\beta}{\int_0^{\pi/2} I(\beta) \sin \beta \, d\beta} \quad (4)$$

Here  $I$  the scattering intensity and  $\beta$  is the azimuthal angle.

## RESULTS AND DISCUSSION

The nonlinear rheological response of the Lupolen 3020D in uniaxial extension is shown in Figure 2a,b. Symbols along the stress curve indicate points at which samples were quenched and nonisothermally crystallized. In Figure 2a it is seen that filaments were quenched at Hencky strains before the overshoot, at the overshoot, after the overshoot, and well into the steady state. At the highest strain rates  $\dot{\epsilon} = 0.3$  and  $0.6$  s<sup>-1</sup> it was not possible to obtain points past the overshoot due to fracture of the filament.<sup>31</sup> In Figure 2b, samples stretched at  $\dot{\epsilon} = 0.1$  s<sup>-1</sup> and varying temperatures are seen. No significant change in the stress response for LDPE above  $T_m$  is observed—only an expected small, vertical shift which is explained by the time–temperature superposition principle.<sup>32</sup> Below  $T_m$  there seems to be a small indication of crystallization taking place toward the very end of

the experiments. This effect is best seen for the stretch performed at  $T = 110$  °C where a small upturn appears around a Hencky strain  $\epsilon = 3$ . An experiment performed at an even lower temperature  $T = 108$  °C was also conducted. Here the rate of crystallization was so severe that the stress response diverged completely and fracture occurred before the end of the experiment, disqualifying the sample for further testing.

Figures 2c and 2d show orientation of the crystalline domains for the quenched samples, whose nonlinear response is shown in Figures 2a and 2b, respectively. The orientation is expressed in terms of Herman's orientation factor ( $F_H$ ) extracted from SAXS images<sup>30</sup> (e.g., top row of Figure 3).  $F_H$  gives an overall indication of the crystalline orientation based on scattering from kebabs in the crystalline domains. From the definition in eqs 3 and 4, isotropic orientation of crystallites gives  $F_H = 0$ . Complete orientation with respect to the flow direction, i.e., shish oriented 100% along the flow direction and kebabs only growing perpendicular to it, gives  $F_H = 1$ . The opposite scenario where shish grows perpendicular to the flow would yield  $F_H = -1/2$ .

Overall, the orientation in Figures 2c and 2d mirrors the stress response in melt state Figures 2a and 2b, respectively. For the samples stretched at  $\dot{\epsilon} = 0.03$  and  $0.1$  s<sup>-1</sup> in Figure 2c where a number of samples have been quenched at different strain values,

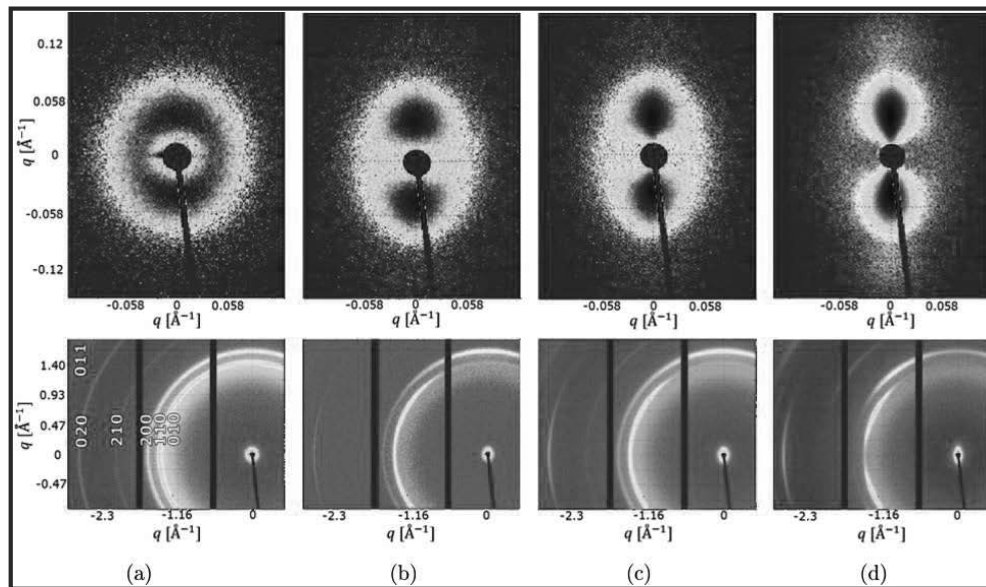


**Figure 3.** SAXS (top) and WAXD (bottom) patterns of LDPE filaments quenched at various stress (a) 30, (b) 126, (c) 262, and (d) 518 kPa. All filaments have been elongated at  $T = 130$  °C, and flow direction is vertical.

an overshoot in the orientation at intermediate strains is observed; i.e., the overshoot in the melt state is reflected in the final orientation of the filaments which further proves that the overshoot is real. We note that one data point at  $(\epsilon, \dot{\epsilon}) = (3.1, 0.1 \text{ s}^{-1})$  seems lower than expected, although the measurement has been repeated several times (error bars are less than the size of the symbol). This is the point at which the arms, according to theory, should collapse, leaving the backbone to retract. Stress relaxation data obtained by Huang et al.<sup>14</sup> show that the rate of relaxation increases at this point, and this was further justified from simulations performed by Hawke et al.<sup>9</sup> The consequence of an increased rate of relaxation is that the rate of quenching has to be faster in order for the backbone not to contract before crystallization takes place. With that in mind, it is very likely that the point would lie higher if the rate of quenching had been faster. This is further supported by the fact that reducing the difference between the experimental temperature and  $T_m$  (i.e., increasing the rate of quench) by just a few degrees produce a significantly higher orientation despite the fact the stress at quench is very similar (see Figure 2d).

Figure 3 shows a representative range of SAXS patterns (top row) and WAXD patterns (bottom row) from samples in Figure 2. The patterns from left to right have been quenched at increasing stresses which seems to correlate with the anisotropy of the patterns.

The SAXS patterns are characterized by a two-point pattern with intensity peaks along the meridian. This indicates the presence of aligned lamellae planes perpendicular to the flow direction (kebabs).<sup>33</sup> The “tear drop” shape of the two last samples (c) and (d) indicates a mixed spacing between lamellae planes which is a known result of interlocking of the side branches.<sup>34</sup> The long spacing is more constant for the two first samples (a) and (b) as the stress at quench is lower, and hence less interlocking occurs.

The WAXD patterns in Figure 3 show a gradual change in orientation of crystal planes from almost isotropic to highly unidirectional. For sample (a) the random orientation suggests a morphology dominated by spherulites. The WAXD patterns of samples (b) and (c) are rather similar, with intensity peaks along the meridian, off-axis, and equatorial for crystal planes (110), (200), and (020), respectively. This is a clear indication of shish-kebab structures with twisted lamellae.<sup>29</sup> The only difference between samples (b) and (c) is that the intensity peaks of (c) are narrower, indicating a greater alignment of domain structures relative to (b). That is despite the fact that (b) has been quenched at higher  $\epsilon$  (quench at steady state for  $\dot{\epsilon} = 0.1 \text{ s}^{-1}$ ) than (c) (quench at stress max for  $\dot{\epsilon} = 0.1 \text{ s}^{-1}$ ). The last sample (d) quenched at a very high stress shows an interesting feature. The intensity peak of the (200) plane has shifted to the off axis. This indicates a kebab structure of mixed twisted and straight lamellae.<sup>35</sup> This type of morphology is rare for LDPE, and to our knowledge it has never been reported. However, it has been observed for HDPE.<sup>35</sup>

Both the raw SAXS and WAXD patterns (Figure 3) and the similarity in the stress in melt state and orientation in solid state (Figure 2) suggest that stress at quench and final morphology of the solid samples are closely related. This is confirmed in Figure 4 where Herman’s orientation factor for all samples in this study is plotted against the stress at quench.

Regardless of  $\dot{\epsilon}$ ,  $\epsilon$ , and  $T$ , all samples seem to fall onto the same master curve, however, with some scattering. It seems that stress at quench is the governing parameter for the final morphology which is in line with ideas formulated in 1994 by Tas.<sup>36</sup> It is also in agreement with very recent nonequilibrium in-situ crystallization data on linear and cross-linked polyethylenes.<sup>37</sup> One reason behind this collapse of data onto one master curve can be found by looking at nonlinear constitutive models for polymeric liquids.

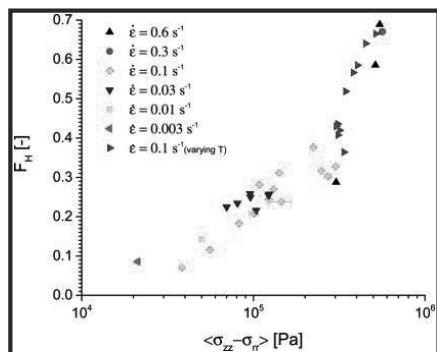


**Figure 4.** Herman's orientation factor vs stress at quench. All samples have been stretched at  $T = 130$  °C except (green ►) which have been stretched at varying  $T$  from 110 to 130 °C.

The stress during deformation reflects the molecular configuration. More specifically, the deviation from linear behavior in the response of a polymeric liquid in flow is a result of the polymer being deformed significantly beyond its equilibrium configuration (random coil).<sup>38</sup> Generally there are two types of chain deformation in entangled polymer systems: the mildly deformed state (oriented) and the highly deformed state (stretched).<sup>39</sup> In the oriented deformation state the polymer chain is aligned by the flow but only as far as the chain configuration between two entanglements remains Gaussian. In the stretched deformation state the conformation of the chain may be classified as either moderately stretched (Gaussian) or highly stretched (non-Gaussian).

The oriented state is successfully modeled using the classical Doi and Edwards (DE) model.<sup>40</sup> Unfortunately, this model is incapable of capturing many of the nonlinear phenomena seen in extension, e.g., strain hardening and stress overshoot. The DE model has served as a basis upon which a number of more complex models have been built in order to capture the nonlinear phenomena mentioned above. A common feature of these models is that they ascribe deviation from the DE model to some form of backbone stretch  $\lambda$ .<sup>39</sup> The difference between the models lies in the physics included in order to predict the evolution of the backbone stretch. A wide range of phenomena can be included depending on the composition of the fluid and the architecture of the molecules, e.g., interchain tube pressure,<sup>41</sup> finite extensibility,<sup>42</sup> friction reduction,<sup>43</sup> and branch point withdrawal.<sup>10</sup>

One model, the pom-pom model, originally introduced by Mcleish and Larson in 1998, has proven quite effective in capturing the nonlinear behavior of LDPE.<sup>10</sup> In particular, Huang et al. showed that the multimode version<sup>44,45</sup> captures the transient nonlinear response of LDPE up until the stress maximum. Hawke et al. extended the model by incorporating entanglement loss and obtained a model that can predict nonlinear behavior of LDPE including stress overshoot, steady state, and the increased relaxation rate at the overshoot.

In this work we focus on the chain stretch and its relation to the final morphology. We use a simplified version of the multimode pom-pom to extract a chain stretch ( $\lambda$ ) from experimental data (eqs 5 and 6).  $\tau_{b,i}$  are time constants and  $g_i$  are corresponding moduli obtained by fitting a multimode Maxwell model to the linear data (see Supporting Information for values of the constants and the linear data). At the conditions employed in this study, it is primarily the two longest modes that stretch during

deformation.<sup>14</sup> As  $g_1 \ll g_2$ , the contribution of the longest mode (mode 1) to the stress and, probably, to the crystallization is small compared to mode 2. We thus define  $\lambda$  as the average stretch of the two longest modes and express the stress  $\sigma$  as follows:

$$\sigma = 3(\lambda^2(t) \sum_{i=1}^2 g_i S_i(t) + \sum_{i=3}^p g_i S_i(t)) \quad (5)$$

$S_i = A_i / \text{Tr } A_i$  is the normalized orientation tensor expressed by the conformation tensor ( $A_i$ ) whose evolution is given by

$$\frac{D}{Dt} A_i = \kappa \cdot A_i + A_i \cdot \kappa^T - \frac{1}{\tau_{b,i}} (A_i - I) \quad (6)$$

with initial condition  $A_i = I$  where  $I$  is the unit tensor.  $\kappa$  is the transpose of the velocity gradient tensor. As seen, the only free parameter in this model is the average chain stretch  $\lambda$  which is obtained by fitting the model to the experimental data. In so doing, an estimate of the chain stretch at quench for each of the samples was obtained.

Figure 5 shows the Herman's orientation factor,  $F_H$ , as a function of the extracted chain stretch  $\lambda$ . It is seen that there is a

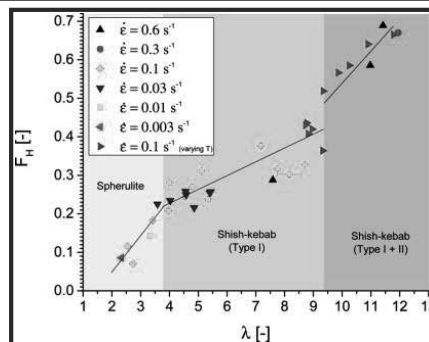


**Figure 5.** Herman's orientation factor vs average stretch of the backbone for the two highest Maxwell models. Vertical lines indicate regions of different morphologies.

good correlation between the chain stretch in the melt state and the final crystalline orientation. Furthermore, it is seen that the slope changes going from a spherulitic morphology to an oriented morphology and again going from shish kebabs of Type I to the intermediate morphology of mixed Type I and II shish kebabs.

We note that the peak values of  $\lambda$  in Figure 5 are much in excess of the maximum value computed from the number of Kuhn steps between entanglements, which gives this maximum as less than 3 for PE.<sup>46</sup> This could indicate that entanglements have been lost in the stretching process or it may be an artifact of the simplified pom-pom analysis. Regardless, we believe that the segments have been stretched close to their maximum length (outside the Gaussian regime) since some polymer filaments fractured.

## CONCLUSION

In summary, we have shown that the stress overshoot observed in uniaxial extension of LDPE is reflected in the final morphology of the quenched samples. To our knowledge, this is the first time that a decrease in degree of crystalline orientation with increasing

strain has been reported. This, first of all, confirms that the stress overshoot has real physical origin. It also confirms that the stretch of the backbone does govern the final morphology of the crystallized sample even for a complex architecture like long-chain branched PE. Finally, we conclude that the backbone stretch is reflected in the extensional stress which is directly measurable. Hence, stress in the melt state is the key parameter needed in order to connect chain extension and crystal morphology.

## ■ ASSOCIATED CONTENT

### Supporting Information

The Supporting Information is available free of charge on the ACS Publications website at DOI: 10.1021/acs.macromol.6b02543.

Figures S1–S5, Tables S1 and S2, and supplemental text (PDF)

## ■ AUTHOR INFORMATION

### Corresponding Author

\*E-mail: oh@kt.dtu.dk (O.H.).

### ORCID

Sara Lindeblad Wingstrand: 0000-0002-4555-4571

Kell Mortensen: 0000-0002-8998-9390

Qian Huang: 0000-0001-8777-4241

Ole Hassager: 0000-0003-2695-6791

### Notes

The authors declare no competing financial interest.

## ■ ACKNOWLEDGMENTS

The authors thank Aage og Johanne Louis-Hansen fonden for financial support. We also thank Professor Julie A. Kornfield and Professor Gerrit Peters for fruitful discussions on the work.

## ■ REFERENCES

- (1) Costeux, S.; Wood-Adams, P.; Beigzadeh, D. Molecular Structure of Metallocene-Catalyzed Polyethylene: Rheologically Relevant Representation of Branching Architecture in Single Catalyst and Blended Systems. *Macromolecules* **2002**, *35*, 2514–2528.
- (2) An, Y.; Holt, J. J.; Mitchell, G. R.; Vaughan, A. S. Influence of molecular composition on the development of microstructure from sheared polyethylene melts: Molecular and lamellar templating. *Polymer* **2006**, *47*, 5643–5656.
- (3) Bustos, F.; Cassagnau, P.; Fulchiron, R. Effect of molecular architecture on quiescent and shear-induced crystallization of polyethylene. *J. Polym. Sci., Part B: Polym. Phys.* **2006**, *44*, 1597–1607.
- (4) Kornfield, J. Interplay of Macromolecular Architecture and Flow in Polymer Crystallization, American Chemical Society National Meeting & Exposition, San Diego, 2016.
- (5) Sperati, C. A.; Franta, W. A.; Starkweather, H. W. The Molecular Structure of Polyethylene. V. The Effect of Chain Branching and Molecular Weight on Physical Properties. *J. Am. Chem. Soc.* **1953**, *75*, 6127–6133.
- (6) Das, C.; Inkson, N. J.; Read, D. J.; Kelmanson, M. A.; McLeish, T. C. B. Computational linear rheology of general branch-on-branch polymers. *J. Rheol.* **2006**, *50*, 207.
- (7) Rasmussen, H. K.; Nielsen, J. K.; Bach, A.; Hassager, O. Viscosity overshoot in the start-up of uniaxial elongation of low density polyethylene melts. *J. Rheol.* **2005**, *49*, 369.
- (8) Huang, Q.; Hengeller, L.; Alvarez, N. J.; Hassager, O. Bridging the Gap between Polymer Melts and Solutions in Extensional Rheology. *Macromolecules* **2015**, *48*, 4158–4163.
- (9) Hawke, L. G. D.; Huang, Q.; Hassager, O.; Read, D. J. Modifying the pom-pom model for extensional viscosity overshoots. *J. Rheol.* **2015**, *59*, 995–1017.
- (10) McLeish, T. C. B.; Larson, R. G. Molecular constitutive equations for a class of branched polymers: The pom-pom polymer. *J. Rheol.* **1998**, *42*, 81.
- (11) Burghellea, T. I.; Starý, Z.; Münstedt, H. On the “viscosity overshoot” during the uniaxial extension of a low density polyethylene. *J. Non-Newtonian Fluid Mech.* **2011**, *166*, 1198–1209.
- (12) Rasmussen, H. K.; Hassager, O. Reply to: “On the “viscosity overshoot” during the uniaxial extension of a low density polyethylene”. *J. Non-Newtonian Fluid Mech.* **2012**, *171*–172, 106.
- (13) Burghellea, T. I.; Starý, Z.; Munstedt, H. Response to the “Reply to: “On the “viscosity overshoot” during the uniaxial extension of a low density polyethylene” by Rasmussen et al. *J. Non-Newtonian Fluid Mech.* **2012**, *171*–172, 107–108.
- (14) Huang, Q.; Rasmussen, H. K.; Skov, A. L.; Hassager, O. Stress relaxation and reversed flow of low-density polyethylene melts following uniaxial extension. *J. Rheol.* **2012**, *56*, 1535.
- (15) Alvarez, N. J.; Marin, J. M. R.; Huang, Q.; Michelsen, M. L.; Hassager, O. Creep Measurements Confirm Steady Flow after Stress Maximum in Extension of Branched Polymer Melts. *Phys. Rev. Lett.* **2013**, *110*, 168301.
- (16) Hassell, D. G.; Hoyle, D.; Auhl, D.; Harlen, O.; Mackley, M. R.; McLeish, T. C. B. Effect of branching in cross-slot flow: The formation of “W cusps”. *Rheol. Acta* **2009**, *48*, 551–561.
- (17) Hoyle, D. M.; Huang, Q.; Auhl, D.; Hassell, D.; Rasmussen, H. K.; Skov, A. L.; Harlen, O. G.; Hassager, O.; McLeish, T. C. B. Transient overshoot extensional rheology of long-chain branched polyethylenes: Experimental and numerical comparisons between filament stretching and cross-slot flow. *J. Rheol.* **2013**, *57*, 293.
- (18) Schrauwen, B. A. G.; Breemen, L. C. A. V.; Spoelstra, A. B.; Govaert, L. E.; Peters, G. W. M.; Meijer, H. E. H. Structure, deformation, and failure of flow-oriented semicrystalline polymers. *Macromolecules* **2004**, *37*, 8618–8633.
- (19) Keith, H. D.; Padden, J. F. Spherulite crystallization in polypropylene. *J. Appl. Phys.* **1959**, *30*, 1479.
- (20) Hsiao, B. S.; Yang, L.; Somani, R. H.; Avila-Orta, C. A.; Zhu, L. Unexpected Shish-Kebab Structure in a Sheared Polyethylene Melt. *Phys. Rev. Lett.* **2005**, *94*, 117802.
- (21) Seki, M.; Thurman, D. W.; Oberhauser, J. P.; Kornfield, J. A. Shear-Mediated Crystallization of Isotactic Polypropylene: The Role of Long Chain-Long Chain Overlap. *Macromolecules* **2002**, *35*, 2583–2594.
- (22) Meijer, H. E. H. *Materials Science and Technology, Processing of Polymers*, 11th ed.; Materials Science and Technology; Wiley: 1997; p 787.
- (23) Graham, R. S.; Olmsted, P. D. Coarse-Grained Simulations of Flow-Induced Nucleation in Semicrystalline Polymers. *Phys. Rev. Lett.* **2009**, *103*, 1–4.
- (24) Steenbakkens, R. J. A.; Peters, G. W. M.; Meijer, H. E. H. Rheological Modeling of Flow Induced Crystallization in Polymer Melts and Limitations on Classification of Experiments. *AIP Conf. Proc.* **2008**, *1027*, 493–495.
- (25) Two samples are stretched below  $T_m$ .
- (26) Bach, A.; Almdal, K.; Rasmussen, H. K.; Hassager, O. Elongational Viscosity of Narrow Molar Mass Distribution Polystyrene. *Macromolecules* **2003**, *36*, 5174.
- (27) Román Marin, J. M.; Huusom, J. K.; Alvarez, N. J.; Huang, Q.; Rasmussen, H. K.; Bach, A.; Skov, A. L.; Hassager, O. A control scheme for filament stretching rheometers with application to polymer melts. *J. Non-Newtonian Fluid Mech.* **2013**, *194*, 14.
- (28) Rasmussen, H. K.; Bejenariu, A. G.; Hassager, O.; Auhl, D. Experimental evaluation of the pure configurational stress assumption in the flow dynamics of entangled polymer melts. *J. Rheol.* **2010**, *54*, 1325.
- (29) van Drongelen, M.; Cavallo, D.; Balzano, L.; Portale, G.; Vittorias, I.; Bras, W.; Alfonso, G. C.; Peters, G. W. M. Structure Development of Low-Density Polyethylenes During Film Blowing: A Real-Time Wide-

Angle X-ray Diffraction Study. *Macromol. Mater. Eng.* **2014**, *299*, 1494–1512.

(30) van Erp, T. B.; Balzano, L.; Spoelstra, A. B.; Govaert, L. E.; Peters, G. W. M. Quantification of non-isothermal, multi-phase crystallization of isotactic polypropylene: The influence of shear and pressure. *Polymer* **2012**, *53*, 5896–5908.

(31) Huang, Q.; Alvarez, N. J.; Shabbir, A.; Hassager, O. Multiple Cracks Propagate Simultaneously in Polymer Liquids in Tension. *Phys. Rev. Lett.* **2016**, *117*, 087801.

(32) Dealy, J.; Plazek, D. Time-temperature superposition - a users guide. *Rheol. Bull.* **2009**, *78*, 16–21.

(33) Toki, S.; Sics, I.; Burger, C.; Fang, D.; Liu, L.; Hsiao, B. S.; Datta, S.; Tsou, A. H. Structure Evolution during Cyclic Deformation of an Elastic Propylene-Based Ethylene-Propylene Copolymer. *Macromolecules* **2006**, *39*, 3588–3597.

(34) Zhang, X.; Elkoun, S.; Aiji, A.; Huneault, M. Oriented structure and anisotropy properties of polymer blown films: HDPE, LLDPE and LDPE. *Polymer* **2004**, *45*, 217–229.

(35) Keum, J. K.; Burger, C.; Zuo, F.; Hsiao, B. S. Probing nucleation and growth behavior of twisted kebabs from shish scaffold in sheared polyethylene melts by in situ X-ray studies. *Polymer* **2007**, *48*, 4511–4519.

(36) Tas, P. P. Film blowing - from polymer to product. PhD Thesis, Technische Universiteit Eindhoven, 1994.

(37) Wang, Z.; Ju, J.; Yang, J.; Ma, Z.; Liu, D.; Cui, K.; Yang, H.; Chang, J.; Huang, N.; Li, L. The non-equilibrium phase diagrams of flow-induced crystallization and melting of polyethylene. *Sci. Rep.* **2016**, *6*, 32968.

(38) Bird, R. B. R. B.; Armstrong, R. C.; Hassanger, O. *Dynamics of Polymeric Liquids*; Wiley: 1987; Vol. 1.

(39) Marrucci, G. Fast flows of concentrated polymers - predictions of the tube model on chain stretching. *Gazz. Chim. Ital.* **1988**, *118*.

(40) Doi, M.; Edwards, S. *The Theory of Polymer Dynamics*; Clarendon: 1986; p 391.

(41) Marrucci, G.; Ianniruberto, G. Interchain Pressure Effect in Extensional Flows of Entangled Polymer Melts. *Macromolecules* **2004**, *37*, 3934–3942.

(42) van Ruymbeke, E.; Nielsen, J.; Hassager, O. Linear and nonlinear viscoelastic properties of bidisperse linear polymers: Mixing law and tube pressure effect. *J. Rheol.* **2010**, *54*, 1155.

(43) Ianniruberto, G.; Brasiello, A.; Marrucci, G. Simulations of fast shear flows of PS oligomers confirm monomeric friction reduction in fast elongational flows of monodisperse PS melts as indicated by rheo-optical data. *Macromolecules* **2012**, *45*, 8058.

(44) Inkson, N. J.; McLeish, T. C. B.; Harlen, O. G.; Groves, D. J. Predicting low density polyethylene melt rheology in elongational and shear flows with "pom-pom" constitutive equations. *J. Rheol.* **1999**, *43*, 873.

(45) Blackwell, R. J.; Harlen, O. G.; McLeish, T. C. B. Theoretical Linear and Nonlinear Rheology of Symmetric Treelike Polymer Melts. *Macromolecules* **2001**, *34*, 2579–2596.

(46) Fetters, L. J.; Lohse, D. J.; Colby, R. H. *Physical Properties of Polymers*, 2nd ed.; Springer: New York, 2007; Chapter 25, p 1073.

## B.2 Supplemental Material

Supplemental material contains following:

- Figures S1 - S5
- Tables S1 and S2
- Supplemental text

## Supplemental figures

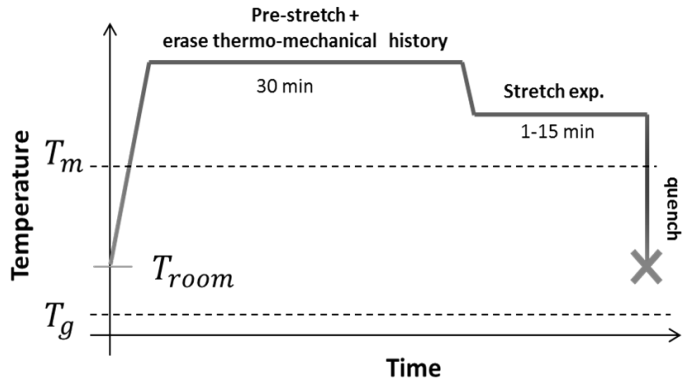


Figure S1: Sketch of the thermal protocol employed in the filament stretch and quenching.

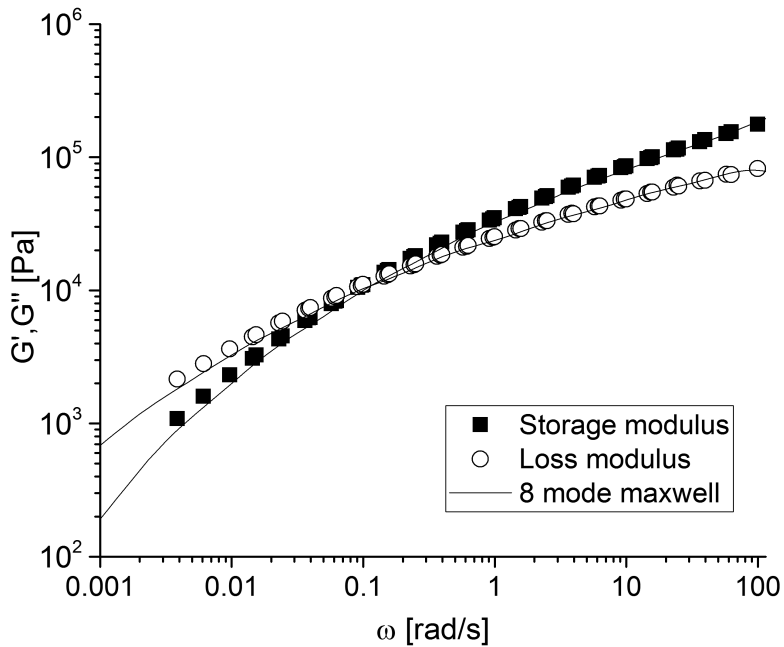


Figure S2: Linear behavior of Lupolen 3020D (symbols) at  $T = 130^\circ\text{C}$  obtained from small amplitude oscillatory shear along with the eight mode maxwell fit (lines) (see Huang et al.<sup>1</sup> for further explanation of the multimode maxwell fit)

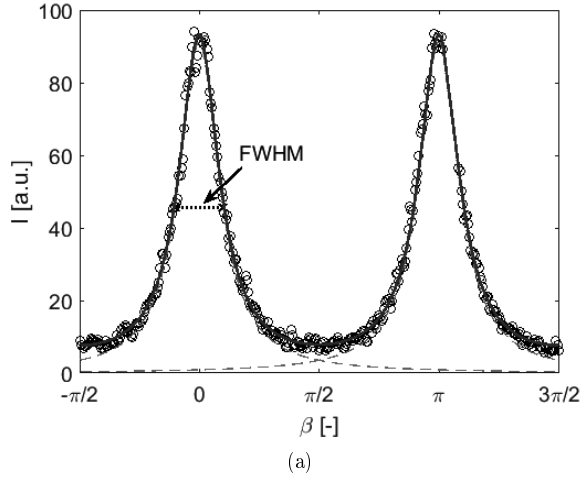


Figure S3: Azimuthal intensity profile (o) obtained from SAXS images along with the sum of the fitted Lorentzian peaks (—) and the individual peaks (---). The full width at half maximum (···) is indicated as well.

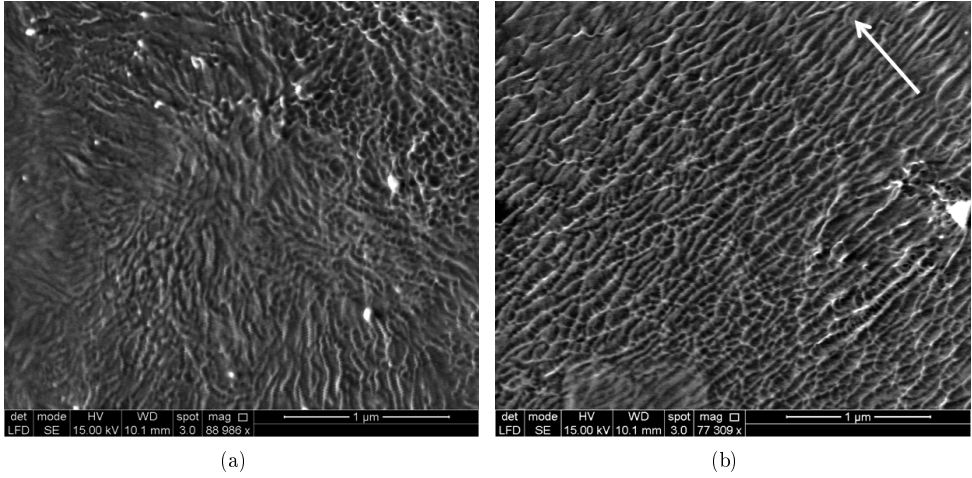


Figure S4: SEM images of LDPE crystallized under a) quiescent conditions (b) just before the stress maximum  $\varepsilon = 2.75$  for  $\dot{\varepsilon} = 0.1\text{s}^{-1}$ . Stretching temperature is  $T = 130^\circ\text{C}$ .

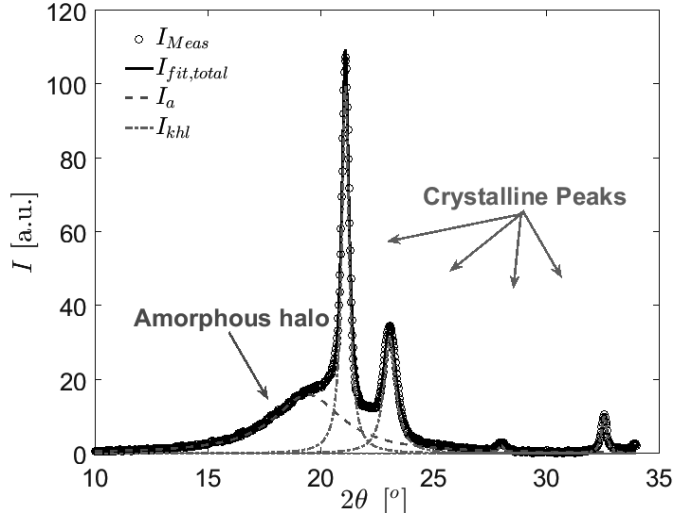


Figure S5: Radially integrated intensity profile obtained from WAXD ( $\circ$ ) resolved in amorphous halo ( $- -$ ) and diffraction peaks ( $- \cdot -$ ) for the determination of crystallinity. The total fit is given as ( $-$ )

## Supplemental data

Table S1: Pom-Pom parameters for Lupolen 3020D at  $T = 130^\circ\text{C}$  obtained by fitting a multimode Maxwell model to the linear data given in Figure S2 originally published by Huang et al.<sup>1</sup>

mode, $i$	$\tau_{b,i}$ [s]	$g_i$ [Pa]
1	$2.098 \times 10^3$	$1.02 \times 10^2$
2	$3.290 \times 10^2$	$9.83 \times 10^2$
3	$5.793 \times 10^1$	$3.55 \times 10^3$
4	$1.041 \times 10^1$	$9.17 \times 10^3$
5	$1.827 \times 10^0$	$2.02 \times 10^4$
6	$3.198 \times 10^{-1}$	$3.35 \times 10^4$
7	$6.131 \times 10^{-2}$	$5.35 \times 10^4$
8	$9.421 \times 10^{-3}$	$1.40 \times 10^5$

Table S2: Horizontal and vertical shift factors for Lupolen 3020D to the reference temperature  $T = 130^\circ\text{C}$ . Horizontal shift factors were used for the determination of the activation energy in the Arrhenius equation for samples stretched at temperatures different from  $T = 130^\circ\text{C}$ . Data originally published by Huang et al.<sup>1</sup>

$T^\circ\text{C}$	$\mathbf{a}_T[-]$	$\mathbf{b}_T[-]$
130	1	1
150	0.364	0.953
170	0.154	0.910

## Supplemental Text

### Electron microscopy

Scanning electron microscopy (SEM) was performed on two samples using a FEG-SEM (FEI Quanta 200 ESEM FEG) at low vacuum and low voltage of 15 kV. The SEM was performed on the surface of the filaments mounted on carbon tape and scanning was performed around the mid-filament plane. No pre-treatment of the samples was performed.

### Crystallinity from WAXD

The degree of crystallinity is determined from the average radial intensity profiles of WAXD patterns.<sup>2</sup> The spectrum is resolved into an amorphous halo and crystalline peaks (Figure S5) using the Lorentzian distribution:

$$I_L(\beta) = \frac{I_{max}}{1 + \left(\frac{\beta - \beta_0}{\gamma}\right)^2} \quad (1)$$

Here  $\beta$  is the azimuthal angle,  $I_{max}$ ,  $\beta_0$  and  $\gamma$  are fitting parameters signifying, the maximum intensity, horizontal shift, and half width at half maximum of the peak, respectively. According to Hermans-Weidinger's definition, the degree of crystallinity  $X_c$  is then found as:<sup>3</sup>

$$X_c = \frac{\sum_{hkl} I_{hkl}}{\sum_{hkl} I_{hkl} + I_a} \quad (2)$$

Where  $I_{hkl}$  and  $I_a$  are the integrated diffraction peaks of the crystalline peaks and the integrated amorphous halo respectively. Good fits were always obtained as can be seen in Figure S5.

The degree of crystallinity for all samples stretched at 130 °C was between 53% and 56% and did not seem to vary systematically. Hence the cooling rate can be considered comparable for these samples. The samples stretched at varying temperatures showed a slight increase in crystallinity 51% to 57% going from  $T = 110^\circ\text{C}$  to  $130^\circ\text{C}$ . A larger difference was expected as the quench history differed for these samples. WAXD was measured twice for some samples with one month interval. The crystallinity was found to be constant over this period of time and hence we consider all samples to be stable within the time frame of the study.

## References

- (1) Huang, Q.; Rasmussen, H. K.; Skov, A. L.; Hassager, O. *Journal of Rheology* **2012**, *56*, 1535.
- (2) Rabiej, S.; Wlochowicz, A. *Die Angewandte Makromolekulare Chemie* **1990**, *175*, 81–97.
- (3) Hsiao, B. S.; Zuo, F.; Mao, Y.; Schick, C. *Handbook of Polymer Crystallization*; John Wiley & Sons, Inc., 2013; pp 1–30.

## APPENDIX C

# Supplemental material for: Chapter 4

---

**Rheological link between polymer melts with a high molecular weight tail and enhanced formation of shish-kebabs**

Supplemental material contains following:

- Supplemental text
- Tables S1
- Figures 1S-5S

## Supplemental Text

### Details on Rheological measurements

**Creep** The samples were shaped into discotic specimens at 150C using a home-made vacuum press mold for twenty minutes and then loaded on the rheometer at the same temperature. We used a stress-controlled rheometer MCR702 (Anton Paar, Austria). The specimen was placed between two stainless steel parallel plates of 8 mm diameter and gap about 0.7 mm, calibrated for thermal expansion. Temperature control was achieved by means of a hybrid temperature control system CTD180 which has intermediate characteristics between a Peltier cell and a convection oven. All tests were performed in nitrogen atmosphere in order to reduce the risk of sample degradation. The measurement protocol consisted of three steps: (i) equilibration and stability of the samples was monitored by running dynamic frequency sweep tests (SAOS) in strain-controlled mode at the same conditions and different times (starting from 20 min after loading, up to 1 hour), checking for the overlap of the dynamic moduli ; (ii) dynamic strain sweeps at 100 rad/s and varying strain amplitude from 0.1% to 10% in order to detect the limits of linear viscoelastic response; a strain amplitude of 1% was found appropriate for all tests ; (iii) dynamic frequency sweeps in the range from 100 to 0.1 rad/s in order to probe the linear viscoelastic response. Subsequently, creep experiments were performed over a range of stresses between 30 and 80 Pa. For each specimen, a creep test was repeated three times at different stresses to ensure that the measurements were performed in the linear regime (see Figure 4S. This was crucial since the creep data were eventually transformed into frequency spectra.

**Filament stretching** We performed nonlinear extensional rheology using an FSR - Filament Stretch Rheometer (VADER 1000 from Rheofilament). The basic working principle of the instrument is the following: A molten sample-disc sandwiched between a bottom and a top plate is deformed by moving the upper plate axially. The deformation of the sample midplane is monitored via a laser micrometer. A feedback loop enables the deformation to

be controlled while the response of the material is monitored by a force cell mounted on the bottom plate. The deformation of the midfilament plane is measured in terms of Hencky strain ( $\varepsilon = -2 \ln \frac{D(t)}{D_0}$ ). Here  $D(t)$  and  $D_0$  are the diameter measured at a given time ( $t$ ) and the initial diameter, respectively. The response of the material is given by the normal stress difference  $\langle \sigma_{zz} - \sigma_{rr} \rangle = (F - \frac{1}{2}mg) / \frac{\pi}{4}D(t)^2$ . Here  $F$  is the force measured on the bottom plate,  $m$  is the mass of the sample and  $g$  is the gravitational acceleration.

The VADER 1000 has two features that are crucial for this study. 1) The feedback control loop providing active control of the deformation and thus enables high Hencky strains ( $\varepsilon > 7$ ) to be reached without experiencing failure due to uncontrolled neck propagation. 2) Fast oven removal enabling quench of filaments to room temperature. The oven surrounding the sample can be pushed up leaving the sample exposed to ambient conditions. The quenching rate for filaments with a diameter of 1 mm has been estimated to be  $> 10$  K/s.

The experimental protocol for filament stretching was the following. The sample was pre-stretched at  $150^\circ\text{C}$  and subsequently relaxed for 15 min to erase all thermo-mechanical history. We found  $150^\circ\text{C}$  sufficiently high as samples relaxed at higher temperatures showed the same extensional behavior. The temperature was subsequently lowered to  $140^\circ\text{C}$ , stretched at a constant Hencky strain rate  $\dot{\varepsilon}$  and quenched at  $\varepsilon = 5.5$ . We observed no signs of flow induced crystallization during stretching. In order for all samples to experience the same quench history, the final filament diameter at quench for all samples was  $0.47 - 0.5$ . Ex-situ SAXS patterns of the quenched filaments were collected using a SAXSLAB instrument (Ganesha from SAXSLAB, Denmark) with a 300k Pilatus detector (pixel sizes  $172 \times 172 \mu\text{m}$ ). The wavelength of the X-ray beam was  $1.54 \text{ \AA}$  and the sample-to-detector distance was  $1491 \text{ mm}$ . Patterns with exposure times of  $6 \cdot 10^2 - 10^4 \text{ s}$  were collected from the midfilament plane of vertically mounted filaments.

## Multimode Maxwell model

The linear rheological response is model using the Multimode Maxwell model. It considers the total response of a material to be a sum of contributions from  $i$  number of modes with relaxation times  $\tau_i$  and corresponding moduli  $g_i$ . The storage modulus  $G'$  and loss modulus  $G''$  is thus given by:

$$G' = \sum_i \frac{g_i(\tau_i\omega)^2}{1 + (\tau_i\omega)^2} \quad (1)$$

$$G'' = \sum_i \frac{g_i\tau_i\omega}{1 + (\tau_i\omega)^2} \quad (2)$$

We used the software Reptate to perform the fit. The full Maxwell spectrum is given in Table 1S

## Hermans Orientation factor from SAXS

The average cosine squared ( $\langle \cos^2 \phi \rangle$ ) of the angle between the normal of a plane in the crystalline domains and the macroscopic direction in Eq. (1) of the main article, can be determined from azimuthally integrated SAXS patterns using:

$$\langle \cos^2 \phi \rangle = \frac{\int_0^{\pi/2} I_\beta \cos^2 \beta \sin \beta \, d\beta}{\int_0^{\pi/2} I_\beta \sin \beta \, d\beta} \quad (3)$$

Here  $\beta$  is the azimuthal angle and  $I_\beta$  is the corresponding intensity corrected for the contribution from shish.

The SAXS patterns obtained in this work show a significant scattering contribution from shish (see intensity peak along the equatorial in Figure 1S (a)). The resulting azimuthal intensity profiles from which  $F_H$  is extracted thus contains unwanted peaks at  $\pi/2$  and  $3\pi/2$  that does not arise from kebab-scattering. (see Figure1S (b)). This contribution must be subtracted to obtain the correct values of  $F_H$ . The shish contribution is subtracted from

the azimuthal intensity profiles by decomposition into an intensity contribution from kebabs ( $I_k$ ) and shish ( $I_s$ ) as well as an isotropic contribution  $I_{iso}$ .

$$I = I_k + I_s + I_{iso} \quad (4)$$

The two peak contributions  $I_k$  and  $I_s$  are described by periodically spaced peaks with a Lorentzian type distribution, while  $I_{iso}$  is a constant:

$$I_{kebab} = \frac{I_k}{1 + \left(\frac{\beta - (p\pi + \beta_0)}{\gamma_k}\right)^2} \quad I_{shish} = \frac{I_s}{1 + \left(\frac{\beta - (\pi(p+1/2) + \beta_0)}{\gamma_s}\right)^2} \quad I_{iso} = const. \quad (5)$$

Here  $I_k$  and  $I_s$  are the maximum intensities of the kebab and shish peaks, respectively while  $\gamma_k$  and  $\gamma_s$  are the corresponding "half width at half maximum" of the peaks.  $\beta_0$  enables a horizontal shift for samples that were slightly rotated in the beamline during the recording of the SAXS patterns.  $p = -1, 0, 1, 2$  and ensures that all periodic peaks contributing to the patterns are included. To obtain an expression for the azimuthal intensity profile  $I_\beta$  without the shish contribution we simply subtract  $I_s$  from the raw data  $I_{raw}$  such that:

$$I_\beta = I_{raw} - I_s \quad (6)$$

From this it is now possible to obtain a more accurate value of  $F_H$

## Supporting Tables

Table 1S: Multimode Maxwell parameters for the UH-blend and the matrix at  $T = 140^\circ\text{C}$

mode, $i$	UH-blend		Matrix	
	$\tau_i$ [s]	$g_i$ [Pa]	$\tau_i$ [s]	$g_i$ [Pa]
10	1.4E+03	2.4E+01	1.3E+03	1.1E-02
9	3.1E+02	1.8E+01	3.0E+02	1.7E+01
8	7.0E+01	1.5E+02	6.9E+01	6.0E+01
7	1.6E+01	5.5E+02	1.6E+01	3.8E+02
6	3.5E+00	2.4E+03	3.5E+00	2.2E+03
5	7.9E-01	1.2E+04	8.0E-01	1.1E+04
4	1.8E-01	4.4E+04	1.8E-01	4.6E+04
3	4.0E-02	1.4E+05	4.1E-02	1.4E+05
2	8.9E-03	2.3E+05	9.4E-03	2.1E+05
1	2.0E-03	5.6E+05	2.1E-03	5.4E+05

## Supporting Figures

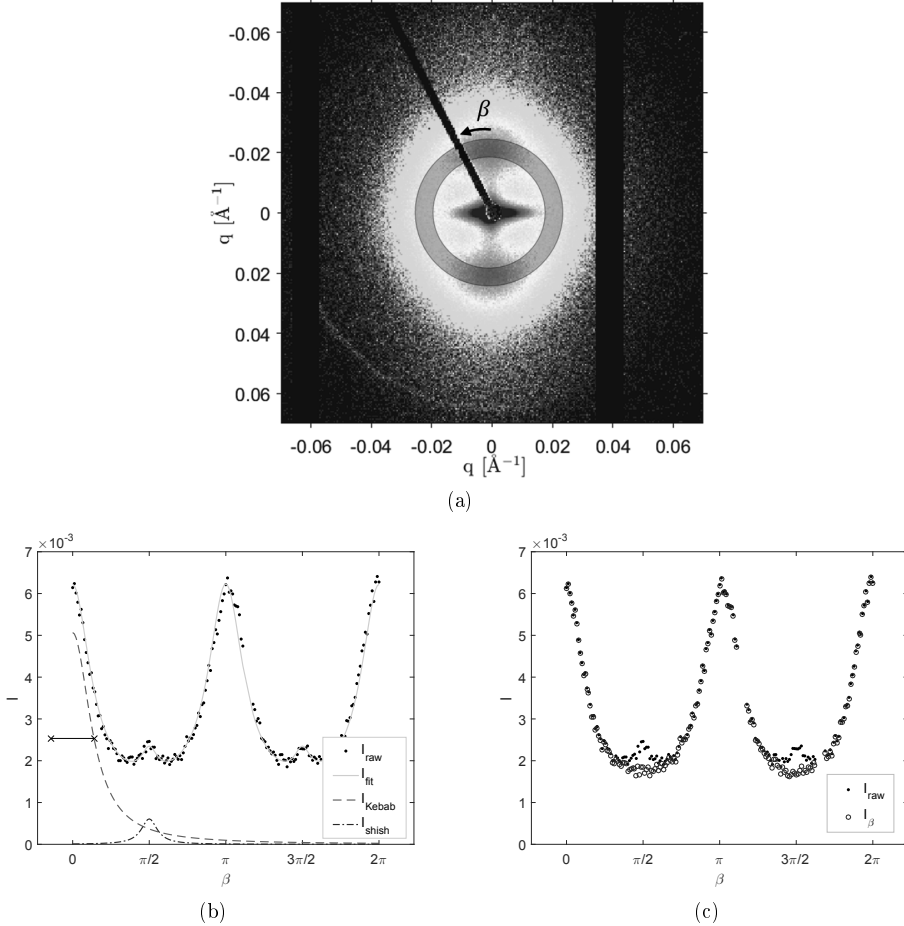


Figure 1S: Illustration of how scattering intensities from kebabs are extracted from SAXS-patterns while omitting the contribution from shish. (a) Example of the raw SAXS pattern. The shaded area indicate the area over which the azimuthal integration is performed. With the arrow showing the direction of the azimuthal angle  $\beta$ . (b) Azimuthal intensity profile where (black  $\cdot$ ) is the raw data, (green  $-$ ) is the total fit using Eq. (4) with (red  $-$ ) and (blue  $\cdot$ ) signifying the scattering contribution from kebabs and shish, respectively, with  $p = -1$ . (c) Compares the raw azimuthal intensity profile (black  $\cdot$ ) and the profile where the shish-contribution has been removed (blue  $\circ$ ) by subtracting the fitted shich contribution shown in (b).

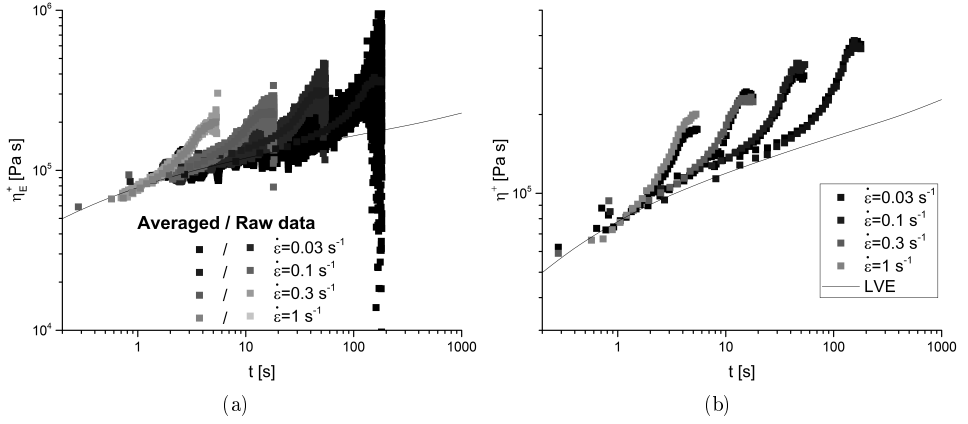


Figure 2S: Uniaxial extensional data for the UH-blend at 140°C (a) Shows the raw data (gray scale symbols) and the averaged data (blue scale symbols) (b) Shows the reproducibility of the stretches for two sets of stretch experiments (blue and black symbols, respectively)

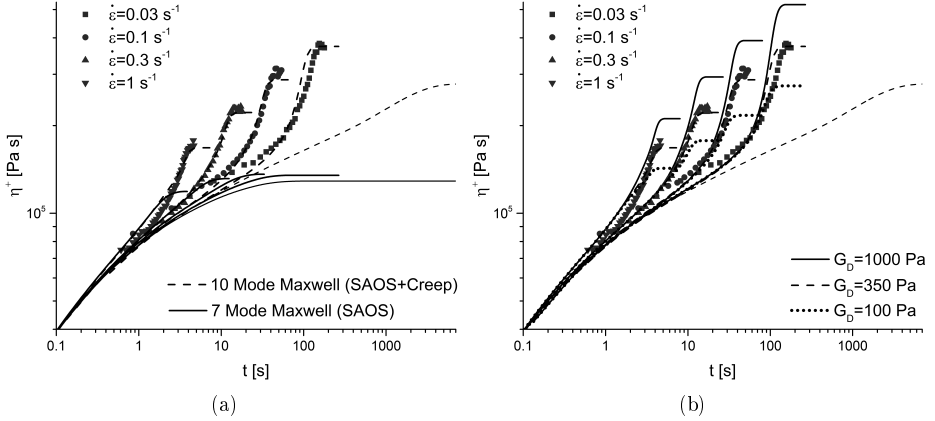


Figure 3S: Parameter Sensitivity for the HMMSF modelling (lines) of constant rate extensional data (symbols) at 140°C. (a) Compares the HMMSF prediction using the full 10 mode frequency Maxwell spectrum obtained by combining SAOS and creep data with the prediction using the limited 7 mode spectrum obtained from SAOS alone. (b) Shows the HMMSF prediction using different values of  $G_D$ .

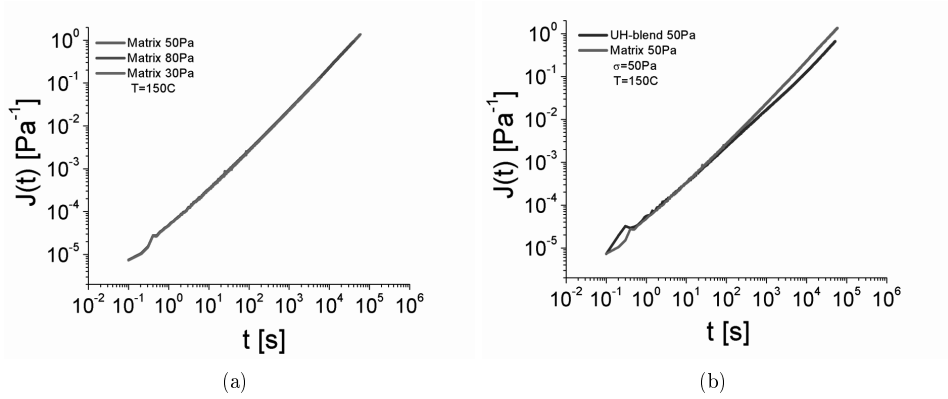


Figure 4S: Rheological response in creep. (a) Creep compliance curves for the matrix obtained at various stresses at  $150^\circ\text{C}$ . The overlap confirms that measurements are performed in the linear regime. (b) Comparison of creep compliance curves for the UH-blend and the matrix.

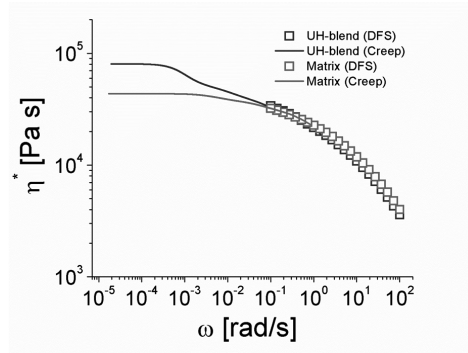


Figure 5S: Dynamic shear viscosity  $150^\circ\text{C}$  for the UH-blend and the matrix obtained via SAOS (symbols) and creep (lines). Note the difference in zero-shear-rate viscosity at low frequencies

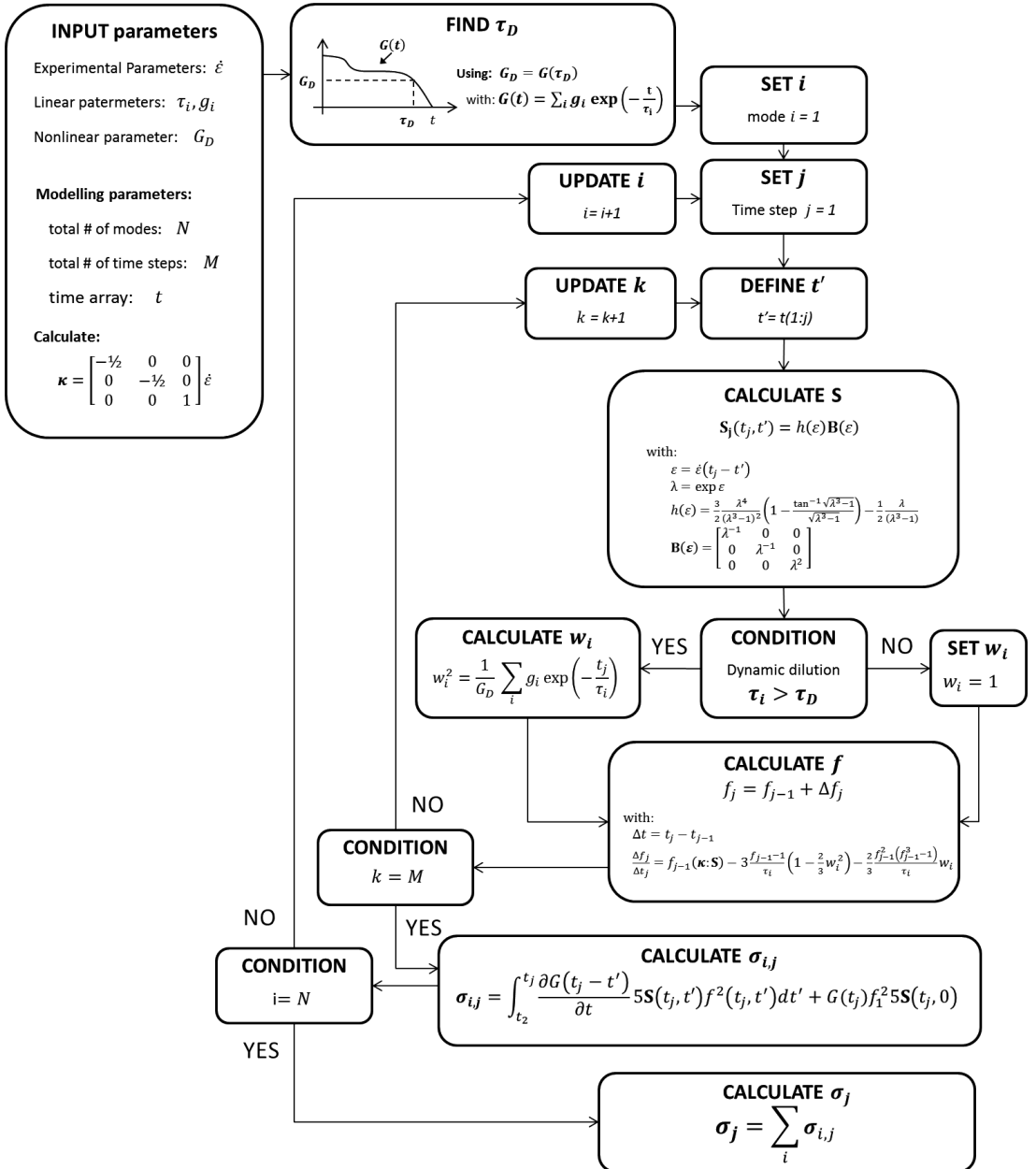


Figure S1: A schematic showing the algorithm for the implementation of the HMMSF model in MatLab

APPENDIX D

# Supplemental material for Chapter 5

---

**Extension induced phase separation and crystallization in semidilute solutions of ultra high molecular weight polyethylene "**

Supplemental material contains following:

- Figures S-1, S-2

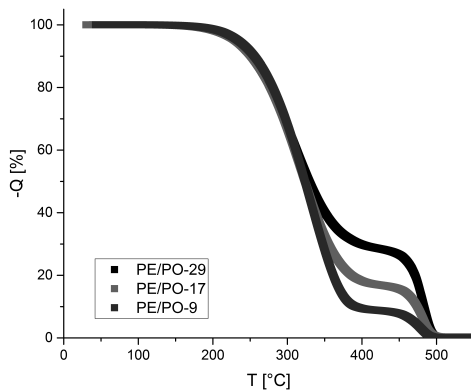


Figure 1S: TGA curves for the three samples used for determination of polymer concentration.

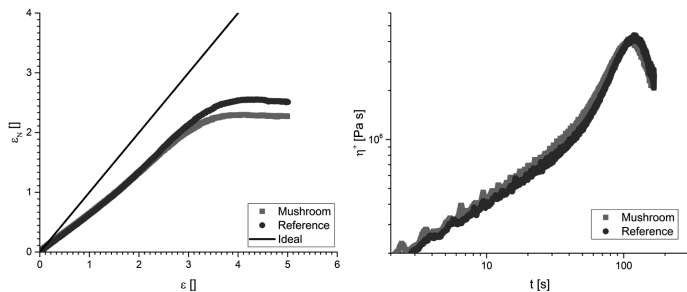


Figure 2S: Validation of the plate design. (a) Shows the response of a well know LDPE in extension using a standard plate set and the new mushroom plate set. (b) shows the nominal strain vs. Hencky strain for standard plate set and mushroom plate set. Despite the difference in plate motion the response is the same because both deformation and reponse is measured in the midplate only.

APPENDIX E

# Supplemental material for: Chapter 6

---

**Shish formation above the melting temperature stabilizes the filaments of HDPE in extensional flow**

Supplemental material contains following:

- Tables S1
- Figures S1

## Supporting Table

**Table E.1:** Multimode Maxwell parameters for PE-460k at  $T = 140^\circ\text{C}$

mode, $i$	$\tau_i$ [s]	$g_i$ [Pa]
9	4.63E+04	2.73E+01
8	6.63E+03	1.77E+01
7	9.48E+02	3.86E+02
6	1.36E+02	6.61E+02
5	1.94E+01	5.16E+04
4	2.78E+00	2.58E+05
3	3.98E-01	5.65E+05
2	5.69E-02	4.56E+05
1	8.14E-03	4.42E+05

## Supporting Figure

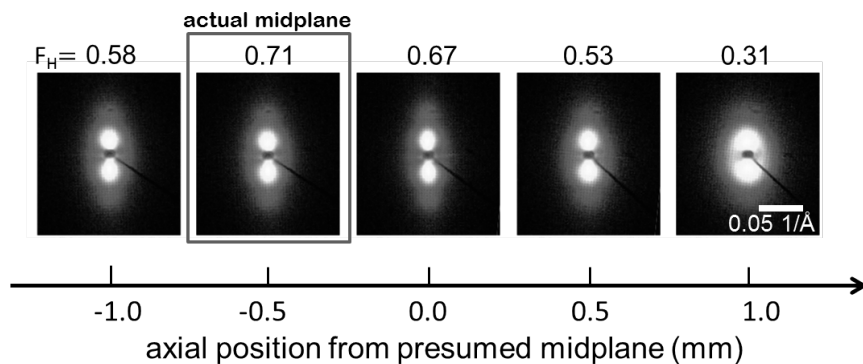


Figure S1: SAXS patterns from an axial scan of a filament. Herman's orientation factor is shown above the patterns. The actual midfilament plane is determined from the highest value of Herman's orientation factor. Here the actual position of the midfilament plane turn out to be at (-0.5) which is different from the presumed position of the midfilament plane at (0.0).

## APPENDIX F

# Additional publication: "Oscillatory squeeze flow for the study of linear viscoelastic behavior"

---

This appendix contains the full manuscript of an article that was drafted, finalized and published during this PhD study. While my contribution is concerned with linear rheology, the mathematical derivation and the tests performed on the FSR, the overall scope appeared too far from the main objective of my studies to make an actual chapter of the thesis. Hence it is attached as appendix.

# Oscillatory squeeze flow for the study of linear viscoelastic behavior

Sara L. Wingstrand



*Department of Chemical and Biochemical Engineering, Technical University of Denmark,  
DK-2800 Kgs Lyngby, Denmark*

Nicolas J. Alvarez

*Department of Chemical and Biological Engineering, Drexel University, Philadelphia, Pennsylvania 19104*

Ole Hassager<sup>a)</sup>

*Department of Chemical and Biochemical Engineering, Technical University of Denmark,  
DK-2800 Kgs Lyngby, Denmark*

John M. Dealy

*Department of Chemical Engineering, McGill University, Montreal, Quebec H3A 0C4, Canada*

(Received 28 September 2015; final revision received 9 February 2016; published 28 March 2016)

## Abstract

The squeezing of a sample between parallel plates has been used for many years to characterize the rheological behavior of soft, purely viscous materials, and in recent times, small-amplitude oscillatory squeezing has been proposed as a means to determine the linear viscoelastic properties of molten polymers and suspensions. The principal advantage of squeeze flow rheometer over rotational devices is the simplicity of the apparatus. It has no air bearing and is much less expensive and easier to use. Accuracy may be somewhat reduced, but for quality control purposes, it could be quite useful. It might also find application as the central component of a high-throughput rheometer for evaluating experimental materials. The deformation is not simple shear, but equations have been derived to show that the oscillatory compressive (normal) force that is measured can serve as a basis for calculating the storage and loss moduli. These theories as well as instruments that have been developed to generate the required deformation are described, and applications to a variety of materials are described. © 2016 The Society of Rheology. [<http://dx.doi.org/10.1122/1.4943984>]

## I. INTRODUCTION

Engmann *et al.* [1] published a useful review of squeeze flow rheometry, emphasizing its use for fluids with yield stress but saying little about oscillatory squeeze flow. We begin with a brief review of the use of squeezing flows for the characterization of purely viscous (inelastic) materials. Squeezing flow is not a viscometric flow, and devices using this deformation for non-Newtonian fluids can be used only for qualitative purposes unless a constitutive model is available.

There are two methods of operation: constant area and constant volume. In a “squeeze film” device, the sample initially has the same size as the circular plates between which it is compressed so that the area of the sample under compression is constant. A constant normal force,  $F$ , is applied to the upper plate, most simply by means of a weight, and the decreasing plate spacing,  $H(t)$ , is measured. In a “parallel-plate plastometer,” the sample is smaller than the plates so that the sample volume remains constant rather

than its compressed area. A device based on this concept is used in a standard test method for measuring an “apparent viscosity” of bitumen [2]. The constant area method is sometimes preferred, because if a smaller sample is used, its volume and thus its radius during testing must be precisely known. It is also desirable that it be centered in the gap to ensure symmetric loading.

Another mode of operation involves a constant speed rather than a constant normal force with the force monitored as a function of time, and there are thus four possible combinations of constant-volume/constant-radius and constant-speed/constant-force. Some devices also work at exponentially decaying speed to achieve a nominally constant rate of compression.

The modeling of nonoscillatory squeeze flow assumes that inertia can be neglected (very low  $Re$ ) and that the velocity distribution has a certain form. Equations for the interpretation of data in terms of viscosity are described in detail by Bird *et al.* [3], and we present here only a brief summary. Considering first constant area flow, for a Newtonian fluid, the deformation is governed by the Stefan equation, shown as

<sup>a)</sup>Author to whom correspondence should be addressed; electronic mail: [oh@kt.dtu.dk](mailto:oh@kt.dtu.dk)

$$F(t) = \frac{3\pi R^4 \eta (-dH/dt)}{2[H(t)]^3}. \quad (1)$$

Here,  $R$  is the radius of the sample and  $\eta$  is the Newtonian viscosity. For a constant compressive (normal) force  $F_0$  and initial condition  $H(0) = H_0$ , the gap spacing is given by

$$\frac{1}{H^2} = \frac{1}{H_0^2} + \frac{4F_0 t}{3\pi R_0^4 \eta}. \quad (2)$$

At very short times, inertia cannot be neglected, so if  $(1/H^2)$  is plotted versus time, the first points will not lie on a line, but if the data approach a line, the slope can be used to calculate the viscosity. If the deformation is sufficiently slow, this technique should provide a reasonable approximation of the zero-shear viscosity of a molten polymer.

For a constant volume flow, Dienes and Klemm [4] derived the following relationship for a Newtonian fluid, where  $V$  is the volume of the sample:

$$F = \frac{3\eta V^2}{2\pi H^5} \left( -\frac{dH}{dt} \right). \quad (3)$$

For a constant normal force  $F_0$  and a constant volume, integration with the initial condition  $H(0) = H_0$  gives

$$\frac{1}{H^4} = \frac{1}{H_0^4} + \frac{8\pi F_0}{3\eta V^2} t. \quad (4)$$

Gent [5] reported that the assumptions regarding the velocity profile are only valid when  $R_0 > 10H_0$  ( $\Lambda < 0.1$ ).

Because the strain is not uniform throughout the flow, the interpretation of data for non-Newtonian fluids requires a viscosity model, and Engmann *et al.* [1] have compiled an extensive list of all the fluid models for which squeeze flow equations have been reported, including both inelastic and elastic materials and with no-slip, slip, and partial-slip boundary conditions. For example, for a power-law fluid with consistency index  $m$  and power law parameter  $n$ , the Scott equation describes the flow with a constant force and volume

$$F = \left( \frac{2\pi m R^{n+3}}{n+3} \right) \left( \frac{2n+1}{n} \right) \frac{(-dH/dt)^n}{H^{2n+1}}. \quad (5)$$

Gibson *et al.* [6] used squeezing flow to study the behavior of suspensions of planar fibers in polypropylene. Pham and Meinecke [7,8] employed squeezing flow at a constant plate speed rather than a constant normal force for the evaluation of commercial polymers. Shaw [9] used a squeeze-flow apparatus to deal with the difficult problem of characterizing the flow behavior of ultrahigh-density polyethylene, which has a very high viscosity. The driving pressure was maintained constant, and  $H(t)$  was measured. Even at very low shear rates, this material is still pseudoplastic, but the Stefan equation was used to calculate an apparent viscosity that was related to molecular weight by an empirically established relationship. About 25 min were required for a measurement. Cua and Shaw [10] used a similar method to determine the low-shear rate viscosity of a polydimethylsiloxane.

Squeeze flow has also been used to measure the response of molten polymers to biaxial extension, a deformation that is difficult to generate in the laboratory. To address this problem, squeezing between lubricated plates (LSF) has been used to eliminate the shearing component of the flow field. The LSF method of biaxial stretching was first proposed by Chatraei *et al.* [11] and was later used by Nishioka *et al.* [12] and by Kompani and Venerus [13]. The latter authors replenished the lubricant continuously during a test to avoid the development of dry regions. They reviewed the history of the LSF technique and developed the basic equations for the interpretation of data in terms of the biaxial extensional viscosity. Guaderama-Medina *et al.* [14] compared results for a low-density polyethylene obtained by LSF with those obtained using a complex instrument in which a circular sheet of polymer is stretched by six pairs of rotary clamps [15]. It was found that the LSF data were not reliable at Hencky strains greater than one.

## II. THEORY OF OSCILLATORY SQUEEZE FLOW

We turn now to small amplitude oscillatory flow as described by the theory of linear viscoelasticity. We begin by recalling the correspondence principle by Pipkin [16], which applies to general quasisteady deformations (i.e., no inertia). Pipkin demonstrated that it is possible to go from the solution to an equilibrium elasticity problem to a corresponding quasisteady linearly viscoelastic problem. In a similar development, Phan-Thien [17] and Field *et al.* [18] transformed the Stefan equation for Newtonian fluids to the corresponding functional relation for linear viscoelastic materials, again for deformations with negligible inertia by appropriate substitution of the constant viscosity by the complex viscosity. We make use of this relationship below [Eq. (46)].

We here describe how linear viscoelastic behavior can be measured by the use of squeeze flow, but in a form that is not necessarily restricted to negligible inertia.

Consider a fluid sandwiched between two plates as illustrated in Fig. 1. With the bottom plate located at an axial position  $z=0$ , the top plate position ( $H$ ) also signifies the height of the gap between the top and bottom plates. The top plate oscillates axially about a mean height  $H_0$  to impose oscillatory squeezing described by

$$H(t) = H_0(1 + a \sin \omega t). \quad (6)$$

Here,  $H_0$  is the top plate position at time  $t=0$ ,  $aH_0$  is the amplitude, and  $\omega$  is frequency. The speed of the top plate  $\dot{H}$  can thus be expressed as

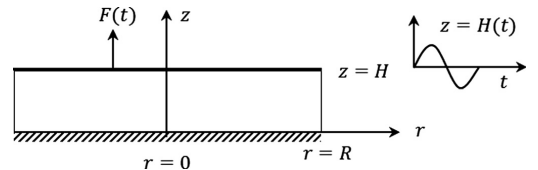


FIG. 1. Sketch of an oscillatory squeeze flow geometry.

$$\dot{H} = \frac{dH}{dt} = aH_0\omega\Re\{e^{i\omega t}\}, \quad (7)$$

where  $\Re\{\}$  indicates the real part of the complex quantity inside the brackets.

As we are concerned here only with linear viscoelastic characterization,  $a$  is assumed to be small. The permissible magnitude of  $a$  depends on the aspect ratio  $\Lambda \equiv H_0/R_0$ . Konigsberg [19] has discussed the problem of defining a characteristic value of strain, but the value of the maximum strain, which occurs at the rim, can be evaluated, as shown in the following discussion, and this governs the limit for the applicability of the linear viscoelasticity (LVE) governing equations. By restricting the analysis to small deformations the following simplifications can be made:

- (1) The convection term ( $\mathbf{v} \cdot \nabla \mathbf{v}$ ) in the equation of motion, where  $\mathbf{v}$  is velocity, can be neglected, as it is of order  $O(a^2)$  [20].<sup>1</sup>
- (2) The governing equations of linear viscoelasticity may be used.

Based on these considerations  $\mathbf{v}$  and the pressure  $p$  can be represented as follows:

$$\mathbf{v} = \Re\{\bar{\mathbf{v}}(\mathbf{x})e^{i\omega t}\}, \quad (8)$$

$$p = \Re\{\bar{p}(\mathbf{x})e^{i\omega t}\}, \quad (9)$$

where  $\bar{\mathbf{v}}(\mathbf{x})$  and  $\bar{p}(\mathbf{x})$  are complex functions that only vary spatially so that the extra stress tensor  $\boldsymbol{\sigma}$  can be written simply as

$$\boldsymbol{\sigma} = \Re\{\eta^*[(\nabla\bar{\mathbf{v}}) + (\nabla\bar{\mathbf{v}}^T)]e^{i\omega t}\}. \quad (10)$$

It follows that the velocity field for flow of a linear viscoelastic fluid is described by the governing equations of a Newtonian fluid, i.e., Navier–Stokes equations, with viscosity replaced by the complex viscosity  $\eta^*$ . This is in accord with the correspondence principle of Pipkin [16] who showed a similar analogy to elasticity problems. Here, we use this technique to derive the velocity distribution for the oscillatory squeeze flow.

In setting up the equations of motion, we assume incompressibility and neglect flow in the angular direction ( $\theta$ ) so that  $v_\theta = 0$ , and  $\partial/\partial\theta = 0$ . Also, we introduce dimensionless complex variables  $\hat{r}$ ,  $\hat{z}$ ,  $\hat{v}_r$ ,  $\hat{v}_z$ , and  $\hat{p}$  as follows:

$$\hat{r} = r/R_0, \quad (11)$$

$$\hat{z} = z/H_0, \quad (12)$$

$$v_r = aR_0\omega\Re\{\hat{v}_r(\hat{r}, \hat{z})e^{i\omega t}\}, \quad (13)$$

$$v_z = aH_0\omega\Re\{\hat{v}_z(\hat{z})e^{i\omega t}\}, \quad (14)$$

$$p = p_{\text{atm}} + \frac{a\omega R_0^2}{H_0^2}\Re\{\eta^*\hat{p}(\hat{r}, \hat{z})e^{i\omega t}\}. \quad (15)$$

Here,  $p_{\text{atm}}$  is the atmospheric pressure. Using Eqs. (11)–(15), the following dimensionless complex equations of continuity and motion are obtained:

$$\frac{1}{\hat{r}}\frac{\partial}{\partial\hat{r}}(\hat{r}\hat{v}_r) + \frac{\partial\hat{v}_z}{\partial\hat{z}} = 0, \quad (16)$$

$$\text{Re}\hat{v}_r = -\frac{\partial\hat{p}}{\partial\hat{r}} + \left[\Lambda^2\frac{\partial}{\partial\hat{r}}\left(\frac{1}{\hat{r}}\frac{\partial}{\partial\hat{r}}(\hat{r}\hat{v}_r)\right) + \frac{\partial^2\hat{v}_r}{\partial\hat{z}^2}\right], \quad (17)$$

$$\Lambda^2\text{Re}\hat{v}_z = -\frac{\partial\hat{p}}{\partial\hat{z}} + \left[\Lambda^4\frac{1}{\hat{r}}\frac{\partial}{\partial\hat{r}}\left(\hat{r}\frac{\partial\hat{v}_z}{\partial\hat{r}}\right) + \Lambda^2\frac{\partial^2\hat{v}_z}{\partial\hat{z}^2}\right]. \quad (18)$$

Here,  $\rho$  is the density, and we define the Reynolds number as

$$\text{Re} = \frac{i\rho\omega H_0^2}{\eta^*}. \quad (19)$$

Note that various definitions of Re have been used for oscillatory squeeze flow (OSF). Field *et al.* [18] define it as a real number and use  $aH_0$  as the characteristic length to obtain  $\text{Re} = \rho\omega aH_0^2/\eta^*$ . Debbaut and Thomas [21] do not define a Reynolds number but introduce the number  $\alpha^2 = i\omega\rho/\eta^*$ .  $\alpha$  has dimensions of  $m^{-1}$  but always appears in the group  $\alpha^2 H_0^2$ , which is dimensionless and equal to the Re defined here [22].

Assuming that material planes remain parallel to the plates, we find that  $\hat{v}_z$  is independent of  $\hat{r}$  so that mass conservation Eq. (16) yields

$$\hat{v}_r = -\frac{1}{2}f'(\hat{z})\hat{r}, \quad (20)$$

$$\hat{v}_z = f(\hat{z}). \quad (21)$$

Here,  $f(\hat{z})$  is a function that varies only with  $\hat{z}$ , and  $f'(\hat{z})$  is the derivative. Inserting Eqs. (20) and (21) into Eqs. (18) and (19), we obtain

$$\frac{1}{2}\text{Re}\hat{r}f' = \frac{\partial\hat{p}}{\partial\hat{r}} + \frac{1}{2}\hat{r}f''', \quad (22)$$

$$\Lambda^2\text{Re}f = -\frac{\partial\hat{p}}{\partial\hat{z}} + \Lambda^2f''. \quad (23)$$

Performing cross differentiation, the pressure can be eliminated, and the following expression is obtained:

$$\text{Re}f'' = f'''' . \quad (24)$$

With boundary conditions

$$f(1) = 1, \quad f(0) = 0, \quad (25)$$

$$f'(1) = 0, \quad f'(0) = 0. \quad (26)$$

<sup>1</sup>Commercial version of MFR available from GBC Scientific Equipment, Ltd., Dandenong, Victoria, Australia, www.gbcsai.com

Proceeding from here, it is beneficial to identify other simplifying assumptions that might apply. In particular, postulate

- (1) If inertia can be neglected, i.e., if  $\text{Re} \ll 1$ . In this case, the flow can be regarded as a creep flow, and the left hand side of Eqs. (22)–(24) can be set equal to 0.
- (2) If  $\Lambda \ll 1$ , the lubrication approximation can be used so that all terms containing any order of  $\Lambda$  can be neglected in Eq. (23).

We now examine the effect of making either of these assumptions. In all cases, we assume a no-slip boundary condition between the fluid and the plates, although we discuss briefly the effect of a slip or partial-slip boundary condition below.

### A. Negligible inertia

We first assume small  $\text{Re}$  so that inertia is negligible compared to viscous effects, and Eq. (24) reduces to

$$f''' = 0. \quad (27)$$

Using boundary conditions (25) and (26), one obtains

$$f = -2\hat{z}^3 + 3\hat{z}^2. \quad (28)$$

The radial and axial stresses (physical components) are then found to be

$$\sigma_{rr} = \frac{a\omega R_0^2}{H_0^2} \Re\{\eta^* \hat{\sigma}_{rr} e^{i\omega t}\}, \text{ where } \hat{\sigma}_{rr} = 6\Lambda^2(\hat{z}^2 - \hat{z}), \quad (29)$$

$$\sigma_{zz} = \frac{a\omega R_0^2}{H_0^2} \Re\{\eta^* \hat{\sigma}_{zz} e^{i\omega t}\}, \text{ where } \hat{\sigma}_{zz} = -12\Lambda^2(\hat{z}^2 - \hat{z}). \quad (30)$$

Returning to the complex, dimensionless equations of motion [Eqs. (22) and (23)], we can neglect terms containing  $\text{Re}$  and set the right hand sides to 0. Inserting the expression for  $f(\hat{z})$ , one obtains

$$0 = \frac{\partial \hat{p}}{\partial \hat{r}} - 6\hat{r}, \quad (31)$$

$$0 = -\frac{\partial \hat{p}}{\partial \hat{z}} + \Lambda^2(-12\hat{z} + 6). \quad (32)$$

With the solution

$$\hat{p} = 3\hat{r}^2 + 6\Lambda^2(-\hat{z}^2 + \hat{z}) + \hat{p}_0. \quad (33)$$

Here,  $\hat{p}_0$  is an integration constant. The most intuitive boundary condition would be to set the pressure equal to the atmospheric pressure at the outer rim ( $\hat{r} = 1$ ). However, this procedure is problematic since  $\hat{p}$  depends on  $\hat{z}$ . One way to deal with this issue is to set the  $z$ -averaged pressure  $p = p_{\text{atm}}$  [1]. Another approach is to set up a force balance at  $(\hat{r}, \hat{z}) = (1, 1/2)$ . Here, only the stress in the radial direction needs to be considered, leading to the following expressions:

$$0 = \hat{p}\left(1, \frac{1}{2}\right) - \hat{\sigma}_{rr}\left(1, \frac{1}{2}\right), \quad (34)$$

$$\Rightarrow \hat{p}_0 = -3(1 + \Lambda^2). \quad (35)$$

Hence, the complete expression for  $\hat{p}$  is

$$\hat{p} = -3(1 - \hat{r}^2 + \Lambda^2) + 6\Lambda^2(-\hat{z}^2 + \hat{z}). \quad (36)$$

In terms of physical components, we have

$$p - p_{\text{atm}} = \frac{a\omega}{H_0^2} \left[ -3(R_0^2 - r^2 + H_0^2) + 6(-z^2 + H_0 z) \right] \times \Re\{\eta^* e^{i\omega t}\}. \quad (37)$$

The expression  $p - p_{\text{atm}} - \sigma_{zz}$  can then be integrated over either the top or bottom plate, i.e.,  $z = H_0$  or  $z = 0$ , to give the normal force ( $F$ ) on the top plate.

Another approach is to use another fact at our disposal to deal with this tricky boundary condition that will allow us to completely avoid it. This is to use the macroscopic mechanical energy balance adapted to linear viscoelastic liquids [23, Sec. 7.8].

$$F\dot{H} = \int_V \boldsymbol{\sigma} : \nabla \mathbf{v} dV. \quad (38)$$

Since  $\dot{H}$  is completely in phase with  $\mathbf{v}$ , it follows that  $F$  must be in phase with  $\boldsymbol{\sigma}$  and is given by

$$F = (aH_0\omega)^{-1} \int_V \phi_V dV \Re\{\eta^* e^{i\omega t}\}, \quad (39)$$

where

$$\phi_V = 2 \left[ \left( \frac{d\bar{v}_r}{dr} \right)^2 + \left( \frac{d\bar{v}_z}{dz} \right)^2 \right] + \left[ \frac{d\bar{v}_r}{dz} \right]^2. \quad (40)$$

Thus, the volume integral over  $\phi_V$  gives

$$\begin{aligned} \int_V \phi_V dV &= 2\pi(a\omega R_0)^2 H_0 \Re\left\{ \int_{\hat{z}=0}^1 \int_{\hat{r}=0}^1 \left( 2 \left[ \left( \frac{d\bar{v}_r}{d\hat{r}} \right)^2 + \left( \frac{d\bar{v}_z}{d\hat{z}} \right)^2 \right] \right. \right. \\ &\quad \left. \left. + \left[ \frac{R_0 d\bar{v}_r}{H_0 d\hat{z}} \right]^2 \right) \hat{r} d\hat{r} d\hat{z} \right\}, \\ &= \frac{3\pi(a\omega)^2 R_0^4}{2H_0} \left[ 1 + 2 \left( \frac{H_0}{R_0} \right)^2 \right]. \end{aligned} \quad (41)$$

The final expression for  $F$  is obtained by inserting this into Eq. (39) and we get

$$\Rightarrow F = \frac{3\pi a\omega R_0^4}{2H_0^2} \Re\{\eta^* e^{i\omega t}\} \left[ 1 + 2 \left( \frac{H_0}{R_0} \right)^2 \right]. \quad (42)$$

Inserting  $i\omega\eta^* = (G' + iG'')$  and taking the real part of all terms results in following:

$$F = \frac{3\pi a R_0^4}{2H_0^2} (G' \sin \omega t + G'' \cos \omega t) \left[ 1 + 2 \left( \frac{H_0}{R_0} \right)^2 \right]. \quad (43)$$

The factor  $[1 + 2(H_0/R_0)^2]$  weighs the shear contribution to the normal force compared to the extensional contribution. If  $H_0/R_0 \gg 1$ , the second term in brackets dominates the first, and the flow can be considered uniaxial extension. Hence, the relation reduces to the well-established expression for the normal force on the top plate for uniaxial viscoelastic extensional flow [3]

$$F = 3\pi a R_0^2 (G' \sin \omega t + G'' \cos \omega t). \quad (44)$$

But if  $H_0/R_0 \ll 1$ , the first term in Eq. (43) dominates the second so that the deformation is dominated by shear, and Eq. (43) reduces to

$$F = \frac{3\pi a R_0^4}{2H_0^2} (G' \sin \omega t + G'' \cos \omega t). \quad (45)$$

This equation can be derived from the Stefan equation [Eq. (1)] using Pipkin's correspondence principle [16], as shown originally derived by Phan-Thien [17]. Phan-Thien's final expression contained an error later corrected by Field *et al.* [18] who give the correct form shown below:

$$F^* = \frac{3\pi R_0^4 \eta^*}{2H_0^2} \frac{dH^*}{dt}. \quad (46)$$

The price paid for this apparent simplicity is that  $F^*$  and  $H^*$  are now complex functions of time related to the force and the plate separation by  $F = \Re\{F^*\}$  and  $H = \Re\{H^*\}$ , respectively.

The very simple relations, Eqs. (45) and (46), are often applied to OSF as the aspect ratio in most cases is very small, and hence, the deformation can be safely assumed to be dominated by shear. However, if inertia is non-negligible, a correction is needed as is shown below.

## B. Lubrication approximation

Now we assume a small aspect ratio and apply the lubrication approximation (assumption 2 above). However, this does not lead to any simplification of Eq. (24) which we focus on initially in the following. The full solution of Eq. (24), which was derived by Bell *et al.* [22], is rather complicated and thus has limited practical utility. Instead it is beneficial to consider the perturbation solution in  $\text{Re}$ . We represent the full solution  $f$  as a power series in  $\text{Re}$

$$f(\text{Re}, \hat{z}) = f_0 + \text{Re} f_1 + O(\text{Re}^2). \quad (47)$$

So far, we have limited our analysis to a first order approximation in  $\text{Re}$ , and the approach is the same, but it becomes increasingly messy at higher orders. Inserting Eq. (47) into Eq. (24) gives

$$\text{Re} f_0'' = f_0'''' + \text{Re} f_1'''' + O(\text{Re}^2). \quad (48)$$

Collecting terms of equal order in  $\text{Re}$  yields following system of equations:

$$f_0'''' = 0, \quad (49)$$

$$f_0'' - f_1'''' = 0. \quad (50)$$

With the following boundary conditions:

$$f_0(1) = 1, \quad f_0(0) = 0, \quad (51)$$

$$f_0'(1) = 0, \quad f_0'(0) = 0, \quad (52)$$

$$f_1(1) = 0, \quad f_1(0) = 0, \quad (53)$$

$$f_1'(1) = 0, \quad f_1'(0) = 0. \quad (54)$$

Terms of  $O(\text{Re}^2)$  are disregarded, as they are assumed to be negligibly small. We see that Eq. (49) is identical to Eq. (27). This is expected, since both are of order  $O(\text{Re}^0)$ , and it obviously follows that both have the same solution. This solution is subsequently applied when solving for  $f_1$  and we obtain

$$f_0 = -2\hat{z}^3 + 3\hat{z}^2, \quad (55)$$

$$f_1 = -\frac{1}{10}\hat{z}^5 + \frac{1}{4}\hat{z}^4 - \frac{1}{5}\hat{z}^3 + \frac{1}{20}\hat{z}^2. \quad (56)$$

Until now, no simplifications based on lubrication have been made. However, returning to the equations of motion [Eqs. (22) and (23)], the lubrication approximation can be applied by eliminating all terms containing any order of  $\Lambda$ . If we also insert the 1st order perturbation solution  $f = f_0 + \text{Re} f_1 + O(\text{Re}^2)$ , we obtain

$$\frac{d\hat{p}}{d\hat{r}} = -\frac{1}{2}\hat{r}[f_0'''' + \text{Re}(f_1'''' - f_0'')], \quad (57)$$

$$\frac{d\hat{p}}{d\hat{z}} = 0. \quad (58)$$

We see that in this case  $\hat{p}$  is independent of  $\hat{z}$ . Inserting the expressions for  $f_0$  and  $f_1$  in Eq. (57) yields the following differential equation:

$$\frac{d\hat{p}}{d\hat{r}} = 6\hat{r} \left( 1 + \frac{1}{10}\text{Re} \right), \quad (59)$$

whose solution is

$$\hat{p} = 3\hat{r}^2 \left( 1 + \frac{1}{10}\text{Re} \right) + \hat{p}_1. \quad (60)$$

Here,  $\hat{p}_1$  is a dimensionless integration constant. At the rim,  $\hat{r} = 1$  and we apply the boundary condition that  $p = p_{\text{atm}}$  leading to  $\hat{p} = 0$ , and we obtain the following expression for  $\hat{p}$ :

$$\hat{p} = -3(1 - \hat{r}^2) \left( 1 + \frac{1}{10}\text{Re} \right). \quad (61)$$

In terms of physical components, the pressure is

$$p - p_{\text{atm}} = -\frac{3a\omega R_0^2}{H_0^2} \left[ 1 - \left( \frac{r}{R_0} \right)^2 \right] \times \Re \left\{ \eta^* \left( 1 + \frac{1}{10} \text{Re} \right) e^{i\omega t} \right\}. \quad (62)$$

The normal force  $F$  is obtained by integration of  $p - p_{\text{atm}}$ , and the following expression is obtained:

$$F = -2\pi \int_0^{R_0} (p - p_{\text{atm}}) r dr, \quad (63)$$

$$\Rightarrow F = \frac{3\pi a\omega R_0^4}{2H_0^2} \Re \left\{ \eta^* \left( 1 + \frac{1}{10} \text{Re} \right) e^{i\omega t} \right\}, \quad (64)$$

$$\Rightarrow F = \frac{3\pi a R_0^4}{2H_0^2} \left[ \left( G' - \frac{\rho\omega^2 H_0^2}{10} \right) \sin \omega t + G'' \cos \omega t \right]. \quad (65)$$

Thus, the first order inertial correction only influences the storage modulus  $G'$ . In situations where  $\text{Re} \approx 1$ , an error of about 10% in  $G'$  is expected if the first order correction term is not included. This is in good agreement with results obtained by Debbaut and Thomas [21], who compared computational fluid dynamics (CFD) calculations to analytic expressions for systems where inertia plays a non-negligible role. Additionally, it should be noted that when  $\text{Re} \rightarrow 0$ , Eq. (64) reduces to the creep solution for small aspect ratios [Eq. (45)] as it should. Debbaut and Thomas [21] also simulated nonlinear behavior using a Giesikus viscoelastic model to determine the effects of normal stress differences on the results. Their results revealed that normal stress differences affect data at high strains in a different way than non-linearity affects data from rotational measurements.

The solution can also be derived for higher orders of  $\text{Re}$  as was done by Bell *et al.* [22], who extended earlier work of Phan-Thien [17] and Field *et al.* [18] to obtain the perturbation solution approximated to order  $O(\text{Re}^2)$  as follows:

$$F = \frac{3\pi a\omega R_0^4}{2H_0^2} \Re \left\{ \eta^* \left( 1 + \frac{1}{10} \text{Re} + \frac{1}{8400} \text{Re}^2 \right) e^{i\omega t} \right\}. \quad (66)$$

From the prefactor of  $\text{Re}^2$ , we see that the second order correction is needed only at very high  $\text{Re}$ . More specifically, an error of about 10% is expected when  $\text{Re} \approx 100$ . In this high Reynolds number, the flow is dominated by inertia. This leaves one wondering whether the OSF-technique is of any use for these types of fluids as one has to extract a small fraction of the total normal force to obtain the viscous contribution.

With regard to the 1st and 2nd-order correction terms, however, it is important to note that compared to a torsional rheometer, inertia for OSF is much less significant [22]. In a torsional rheometer, corrections for inertia are required at a much lower  $\text{Re}$  compared to the OSF-rheometer.

In closing, we note that the fundamental solution represented by the function  $f_0$  allows us to get a more accurate estimate of the maximum shear strain at the outer rim. We find that the shear rate at the bottom plate is given by

$$\dot{\gamma}_{rz} = -3a\omega \frac{r}{H_0} \cos \omega t. \quad (67)$$

The shear strain from some given initial time 0 to time  $t$  is then

$$\gamma(t, 0) = \int_{t'=0}^t \dot{\gamma}_{rz} dt' = -3a \frac{r}{H_0} \sin \omega t. \quad (68)$$

The maximum value is therefore  $3a/\Lambda$ .

### C. Slip/partial slip boundary

In this review, only a no-slip boundary condition for the top and bottom plates is considered. However, if the fluid does not fully stick to the wall, partial slip or complete slip will occur. This has been modeled for a nonoscillatory squeeze flow [24], where the degree of slip is accounted for from the slip velocity ( $v_s$ ) at the solid-liquid interphase

$$v_s(r, H) = -\beta \sigma_{rz}(r, H). \quad (69)$$

Here, the slip coefficient  $\beta$  is introduced as a lubrication measure, i.e., if  $\beta = 0$ , a no-slip boundary condition applies, whereas complete slip is obtained in the limit of  $\beta \rightarrow \infty$ . If a full slip boundary condition is applied in the OSF model, one generates biaxial extension, as was mentioned in Sec. I. If fluid sticks only partially to the wall, the situation will be between the no-slip and full slip cases. The less slip, the greater will be the contribution of shearing deformation to the stress.

## III. INSTRUMENTS

### A. Narrow gap squeeze flow devices

Early work on the behavior of elastic fluids in squeeze flow was motivated by the question of whether elasticity enhanced the lubricating ability of a fluid squeezed between flat plates, and this was reviewed by Brindley *et al.* [25]. When the aspect ratio is sufficiently small, the lubrication approximation can be used, or if the viscosity is large, inertia can be ignored, and Eq. (45) can be used to interpret the data. A constant sample area is generally the preferred configuration, because if a smaller sample is used, its initial radius must be precisely known. Also, in the case of a constant volume sample, it is important that it be centered in the gap if symmetric loading is to be achieved. The principal advantage of the squeeze flow rheometer over rotational instruments is the simplicity of the apparatus. It has no air bearing and is much less expensive and easier to use. It might also find application as the central component of a high-throughput rheometer for evaluating experimental materials.

It was some years before an instrument to carry out such a test was described in a presentation by Whittingstall and van Arsdale [26] and a patent by Van Arsdale and Motivala [27]. Figure 2 shows the principle of operation.

The sample fills the gap, so this is a constant area device. The first commercial instrument based on oscillatory squeeze flow was the CP20 Compressional Rheometer made by TA Instruments, a sketch of which is shown in Fig. 3. As in the Van Arsdale device, it is the sample area that is constant rather than its volume. The manufacture and sale of the

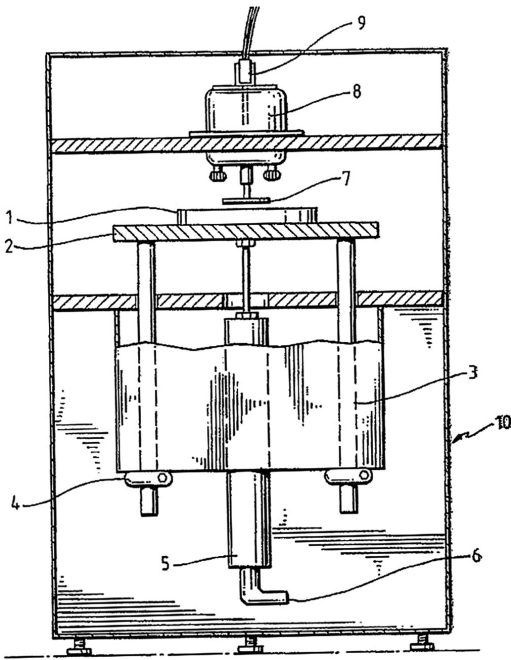


FIG. 2. Sketch showing essential elements of the device patented by van Arsdale and Motivala [27]. (1) Temperature-controlled stationary plate; (2) moveable base plate; (3) pneumatic linear actuator; (4) rings to limit vertical movement; (5) air cylinder; (6) air line; (7) oscillating plate; (8) shaker motor; (9) noncontacting displacement sensor; and (10) frame.

CP20 were later taken over by DB Scientific Instruments, which no longer exists, who called it the CP50 Compressional Rheometer. Figure 4 is a photo of this device. Note that the sample fills the gap under the upper plate.

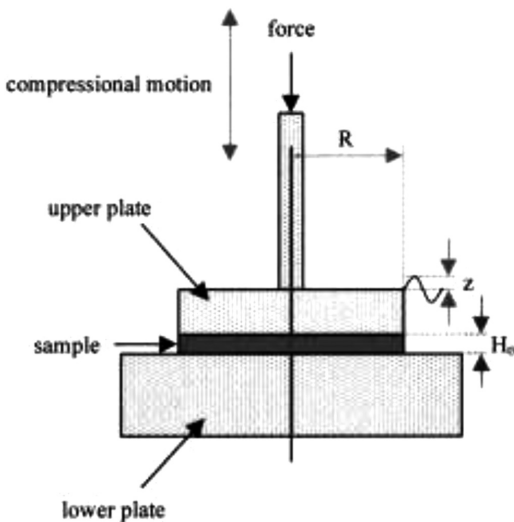


FIG. 3. The basic elements of the CP50 compressional rheometer.

Walberer and McHugh [28] used this device to study highly filled particle suspensions in polydimethylsiloxane.

Crassous *et al.* [29] described a device for high-frequency measurements driven by a piezoelectric axial vibrator. They were able to obtain storage and loss moduli for polymer solutions over a range of frequencies from 10 to 300 Hz. In combination with a rotational rheometer and a set of torsional resonators, they were able to characterize a sample at frequencies from  $10^{-3}$  to 77 kHz without the use of time-temperature superposition. They used this set of devices to characterize an aqueous suspension of thermosensitive latex particles over the same range of frequencies.

**B. Nonsinusoidal deformation**

Nelson and Dealy [30] describe a number of nonsinusoidal waveforms that have been used for linear viscoelastic characterization, including multiple, superposed sine waves, an equistrain waveform designed to generate a uniform strain amplitude across a given band of frequencies, and a pseudorandom binary sequence. The advantage of this approach is that by use of a fast Fourier transform (FFT) program one can obtain results over a range of several decades of frequency in a single test. Nelson and Dealy [30] discussed several problems that arise in the use of the discrete Fourier transform to analyze the results.

Field *et al.* [18] employed pseudorandom squeezing in the device sketched in Fig. 5. A FFT is used to extract the frequency-dependent moduli. A characterization over two decades of frequency is obtained in a very short time.

A commercial version of this instrument is called the micro-Fourier rheometer (MFR), because it can deal with samples as small as 100  $\mu$ l. Figure 6 is a photo of this device.

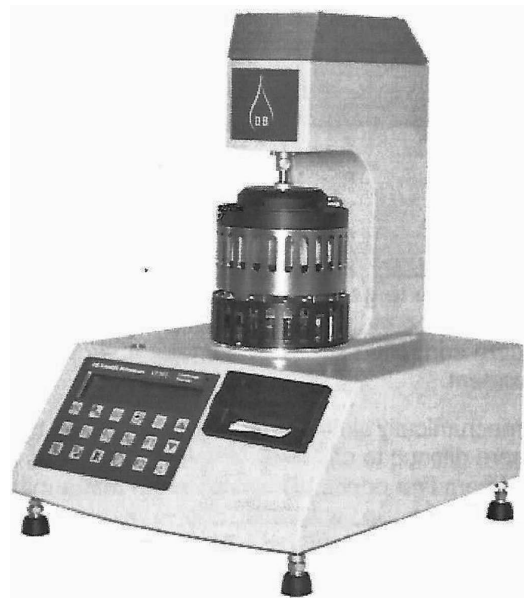


FIG. 4. Photo of the CP20 compressional rheometer.

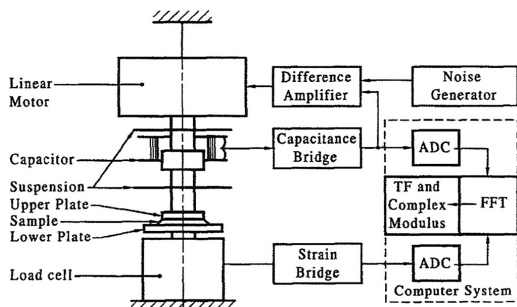


FIG. 5. Essential elements of the MFR of Field *et al.* [18].

The input is random noise of amplitude  $n$  as shown below, where  $\varepsilon \ll 1$

$$h(t) = H_0[1 + \varepsilon n(t)] = H_0 + h'(t). \quad (70)$$

The noise is described by its spectral representation [31]

$$n(t) = \int_{-\infty}^{\infty} e^{i\omega t} dZ(\omega), \quad (71)$$

where  $dZ(\omega)$  is a random function with zero means and a known correlation.

Phan-Thien *et al.* [20] examined the effects of inertia on the operation of this instrument. Because a complete characterization can be carried out quickly, the MFR can be used to track rapid changes in properties. This device has been used, for example, to study particle suspensions [32] and dental composite resins [33].

Sakai [34] modified a MFR for use with fluids employed in the manufacture of micromechanical electric systems. Of special interest here are interactions between dispersed particles and dissolved polymers. The fluid response is primarily

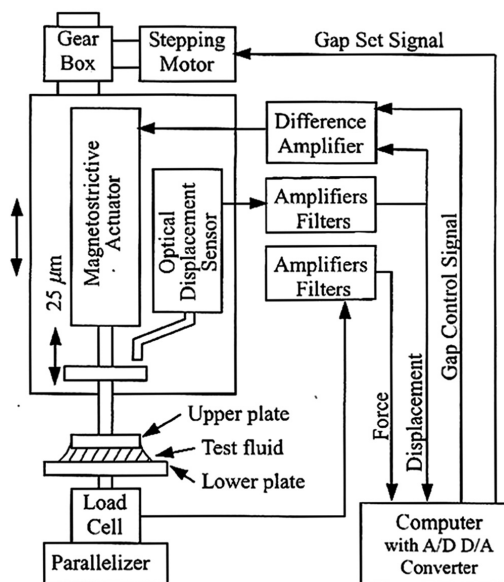


FIG. 7. The MFR of Sakai [34].

viscous, but elasticity is still important, and a major challenge is detecting the very small phase angle of the response to oscillatory squeezing. Figure 7 shows this apparatus, in which the amplitude of the deformation is only  $25 \mu\text{m}$ .

Another device based on the same basic principle was designed for quality assurance in manufacturing processes [35–37].<sup>2</sup> It measures the state of a fluid while it is in process, either in an in-line or side-stream installation.

### C. Filament stretching rheometer

The filament stretching rheometer (FSR) was originally developed for the characterization of polymeric liquids in a nonlinear uniaxial extension [38,39]. It is similar to OSF instruments in the sense that it consists of a top plate and a bottom plate between which the sample is placed. As shown in Fig. 8, the top plate moves in an axial direction while the bottom plate remains fixed and is mounted on a strain-gauge load cell.

The major difference between OSF instruments described above and the FSR is that in the latter the deformation is not measured from the position of the top plate but across the sample midplane using a laser-sheet. Whereas the aspect ratio is about unity, it is very small in the OSF devices described in Secs. III A and III B. For use in OSF, the top-plate undergoes oscillatory displacement to impose a sinusoidal compression on the sample, but in the FSR, a laser moves in-phase at half the speed of the top plate, in order to



FIG. 6. Photo of the MFR2100 MFR of GBC scientific equipment.

<sup>2</sup>Commercial version available from Rheology Solutions, Bacchus Marsh, VIC, Australia, [www.rheologysolutions.com](http://www.rheologysolutions.com)

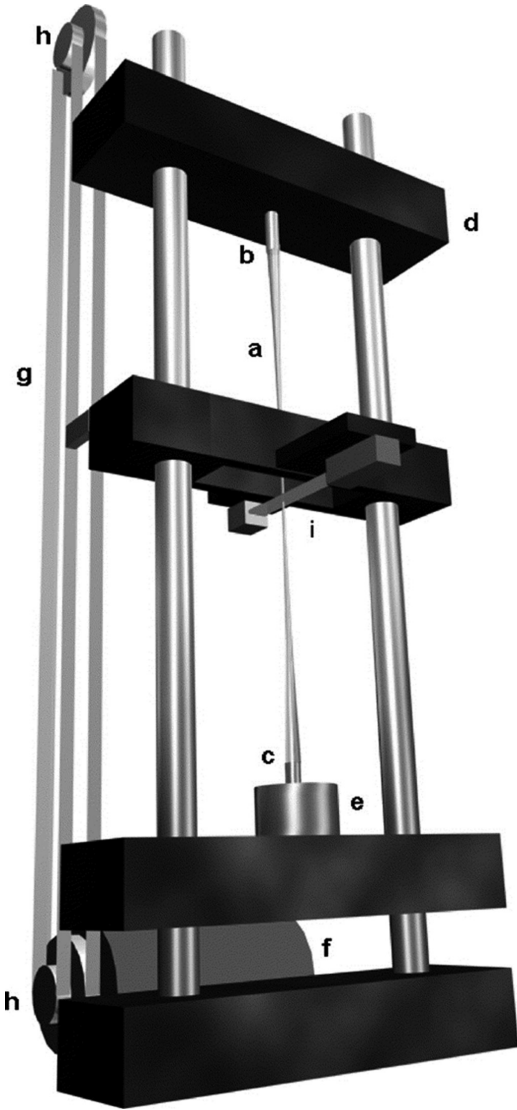


FIG. 8. Sketch of the FSR figures for uniaxial extension. (a) The filament, (b) top plate, (c) bottom plate, (d) top plate support, (e) force transducer, (f) motor, (g) belts, (h) gearing, and (i) laser micrometer [39].

remain at the level of the sample midplane. The relation between the top plate position,  $H(t)$ , and the sample diameter at the midplane, which is  $D = D_0(1 + b \sin \omega t)$  with  $bD_0$  being the amplitude [3], is given by

$$\frac{\dot{H}}{H_0} = -\frac{4}{3} \frac{1}{D_0} \frac{dD}{dt}, \quad (72)$$

$$\Rightarrow b = -\frac{3}{4}a. \quad (73)$$

This relation can simply be substituted into, e.g., Eq. (43) to give  $F$  as a function of deformation across the midplane rather than the top plate

$$F = -\frac{2\pi b R_0^4}{H_0^2} (G' \sin \omega t + G'' \cos \omega t) \left[ 1 + 2 \left( \frac{H_0}{R_0} \right)^2 \right]. \quad (74)$$

This way of measuring deformation overcomes the problem of load cell compliance.

Using the FSR for linear characterization enables linear oscillatory and nonlinear uniaxial characterization using a single instrument with a single sample. More specifically, uniaxial extension can be performed directly after linear characterization. As the aspect ratio ( $\Lambda$ ) of the samples that are used for uniaxial extension in the FSR are much higher ( $\Lambda \approx 1$ ) compared to other OSF techniques, a significant extensional contribution to the stress will be present. Consequently, the lubrication approximation cannot be used. In many cases, Eq. (43) will be sufficient as inertia is rarely a factor with the very viscous fluids characterized in uniaxial extension using the FSR.

At the present time, the FSR in the OSF mode has been used to study only one set of polystyrene melts [40]. Figure 9 shows dynamic moduli data obtained using both the FSR and an Ares G2 for a commercial polystyrene with  $M_w = 230$  kg/mol (PS-230k). Data from the two instruments agree very well, although there is a small vertical shift between the two sets of data.

## IV. APPLICATIONS

### A. Polymer melts and solutions

Polymer melts and solutions have been used in several studies to test OSF technique. One advantage of using polymeric liquids is that inertial effects can be brought out or suppressed as desired due to the high degree of rheological tunability that these materials offer. This approach was employed by [22] to investigate fluids in which inertia was

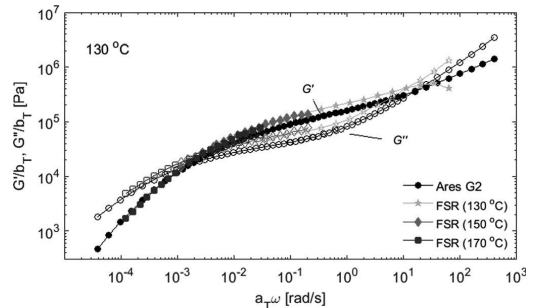


FIG. 9.  $G'$  (closed symbols) and  $G''$  (open symbols) of a commercial PS-230K at 130 °C. Data points obtained using the FSR [Eq. (74)] at various temperatures that has been shifted to 130 °C using shift factors  $a_T$  and  $b_T$ , respectively. Diamonds: FSR (150 °C); Stars: FSR (150 °C); Squares: FSR (170 °C). Circles show data obtained using a commercial torsional Ares G2 rheometer [40].

negligible and fluids for which inertial corrections to the 1st or 2nd order were needed.

Bulk polymers usually have very high viscosities and are thus useful to verify Eqs. (43) and (45), in which inertial effects are neglected. Figure 10 shows storage and loss moduli of a highly viscous polydimethyl sulfate measured using a conventional torsional rheometer (AR 2000) and an OSF rheometer with several gap heights. The OSF results were calculated without correcting for inertia. As seen, the results between the two techniques are in very good agreement, which confirms that a correction for inertia is not needed for highly viscous fluids. Some concentrated polymer solutions, for example, the 30 wt. % polystyrene solution studied by Crassous *et al.* [29], were sufficiently viscous that an inertial correction was not required. In general, this makes characterization of thick fluids very simple and convenient, and OSF is an excellent means for characterization for such fluids. Bell *et al.* [22] showed that compared to a conventional torsional rheometer, one can operate at much higher  $Re$  in the OSF rheometer before a correction for inertia is required.

Several OSF-studies used a polymer solution called the “A1 fluid.” It is a thoroughly tested standard fluid [41] and was used both to validate the accuracy of the OSF rheometer and as a model material in numerical simulations to evaluate the influence of inertia and various boundary conditions [21,22]. The A1 fluid is a 2% (w/v) polyisobutylene solution in a mixture of *cis* and *trans* decalin. Dilution of polymers will normally lower the viscosity, and the inertial effects will become more significant but far from dominant. Results performed both on the A1 fluid and other polymer solutions

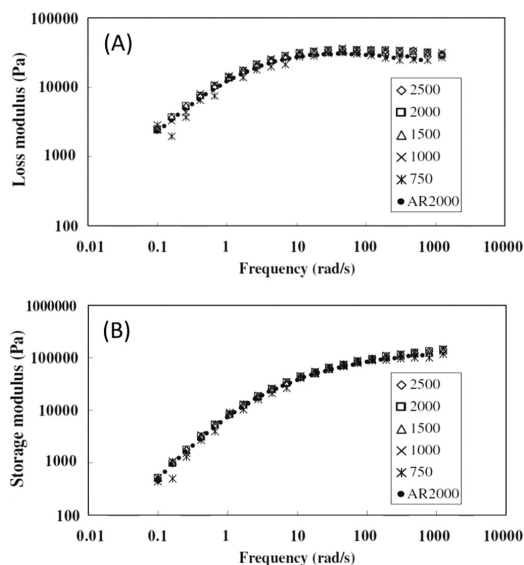


FIG. 10. Rheological characterization of a polydimethyl sulfate solution using the CP50 compressional rheometer; no inertial correction was applied [22]. Symbols indicate various gap heights in microns. (●) shows results obtained using a commercial torsional AR2000 rheometer. (A) The loss modulus and (B) the storage modulus.

such as hyaluronic acid in methylcellulose proved to be in very good agreement with data from commercial rheometers, and in all cases, only an inertial approximation to the 1st order was needed [20,28]. The only material for which a 2nd order inertial correction was needed was a 1% polyacrylamide solution in water [22]. This system was specifically designed to have a low viscosity in order to investigate the 2nd order inertia correction.

## B. Other materials

See *et al.* [32] used a MFR shown in Fig. 5 to study the behavior of a suspension of spheres in a polymeric liquid. Walberer and McHugh [28] used the CP-20 rheometer to study the effects of polymer molecular weight and filler content in a glass-bead-filled polydimethyl siloxane. See and Nguyen [42] used a prototype MFR to monitor the curing of an epoxy resin and a plastic putty. Peng and Zhu [43], See *et al.* [44], and Lee and Wen [45] used OSF to study the behavior of an electrorheological fluid, which they modeled as a Bingham plastic with continuous modification. Kuzhir *et al.* [46] studied a suspension of magnetic particles, and Jiang *et al.* [33] used a MFR to track the curing of dental composite resin cements. They found that the response was linear during the earlier stages of cure but became nonlinear at very small strain amplitude.

### 1. Large-amplitude squeeze flow

Kim and Ahn [47,48] studied combined oscillatory rotation and squeezing flow, which they called “dynamic helical squeeze flow” (DHSQ). They modified a Rheometric RMS800 rheometer to make it possible to do normal torsional flow, OSF, and combined DHSQ flow. In their 2012 paper, they compared the strain for the onset of nonlinear viscoelasticity for DHSQ and OSF for a polybutene with  $M_w = 920$  g/mol and found that the values were 0.02 and 1.0, respectively. The nonlinearities that arise at higher strains for both flows are not related to those observed in large-amplitude oscillatory shear in rotational instruments, as the deformations are quite different in the two flows.

## NOMENCLATURE

### Symbol

- $a$  Oscillation amplitude relative to the sample height, Eq. (6) (-)
- $b$  Oscillation amplitude relative to the sample diameter, Eq. (73) (-)
- $D$  Sample diameter  $2R$  (m)
- $D_0$  Mean sample diameter  $2R_0$  (m)
- $f$  Dimensionless complex function of  $\hat{z}$ , Eqs. (21) and (22) (-)
- $F$  Normal force exerted on a plane by a fluid, Fig. 1 ( $\text{kg m s}^{-2}$ )
- $\hat{f}_0$  Dimensionless complex function of  $\hat{z}$  in the perturbation solution ( $f$ ), contributing an order  $O(\text{Re}^0)$  to the full solution of  $f$ , Eq. (47) (-)

$F_0$  Constant compressive force exerted on a plane by a fluid ( $\text{kg m s}^{-2}$ )

$f_1$  Dimensionless complex function of  $\hat{z}$  in the perturbation solution ( $f$ ), contributing an order  $O(\text{Re}^{-1})$  to the full solution of  $f$ , Eq. (47) (-)

$F^*$  Complex function related to normal force  $F = \Re\{F^*\}$  ( $\text{kg m s}^{-2}$ )

$G^*$  Complex modulus  $G' + iG''$  (Pa)

$G'$  Storage modulus (Pa)

$G''$  Loss modulus (Pa)

$H$  Sample height Fig. 1 (m)

$\dot{H}$  Speed of the top plate  $dH/dt$  ( $\text{m s}^{-1}$ )

$H_0$  Initial sample height Fig. 1 (m)

$H^*$  Complex function related to sample height  $H = \Re\{H^*\}$  (m)

$i$  Imaginary unit  $\sqrt{-1}$  (-)

$m$  Flow consistency index for a power law fluid, Eq. (5) ( $\text{Pa s}^n$ )

$M_w$  Weight average molar mass ( $\text{kg mol}^{-1}$ )

$n$  Power law exponent of a power law fluid, Eq. (5) (-)

$O$  Order of magnitude indication, Eq. (47) (-)

$p$  Isotropic compressive stress (pressure) (Pa)

$p_{\text{atm}}$  Atmospheric pressure (Pa)

$\bar{p}$  Complex function related to pressure, Eq. (9) (Pa)

$\hat{p}$  Dimensionless complex function related to pressure, Eq. (15) (-)

$\hat{p}_0, \hat{p}_1$  Dimensionless complex integration constants for pressure, Eqs. (33) and (60) (-)

$(r, \theta, z)$  Cylindrical coordinates  $[(m, -, m)]$

$R$  Sample radius Fig. 1 (m)

$(\hat{r}, \hat{\theta}, \hat{z})$  Nondimensional cylindrical coordinates  $(r/R_0, \theta, z/H_0) [(-, -, -)]$

$R_0$  Mean sample radius  $\int_0^\infty R(t)dt / \int_0^\infty dt$  (m)

$\text{Re}$  Complex Reynolds number  $i\rho\omega H_0^2/\eta^*$  (-)

$t$  Time (s)

$T$  Temperature ( $K$ )/( $C$ )

$\mathbf{v}$  Velocity vector  $\partial\mathbf{x}/\partial t$  ( $\text{m s}^{-1}$ )

$V$  Sample volume ( $\text{m}^3$ )

$\bar{\mathbf{v}}$  Complex function related to velocity vector, Eq. (8) ( $\text{m s}^{-1}$ )

$\hat{\mathbf{v}}$  Dimensionless complex function related to velocity, Eqs. (13) and (14) (-)

$v_s$  Slip velocity at the wall  $v_r(z=0)$  or  $v_r(z=H)$  ( $\text{m s}^{-1}$ )

$\mathbf{x}$  Position vector

$\hat{\mathbf{x}}$  Nondimensional position vector

$\beta$  Slip coefficient, Eq. (69) ( $\text{m}^2/\text{kg}$ )

$\gamma$  Shear strain, Eq. (68) (-)

$\dot{\gamma}_{rz}$  Shear rate  $\partial v_r/\partial z$  ( $\text{s}^{-1}$ )

$\eta$  Newtonian viscosity  $\sigma/\dot{\gamma}$  (Pa s)

$\eta^*$  Complex viscosity  $(G'' - iG')/\omega$  (Pa s)

$\Lambda$  Aspect ratio of the sample  $H_0/R_0$  (-)

$\rho$  Density of the fluid ( $\text{kg m}^{-3}$ )

$\sigma$  Extra stress tensor (Pa)

$\hat{\sigma}$  Dimensionless complex stress tensor, Eqs. (29) and (30) (-)

$\phi_V$  Viscous dissipation term, Eq. (40) ( $\text{s}^{-2}$ )

$\omega$  Oscillation frequency of the top plate ( $\text{rad/s}^{-1}$ )

References

[1] Engmann, J., C. Servais, and A. S. Burbidge, "Squeeze flow theory and applications to rheometry: A review," *J. Non-Newtonian Fluid Mech.* **132**, 1–27 (2005).

[2] *Standard Test Method for Apparent Viscosity (Flow) of Roofing Bitumens Using Parallel Plate Plastometer*, American Society for Testing and Materials, West Conshocken, PA (2014).

[3] Bird, R. B., R. C. Armstrong, and O. Hassager, *Dynamics of Polymeric Liquids. Vol. 1: Fluid Mechanics*, 2nd ed. (John Wiley, New York, 1987).

[4] Dienes, G. J., and H. F. Klemm, "Theory and applications of parallel plate plastometer," *J. Appl. Phys.* **17**, 458–471 (1946).

[5] Gent, A. N., "Theory of the parallel plate viscometer," *Br. J. Appl. Phys.* **11**, 85–87 (1960).

[6] Gibson, A. G., G. Kotsikos, J. H. Bland, and S. Toll, "Squeeze flow," in *Rheological Measurement*, 2nd ed. (Chapman and Hall, London, 1998), Chap. 18.

[7] Pham, H., and E. A. Meinecke, "Squeeze film rheology of polymer melts: Determination of the characteristic flow curve," *J. Appl. Polym. Sci.* **53**, 257–264 (1994).

[8] Pham, H., and E. A. Meinecke, "Squeeze film flow processability tester," *J. Appl. Polym. Sci.* **53**, 265–273 (1994).

[9] Shaw, M. T., "Melt characterization of ultra-high molecular weight polyethylene using squeeze flow," *Polym. Eng. Sci.* **17**, 266–268 (1977).

[10] Cua, E. C., and M. T. Shaw, "Using creeping squeeze flow to obtain low-frequency linear viscoelastic properties: Low-shear rate measurements on polydimethylsiloxane," *J. Rheol.* **46**, 817–830 (2002).

[11] Chatraei, S. H., C. W. Macosko, and H. H. Winter, "Lubricated squeeze flow: A new biaxial extensional rheometer," *J. Rheol.* **25**, 433–443 (1981).

[12] Nishioka, A., Y. Takagi, T. Takahashi, Y. Masubuchi, J. Takimoto, and K. Koyama, "Measurement of biaxial elongational viscosity of polymer melts using lubricated squeezing flow method," *J. Soc. Mater. Sci. Jpn.* **47**, 1296–1300 (1998).

[13] Kompani, M., and D. C. Venerus, "Equibiaxial extensional flow of polymer melts via lubricated squeezing flow I. Experimental analysis," *Rheol. Acta* **39**, 444–451 (2000).

[14] Guaderama-Medina, T., T.-Y. Shiu, and D. C. Venerus, "Direct comparison of equibiaxial elongational viscosity measurements and the multiaxial dehrheometer," *Rheol. Acta* **48**, 11–17 (2009).

[15] Hachmann, P., and J. Meissner, "Rheometer for equibiaxial and planar elongations of polymer melts," *J. Rheol.* **47**, 989–1010 (2003).

[16] Pipkin, A. C., *Lectures on Viscoelasticity Theory* (Springer, Berlin, 1972).

[17] Phan-Thien, N., "Small strain oscillatory squeeze film flow of simple fluids," *J. Aust. Math. Soc. (B)* **22**, 22–37 (1980).

[18] Field J. S., M. V. Swain, and N. Phan-Thien, "An experimental investigation of the use of random squeezing to determine the complex modulus of viscoelastic fluids," *J. Non-Newtonian Fluid Mech.* **65**, 177–194 (1996).

[19] Konigsberg, D., T. M. Nicholson, P. J. Halley, and K. H. Ahn, "Technical note: Correcting for shear strain in an oscillatory squeeze flow rheometer," *Rheol. Acta* **53**, 103–107 (2014).

[20] Phan-Tien, N., J. S. Field, and M. V. Swain, "Micro-Fourier rheometer: Inertial effects," *Rheol. Acta* **35**, 410–416 (1996).

[21] Debbaut, B., and K. Thomas, "Simulation and analysis of oscillatory squeeze flow," *J. Non-Newtonian Fluid Mech.* **124**, 77–91 (2004).

[22] Bell, D., D. M. Binding, and K. Walters, "The oscillatory squeeze flow rheometer: Comprehensive theory and a new experimental facility," *Rheol. Acta* **46**, 111–121 (2006).

- [23] Bird, R. B., W. E. Stewart, and E. N. Lightfoot, *Transport Phenomena*, 2nd ed. (John Wiley, New York, 2007).
- [24] Laun, H. M., M. Rady, and O. Hassager, "Analytical solutions for squeeze flow with partial wall slip," *J. Non-Newtonian Fluid Mech.* **81**, 1–15 (1999).
- [25] Brindley, G., J. M. Davies, and K. Walters, "Elastic-viscous squeeze films. Part I," *J. Non-Newtonian Fluid Mech.* **1**, 19–37 (1976).
- [26] Whittingstall, P. R., and W. E. Van Arsdale, "A compressional rheometer for viscoelastic fluids," in 70th Annual Meeting, Society of Rheology, Monterrey, CA (1998).
- [27] Van Arsdale, W. E., and H. Motivala, "Device for determining viscoelastic properties of liquids and a method for use," U.S. patent 5,253,513 (1993).
- [28] Walberer, J. A., and A. J. McHugh, "The linear viscoelastic behavior of highly filled polymethylsiloxine measured in shear and compression," *J. Rheol.* **45**, 187–201 (2001).
- [29] Crassous, J. J., R. Régisser, M. Ballauff, and M. N. Willenbacher, "Characterization of the viscoelastic behavior of complex fluids using the piezoelastic axial vibrator," *J. Rheol.* **49**, 851–863 (2005).
- [30] Nelson, B. I., and J. M. Dealy, "Dynamic mechanical analysis using complex waveforms," in *Rheological Measurement*, 2nd ed. (Chapman and Hall, London, 1998), Chap. 4.
- [31] Yaglom, A. M., *An Introduction to the Theory of Stationary Random Functions* (Prentice Hall, Englewood Cliffs, NJ, 1965).
- [32] See, H., P. Jiang, and N. Phan-Tien, "Concentration dependence of the linear viscoelastic properties of particle suspensions," *Rheol. Acta* **39**, 131–137 (2000).
- [33] Jiang, P., H. See, M. V. Swain, and N. Phan-Thien, "Using oscillatory flow to measure the viscoelastic properties of dental composite resins during curing," *Rheol. Acta* **42**, 118–122 (2003).
- [34] Sakai, S., "Improvements of an oscillatory squeezing flow rheometer for small elasticity measurements of liquids," *Rheol. Acta* **44**, 16–28 (2004).
- [35] Konigsberg, D., T. M. Nicholson, P. J. Halley, T. J. Kealy, and P. K. Bhattacharjee, "Online process rheometry using oscillatory squeeze flow," *Appl. Rheol.* **23**(3), 35688-1–35688-10 (2013).
- [36] Konigsberg, D., *The rheology and fluid mechanics of oscillatory squeeze flow*, Doctoral thesis, University of Queensland, St Lucia, Australia, 2014.
- [37] Kealy, T., and P. Bhattacharaya, "On-line rheological measurements for industrial process monitoring and control of complex fluids," in Annual European Rheology Conference, 2014.
- [38] Bach, A., H. K. Rasmussen, P.-Y. Longin, and O. Hassager, "Growth of non-axisymmetric disturbances of the free surface in the filament stretching rheometer: Experiments and simulation," *J. Non-Newtonian Fluid Mech.* **108**, 163–186 (2002).
- [39] Román Marín, J. M., J. K. Huusom, N. J. Alvarez, Q. Huang, H. K. Rasmussen, A. Bach, A. L. Skov, and O. Hassager, "A control scheme for filament stretching rheometers with application to polymer melts," *J. Non-Newtonian Fluid Mech.* **194**, 14–22 (2013).
- [40] Wingstrand, S. L., N. J. Alvarez, and O. Hassager, "Linear viscoelastic characterization from filament stretching rheometry," Annual European Rheology Conference, Nantes, France, 2015.
- [41] Hudson, N. E., and T. E. R. Jones, "The A1 project—An overview," *J. Non-Newtonian Fluid Mech.* **46**, 69–88 (1993).
- [42] See, H., and P. Nguyen, "Using oscillatory squeeze flow to monitor the change in viscoelastic properties of curing materials," *Nihon Reorji Gakkaishi (J. Soc. Rheol., Japan)* **32**, 33–39 (2004).
- [43] Peng, J., and K.-Q. Zhu, "Oscillatory squeeze flow of electrorheological fluid with transitional electric field," *Int. J. Mod. Phys. B* **19**, 1249–1255 (2005).
- [44] See, H., J. S. Field, and B. Pfister, "The response of electrorheological fluid under oscillatory squeeze flow," *J. Non-Newtonian Fluid Mech.* **84**, 149–158 (1999).
- [45] Lee, C. Y., and C. Y. Wen, "The oscillatory squeeze flow of electrorheological fluid considering the inertia effect," *Smart Mater. Struct.* **11**, 553–560 (2002).
- [46] Kuzhir, P., M. T. López-López, G. Vertelov, Ch. Pradille, and G. Bossis, "Oscillatory squeeze flow of suspensions of magnetic polymerized chains," *J. Phys.: Condens. Matter* **20**, 204132 (2008).
- [47] Kim, J. H., and K. H. Ahn, "A new instrument for dynamical helical squeeze flow which superposes oscillatory shear and squeeze flow," *Rev. Sci. Instrum.* **83**, 085105 (2012).
- [48] Kim, J. H., and K. H. Ahn, "Rheological characteristics of poly(ethylene oxide) aqueous solutions under large amplitude oscillatory squeeze flow," *Korea-Aust. Rheol. J.* **24**, 257–266 (2012).



# Bibliography

---

- [1] W. Kauzmann and H. Eyring. The Viscous Flow of Large Molecules. *Journal of the American Chemical Society*, 62(11):3113–3125, 1940.
- [2] P. E. Rouse. A Theory of the Linear Viscoelastic Properties of Dilute Solutions of Coiling Polymers. *The Journal of Chemical Physics*, 21(7):1272, 1953.
- [3] H. Menke. Rouse vs. Zimm Regime: Hydrodynamic Interactions. <https://www.henrimenke.com/documents/hs-theo-handout.pdf>, 2015. Accessed: 2017-05-15.
- [4] B. H. Zimm. Dynamics of Polymer Molecules in Dilute Solution: Viscoelasticity, Flow Birefringence and Dielectric Loss. *The Journal of Chemical Physics*, 24(2):269, 1956.
- [5] P. G. de Gennes. Reptation of a Polymer Chain in the Presence of Fixed Obstacles. *The Journal of Chemical Physics*, 55(2):572, 1971.
- [6] M. Doi and S. F. Edwards. *The theory of polymer dynamics*, volume 73. Oxford University Press, 2nd edition, 1988.
- [7] S. T. Milner and T. C. B. McLeish. Parameter-Free Theory for Stress Relaxation in Star Polymer Melts. *Macromolecules*, 30(7):2159–2166, 1997.
- [8] S. T. Milner. Reptation and Contour-Length Fluctuations in Melts of Linear Polymers. *Physical Review Letters*, 81(3):725–728, 1998.
- [9] E. V. Ruymbeke, C.-y. Liu, and C. Bailly. Quantitative tube model predictions for the linear viscoelasticity of linear polymers. *Rheology Reviews*, 2007:53–134, 2007.
- [10] A. E. Likhtman and T. C. B. McLeish. Quantitative Theory for Linear Dynamics of Linear Entangled Polymers. *Macromolecules*, 35(16):6332–6343, 2002.
- [11] V. Shchetnikava, J. J. M. Slot, and E. van Ruymbeke. A Comparison of Tube Model Predictions of the Linear Viscoelastic Behavior of Symmetric Star Polymer Melts. *Macromolecules*, 47(10):3350–3361, 2014.

- [12] E. van Ruymbeke, J. Nielsen, and O. Hassager. Linear and nonlinear viscoelastic properties of bidisperse linear polymers: Mixing law and tube pressure effect. *Journal of Rheology*, 54(5):1155–1172, 2010.
- [13] L. J. Fetters, D. J. Lohse, and R. H. Colby. Chain Dimensions and Entanglement Spacings. In *Physical Properties of Polymers*, chapter 25, page 1073. Springer, New York, 2nd edition, 2007.
- [14] M. Doi. *Introduction to polymer physics*. Oxford university press, Oxford, 1st edition, 1996.
- [15] H. Watanabe, Y. Matsumiya, and E. van Ruymbeke. Component Relaxation Times in Entangled Binary Blends of Linear Chains: Reptation/CLF along Partially or Fully Dilated Tube. *Macromolecules*, 46(23):9296–9312, 2013.
- [16] S. J. Park and R. G. Larson. Tube Dilation and Reptation in Binary Blends of Monodisperse Linear Polymers. *Macromolecules*, 37(2):597–604, 2004.
- [17] E. van Ruymbeke, R. Keunings, V. Stéphenne, A. Hagenaars, and C. Bailly. Evaluation of Reptation Models for Predicting the Linear Viscoelastic Properties of Entangled Linear Polymers. *Macromolecules*, 35(7):2689–2699, 2002.
- [18] J. M. Dealy. Weissenberg and Deborah Numbers - Their Definition and Use. *Rheology Bulletin*, 79(2):14, 2010.
- [19] R. Bird, R. C. Armstrong, and O. Hassanger. *Dynamics of polymeric liquids. Vol.1: fluid mechanics*. Wiley, 1987.
- [20] T. C. B. McLeish and R. G. Larson. Molecular constitutive equations for a class of branched polymers: The pom-pom polymer. *Journal of Rheology*, 42(1):81, 1998.
- [21] J. E. Mark. *Physical Properties of Polymers Handbook*. Springer, New York, 2nd edition, 2006.
- [22] C. R. López-Barrón, Y. Zeng, and J. J. Richards. Chain stretching and recoiling during startup and cessation of extensional flow of bidisperse polystyrene blends. *Journal of Rheology*, 61(4):697–710, 2017.
- [23] O. Hassager, K. Mortensen, A. Bach, K. Almdal, H. K. Rasmussen, and W. Pyckhout-Hintzen. Stress and neutron scattering measurements on linear polymer melts undergoing steady elongational flow. *Rheologica Acta*, 51(5):385–394, 2012.
- [24] D. Auhl, P. Chambon, T. McLeish, and D. Read. Elongational Flow of Blends of Long and Short Polymers: Effective Stretch Relaxation Time. *Physical Review Letters*, 103(13):136001, 2009.

- [25] M. H. Nafar Sefiddashti, B. J. Edwards, and B. Khomami. Individual chain dynamics of a polyethylene melt undergoing steady shear flow. *Journal of Rheology*, 59(1):119–153, 2014.
- [26] A. Bach, H. K. Rasmussen, P.-Y. Longin, and O. Hassager. Growth of non-axisymmetric disturbances of the free surface in the filament stretching rheometer: experiments and simulation. *Journal of Non-Newtonian Fluid Mechanics*, 108(1):163, 2002.
- [27] M. Sentmanat, B. N. Wang, and G. H. McKinley. Measuring the transient extensional rheology of polyethylene melts using the SER universal testing platform. *Journal of Rheology*, 49(3):585, 2005.
- [28] S. M. Fielding. Criterion for Extensional Necking Instability in Polymeric Fluids. *Phys. Rev. Lett.*, 107(25):258301, 2011.
- [29] D. M. Hoyle and S. M. Fielding. Criteria for extensional necking instability in complex fluids and soft solids. Part I: Imposed Hencky strain rate protocol. *Journal of Rheology*, 60(6):1347–1375, 2016.
- [30] D. M. Hoyle and S. M. Fielding. Criteria for extensional necking instability in complex fluids and soft solids. Part II: Imposed tensile stress and force protocols. *Journal of Rheology*, 60(6):1377–1397, 2016.
- [31] A. Bach, K. Almdal, H. K. Rasmussen, and O. Hassager. Elongational Viscosity of Narrow Molar Mass Distribution Polystyrene. *Macromolecules*, 36(14):5174–5179, 2003.
- [32] J. M. Román Marín, J. K. Huusom, N. J. Alvarez, Q. Huang, H. K. Rasmussen, A. Bach, A. L. Skov, and O. Hassager. A control scheme for filament stretching rheometers with application to polymer melts. *Journal of Non-Newtonian Fluid Mechanics*, 194:14–22, 2013.
- [33] P. Szabo. Transient filament stretching rheometer. *Rheologica Acta*, 36(3):277, 1997.
- [34] H. K. Rasmussen, A. G. Bejenariu, O. Hassager, and D. Auhl. Experimental evaluation of the pure configurational stress assumption in the flow dynamics of entangled polymer melts. *Journal of Rheology*, 54(6):1325, 2010.
- [35] Filament stretching rheometer - product details. <http://rheofilament.com>. Accessed: 2017-02-12.
- [36] H. Janeschitz-Kriegl. *Crystallization Modalities in Polymer Melt Processing*. Springer Vienna, Vienna, 2010.
- [37] P. C. Roozmond and G. W. M. Peters. Flow-enhanced nucleation of poly(1-butene): Model application to short-term and continuous shear and extensional flow. *Journal of Rheology*, 57(6):1633–1653, 2013.

- [38] A. Keller and H. W. H. Kolnaar. *Flow-induced orientation and structure formation*, volume 17, pages 187 – 268. VCH Verlagsgesellschaft mbH, Weinheim, 1997.
- [39] S. Mitsuhashi. On Polyethylene crystals grown from flowing solutions in xylene. *Bull. Text. Res. Inst. Jpn*, 66:1–10, 1963.
- [40] H. D. Keith and J. F. Padden. Spherulite crystallization in polypropylene. *Journal of Applied Physics*, 30(10), 1959.
- [41] B. S. Hsiao, L. Yang, R. H. Somani, C. A. Avila-Orta, and L. Zhu. Unexpected Shish-Kebab Structure in a Sheared Polyethylene Melt. *Physical Review Letters*, 94(11):117802, 2005.
- [42] M. Seki, D. W. Thurman, J. P. Oberhauser, and J. A. Kornfield. Shear-Mediated Crystallization of Isotactic Polypropylene: The Role of Long Chain-Long Chain Overlap. *Macromolecules*, 35(7):2583–2594, 2002.
- [43] M. van Drongelen, D. Cavallo, L. Balzano, G. Portale, I. Vittorias, W. Bras, G. C. Alfonso, and G. W. M. Peters. Structure Development of Low-Density Polyethylenes During Film Blowing: A Real-Time Wide-Angle X-ray Diffraction Study. *Macromolecular Materials and Engineering*, 299(12):1494–1512, 2014.
- [44] L. Balzano, N. Kukalyekar, S. Rastogi, G. W. M. Peters, and J. C. Chadwick. Crystallization and Dissolution of Flow-Induced Precursors. *Physical Review Letters*, 100(4):048302, 2008.
- [45] J.-W. Housmans, R. J. A. Steenbakkers, P. C. Roozmond, G. W. M. Peters, and H. E. H. Meijer. Saturation of Pointlike Nuclei and the Transition to Oriented Structures in Flow-Induced Crystallization of Isotactic Polypropylene. *Macromolecules*, 42(15):5728–5740, 2009.
- [46] G. W. M. Peters, L. Balzano, and R. J. A. Steenbakkers. Flow-Induced Crystallization. In *Handbook of Polymer Crystallization*, pages 399–432. John Wiley & Sons, Inc., New Jersey, 1st edition, 2013.
- [47] G. Eder, H. Janeschitz-Kriegl, and S. Liedauer. Crystallization processes in quiescent and moving polymer melts under heat transfer conditions. *Progress in Polymer Science*, 15(4):629–714, 1990.
- [48] H. E. H. Meijer. *Materials Science and Technology, Processing of Polymers*. Materials Science and Technology. Wiley, 11th edition, 1997.
- [49] S. Liedauer, G. Eder, H. Janeschitz-Kriegl, P. Jerschow, W. Geymayer, and E. Ingolic. On the Kinetics of Shear Induced Crystallization in Polypropylene. *International Polymer Processing*, 8(3):236–244, 1993.

- [50] J. A. Kornfield, G. Kumaraswamy, and A. M. Issaian. Recent Advances in Understanding Flow Effects on Polymer Crystallization. *Industrial & Engineering Chemistry Research*, 41:6383–6392, 2002.
- [51] B. A. G. Schrauwen, L. C. A. V. Breemen, A. B. Spoelstra, L. E. Govaert, G. W. M. Peters, and H. E. H. Meijer. Structure, deformation, and failure of flow-oriented semicrystalline polymers. *Macromolecules*, 37(23):8618–8633, 2004.
- [52] R. S. Graham and P. D. Olmsted. Coarse-Grained Simulations of Flow-Induced Nucleation in Semicrystalline Polymers. *Physical Review Letters*, 103(11):1–4, 2009.
- [53] E. E. B. White, H. H. Winter, and J. P. Rothstein. Extensional-flow-induced crystallization of isotactic polypropylene. *Rheologica Acta*, 51(4):303, 2012.
- [54] C. Hadinata, D. Boos, C. Gabriel, E. Wassner, M. Rüllmann, N. Kao, and M. Laun. Elongation-induced crystallization of a high molecular weight isotactic polybutene-1 melt compared to shear-induced crystallization. *Journal of Rheology*, 51(2), 2007.
- [55] K. Cui, L. Meng, N. Tian, W. Zhou, Y. Liu, Z. Wang, J. He, and L. Li. Self-Acceleration of Nucleation and Formation of Shish in Extension-Induced Crystallization with Strain Beyond Fracture. *Macromolecules*, 45(13):5477–5486, 2012.
- [56] M. Derakhshandeh and S. G. Hatzikiriakos. Flow-induced crystallization of high-density polyethylene: The effects of shear and uniaxial extension. *Rheologica Acta*, 51(4):315–327, 2012.
- [57] G. Ianniruberto, A. Brasiello, and G. Marrucci. Simulations of Fast Shear Flows of PS Oligomers Confirm Monomeric Friction Reduction in Fast Elongational Flows of Monodisperse PS Melts As Indicated by Rheo-optical Data. *Macromolecules*, 45(19):8058–8066, 2012.
- [58] L. Hengeller, Q. Huang, A. Dorokhin, N. J. Alvarez, K. Almdal, and O. Hassager. Stress relaxation of bi-disperse polystyrene melts Exploring the interactions between long and short chains in non-linear rheology. *Rheologica Acta*, 55:303–314, 2016.
- [59] D. J. Read, D. Auhl, C. Das, J. den Doelder, M. Kapnistos, I. Vittorias, and T. C. B. McLeish. Linking Models of Polymerization and Dynamics to Predict Branched Polymer Structure and Flow. *Science*, 333(6051):1871–1874, 2011.
- [60] M. W. Collis, A. K. Lele, M. R. Mackley, R. S. Graham, D. J. Groves, A. E. Likhtman, T. M. Nicholson, O. G. Harlen, T. C. B. McLeish, L. R. Hutchings, C. M. Fernyhough, and R. N. Young. Constriction flows of monodisperse linear

- entangled polymers: Multiscale modeling and flow visualization. *Journal of Rheology*, 49(2):501–522, 2005.
- [61] Q. Huang, O. Mednova, H. K. Rasmussen, N. J. Alvarez, A. L. Skov, K. Almdal, and O. Hassager. Concentrated Polymer Solutions are Different from Melts: Role of Entanglement Molecular Weight. *Macromolecules*, 46(12):5026–5035, 2013.
- [62] Q. Huang, N. J. Alvarez, Y. Matsumiya, H. K. Rasmussen, H. Watanabe, and O. Hassager. Extensional Rheology of Entangled Polystyrene Solutions Suggests Importance of Nematic Interactions. *ACS Macro Letters*, 2(8):741–744, 2013.
- [63] T. Sridhar, M. Acharya, D. A. Nguyen, and P. K. Bhattacharjee. On the Extensional Rheology of Polymer Melts and Concentrated Solutions. *Macromolecules*, 47(1):379–386, 2014.
- [64] C. Luap, C. Müller, T. Schweizer, and D. C. Venerus. Simultaneous stress and birefringence measurements during uniaxial elongation of polystyrene melts with narrow molecular weight distribution. *Rheologica Acta*, 45(1):83, 2005.
- [65] J. Fang, M. Kröger, and H. C. Öttinger. A thermodynamically admissible reptation model for fast flows of entangled polymers. II. Model predictions for shear and extensional flows. *Journal of Rheology*, 44(6):1293, 2000.
- [66] H. K. Rasmussen and Q. Huang. The missing link between the extensional dynamics of polymer melts and solutions. *Journal of Non-Newtonian Fluid Mechanics*, 204:1–6, 2014.
- [67] T. Yaoita, T. Isaki, Y. Masubuchi, H. Watanabe, G. Ianniruberto, and G. Marrucci. Primitive Chain Network Simulation of Elongational Flows of Entangled Linear Chains: Role of Finite Chain Extensibility. *Macromolecules*, 44(24):9675–9682, 2011.
- [68] R. S. Graham, A. E. Likhtman, T. C. B. McLeish, and S. T. Milner. Microscopic theory of linear, entangled polymer chains under rapid deformation including chain stretch and convective constraint release. *Journal of Rheology*, 47(5):1171–1200, 2003.
- [69] D. J. Read, K. Jagannathan, S. K. Sukumaran, and D. Auhl. A full-chain constitutive model for bidisperse blends of linear polymers. *Journal of Rheology*, 56(4):823–873, 2012.
- [70] E. van Ruymbeke, Y. Masubuchi, and H. Watanabe. Effective Value of the Dynamic Dilution Exponent in Bidisperse Linear Polymers: From 1 to  $4/3$ . *Macromolecules*, 45(4):2085–2098, 2012.

- [71] T. Yaoita, T. Isaki, Y. Masubuchi, H. Watanabe, G. Ianniruberto, and G. Marrucci. Primitive Chain Network Simulation of Elongational Flows of Entangled Linear Chains: Stretch/Orientation-induced Reduction of Monomeric Friction. *Macromolecules*, 45(6):2773–2782, 2012.
- [72] Values differ between the two PMMAs due to a difference in tacticity [73].
- [73] K. Fuchs, C. Friedrich, and J. Weese. Viscoelastic Properties of Narrow-Distribution Poly(methyl methacrylates). *Macromolecules*, 29(18):5893–5901, 1996.
- [74] J. K. Nielsen, H. K. Rasmussen, O. Hassager, and G. H. McKinley. Elongational viscosity of monodisperse and bidisperse polystyrene melts. *Journal of Rheology*, 50(4):453–476, 2006.
- [75] M. Baumgaertel, A. Schausberger, and H. H. Winter. The relaxation of polymers with linear flexible chains of uniform length. *Rheologica Acta*, 29(5):400–408, 1990.
- [76] R. G. Larson. Going with the Flow. *Science*, 318(5847):57 – 58, 2007.
- [77] K. Horio, T. Uneyama, Y. Matsumiya, Y. Masubuchi, and H. Watanabe. Rheo-Dielectric Responses of Entangled cis-Polyisoprene under Uniform Steady Shear and LAOS. *Macromolecules*, 47(1):246–255, 2014.
- [78] A. Blanchard, R. S. Graham, M. Heinrich, W. Pyckhout-Hintzen, D. Richter, A. E. Likhtman, T. C. B. McLeish, D. J. Read, E. Straube, and J. Kohlbrecher. Small Angle Neutron Scattering Observation of Chain Retraction after a Large Step Deformation. *Phys. Rev. Lett.*, 95(16):166001, 2005.
- [79] S. Costeux, P. Wood-Adams, and D. Beigzadeh. Molecular Structure of Metallocene-Catalyzed Polyethylene: Rheologically Relevant Representation of Branching Architecture in Single Catalyst and Blended Systems. *Macromolecules*, 35(7):2514–2528, 2002.
- [80] Y. An, J. J. Holt, G. R. Mitchell, and A. S. Vaughan. Influence of molecular composition on the development of microstructure from sheared polyethylene melts: Molecular and lamellar templating. *Polymer*, 47(15):5643–5656, 2006.
- [81] F. Bustos, P. Cassagnau, and R. Fulchiron. Effect of molecular architecture on quiescent and shear-induced crystallization of polyethylene. *Journal of Polymer Science Part B: Polymer Physics*, 44(11):1597–1607, 2006.
- [82] J. Kornfield. Interplay of macromolecular architecture and flow in polymer crystallization. In *American Chemical Society National Meeting & Exposition*, San Diego, 2016.

- [83] C. A. Sperati, W. A. Franta, and H. W. Starkweather. The Molecular Structure of Polyethylene. V. The Effect of Chain Branching and Molecular Weight on Physical Properties. *Journal of the American Chemical Society*, 75(24):6127–6133, 1953.
- [84] C. Das, N. J. Inkson, D. J. Read, M. a. Kelmanson, and T. C. B. McLeish. Computational linear rheology of general branch-on-branch polymers. *Journal of Rheology*, 50(2):207, 2006.
- [85] H. K. Rasmussen, J. K. Nielsen, A. Bach, and O. Hassager. Viscosity overshoot in the start-up of uniaxial elongation of low density polyethylene melts. *Journal of Rheology*, 49(2):369, 2005.
- [86] Q. Huang, L. Hengeller, N. J. Alvarez, and O. Hassager. Bridging the Gap between Polymer Melts and Solutions in Extensional Rheology. *Macromolecules*, 48(12):4158–4163, 2015.
- [87] L. G. D. Hawke, Q. Huang, O. Hassager, and D. J. Read. Modifying the pom-pom model for extensional viscosity overshoots. *Journal of Rheology*, 59(4):995–1017, 2015.
- [88] T. I. Burghilea, Z. Starý, and H. Münstedt. On the "viscosity overshoot" during the uniaxial extension of a low density polyethylene. *Journal of Non-Newtonian Fluid Mechanics*, 166(19-20):1198–1209, 2011.
- [89] H. K. Rasmussen and O. Hassager. Reply to: 'On the "viscosity overshoot" during the uniaxial extension of a low density polyethylene'. *Journal of Non-Newtonian Fluid Mechanics*, 171-172:106, 2012.
- [90] T. I. Burghilea, Z. Sary, and H. Munstedt. Response to the "Reply to: 'On the "viscosity overshoot" during the uniaxial extension of a low density polyethylene' by Rasmussen et al.". *Journal of Non-Newtonian Fluid Mechanics*, 171-172:107–108, 2012.
- [91] Q. Huang, H. K. Rasmussen, A. L. Skov, and O. Hassager. Stress relaxation and reversed flow of low-density polyethylene melts following uniaxial extension. *Journal of Rheology*, 56(6):1535, 2012.
- [92] N. J. Alvarez, J. M. R. Marín, Q. Huang, M. L. Michelsen, and O. Hassager. Creep Measurements Confirm Steady Flow after Stress Maximum in Extension of Branched Polymer Melts. *Physical Review Letters*, 110(16):168301, 2013.
- [93] D. G. Hassell, D. Hoyle, D. Auhl, O. Harlen, M. R. Mackley, and T. C. B. McLeish. Effect of branching in cross-slot flow: The formation of "W cusps". *Rheologica Acta*, 48(5):551–561, 2009.

- [94] D. M. Hoyle, Q. Huang, D. Auhl, D. Hassell, H. K. Rasmussen, A. L. Skov, O. G. Harlen, O. Hassager, and T. C. B. McLeish. Transient overshoot extensional rheology of long-chain branched polyethylenes: Experimental and numerical comparisons between filament stretching and cross-slot flow. *Journal of Rheology*, 57(1):293, 2013.
- [95] R. J. A. Steenbakkens, G. W. M. Peters, and H. E. H. Meijer. Rheological Modeling of Flow Induced Crystallization in Polymer Melts and Limitations on Classification of Experiments. *AIP Conference Proceedings*, 1027(1):493–495, 2008.
- [96] two samples are stretched below  $T_m$ .
- [97] T. B. van Erp, L. Balzano, A. B. Spoelstra, L. E. Govaert, and G. W. M. Peters. Quantification of non-isothermal, multi-phase crystallization of isotactic polypropylene: The influence of shear and pressure. *Polymer*, 53(25):5896–5908, 2012.
- [98] Q. Huang, N. J. Alvarez, A. Shabbir, and O. Hassager. Multiple Cracks Propagate Simultaneously in Polymer Liquids in Tension. *Phys. Rev. Lett.*, 117(8):87801, 2016.
- [99] J. Dealy and D. Plazek. Time-temperature superposition - a users guide. *Rheol. Bull*, 78(2):16–21, 2009.
- [100] S. Toki, I. Sics, C. Burger, D. Fang, L. Liu, B. S. Hsiao, S. Datta, and A. H. Tsou. Structure Evolution during Cyclic Deformation of an Elastic Propylene-Based Ethylene-Propylene Copolymer. *Macromolecules*, 39(10):3588–3597, 2006.
- [101] X. Zhang, S. Elkoun, A. Ajji, and M. Huneault. Oriented structure and anisotropy properties of polymer blown films: HDPE, LLDPE and LDPE. *Polymer*, 45(1):217–229, 2004.
- [102] J. K. Keum, C. Burger, F. Zuo, and B. S. Hsiao. Probing nucleation and growth behavior of twisted kebabs from shish scaffold in sheared polyethylene melts by in situ X-ray studies. *Polymer*, 48(15):4511–4519, 2007.
- [103] G. Marrucci. Fast flows of concentrated polymers - predictions of the tube model on chain stretching. *Gazzetta Chimica Italiana*, 118(3), 1988.
- [104] G. Marrucci and G. Ianniruberto. Interchain Pressure Effect in Extensional Flows of Entangled Polymer Melts. *Macromolecules*, 37(10):3934–3942, 2004.
- [105] N. J. Inkson, T. C. B. McLeish, O. G. Harlen, and D. J. Groves. Predicting low density polyethylene melt rheology in elongational and shear flows with "pom-pom" constitutive equations. *Journal of Rheology*, 43(4):873, 1999.

- [106] R. J. Blackwell, O. G. Harlen, and T. C. B. McLeish. Theoretical Linear and Nonlinear Rheology of Symmetric Treelike Polymer Melts. *Macromolecules*, 34(8):2579–2596, 2001.
- [107] P. P. Tas. *Film blowing - from polymer to product*. Phd thesis, Technische Universiteit Eindhoven, 1994.
- [108] Z. Wang, J. Ju, J. Yang, Z. Ma, D. Liu, K. Cui, H. Yang, J. Chang, N. Huang, and L. Li. The non-equilibrium phase diagrams of flow-induced crystallization and melting of polyethylene. *Scientific Reports*, 6:32968, 2016.
- [109] A. J. Pennings, R. J. van der Hooft, A. R. Postema, W. Hoogsteen, and G. ten Brinke. High-speed gel-spinning of ultra-high molecular weight polyethylene. *Polymer Bulletin*, 16(2-3):167–174, 1986.
- [110] A. Pennings. Further studies on the high-speed gel-spinning of ultra-high molecular weight polyethylene. *Polymer Bulletin*, 23(3), 1990.
- [111] B. Shen, Y. Liang, J. A. Kornfield, and C. C. Han. Mechanism for Shish Formation under Shear Flow: An Interpretation from an in Situ Morphological Study. *Macromolecules*, 46(4):1528–1542, 2013.
- [112] S. Kimata, T. Sakurai, Y. Nozue, T. Kasahara, N. Yamaguchi, T. Karino, M. Shibayama, and J. A. Kornfield. Molecular Basis of the Shish-Kebab Morphology in Polymer Crystallization. *Science*, 316(5827):1014–1017, 2007.
- [113] L. Yang, R. H. Somani, I. Sics, B. S. Hsiao, R. Kolb, and D. Lohse. The role of high molecular weight chains in flow-induced crystallization precursor structures. *Journal of Physics: Condensed Matter*, 18(36):S2421–S2436, 2006.
- [114] A. Nogales, B. Hsiao, R. Somani, S. Srinivas, A. Tsou, F. Balta-Calleja, and T. Ezquerro. Shear-induced crystallization of isotactic polypropylene with different molecular weight distributions: in situ small- and wide-angle X-ray scattering studies. *Polymer*, 42(12):5247–5256, 2001.
- [115] Y. Ogino, H. Fukushima, G. Matsuba, N. Takahashi, K. Nishida, and T. Kanaya. Effects of high molecular weight component on crystallization of polyethylene under shear flow. *Polymer*, 47(15):5669–5677, 2006.
- [116] G. Matsuba, S. Sakamoto, Y. Ogino, K. Nishida, and T. Kanaya. Crystallization of Polyethylene Blends under Shear Flow. Effects of Crystallization Temperature and Ultrahigh Molecular Weight Component. *Macromolecules*, 40(20):7270–7275, 2007.
- [117] S. Costanzo, Q. Huang, G. Ianniruberto, G. Marrucci, O. Hassager, and D. Vlassopoulos. Shear and Extensional Rheology of Polystyrene Melts and Solutions with the Same Number of Entanglements. *Macromolecules*, 49(10):3925–3935, 2016.

- [118] K. Cui, Z. Ma, Z. Wang, Y. Ji, D. Liu, N. Huang, L. Chen, W. Zhang, and L. Li. Kinetic Process of Shish Formation: From Stretched Network to Stabilized Nuclei. *Macromolecules*, 48(15):5276–5285, 2015.
- [119] M. F. Diop, W. R. Burghardt, and J. M. Torkelson. Well-mixed blends of HDPE and ultrahigh molecular weight polyethylene with major improvements in impact strength achieved via solid-state shear pulverization. *Polymer (United Kingdom)*, 55(19):4948–4958, 2014.
- [120] L. Yang, R. H. Somani, I. Sics, B. S. Hsiao, R. Kolb, H. Fruitwala, and C. Ong. Shear-Induced Crystallization Precursor Studies in Model Polyethylene Blends by in-Situ Rheo-SAXS and Rheo-WAXD. *Macromolecules*, 37(13):4845–4859, 2004.
- [121] J. Honerkamp and J. Weese. A nonlinear regularization method for the calculation of relaxation spectra. *Rheologica Acta*, 32(1):65–73, 1993.
- [122] C. Gabriel, J. Kaschta, and H. Münstedt. Influence of molecular structure on rheological properties of polyethylenes. *Rheologica Acta*, 37(1):7–20, 1998.
- [123] H. Münstedt and F. R. Schwarzl. *Deformation and flow of polymeric materials*. Springer Berlin Heidelberg, 2014.
- [124] E. Narimissa and M. H. Wagner. A hierarchical multimode molecular stress function model for linear polymer melts in extensional flows. *Journal of Rheology*, 60(4):625–636, 2016.
- [125] M. H. Wagner, H. Bastian, P. Hachmann, J. Meissner, S. Kurzbeck, H. Münstedt, and F. Langouche. The strain-hardening behaviour of linear and long-chain-branched polyolefin melts in extensional flows. *Rheologica Acta*, 39(2):97–109, 2000.
- [126] O. Urakawa, M. Takahashi, T. Masuda, and N. G. Ebrahimi. Damping Functions and Chain Relaxation in Uniaxial and Biaxial Extensions: Comparison with the Doi-Edwards Theory. *Macromolecules*, 28(21):7196–7201, 1995.
- [127] P. Currie. Constitutive equations for polymer melts predicted by the Doi-Edwards and Curtiss-Bird kinetic theory models. *Journal of Non-Newtonian Fluid Mechanics*, 11(1-2):53–68, 1982.
- [128] O. Hassager and R. Hansen. Constitutive equations for the Doi-Edwards model without independent alignment. *Rheologica Acta*, 49(6):555–562, 2010.
- [129] H. Zuidema, G. W. M. Peters, and H. E. H. Meijer. Development and Validation of a Recoverable Strain-Based Model for Flow-Induced Crystallization of Polymers. *Macromolecular Theory and Simulations*, 10(5):447–460, 2001.

- [130] Y. Ohta, H. Murase, H. Sugiyama, and H. Yasuda. Non-newtonian rheological behavior of semi-dilute ultra-high molecular weight polyethylene solution in gel-spinning process. 1: Concentration effect on the fundamental rheological properties. *Polymer Engineering & Science*, 40(11):2414–2422, 2000.
- [131] H. Murase, T. Kume, T. Hashimoto, Y. Ohta, and T. Mizukami. Shear-Induced Concentration Fluctuations in Ultrahigh Molecular Weight Polyethylene Solutions. 1. Observation above the Melting Point. *Macromolecules*, 28(23):7724–7729, 1995.
- [132] H. Murase, T. Kume, T. Hashimoto, and Y. Ohta. Shear-Induced Structures in Semidilute Solution of Ultrahigh Molecular Weight Polyethylene at Temperature Close to Equilibrium Dissolution Temperature. *Macromolecules*, 38(15):6656–6665, 2005.
- [133] H. Murase, T. Kume, T. Hashimoto, and Y. Ohta. Time Evolution of Structures under Shear-Induced Phase Separation and Crystallization in Semidilute Solution of Ultrahigh Molecular Weight Polyethylene †. *Macromolecules*, 38(21):8719–8728, 2005.
- [134] H. Murase, Y. Ohta, and T. Hashimoto. A New Scenario of Shish-Kebab Formation from Homogeneous Solutions of Entangled Polymers: Visualization of Structure Evolution along the Fiber Spinning Line. *Macromolecules*, 44(18):7335–7350, 2011.
- [135] P. Flory. *Principles of Polymer Chemistry*. Cornell University Press,, 1953.
- [136] M. Kapnistos, A. Hinrichs, D. Vlassopoulos, S. H. Anastasiadis, A. Stammer, and B. A. Wolf. Rheology of a Lower Critical Solution Temperature Binary Polymer Blend in the Homogeneous , Phase-Separated , and Transitional Regimes. *Macromolecules*, 29(22):7155–7163, 1996.
- [137] M. Cromer, M. C. Villet, G. H. Fredrickson, L. Gary Leal, R. Stepanyan, and M. J. H. Bulters. Concentration fluctuations in polymer solutions under extensional flow. *Journal of Rheology*, 57(4):1211–1235, 2013.
- [138] B. S. Hsiao, F. Zuo, Y. Mao, and C. Schick. Experimental Techniques. In *Handbook of Polymer Crystallization*, pages 1–30. John Wiley & Sons, Inc., 2013.
- [139] G. Kumaraswamy, R. K. Verma, J. A. Kornfield, F. Yeh, and B. S. Hsiao. Shear-enhanced crystallization in isotactic polypropylene. In-situ synchrotron SAXS and WAXD. *Macromolecules*, 37(24):9005–9017, 2004.
- [140] T. Yan, B. Zhao, Y. Cong, Y. Fang, S. Cheng, L. Li, G. Pan, Z. Wang, X. Li, and F. Bian. Critical Strain for Shish-Kebab Formation. *Macromolecules*, 43(2):602–605, 2010.

- [141] Z. Wang, F. Su, Y. Ji, H. Yang, N. Tian, J. Chang, L. Meng, and L. bin Li. Transition from chain- to crystal-network in extension induced crystallization of isotactic polypropylene. *Journal of Rheology*, 61(4):589–599, 2017.
- [142] S. Coppola, L. Balzano, E. Giuffredi, P. L. Maffettone, and N. Grizzuti. Effects of the degree of undercooling on flow induced crystallization in polymer melts. *Polymer*, 45(10):3249–3256, 2004.
- [143] G. W. Park and G. Ianniruberto. Flow-Induced Nematic Interaction and Friction Reduction Successfully Describe PS Melt and Solution Data in Extension Startup and Relaxation. *Macromolecules*, 50(12):4787–4796, 2017.
- [144] L. Balzano, Z. Ma, D. Cavallo, T. B. van Erp, L. Fernandez-Ballester, and G. W. M. Peters. Molecular Aspects of the Formation of Shish-Kebab in Isotactic Polypropylene. *Macromolecules*, 49(10):3799–3809, 2016.
- [145] M. van Drongelen, P. Roozmond, E. Troisi, A. Doufas, and G. Peters. Characterization of the primary and secondary crystallization kinetics of a linear low-density polyethylene in quiescent- and flow-conditions. *Polymer*, 76:254–270, 2015.
- [146] Z. Wang, Z. Ma, and L. Li. Flow-Induced Crystallization of Polymers: Molecular and Thermodynamic Considerations. *Macromolecules*, 49(5):1505–1517, 2016.
- [147] F. G. Hamad, R. H. Colby, and S. T. Milner. Lifetime of Flow-Induced Precursors in Isotactic Polypropylene. *Macromolecules*, 48(19):7286–7299, 2015.

**Danish Polymer Centre**  
**Department of Chemical and Biochemical Engineering**  
**Technical University of Denmark**  
Søltofts Plads, Building 229  
2800 Kgs. Lyngby  
Denmark

Phone: +45 45 25 28 00  
Web: [www.kt.dtu.dk](http://www.kt.dtu.dk)